AD-A181 249 INVESTIGATIONS OF EURASIAN SEISMIC SOURCES AND UPPER MANTLE STRUCTURE(U) MASSACHUSETTS INST OF TECH CAMBRIDGE DEPT OF EARTH ATMOSPHERI.. T H JORDAN 1/3

UNCLASSIFIED 06 MAR 87 AFGL-TR-87-0101 F19628-85-K-0024 F/G 8/11 NL

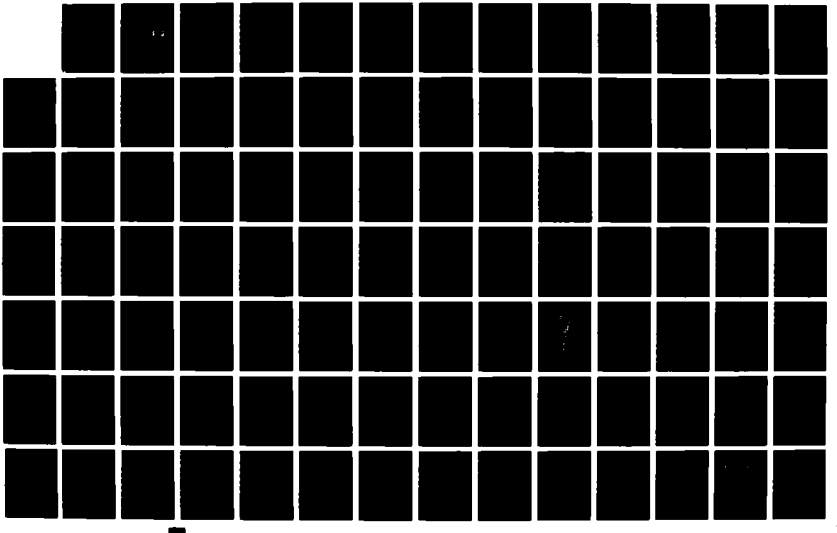

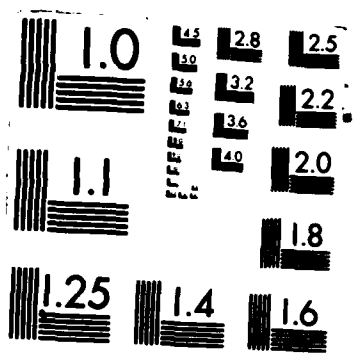
1.0
1.1
1.25
1.4
1.6
1.8
2.0
2.2
2.5
2.8
3.2
3.6
4.0
4.5
5.0
5.6

AFGL-TR-87-0101

Investigations of Eurasian Seismic Sources and Upper Mantle Structure

Thomas H. Jordan

Massachusetts Institute of Technology
Department of Earth, Atmospheric &
Planetary Sciences
Cambridge, MA 02139

Date of Report: March 6, 1987

Final Report
7 December 1984 - 6 December 1986

Approved for public release; distribution unlimited.

AIR FORCE GEOPHYSICS LABORATORY
AIR FORCE SYSTEMS COMMAND
UNITED STATES AIR FORCE
HANSCOM AIR FORCE BASE, MASSACHUSETTS 01731

REPORT DOCUMENTATION PAGE

1a. REPORT SECURITY CLASSIFICATION Unclassified	1b. RESTRICTIVE MARKINGS
2a. SECURITY CLASSIFICATION AUTHORITY	3. DISTRIBUTION/AVAILABILITY OF REPORT Approved for public release; distribution unlimited.
2b. DECLASSIFICATION/DOWNGRADING SCHEDULE	
4. PERFORMING ORGANIZATION REPORT NUMBER(S)	5. MONITORING ORGANIZATION REPORT NUMBER(S) AFGL-TR-87-0101
6a. NAME OF PERFORMING ORGANIZATION Massachusetts Inst of Technology 6b. OFFICE SYMBOL (If applicable)	7a. NAME OF MONITORING ORGANIZATION Air Force Geophysics Laboratory
6c. ADDRESS (City, State and ZIP Code) Dept of Earth, Atmospheric & Planetary Sciences Cambridge, MA 02139	7b. ADDRESS (City, State and ZIP Code) Hanscom AFB Massachusetts 01731
8a. NAME OF FUNDING/SPONSORING ORGANIZATION 8b. OFFICE SYMBOL (If applicable)	9. PROCUREMENT INSTRUMENT IDENTIFICATION NUMBER F19628-85-K-0024
8c. ADDRESS (City, State and ZIP Code)	10. SOURCE OF FUNDING NOS. PROGRAM ELEMENT NO.: 61101F; PROJECT NO.: 5A10; TASK NO.: DA; WORK UNIT NO.: AM
11. TITLE (Include Security Classification) Investigations of Eurasian Seismic Sources and Upper Mantle Structure	
12. PERSONAL AUTHOR(S) Thomas H. Jordan	
13a. TYPE OF REPORT Final Report 13b. TIME COVERED FROM 12/7/84 TO 12/6/86	14. DATE OF REPORT (Yr., Mo., Day) 87-3-6 15. PAGE COUNT 248
16. SUPPLEMENTARY NOTATION	

17. COSATI CODES			18. SUBJECT TERMS (Continue on reverse if necessary and identify by block number)
FIELD	GROUP	SUB. GR.	Eurasian Seismic Sources Upper Mantle Structure

19. ABSTRACT (Continue on reverse if necessary and identify by block number)

This report summarizes the research completed under AFGL Contract #F19628-85-K-0024. The first section describes the observations of first-order mantle reverberations and develops techniques for using these data to constrain upper-mantle velocity and attenuation structure. The second section discusses our work on the waveform inversion of higher-mode surface waves, and the third analyzes the resolving power of the higher-mode data set. The fourth section reviews recent progress in seismic tomography and its implications for mantle dynamics. The fifth section applies methods for the representation and recovery of seismic source parameters to two recent earthquakes.

20. DISTRIBUTION/AVAILABILITY OF ABSTRACT UNCLASSIFIED/UNLIMITED ☐ SAME AS RPT. ☐ DTIC USERS ☐	21. ABSTRACT SECURITY CLASSIFICATION Unclassified	
22a. NAME OF RESPONSIBLE INDIVIDUAL James Lewkowicz	22b. TELEPHONE NUMBER (Include Area Code) (617)377-3028	22c. OFFICE SYMBOL AFGL/LWH

Table of Contents

OBSERVATIONS OF FIRST-ORDER MANTLE REVERBERATIONS*

BY JUSTIN REVENAUGH AND THOMAS H. JORDAN

ABSTRACT

We have observed first-order mantle reverberations, specifically *SH*-polarized ScS_n and $sScS_n$ phases reflected at near normal incidence from upper mantle discontinuities, as discrete phases on long-period digital seismograms of the *HGLP* and *SRO* networks. Such arrivals correspond to an n or n+1 member dynamic ray family denoted by $\{ScS_n, Sd^{\pm}S\}$, where n is the multiple number of the parent phase, 'd^+' signifies a reflection from the top of an internal discontinuity at depth d, and 'd^-' signifies a reflection from the bottom. The travel times and attenuation of these phases place important constraints on the nature of the transition zone. We have applied the phase equalization and stacking algorithm of Jordan and Sipkin (1977) to obtain the differential attenuation operators of $\{sScS_n, S650^+S\} - sScS_n$ and $\{ScS_n, S650^-S\} - ScS_n$ phase pairs from deep-focus Tonga events recorded by the *HGLP* station KIP on the island of Oahu. The apparent Q's of the zeroth- and first-order reverberations over the frequency band 10-30 mHz have been inverted for the average quality factors of the upper mantle (Q_{UM}) and lower mantle (Q_{LM}) and the reflection coefficient of the 650-km discontinuity (R_{650}). At 20 mHz the results are: $Q_{UM} = 82 \pm 18$, $Q_{LM} = 231 \pm 60$ and $|R_{650}| = 0.080 \pm 0.004$ (at normal incidence). The Q_{LM} estimate is significantly less than recent normal mode solutions, suggesting that lower mantle attenuation structure is frequency dependent at very low frequencies. We have measured the differential travel times between the first-order reverberations $\{sScS_n, S400^+S\}$ and $\{sScS_n, S650^+S\}$, which yields a direct estimate of the vertical shear-wave travel time between the discontinuities along the Tonga-to-KIP path. The observed two-way time, 92.2 ± 1.5 s, is less than predicted by some recent oceanic upper-mantle models, indicating either a smaller separation of the discontinuities and/or greater shear velocity in the transition zone. Measurements of differential travel times between first-order reverberations and multiple *ScS* phases suggest that the former is more likely and are consistent with depths of 400 and 650 km for the transition zone discontinuities. Observations of first-order mantle reverberations can potentially provide unique constraints on lateral heterogeneity of the earth's mantle, especially within the transition zone.

INTRODUCTION

The reverberative interval, here defined as that portion of the seismogram between the surface-wave train propagating along the minor arc and the first body-wave arrivals from the major arc, is dominated by core-reflected phases such as ScS_n and other reverberations from internal discontinuities (Figure 1). On a transversely polarized (*SH*) seismogram, free from mode conversions and core-penetrating phases, these reverberations can be conveniently classified by the number of internal mantle reflections they experience; ScS_n and $sScS_n$ phases suffer no such reflections and are therefore termed zeroth-order reverberations, those experiencing one reflection are first-order reverberations, and so forth. Throughout this paper, the term *mantle reverberations* will be used to designate these *SH*-polarized shear waves.

The properties of the zeroth-order reverberations have been investigated in a number of attenuation experiments (*e.g.*, Kovach and Anderson, 1964; Jordan and Sipkin, 1977; Sipkin and Jordan, 1979, 1980b; Nakanishi, 1980) and studies of lateral velocity heterogeneity (*e.g.*, Sipkin and Jordan, 1976, 1980a; Stark and Forsyth, 1983). ScS_n phases sample the entire mantle, have short horizontal path lengths, and are free of some of the complications associated with turning rays. On the same seismogram, ScS_n phases of different reflection number n have similar propagation paths near their endpoints, so that their differential properties are insensitive to instrument response, source structure, and heterogeneity beneath the receivers. Experimental geometries can therefore be devised that selectively sample the upper mantle beneath regions well removed from either seismic sources or receivers. Unfortunately, zeroth-order reverberations alone can resolve only whole-mantle averages. First- and higher-order reverberations, by virtue of the reflections they experience, preferentially sample certain mantle regions and, at least in principle, can be combined with lower-order reverberations to resolve vertically averaged properties of mantle regions delineated by major discontinuities, as well as the impedance contrasts across the discontinuities.

We have observed first-order reverberations--specifically *SH*-polarized ScS_n and $sScS_n$ phases reflected at near normal incidence from upper mantle discontinuities--on long period, digital seismograms of the HGLP and SRO networks (Revenaugh and Jordan, 1985). Such arrivals are the primary contributors to the "background" signal level between the multiple-*ScS* waves in Figure 1. They correspond to a dynamic family of rays which we shall denote by $\{ScS_n,Sd^{\pm}S\}$, where n is the multiple number of the parent (zeroth-order) phase, 'd^+' signifies a reflection from the top of an internal discontinuity at depth d, and 'd^-' signifies a reflection from the bottom. Each $\{ScS_n,Sd^{\pm}S\}$ arrival is comprised of either n or $n+1$ dynamic analogs, depending on the depths of the source and reflector and on whether the reflection is topside or bottomside. In a spherically symmetric earth, these analogs arrive at exactly the same time with the same amplitude and phase to build up an observable arrival; this multiplicity offsets attenuation and helps maintain the amplitude of the ray family as the *ScS* reflection number n increases. (In the real earth, we expect some small degree of destructive interference owing to the splitting of the reverberation by aspherical structure encountered along its various component rays.) Figure 2 illustrates the ray paths for the family $\{ScS_2,S650^+S\}$, the topside reflections from the 650-km discontinuity.

In this paper, we employ observations of zeroth-order and first-order mantle reverberations in the frequency band 10-30 mHz to constrain the shear-wave travel time through the transition zone, the average shear attenuation of the upper and lower mantle, and the reflection coefficient of the

650-km discontinuity.

OBSERVATIONS

We concentrated our initial efforts on paths within the Tonga-Hawaii corridor, which has a favorable geometry for the observation of mantle reverberations. The properties of multiple-*ScS* phases along this relatively uniform swath of old oceanic lithosphere have been investigated extensively by Jordan and Sipkin (1977) and Sipkin and Jordan (1979, 1980a,b). Seismograms from the High Gain Long Period (HGLP) instruments at station KIP, on the island of Oahu, were provided to the authors by S. Sipkin of the U.S. Geological Survey. Eleven Tonga-Fiji events with focal depths ranging from 229 km to 602 km were selected for detailed analysis; their source parameters are listed in Table 1. The events had simple time functions, good *SH* signal-to-noise ratios at KIP, and depths of focus large enough to separate the ScS_n and $sScS_n$ phases. At these epicentral distances (40° to 51°), the reverberative interval is about 50 minutes long and includes reverberations with reflection numbers n between two and four (Figure 1).

Synthetic seismograms of the reverberative interval have been generated by both normal-mode summation and geometrical-optics ray theory. Source mechanisms were taken from Richter (1979), Billington (1980), and Giardini (1984), and the HGLP instrument response was adapted from Berg and Chesley (1976). To compute synthetics, we superposed Lerner-Lam and Jordan's (1987) PA2 model of the western-Pacific upper mantle on the PEM lower mantle of Dziewonski et al. (1975). Anelastic structure was specified by Sipkin and Jordan's (1980b, Table 4) Oceanic Model B, a two-layer model constructed to satisfy ScS_n attenuation data. The ray synthetics include all first-order and second-order reverberations from the two transition-zone discontinuities, located at 400 km and 670 km in the PA2 model.

In the ray synthetics, higher-order reverberations from the transition-zone interfaces are ignored, as are all reflections from the first-order discontinuities at the base of the crust (z = 14 km in PA2), the lid-LVZ boundary (98 km), and the base of the LVZ (180 km). The mode synthetics, computed by summing all toroidal free oscillations with frequencies up to 50 mHz, include all reverberations. As discussed by Anderson and Cleary (1974) and Kennett and Nolet (1979), the reverberation structure associated with internal mantle discontinuities is manifested by harmonic variations in the asymptotic spacing of toroidal eigenfrequencies.

Figure 3 compares the mode and ray synthetics with the data from Event 7. The good

agreement validates the approximations made in the ray summation. Some minor differences can be discerned just prior to the arrival of the ScS_n and $sScS_n$ phases, owing primarily to reflections from shallow discontinuities not included in the ray sum, but the reflections from the free surface, CMB, and transition-zone discontinuities clearly dominate the theoretical seismogram. The comparison shows that geometrical optics provides an excellent description of reflections from sharp discontinuties at center frequencies on the order of 30 mHz.

One advantage of the ray method is that it is easily modified to account for aspherical heterogeneity along the ray paths. Sipkin and Jordan (1980b) have obtained evidence for the existence of small-scale lateral variations along the Tonga-KIP path which perturb the ScS_n travel times by about 0.5%. In this preliminary study, we ignore this heterogeneity and deal exclusively with path-averaged radial structure. However, we do correct our ray synthetics by modifying the travel time of each wavelet according to the average ellipticity along the minor arc. Since the reverberations are primarily sensitive to the average thicknesses of the mantle layers, especially for large multiple number n, this approximation is justified. For the equatorial paths used here, the two-way mantle travel time is increased by about 2.5 s. Although not very obvious in Figure 3, this ellipticity correction improves the agreement between the observed and computed travel times of the ScS_n and $sScS_n$ phases.

At frequencies below about 40 mHz, the theoretical seismograms do a reasonably good job of predicting the signal amplitude in the reverberative interval observed along the Tonga-KIP path, indicating that most of the energy between the $ScS_n/sScS_n$ wavegroups results from coherent reflections off the transition-zone discontinuities. However, the observed seismograms tend to be richer in higher frequency energy than the synthetics. Although some of this discrepancy may result from errors in the HGLP instrument response or complications in the source structure, incoherent scattering by small-scale heterogeneities undoubtably plays a role. Because the primary wave field is concentrated at such high horizontal phase velocities, and back-scattered as well as forward-scattered energy can be observed, the study of broad-band signals within the reverberative interval can potentially provide unique constraints on the statistics of scattering at nearly vertical angles of incidence. The detailed investigation of this problem may require data from an array of three-component, broad-band seismometers of the sort proposed by the PASSCAL program (Incorporated Research Institutions for Seismology, 1984).

Figure 4 compares the observed seismogram with the synthetic for Event 4, a deep-focus Fiji earthquake (h = 515 km) at 50° from KIP. To facilitate the identification of individual phases, the

synthetic has been broken up into families of dynamic analogs corresponding to the first-order topside and bottomside reflections from the two transition-zone discontinuities. We also show separately the contributions from the zeroth-order and all second-order reverberations. Since the latter are small compared to the primary internal reflections, we can safely ignore higher-order reverberations. Figure 5 is a similar comparison for the intermediate-focus Event 2 (h = 229 km). Figure 6 compares observed and theoretical seismograms of the reverberative interval for a suite of focal depths.

Particularly prominent in both the data and synthetics are the topside and bottomside reflections from the 650-km (or 670-km) discontinuity. A close look at the differences between the observed and synthetic seismograms reveals that the topside reflections from this interface are consistently earlier and the bottomside reflections consistently later than predicted by PA2, indicating that the shallower depth is more appropriate to the Tonga-KIP corridor (see below); we have therefore employed d = 650 km in our phase designations. The topside reflections $\{ScS_n,S650^+S\}$ and $\{sScS_n,S650^+S\}$ follow their respective parent phases, ScS_n and $sScS_n$, by the two-way travel time through the upper mantle, $T_{650} \approx 280$ s (4.65 min). For events with intermediate hypocentral depths, this time difference is sufficient to isolate $\{ScS_n,S650^+S\}$ from the zeroth-order reverberations, but for deep-focus events, these arrivals appear as an extra swing at the end of $sScS_n$; this waveform complexity can be observed on the seismogram for Event 9 (Figure 6). The $\{sScS_n,S650^+S\}$ phases are isolated from the zeroth-order reverberations at all focal depths and can be observed for n = 2,3,4 on most of the seismograms in Figure 6. The corresponding bottomside reflections $\{ScS_n,S650^-S\}$ and $\{sScS_n,S650^-S\}$ precede ScS_{n+1} and $sScS_{n+1}$, respectively, by T_{650}. Good examples of the former can be seen for n = 2 on the observed seismograms for the deep-focus earthquakes in Figure 6. On the same seismograms, the latter are evident as precursors to ScS_{n+1}, although their signal-to-noise levels are generally lower than the other first-order reverberations from the 650-km interface. As mentioned in our discussion of Figure 3, some of the energy in this precursory interval may be due to reflections from shallow discontinuities not included in the synthetics.

The first-order reverberations for the 400-km discontinuity are predicted to have only 50% of the amplitude of the 650-km reflections, making them more difficult to identify as individual arrivals. T_{400} is only about 180 s, so that $\{ScS_n,S400^+S\}$ and $\{sScS_n,S400^-S\}$ are obscured by $sScS_n$ and ScS_{n+1} for deep-focus events. However, these two phases can be seen on seismograms of intermediate-focus earthquakes; e.g., n = 2 in Figure 5. Although $\{sScS_n,S400^+S\}$ and $\{ScS_n,S400^-S\}$ interfere with $\{ScS_n,S650^+S\}$ and $\{sScS_n,S650^-S\}$ for

intermediate foci, they can be observed as isolated pulses on the deep-event seismograms in Figure 6.

First-order reverberations from discontinuities at depths other than 400 and 650 km may contribute to the signal levels observed in Figure 6. A matched-filtering technique for isolating such reflections will be the subject of a separate report.

RESULTS

A detailed inspection of Figure 6 reveals that $\{sScS_n,S650^+S\}$ on the observed seismograms arrives earlier than predicted by model PA2, whereas $\{sScS_n,S400^+S\}$, when visible, comes in near the model time; Figure 7 shows two examples on an expanded scale. We have used waveform cross-correlation to measure the travel times of these first-order reverberations relative to the parent $sScS_n$ phase. We denote the residuals of these differential times with respect to PA2 by ΔT_{400} and ΔT_{650}. Although the low signal-to-noise ratios induce considerable scatter, fourteen measurements of $\{sScS_n,S400^+S\} - sScS_n$ and twenty measurements of $\{sScS_n,S650^+S\} - sScS_n$ yield $\Delta T_{400} = 0.9 \pm 1.1$ s and $\Delta T_{650} = -8.9 \pm 0.8$ s, respectively, corroborating the visual observations. Because the ray parameters are small, the differential time $\Delta T_{TZ} \equiv \Delta T_{650} - \Delta T_{400}$ is essentially the difference between the observed two-way vertical shear-wave travel time through the transition zone and that calculated from PA2. It is insensitive to near-source structure and the velocities outside the depth interval 400-650 km. Direct measurements of eight phase pairs propagating from Tonga to KIP gives $\Delta T_{TZ} = -10.6 \pm 1.5$ s. Evidently, the vertical shear-wave travel time from the surface to the 400-km discontinuity predicted by PA2 is approximately correct, but either PA2's average transition-zone shear velocity is too low and/or the discontinuity at the base of the transition zone, located at 670 km in PA2, is too deep. Positive residuals are observed for the differential travel time of the bottomside reflection $\{ScS_n,S650^-S\}$ relative to ScS_n, which is more consistent with the latter hypothesis. Raising the discontinuity by 20 km would bring the theoretical times in line with the data. Therefore, the 650-km depth used to identify this discontinuity is more appropriate for the western Pacific.

The transition-zone residuals referred to other oceanic models are also negative; e.g., $\Delta T_{TZ} = -3.1 \pm 1.5$ s for model PEM-O of Dziewonski *et al.* (1975) and -4.6 ± 1.5 s for model ATL of Grand and Helmberger (1984). Both of these models have 400-km discontinuities which are deeper than model PA2 (420 km for PEM-O; 406 km for ATL) and 650-km discontinuities at the same or shallower depths (670 km for PEM-O; 660 km for ATL), leading to the smaller observed

ΔT_{TZ} values. However, ΔT_{400} and ΔT_{650} are significantly negative for both models, implying that the model discontinuities are too deep. Attempting to explain the data by varying depths alone, we again find the data to be satisfied by discontinuities nearer to 400 km and 650 km.

The similarity of ray paths for first-order reverberations and their parent phases allows us to study the path-averaged properties along the differential path element in a manner analogous to multiple *ScS* studies of whole-mantle quality factors(Q_{ScS}). For the phase pair $\{sScS_n, S650^+S\} - sScS_n$, the differential element consists of a 'pegleg' reflection in the upper mantle, so we can estimate the path-averaged attenuation of the upper mantle independently of either the lower-mantle or whole-mantle values. The average attenuation of the upper mantle is defined by the depth integral

$$Q_{UM}^{-1} = \frac{2}{T_{650}} \int_0^{650} v_s^{-1}(z)\, Q_\mu^{-1}(z)\, dz ,$$

where T_{650} is the two-way travel time. We have applied the phase-equalization and stacking algorithm of Jordan and Sipkin (1977) to twenty $\{sScS_n, S650^+S\} - sScS_n$ phase pairs observed along the Tonga-to-KIP path to obtain a least-squares estimate of the upper-mantle attenuation operator. The moduli and phases at eight frequencies from 13 to 33 mHz are plotted in Figure 8. Although the individual amplitude estimates have a large uncertainty, the frequency variation of amplitude and phase is consistent with the linear, causal, constant-Q assumption. Attributing all the differential attenuation to the upper mantle and using PA2 to calculate propagation corrections and reflection coefficients, we obtain $Q_{UM} = 70 \pm 15$ for the average upper-mantle quality factor. This result is consistent with Nakanishi's (1980) estimate of 70 for the Sea of Japan above 552-km depth, derived from $sScS_n/ScS_n$ spectral ratios, and with Sipkin and Jordan's (1980b) Oceanic Model B, which has $Q_{UM} = 84$.

By a similar procedure, we obtained an average lower-mantle quality factor of $Q_{LM} = 190 \pm 60$ from eighteen $\{ScS_n, S650^-S\} - ScS_n$ phase pairs. As seen in Figure 9, the moduli and phases estimated for this differential response operator are more uncertain, a consequence of the fact that the amplitude and attenuation of the bottomside reflections from 650 km are smaller than the topside reflections.

As a consistency check, we also estimated the whole-mantle attenuation operator by phase-equalizing and stacking ScS_n phases from the same set of seismograms. Twenty six phase

pairs yielded $Q_{ScS} = 150 \pm 10$. (In their comprehensive study, Sipkin and Jordan (1980b) found $Q_{ScS} = 141 \pm 16$ along the Tonga-KIP corridor and 155 ± 11 for all paths crossing the western Pacific.) A whole-mantle attenuation factor can be calculated from the first-order reverberations using the relation

$$Q^{-1}_{ScS} = (T_{UM} Q^{-1}_{UM} + T_{LM} Q^{-1}_{LM})/T_{ScS}$$

Combining the Q_{LM} and Q_{UM} estimates from Figures 8 and 9 in this manner gives $Q_{ScS} = 125 \pm 35$, which is less than the direct measurement, though not significantly so. In other words, there is a slight inconsistency between the whole-mantle quality factors obtained from the first-order and zeroth-order reverberations.

The estimates of Q_{UM} and Q_{LM} quoted above are only apparent values, however, since they depend strongly on the reflection coefficient R_{650}, whose magnitude was set at the PA2 value of 0.0835 (all reflection coefficients are stated at normal incidence). In principle, the three apparent Q observations can be used to solve for the reflection coefficient at the 650-km discontinuity, as well as the integrated attenuation factors in the two mantle layers. To perform this refinement, we linearized the relation between Q^{-1} and R_{650} about a reference frequency of 20 mHz and an angle of incidence of 10°, the average for the reverberations we employed. We sought perturbations to apparent values of Q^{-1}_{UM} and Q^{-1}_{LM} and the PA2 value of R_{650} that matched the attenuation data for both the first-order and zeroth-order reverberations. The perturbations were thus required to satisfy the system of equations:

$$\begin{pmatrix} 1 & 0 & -2/\omega T_{UM} \\ 0 & 1 & -2/\omega T_{LM} \\ T_{UM}/T_{ScS} & T_{LM}/T_{ScS} & 0 \end{pmatrix} \begin{pmatrix} \delta Q^{-1}_{UM} \\ \delta Q^{-1}_{LM} \\ \delta R_{650} \end{pmatrix} = \begin{pmatrix} 0 \\ 0 \\ \Delta Q^{-1}_{ScS} \end{pmatrix}.$$

where ΔQ^{-1}_{ScS} is the difference between the ScS attenuation factors estimated from zeroth-order and first-order reverberations. Evaluating the least-squares solution of this system at $\omega = 20$ mHz, we obtained the revised values

$$Q_{UM} = 82 \pm 18,$$
$$Q_{LM} = 231 \pm 60,$$
$$|R_{650}| = 0.080 \pm 0.004.$$

The uncertainties in the average quality factors are fairly large and strongly correlated with the uncertainty in the reflection coefficient (Figure 10), but the values are consistent with Sipkin and Jordan's (1980b) Oceanic Model B, for which $Q_{UM} = 84$ and $Q_{LM} = 225$. Recent free-oscillation solutions give lower-mantle Q_μ values of 304 (Masters and Gilbert, 1982), 350 [model QMU of Sailor and Dziewonski (1978)] and 360 [model SL8 of Anderson and Hart (1978)] over the mode band 3-10 mHz. These are substantially greater than our 10–30-mHz estimate of 231 ± 60, suggesting Q_μ is frequency dependent in the lower mantle. Therefore, the low Q_{LM} obtained from this experiment corroborates Sipkin and Jordan's (1979, 1980b) arguments that the average attenuation of the lower mantle decreases with frequency between 3 and 30 Mhz.

We note that our reflection-coefficient estimate is relatively insensitive to errors in Q (Figures 10a and 10b), indicating that first-order reverberations can be used to measure R_{650} very stably. The result for this path differs only slightly from the starting model PA2, which satisfies the higher-mode Rayleigh-wave data for the western Pacific, and is consistent with the velocity structures constrained by both body waves and normal modes. For example, model ATL of Grand and Helmberger (1984) gives $|R_{650}| = 0.080$ and PREM (Dziewonski and Anderson, 1981) gives 0.077. Hence, within the Tonga-KIP corridor, the impedance contrast across the 650-km discontinuity is similar to these models.

On the other hand, estimates of the P-wave reflection coefficient made from *P'650P'/P'P'* amplitude ratios at similar angles of incidence, but much higher frequencies (~1 Hz), are greater than predicted values; the observations range from 7 to 13%, compared to 6-7% predicted by most earth models (Richards, 1972; Lees *et al.*, 1983). There are, however, several potential sources of bias in these observations, such as proximity to caustics, locally tuned reflectors and scattering of *P'P'* in the upper mantle and crust. To the extent that the discontinuity structure of the western Pacific is representative, the robustness of our estimate of R_{650} suggests that one or more of these sources of bias are affecting the *P'650P'* observations. Estimates obtained from the amplitude ratio of integrated *P'P'* and *P'650P'* wavetrains give results more compatible with our value (Lees et al., 1983), suggesting that scattering may be the primary source of bias.

DISCUSSION

In this brief report, we have documented (evidently for the first time) that first-order mantle reverberations can be observed as discrete phases on the seismogram. Moreover, we have demonstrated that these reflected phases can be used to estimate the average properties of the major

mantle layers over relatively short path lengths. The agreement obtained between data and ray-theory seismograms implies that most of the low-frequency energy arriving within the reverberative interval can be parameterized by eight quantities; namely, the travel times and average Q's for the upper mantle, transition zone and lower mantle, and the reflection coefficients of the 400-km and 650-km discontinuities. Further refinement of the methodology, specifically the use of full waveform inversion, should allow the estimation of these eight parameters from a single seismogram. It may then be possible to recover from large sets of seismograms the lateral variations in these eight quantities by tomographic techniques.

ACKNOWLEDGMENTS

We are grateful to S. Sipkin of the U.S. Geological Survey for supplying us with HGLP data, and to A. L. Lerner-Lam for his assistance with the normal-mode synthetics. This work was supported by DARPA under AFGL contract #F19628-85-K-0024 and by a Shell Doctoral Fellowship (JR).

REFERENCES

Anderson, D. L. and R. S. Hart (1978). Attenuation models of the earth, *Phys. Earth Planet. Inter.* **16**, 289-306.

Anderson, R. S. and J. R. Cleary (1974). Asymptotic structure in torsional free oscillations of the Earth - I. Overtone structure, *Geophys. J. R. Astr. Soc.*, **39**, 241-268.

Berg, E. and D. M. Chesley (1976). Automated high-precision amplitude and phase calibration of seismic systems, *Bull. Seism. Soc. Am.* **66**, 1413-1424.

Billington, S. (1980). The morphology and tectonics of the subducted lithosphere in the Tonga-Fiji-Kermadec region from seismicity and focal mechanism solutions, *Ph.D. Dissertation*, Cornell, 280 pp.

Dziewonski, A. M. and D. L. Anderson (1981). Preliminary reference earth model, *Phys. Earth Planet. Inter.* **25**, 297-356.

Dziewonski, A. M., A. L. Hales and E. R. Lapwood (1975). Parametrically simple earth models consistent with geophysical data, *Phys. Earth Planet. Inter.* **10**, 12-48.

Giardini, D. (1984). Systematic analysis of deep seismicity: 200 centroid-moment tensor solutions for earthquakes between 1977 and 1980, *Geophys. J. R. Astr. Soc.* **77**, 883-914.

Grand, S. P. and D. V. Helmberger (1984). Upper mantle shear structure beneath the northwest Atlantic ocean, *J. Geophys. Res.*, **89**, 11465-11475.

Jordan, T. H. and S. A. Sipkin (1977). Estimation of the attenuation operator for multiple *ScS* waves, *Geophys. Res. Lett.* **4**, 167-170.

Kennett, B. and G. Nolet (1979). The influence of upper mantle discontinuities on the toroidal free oscillations of the Earth, *Geophys. J. R. Astr. Soc.*, **56**, 283-308.

Kovach, R. L. and D. L. Anderson (1964). Attenuation of shear waves in the upper and lower mantle, *Bull. Seism. Soc. Am.* **54**, 1855-1864.

Lees, A. L., M. S. T. Bukowinski and R. Jeanloz (1983). Reflection properties of phase transition and compositional change models of the 670-km discontinuity, *J. Geophys. Res.* **88**, 8145-8159.

Lerner-Lam, A. L. and T. H. Jordan (1987). How thick are the continents?, *J. Geophys. Res.* (in press).

Masters, G. and F. Gilbert (1982). Attenuation in the Earth at low frequencies, *Phil. Trans. R. Soc. Lond. A* 308, 479-522.

Nakanishi, I. (1980). Attenuation of shear waves in the upper mantle beneath the Sea of Japan, *J. Phys. Earth* 28, 261-272.

Revenaugh, J. S. and T. H. Jordan (1985). Observation of first-order mantle reverberations, (abstract) *EOS Trans. AGU*, 66, 967.

Richards, P. G. (1972). Seismic waves reflected from velocity gradient anomalies within the Earth's upper mantle, *J. Geophys.*, 38, 517-527.

Richter, F. M. (1979). Focal mechanisms and seismic energy release of deep and intermediate earthquakes in the Tonga-Kermadec region and their bearing on the depth extent of mantle flow, *J. Geophys. Res.* 84, 6783-6795.

Sailor, R. V. and A. M. Dziewonski (1978). Measurements and interpretation of normal mode attenuation, *Geophys. J. R. astr. Soc.* 53, 559-581.

Sipkin, S. A. and T. H. Jordan (1976). Lateral heterogeneity of the upper mantle determined from the travel times of multiple ScS, *J. Geophys. Res.* 81, 6307-6320.

Sipkin, S. A. and T. H. Jordan (1979). Frequency dependence of Q_{ScS}, *Bull. Seism. Soc. Am.* 69, 1055-1079.

Sipkin, S. A. and T. H. Jordan (1980a). Multiple ScS travel times in the western Pacific: implications for mantle heterogeneity, *J. Geophys. Res.* 85, 853-861.

Sipkin, S. A. and T. H. Jordan (1980b). Regional variation of Q_{ScS}, *Bull. Seism. Soc. Am.* 70, 1071-1102.

Stark, M. and D. W. Forsyth (1983). The geoid, small-scale convection, and the differential travel time anomalies of shear waves in the Central Indian ocean, *J. Geophys. Res.* 88, 2273-2288.

DEPARTMENT OF EARTH, ATMOSPHERIC AND PLANETARY SCIENCES
MASSACHUSETTS INSTITUTE OF TECHNOLOGY
CAMBRIDGE, MASSACHUSETTS 02139

TABLE 1

PARAMETERS OF THE EVENTS USED IN THIS STUDY

No.	Date	Origin Time (UTC)	Latitude (deg.)	Longitude (deg.)	Depth (km)	m_b	Δ to KIP (deg.)
1	21 July 1973	04:19:13.7	24.83S	179.19 W	419	5.9	50.37
2	19 Dec 1973	12:55:51.1	20.60S	176.32 W	229	5.8	45.43
3	28 Dec 1973	05:31:03.8	23.88S	180.00 W	526	6.4	49.85
4	23 Mar 1974	14:28:33.0	23.92S	179.88 E	515	6.1	49.94
5	04 June 1974	04:14:13.8	15.89S	175.04 W	275	6.0	40.67
6	21 Oct 1974	04:12:28.7	17.97S	178.49 W	596	6.0	43.99
7	22 Feb 1975	22:04:33.5	24.98S	178.88 W	373	6.2	50.38
8	19 Nov 1975	06:18:33.7	24.01S	179.09 E	551	5.8	50.35
9	03 Feb 1976	12:27:30.1	25.14S	179.69 E	477	5.8	51.10
10	21 Jan 1977	06:11:05.3	18.06S	178.37 W	602	5.8	44.01
11	06 July 1977	11:28:31.5	21.00S	178.58 W	597	5.8	46.70

FIGURE CAPTIONS

Figure 1. *SH*-polarized seismogram of a deep-focus earthquake in the Tonga seismic zone (Event 9 of Table 1) recorded by the HGLP station KIP on the island of Oahu. Time is minutes after origin time. The reverberative interval is defined as the portion of the seismogram between the fundamental-mode surface wave (G) and the first arrivals propagating along the major arc (SSS_2). The signal levels between the ScS_n and $sScS_n$ phases (zeroth-order reverberations) are dominated by first-order reverberations corresponding to reflections from internal mantle discontinuities.

Figure 2. Schematic ray paths for the three members of the family $\{ScS_2,S650^+S\}$, the first-order reverberation from the topside of the 650-km discontinuity, for a surface-focus source. The three phases shown here are dynamic analogs; i.e., they have the same travel time, amplitude and phase at the receiver and thus constructively interfere to produce an observable arrival.

Figure 3. *SH*-polarized seismograms showing the reverberative interval at KIP for Event 7 (h = 373 km, Δ = 50.4°). Top three traces are synthetic seismograms generated by normal-mode summation, geometrical-optics ray summation, and ray summation with an approximate ellipticity correction. Bottom trace is data from the HGLP instruments at KIP. Ray summation includes only zeroth-order reverberations and first- and second-order reverberations from the 400-km and 650-km discontinuities; they do not include direct arrivals along the minor and major arcs, nor any reverberations from other mantle discontinuities. Normal-mode summation is complete to 50 mHz. Time is minutes after origin time.

Figure 4. *SH*-polarized seismograms showing the reverberative interval for Event 4 (h = 515 km, Δ = 49.9°). Bottom trace is data; all others are synthetics computed by geometrical-optics ray theory. The trace labeled *zeroth* comprises the ScS_n and $sScS_n$ phases, beginning with ScS_2 and $sScS_2$. The traces labelled 650^+, 400^+, 650^- and 400^- are the first-order reverberations reflecting from the top and bottom of the 650-km and 400-km discontinuities, respectively. The trace labelled *2nd* contains all the second-order reverberations from the 400-km and 650-km discontinuities. The first-order reverberations decay slowly with increasing multiple number n, owing to the constructive interference among members of each dynamic ray family. Time is minutes after origin time.

Figure 5. *SH*-polarized seismograms showing the reverberative interval for Event 2 (h = 229 km,

Δ = 45.4°). Bottom trace is data; all others are synthetics computed by geometrical-optics ray theory. Conventions are the same as in Figure 4.

Figure 6. *SH*-polarized seismograms of the reverberative interval at KIP for seven earthquakes in the Tonga seismic zone arrayed according to focal depth. The numbers along the left hand margin refer to the events listed in Table 1. The bottom trace for each event is data; the top trace is the ray-summation synthetic containing zeroth-order reverberations and first- and second-order reverberations from the 400-km and 650-km discontinuities. Time is minutes after origin time. Large-amplitude phases seen in the data beyond ~76 min are the first arrivals along the major arc; they are not included in the synthetics.

Figure 7. (a) Enlargement of the seismogram near the arrival of $sScS_3$ for Event 3. Top trace is data; bottom trace is ray-theory synthetic. (b) Similar enlargement of the seismogram near $sScS_2$ for Event 9. The first-order reverberations $\{ScS_3,S400^+S\}$ and $\{ScS_3,S650^+S\}$ are labeled. The latter shows an offset between the data and the PA2-predicted arrival times based on a discontinuity at 670 km. The magnitude of the offset on these and other seismograms is consistent with a discontinuity depth of 650 km beneath the western Pacific.

Figure 8. Modulus and phase of the upper-mantle differential response operator, showing estimates derived from twenty $\{sScS_n,S650^+S\}$- $sScS_n$ phase pairs using the phase-equalization and stacking algorithm of Jordan and Sipkin (1977). Lines represent predicted differential response for a linear, causal, constant-Q model with Q_{UM} = 70. Error bars are one-sigma.

Figure 9. Modulus and phase of the lower-mantle differential response operator, showing estimates derived from eighteen $\{sScS_n,S650^-S\}$- $sScS_n$ phase pairs using the phase-equalization and stacking algorithm of Jordan and Sipkin (1977). Lines represent predicted differential response for a linear, causal, constant-Q model with Q_{LM} = 190. Error bars are one-sigma.

Figure 10. Estimates and one-sigma error ellipses obtained by inverting the apparent Q's from zeroth-order and first-order reverberations for self-consistent estimates of Q_{UM}, Q_{LM}, and R_{650}. *(a)* Correlation between R_{650} and Q_{UM}^{-1}. *(b)* Correlation between R_{650} and Q_{LM}^{-1}. *(c)* Correlation between Q_{UM}^{-1} and Q_{LM}^{-1}.

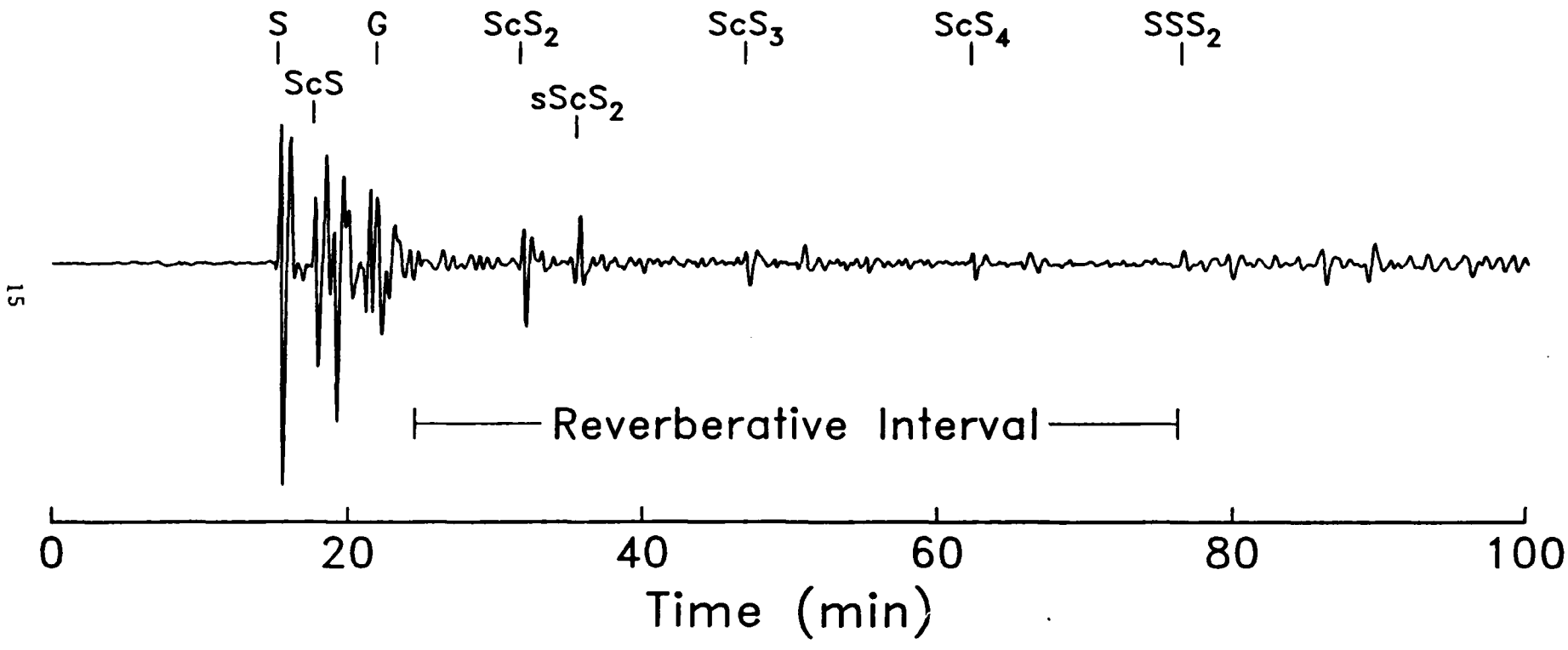
S
ScS
G
ScS2
sScS2
ScS3
ScS4
SSS2
Reverberative Interval
0
20
40
60
80
100
Time (min)

Figure 1

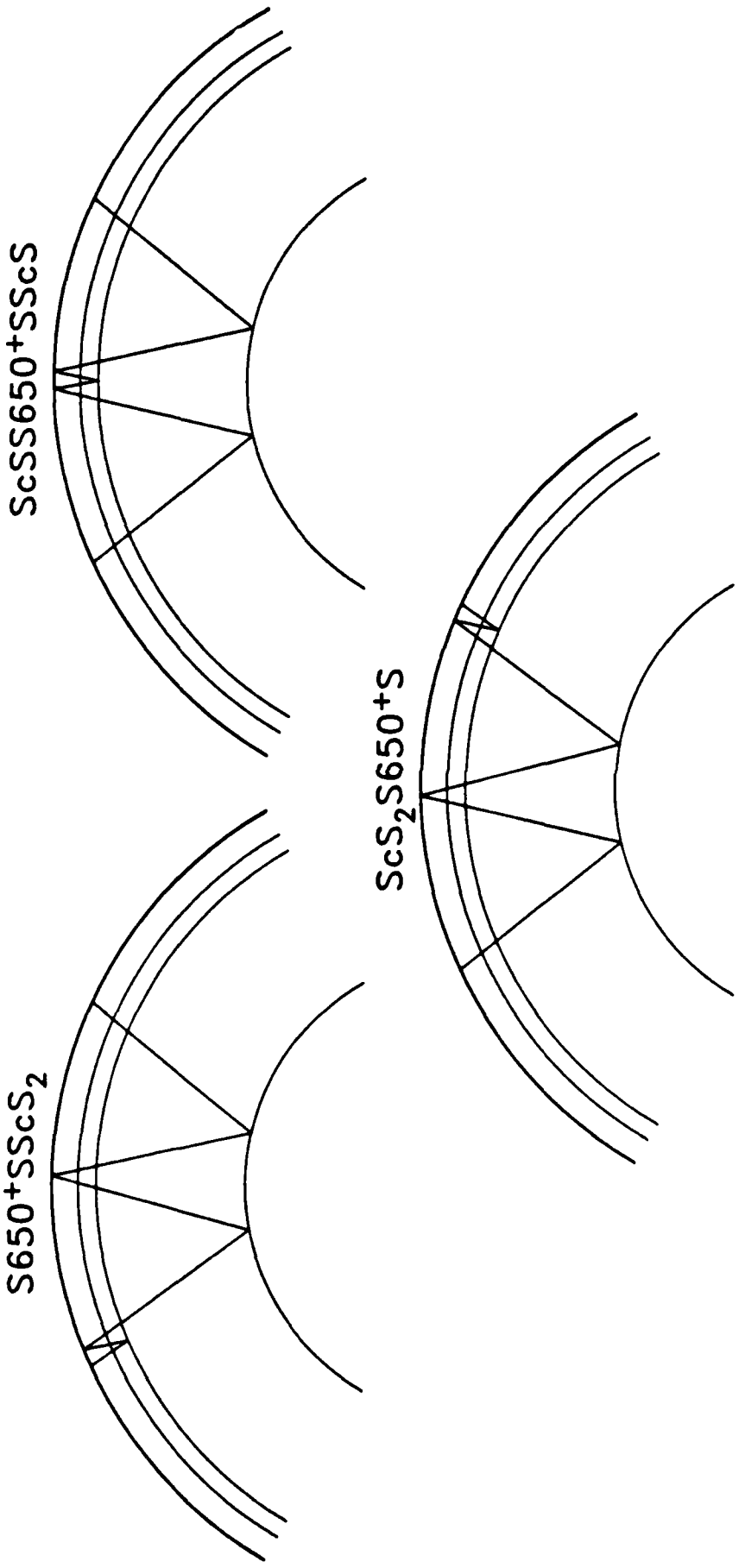

Figure 2

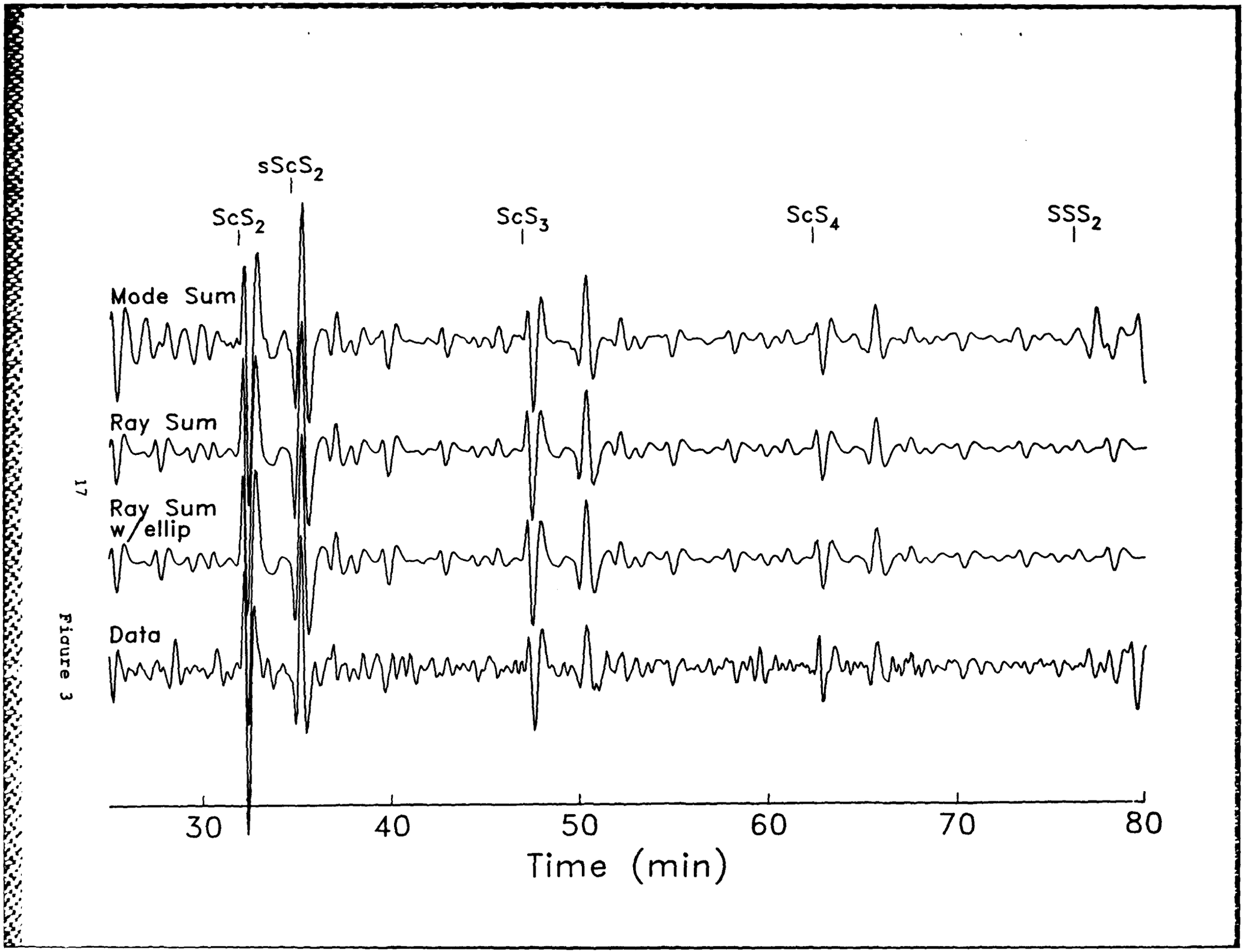
sScS2
ScS2
ScS3
ScS4
SSS2
Mode Sum
Ray Sum
Ray Sum w/ellip
Data
30
40
50
60
70
80
Time (min)

Figure 3

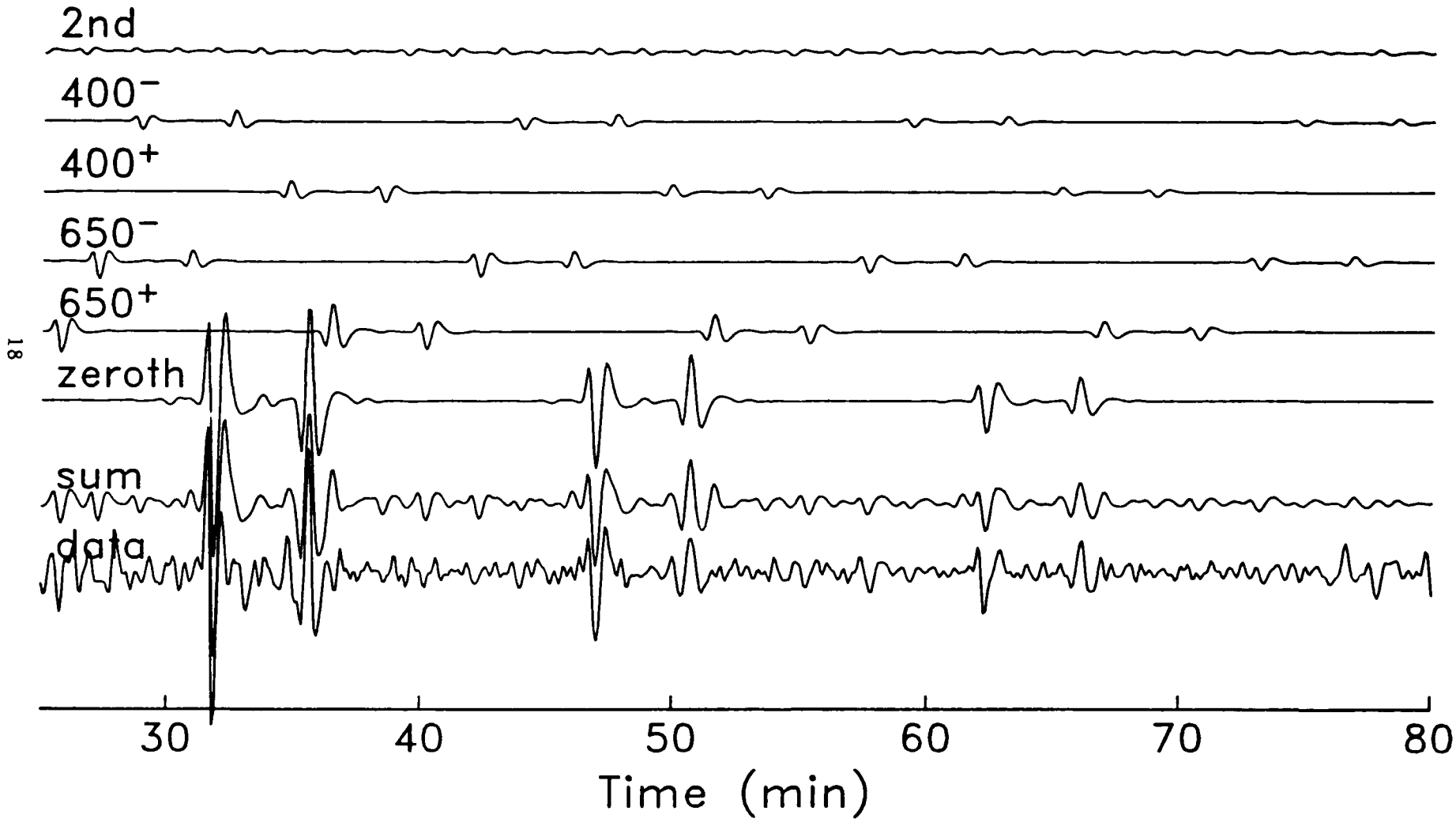

Figure 4

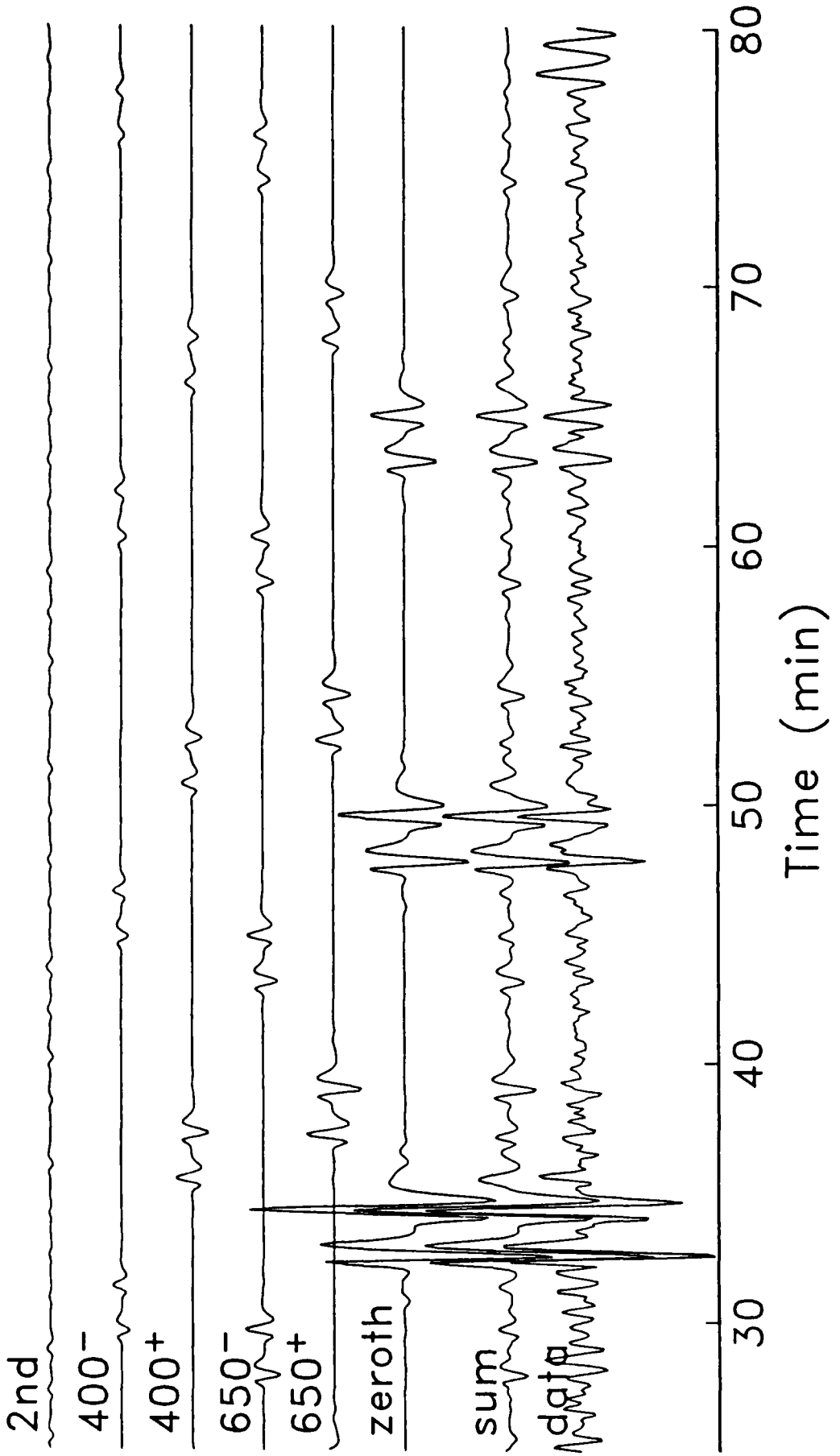

Figure 5

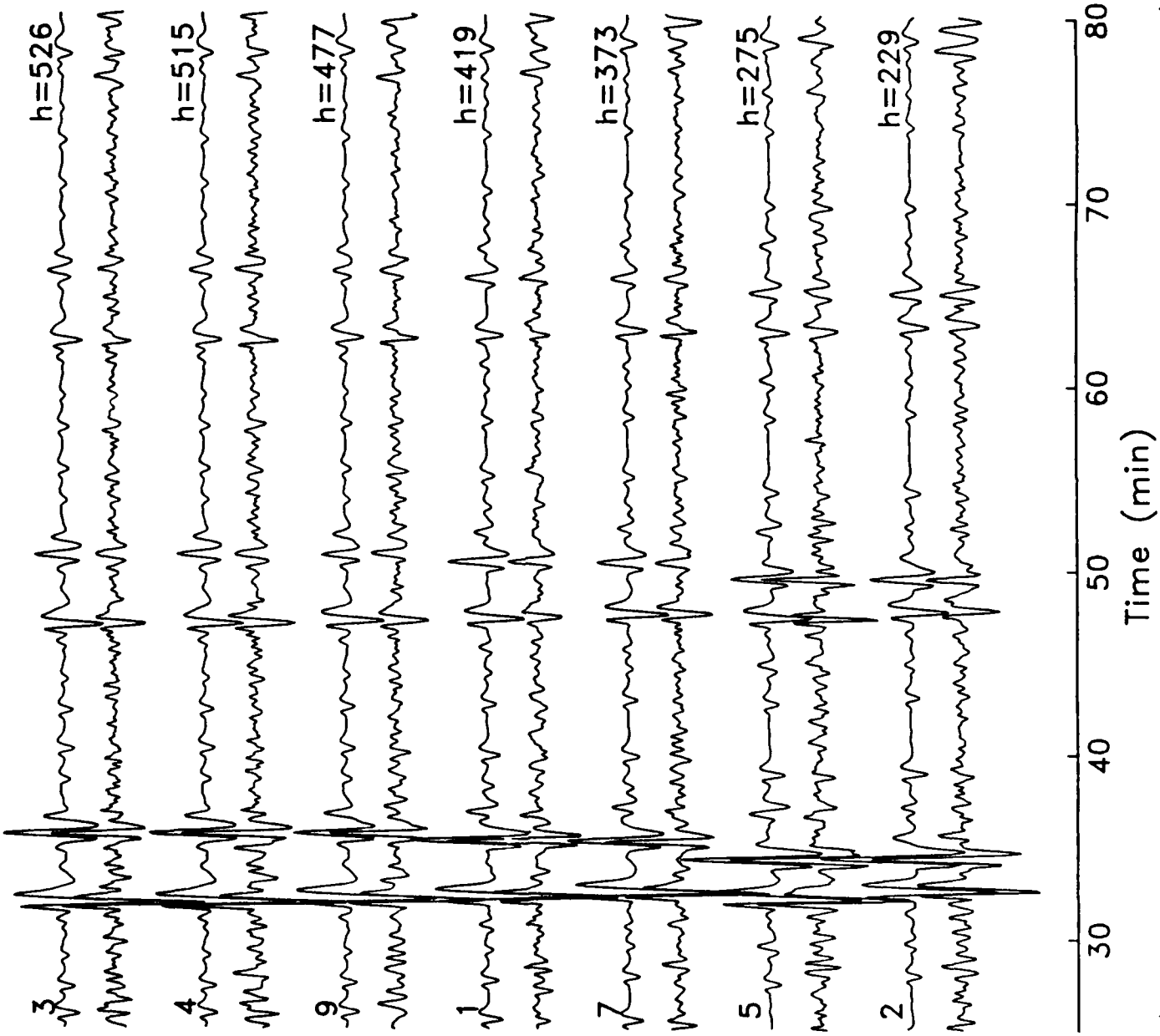
h=526
h=515
h=477
h=419
h=373
h=275
h=229
3
4
9
1
7
5
2
30
40
50
60
70
80
Time (min)

Figure 6

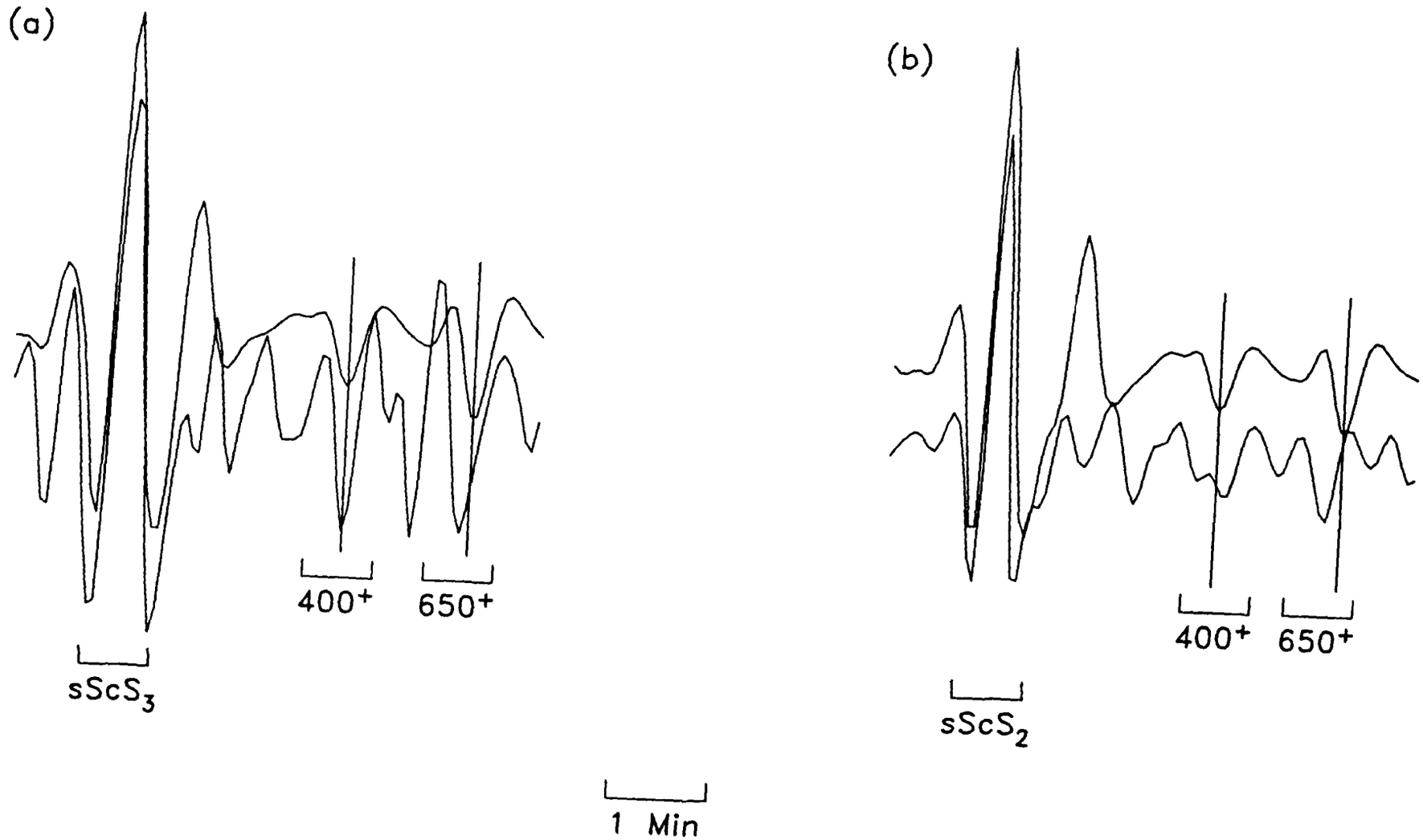

Figure 7

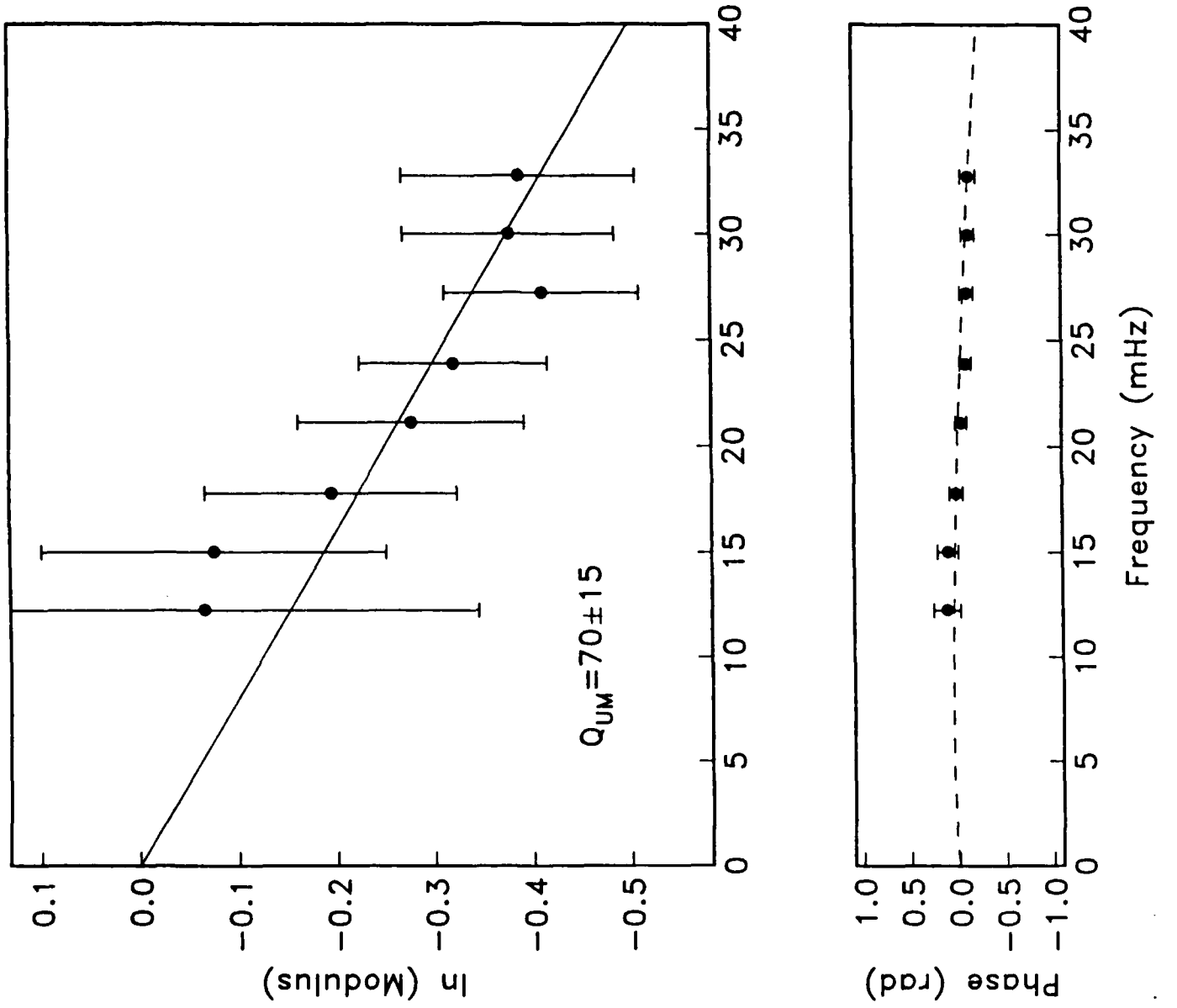
ln (Modulus)
0.1
0.0
-0.1
-0.2
-0.3
-0.4
-0.5
Q_{UM}=70±15
0
5
10
15
20
25
30
35
40
Phase (rad)
1.0
0.5
0.0
-0.5
-1.0
Frequency (mHz)

Figure 8

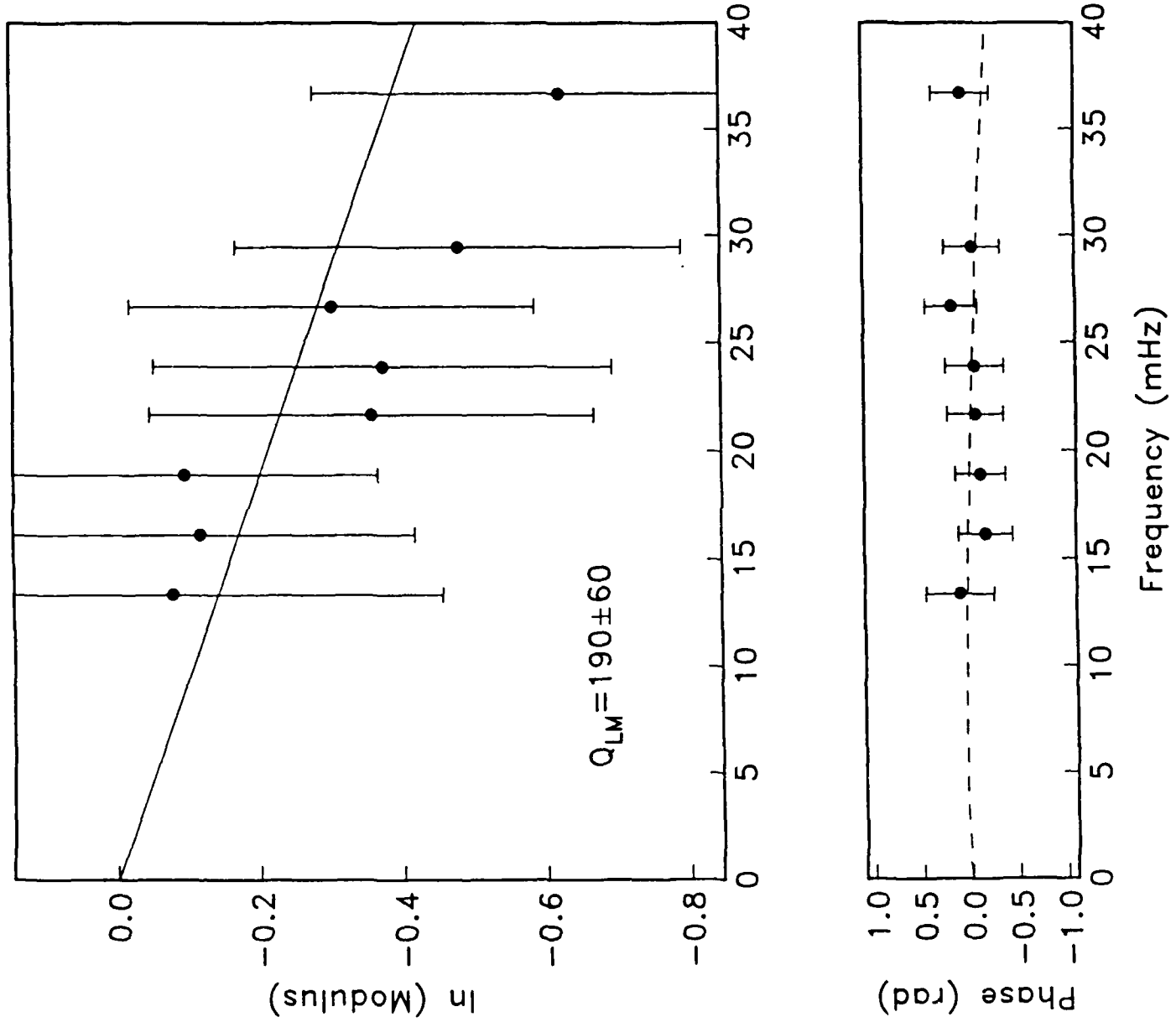
ln (Modulus)
0.0
-0.2
-0.4
-0.6
-0.8
0
5
10
15
20
25
30
35
40
Q_{LM}=190±60
Phase (rad)
1.0
0.5
0.0
-0.5
-1.0
Frequency (mHz)

Figure 9

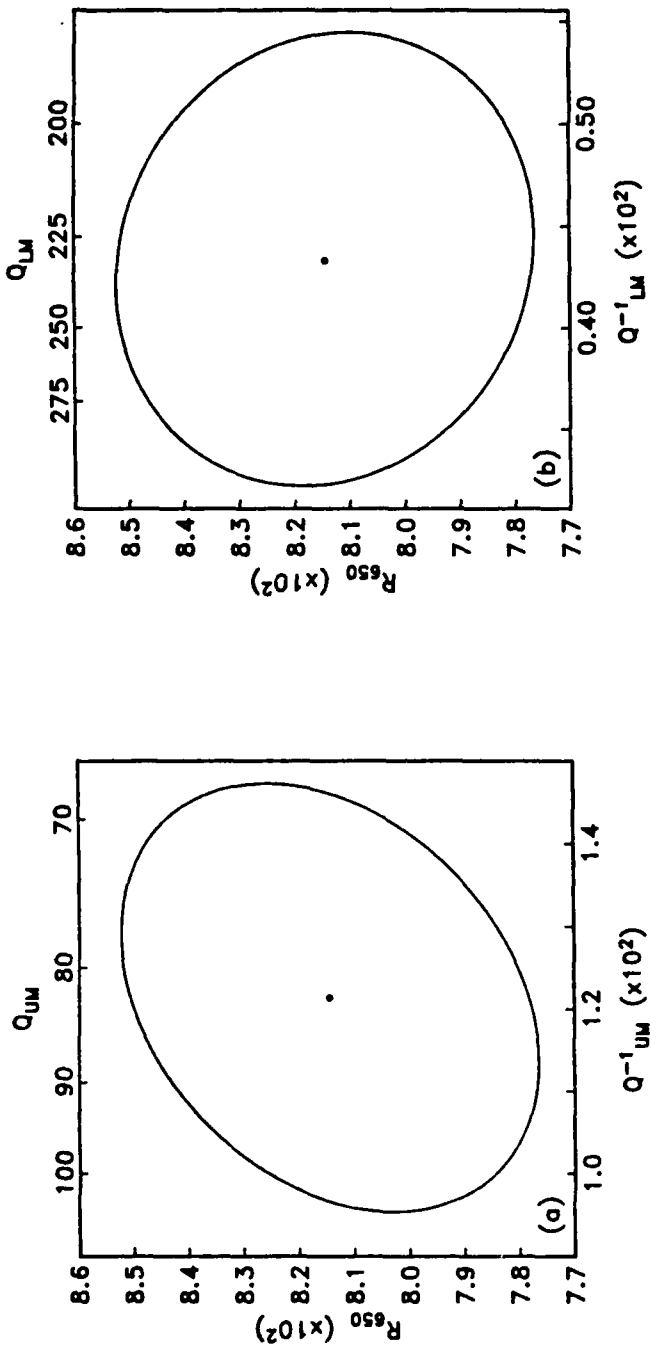

Figure 10

How Thick Are the Continents?

ARTHUR L. LERNER-LAM

Lamont-Doherty Geological Observatory, Columbia University

THOMAS H. JORDAN

Department of Earth, Atmospheric and Planetary Sciences
Massachusetts Institute of Technology

Abstract: Fundamental and higher-mode Rayleigh waves propagating across northern Eurasia and the western Pacific Ocean have been used to construct a lower bound on z_{max}, the maximum depth extent of seismic velocity differences between old continents and old oceans. The waveform-inversion procedure of *Lerner-Lam and Jordan* [1983a] has been modified to search for optimum path-averaged elastic models whose significant structural differences are "squeezed" above some chosen depth z^*. An inversion with z^* unconstrained yielded two reference models, EU0 for northern Eurasia and PA0 for the western Pacific. The reference models provide good fits to the vertical-component waveform data out to the fourth overtone, but they are characterized by substantial velocity differences extending into the lower mantle. Resolving-power calculations suggests that such deep variations are not required by the data. Using EU0 and PA0 as starting models for additional inversions and their fit to the data to define noise levels, we constructed a pair of acceptable models, EU2 and PA2, whose shear-velocity differences are squeezed above $z^* = 400$ km and compressional-velocity differences squeezed above $z^* = 220$ km. However, we were unable to obtain a successful fit to the data with $z^* = 220$ km for shear velocity, and thus reject the hypothesis $z_{max} \leq 220$ km in favor of the alternative $z_{max} > 220$ km. The EU2–PA2 differences in shear velocities are generally consistent with other recent seismological models of continent-ocean heterogeneity, including the regional models SNA and ATL of *Grand and Helmberger* [1984a,b] and the global model M84C of *Woodhouse and Dziewonski* [1984]. The average upper-mantle shear velocities in our *P-SV* models are substantially lower than Grand and Helmberger's *SH* models, however; this discrepancy cannot be explained by simple path differences and points to the importance of polarization anisotropy. The high-velocity zones underlying the ancient cratonic nuclei are inferred to be part of the tectosphere, translating coherently with the continents during plate motions. This and other studies of upper-mantle structure are more consistent with *Jordan's* [1978] thick-plate, compositionally stratified model of the cratons than with the conventional thin-plate models of continental thermal structure.

INTRODUCTION

According to the conventional theory of plate tectonics, the differences between continents and oceans are confined to the crust and shallow levels of the mantle; the thermal, mechanical and chemical properties of the lithospheric plates below a depth of 100 km or so are largely independent of crustal type and can be couched in a unified boundary-layer model of thermal evolution [*Crough and Thompson*, 1976; *Kono and Amano*, 1978; *Sclater et al.*, 1980, 1981]. This conventional thermal-boundary-layer model has considerable intuitive appeal, but it provides no simple explanation for a diverse set of observations related to the structure and tectonic durability of the ancient continental nuclei, including the low temperatures, high seismic velocities, and peculiar geochemical and petrological properties of the sub-cratonic upper mantle [*Jordan*, 1978, 1981a]. An alternative view maintains that the stable interior cratons of the continents are underlain by an extensive layer of anomalous mantle material, geographically variable and up to several hundred kilometers thick, which translates with the continents during plate motions.

Since it was first proposed a decade ago [*Jordan*, 1975], the hypothesis that the plates in old continental regions are much thicker on the average than even the oldest oceanic plate has been controversial. In a review of seismological and other evidence, *Anderson* [1979] dismissed the thick-plate hypothesis, stating, "Continental roots extend no deeper than about 150-200 km... Oceanic and continental geotherms converge above about 200 km and become less steep than the melting gradient at greater depth." *Sclater et al.* [1980, 1981] presented a comprehensive analysis of plate thermal structure in both continental and oceanic regions and concluded "that the range in possible geotherms at depths below 100 to 150 km under continents and oceans overlaps and that the thermal structure beneath an old stable continent is indistinguishable from that beneath an old ocean were it at equilibrium. Oceans and continents are part of the same thermal system" [*Sclater et al.*, 1981, p.11535].

The hypothesis that old continents and old oceans have similar thermal and compositional structures can be tested by seismological experiments. It has been appreciated for some time that the average shear velocity in the upper mantle beneath the continental cratons is significantly greater than the averages for oceanic and orogenic provinces [*Brune and Dorman*, 1963; *Toksöz and Anderson*, 1966; *Knopoff*, 1972], but the depth extent of these variations has been uncertain. Nearly all of the early work on continent-ocean heterogeneity was based on measurements of the phase and group velocities of fundamental-mode surface waves. In the frequency band typically observed by traveling-wave methods (0.005-0.10 Hz), the fundamental-mode data alone have poor resolving power below about 200 km, and they are particularly insensitive to structural variations in

the 200-400 km depth range. *Dziewonski* [1971], for example, was able to satisfy a large, global set of fundamental-mode Rayleigh-wave data with models where the only significant differences between continental and oceanic structures were confined above 200 km.

An additional constraint on continent-ocean heterogeneity was introduced by *Sipkin and Jordan* [1975, 1976], who estimated the lateral variations in the shear-wave slowness integrated over the entire upper mantle from the travel times of ScS_n phases. They showed that the continent-ocean heterogeneity implied by ScS_n travel times was much larger than predicted by *Dziewonski's* [1971] regionalized models. They argued that, since the surface-wave data fix the average velocities in the upper 200 km or so, there must exist substantial lateral variations below this depth that correlate with crustal type. *Jordan* [1975] applied *Parker's* [1972] quadratic programming technique to demonstrate a lower bound of 310 km on the depth extent of continent-ocean heterogeneity from two numbers, *Sipkin and Jordan's* [1975] average *ScS* time difference and *Kanamori's* [1970] difference in the average phase velocities of 190-s Love waves. He also stated that a more comprehensive set of fundamental-mode data increased the lower bound to 400 km.

In a parallel study of ScS_2-*ScS* differential travel times, *Okal and Anderson* [1975] argued that old continents and old oceans have similar residuals and concluded that the difference between them could be confined above 200 km. The discrepancy between the Sipkin-Jordan and Okal-Anderson results was used by *Sclater et al.* [1980] to argue against the thick-plate model. However, *Sipkin and Jordan* [1980] obtained a much larger set of ScS_m-ScS_n differential travel times from the newly installed digital seismic networks. They found a one-way travel-time difference averaging $+2.6 \pm 0.6$ seconds between western-Pacific and continental paths, compared to an average difference of +3.0 s between old oceans and stable continents according to *Jordan's* [1981b] regionalization of the Sipkin-Jordan ScS_2-*ScS* times.

The thick-plate model has received support from a series of recent studies of higher-mode surface waves and multiply reflected body waves. The dispersion of higher-mode Rayleigh waves is capable of giving good resolution in the 200-400 km depth range, but the measurement of this dispersion is complicated by the interference of the various mode groups. Frequency-wavenumber filtering methods have been developed which can successfully separate the mode branches out to the fourth overtone when applied to seismometer arrays having apertures on the order of 1000 km [*Nolet*, 1975, 1977; *Nolet and Panza*, 1976; *Cara*, 1978]. Data has been obtained in the band 0.01-0.05 Hz by these techniques over Eurasian [*Nolet*, 1975, 1977] and Pacific [*Cara*, 1979] paths. Inversions show substantially greater (>0.2 km/s) shear velocities beneath Eurasia in the depth range 100-200 km; differences as large as 0.1 km/s persist to depths exceeding 250 km

[*Cara et al.*, 1980].

The interval on the seismogram corresponding to the group arrival times of the higher modes lies between the direct *S* phase and the fundamental-mode Rayleigh wave. Advances in numerical techniques now make it possible to obtain relatively complete synthetic seismograms for this interval from spherically symmetric structures. To take advantage of this capability, *Lerner-Lam and Jordan* [1983a] developed an inversion procedure which derives the path-averaged properties of the crust and upper mantle by fitting the observed time-domain waveforms with synthetic waveforms. Because the complex interference patterns among the higher-mode wave groups are modeled directly without attempting to extract the spectral properties of individual higher modes, the method is less susceptible to bias than mode-separation techniques, and good resolution of path-averaged structures can be obtained to depths of 500 km or so with smaller data sets [*Lerner-Lam*, 1982; *Gee et al.*, 1985]. *Lerner-Lam and Jordan* [1983a] applied this procedure to study the Eurasian continent and the Pacific Ocean using source and receiver distributions similar to those employed by *Cara* [1979] and *Cara et al.* [1980]. They obtained continental and oceanic models with shear-velocity differences to depths on the order of 400 km, consistent with the previous studies.

The waveforms on the seismogram between the direct *S* phase and the fundamental-mode surface waves can be described in terms of the interference of higher modes or, equivalently, as the superposition of various body waves, of which the multiply reflected *S* waves are the most prominent. The modal decomposition used by *Lerner-Lam and Jordan* [1983a] is more convenient for the *P-SV* system, whereas the body-wave decomposition is more convenient for *SH*. *Grand and Helmberger* [1984a,b; 1985] have applied a body-wave analysis to the study of *SH*-polarized *S*, *SS* and *SSS* waves in the distance range 10° to 80° and have obtained models satisfying the travel times and waveforms. Their *SH*-velocity structure for stable North America (model SNA) is considerably faster than that for the western Atlantic Ocean (model ATL) in the 200-400 km depth range. Grand and Helmberger inverted their data by trial-and-error and have not yet attempted any formal resolving power analysis, but it is clear that their resolution of structural details below 200 km is at least comparable, if not superior, to the *P-SV* data used by *Lerner-Lam and Jordan* [1983a] and *Gee et al.* [1985].

Complementary to these high-resolution, regionalized studies of body-wave propagation and surface-wave dispersion are global analyses of aspherical structure based upon spherical harmonic representations of lateral heterogeneity [*Masters et al.*, 1982; *Woodhouse and Dziewonski*, 1984; *Nataf et al.*, 1984]. Because no *a priori* assumptions about the relationship between upper-mantle

structure and surface tectonics are made, models parameterized in this manner can be used to assess the importance of continent-ocean heterogeneity relative to other (sub-tectospheric) features and to examine the structural variability among the different continental cratons and old ocean basins. *Woodhouse and Dziewonski* [1984] have inverted 2000 seismograms from global digital networks for a degree-eight model of shear velocities. Their method makes use of complete waveforms, including higher-mode data, and should afford reasonably good vertical resolution. They obtain a good correlation between shear-velocity variations in the uppermost mantle and surface tectonics and find that the high velocities associated with the larger cratons persist to depths on the order of 350 km.

Of course, the existence of seismological models with continent-ocean differences to some maximum depth z^* does not imply that such differences must exist. The models are not unique, and all we can really assert is that extending structural differences down to the level z^* is consistent with the data; that is, we cannot reject the null hypothesis that $z_{max} \leq z^*$, where z_{max} is an upper bound on the actual depth of continent-ocean variations. However, if *no* models with differences confined shallower than z^* can be found that fit the data adequately, then we have grounds for rejecting the null hypothesis in favor of the alternative $z_{max} > z^*$. In this paper we combine this hypothesis-testing approach with the waveform-inversion method of *Lerner-Lam and Jordan* [1983a] to determine a useful lower bound on z_{max} from fundamental and higher-mode Rayleigh waves. The surface-wave paths in our data set sample the stable continental platforms of northern Eurasia and the oceanic lithosphere of the western Pacific, the earth's largest expanses of old continent and old ocean.

LINEARIZED WAVEFORM INVERSION

Our formulation is based on the mode-isolation and waveform-inversion techniques described by *Lerner-Lam and Jordan* [1983a]. The observed seismogram is represented as the sum of fundamental ($n = 0$) and higher-mode ($n \geq 1$) surface waves:

$$s(t) = \sum_{n=0}^{N} u_n(t) \tag{1}$$

$u_n(t)$ is the seismogram for the n^{th} mode branch. A synthetic seismogram $\bar{s}(t)$ is calculated for a chosen spherically symmetric earth model $\bar{\mathbf{m}}$:

$$N$$

$$\bar{s}(t) = \sum_{n=0} \bar{u}_n(t) \tag{2}$$

Although a complete representation of the time series requires the summation over an infinite number of branch seismograms, the data discussed in this paper are derived from the interval following the direct *S* phase, where the vertical-component displacements are dominated by modes of low phase velocity, and the mode expansion can be truncated at small N. (Our calculations take $N = 7$.) We have developed an efficient algorithm for computing branch synthetics on a spherical earth; the algorithm is based on adaptive Filon quadrature and reduces computation time by an order of magnitude over conventional mode-summation techniques [*Lerner-Lam and Jordan*, 1983a].

In the time domain, the interference among the higher modes can be strong, complicating traditional methods for estimating dispersion along a particular mode branch. Spatial filtering techniques have been successfully applied to the problem of resolving the dispersion curves of the first several higher modes [*Nolet and Panza*, 1976; *Cara*, 1978; *Cara et al.*, 1980], but large seismograph arrays are required to achieve this separation, and the potential bias due to cross-mode contamination is difficult to evaluate. Complete mode separation is not necessary, however, if the interference among the higher modes can be modeled by seismogram synthesis; the waveforms can then be inverted directly [*Dziewonski and Steim*, 1982; *Lerner-Lam and Jordan*, 1983a; *Woodhouse and Dziewonski*, 1984; *Nolet et al.*, 1986].

Our approach to waveform inversion is to isolate the information from a particular set of modes by matched filtering individual seismograms in the time domain, without attempting to separate these modes in the frequency-wavenumber domain. To increase the signal-to-noise ratio (SNR) for a specified mode and to reduce the interference from spurious signals and other modes, we use synthetic branch seismograms as matched filters. At the lag time τ we define the observed branch cross-correlation function (BCCF) for the m^{th} mode

$$S_m(\tau) = \bar{u}_m(t)^* s(t) = \int_{-\infty}^{\infty} \bar{u}_m(t)\, s(t+\tau)\, dt \tag{3}$$

and the synthetic BCCF, $\bar{S}_m(\tau) = \bar{u}_m(t)^* \bar{s}(t)$. Since the latter provides an approximate description of both the mode-mode autocorrelation and the cross-mode interference, an appropriate data functional for the structural inverse problem is the differential BCCF,

$$\Delta S_m(\tau) = S_m(\tau) - \bar{S}_m(\tau) \tag{4}$$

We solve for a model perturbation which minimizes to first order a quadratic form in ΔS_m. The quadratic form includes a symmetric taper about zero lag, so that the points near $\tau = 0$, where the SNR is greatest, receive the most weight.

For first-orbit, vertical-component surface waves received at stations far away from the source and its antipode, branch seismograms can be approximated by an integral over continuous wavenumber λ whose asymptotic form is

$$u_n(t) = \int_0^\infty G_n(\lambda,t) \cos \xi_n(\lambda,t)\, d\lambda \tag{5}$$

G_n and ξ_n are amplitude and phase kernels that depend on the displacement and excitation scalars, the source phase, a dispersion function $\omega_n(\lambda)$, and a dissipation function $\alpha_n(\lambda) = \omega_n(\lambda)/2Q_n(\lambda)$. Departures of the real earth from the spherically symmetric reference model $\bar{\mathbf{m}}$ are represented as perturbations to the amplitude and phase kernels:

$$G_n(\lambda,t) = \bar{G}_n(\lambda,t)\ [1 + \gamma_n(\lambda)] \tag{6}$$

$$\xi_n(\lambda,t) = \bar{\xi}_n(\lambda,t) - \Delta\omega_n(\lambda)\, t \tag{7}$$

Here γ_n is the perturbation to the relative amplitude of the n^{th} mode, and $\Delta\omega_n = \omega_n - \bar{\omega}_n$ is the perturbation to its dispersion function. If the excitation and displacement scalars are computed from earth models that are good approximations to the local structure in the vicinity of the source and receiver and the lateral variations along the path are small, then the relative amplitude perturbation is proportional to a perturbation to the specific attenuation Q_n^{-1}:

$$\gamma_n(\lambda) = -\Delta\alpha_n(\lambda)\, t = -\omega_n(\lambda)\, t\, \Delta Q_n^{-1}(\lambda)/2 \tag{8}$$

In terms of the differential BCCF, the linearized forward problem becomes

$$\Delta S_m(\tau) = \sum_{n=0}^{N} \int_0^\infty [B_{mn}(\lambda,\tau)\, \Delta\omega_n(\lambda) + D_{mn}(\lambda,\tau)\, \Delta\alpha_n(\lambda)]\ d\lambda \tag{9}$$

The partial derivatives B_{mn} and D_{mn} can be evaluated by the same adaptive Filon algorithm used to

compute the synthetic seismograms [*Lerner-Lam and Jordan*, 1983a]. The integrals over wavenumber are thereby discretized on the Filon grids $\{\lambda_l: l = 1, 2,..., L_n\}$. A matrix system describing the differential BCCFs for $M+1$ mode branches ($m = 0, 1,..., M \leq N$) at each of P stations ($p = 1, 2,..., P$) is set up by discretizing the cross-correlations at the set of lag times $\{\tau_k = k\,\Delta\tau: k = -K,-K+1,..., 0,..., K-1, K\}$:

$$\mathbf{B}\,\Delta\boldsymbol{\omega} + \mathbf{D}\,\Delta\boldsymbol{\alpha} = \Delta\mathbf{S} \tag{10}$$

The matrices appearing in this linear system have $I = (M+1)\times P\times(2K+1)$ rows and $J = \sum L_n$ columns. In the experiments discussed here, these dimensions are on the order of 10^4 and 10^2, respectively.

The vector $\Delta\mathbf{S}$ can be computed from a set of observed seismograms, and equation (10) inverted for perturbations to the dispersion and the attenuation functions. For the data sets of relatively narrow bandwidth used in this study, the BCCFs are only weakly sensitive to reasonable variations in attenuation structure. Therefore, we can drop the second term on the left-hand side of (10) and parameterize the vector $\Delta\boldsymbol{\omega}$ by a purely elastic perturbation $\Delta\mathbf{m}$ to the radial starting model $\bar{\mathbf{m}}$ using the Fréchet kernels given by *Backus and Gilbert* [1967] and *Woodhouse and Dahlen* [1978]. Equation (10) can then be expressed as the linear system

$$\mathbf{A}\,\Delta\mathbf{m} = \Delta\mathbf{S} \tag{11}$$

where the rows of the matrix **A** are the linear combination of Fréchet kernels specified by the rows of **B**. This constrains the perturbed seismograms to correspond to a realistic earth structure, and if the number of model parameters is small, as in the simple layer parameterizations used here, it can considerably reduce the column dimension of **A**.

Iterative least-squares inversion procedures based on this linearized formulation have been succesfully applied to waveform data in our previous study [*Lerner-Lam and Jordan*, 1983a]. The most severe nonlinearities in the relationship between the BCCFs and earth structure result from the simple trigonometric dependence of the seismogram on the dispersion function $\omega_n(\lambda)$, rather than the more complex dependence of $\omega_n(\lambda)$ on the earth model, so it is numerically advantageous to employ the two-loop iteration scheme discussed in section 5.3 of *Lerner-Lam and Jordan* [1983a] (see also *Nolet et al.* [1986]). We have generally found it possible to avoid spurious local minima associated with "cycle skipping" by initializing the inversions with starting models which approximately fit the arrival times of the principal wave groups. Once convergence is achieved, the resolution and variance

of the final model can be assessed using standard linear techniques [*Lerner-Lam*, 1982; *Gee et al.*, 1985].

DATA SELECTION

To examine the average structural differences between old continents and old oceans we selected two sets of long-period, vertical-component seismograms recorded by the World Wide Standardized Seismographic Network (WWSSN) from five earthquakes in the Kuril-Kamchatka and Japan seismic zones. The first set of paths crossed northern Eurasia to six stations in western Europe, and the second crossed the western Pacific to five stations on oceanic islands (Figure 1). In order to vary the relative excitation levels of the fundamental and higher modes, events were chosen with focal depths ranging from 134 km to 544 km; their source parameters are listed in Table 1. A total of 27 records satisfying visual criteria of signal quality and source simplicity were digitized, detrended, dehelixed, and normalized to the nominal WWSSN instrument response of *Hagiwara* [1958]. These seismograms were then band-passed between 5 and 35 millihertz (mHz) and decimated to an 8-s sample interval.

The 14 paths crossing northern Eurasia are similar to those employed in the higher-mode studies of *Nolet* [1975], *Cara* [1979], and *Cara et al.* [1980] and identical to the data set used by *Lerner-Lam and Jordan* [1983a]. The epicentral distances, which range from 55° to 78°, are sufficient to provide the separation and differential moveout of the multiple-*S* wave groups desirable in the higher-mode analysis. Although the paths sample a variety of tectonic structures, including the marginal basins and active foldbelts east of the Verkhoyansk suture, most of their length traverses the stable continental regions of the Siberian and Russian platforms and the Anabar and Fennoscandian shields.

The 13 western-Pacific paths span epicentral distances from 47° to 84° and cross the largest piece of old oceanic lithosphere now in existence. Higher-mode analysis has been applied to paths traversing the eastern Pacific Ocean [*Cara*, 1979; *Cara et al.*, 1980; *Lerner-Lam and Jordan*, 1983a], but previous surface-wave work on the structure of the western Pacific appears to have been limited to studies of fundamental-mode dispersion [e.g., *Leeds*, 1975; *Yu and Mitchell*, 1979]. The ages sampled by our data range from late Cretaceous to Jurassic, with all paths except those to station KIP lying predominantly on oceanic lithosphere greater than 100 Ma old (Figure 1). The paths were selected to avoid as much as possible the involvement of island arcs and marginal basins.

PATH-AVERAGED STRUCTURES

Despite our efforts to chose "pure-path" geometries that minimize structural complexities, significant heterogeneity undoubtably exists along both sets of paths shown in Figure 1. For example, *Sipkin and Jordan* [1976] used ScS_n-ScS_m differential travel times to document strong lateral gradients associated with the Phanerozoic mobile belts in northern Eurasia; they observed a systematic increase of 8-10 s in two-way vertical travel time across the transition from the Anabar shield to the Arctic Ocean basin, which they associated with tectospheric thinning. A similar study of ScS_n-ScS_m times in the western Pacific revealed variations of comparable magnitude not correlated with crustal age or other obvious manifestations of surface tectonics; these Pacific features appear to be elongated in the direction of plate motion and are possibly related to small-scale convection in the oceanic upper mantle [*Sipkin and Jordan*, 1980].

To quantify how well one-dimensional structures can fit the waveform data, we inverted equation (11) for path-averaged models of northern Eurasia and the western Pacific using a parameterization similar to that adopted for the Preliminary Reference Earth Model (PREM) of *Dziewonski and Anderson* [1981]. The density and seismic velocities in each layer were specified by low-order polynomials in radius, which are taken to be constant or linear in the upper mantle above a depth of 670 km. Perturbations to the model were thus parameterized as perturbations to the polynomial coefficients and the radii of the layer discontinuities. The starting models for both data sets were identical to PREM in the lower mantle and core. The compressional-velocity contrasts at the 400-km and 670-km discontinuities were chosen to match model T7 of *Burdick and Helmberger* [1978] and the shear-velocity contrasts were set equal to those of *Grand and Helmberger's* [1984b] model ATL. Based on the studies of *Belyaevsky et al.* [1973], *Sellevoll* [1980], *Bungum et al.* [1980], *Vinnik and Ryaboy* [1981] and our own work on northern Eurasia [*Lerner-Lam and Jordan*, 1983a,b], we initialized the inversion of the Eurasian data set with a three-layer, 40-km crust, a constant-velocity upper mantle to a depth of 220 km, and linearly increasing velocities between 220 and 400 km. The Eurasian starting model thus had continuous velocity profiles with no low-velocity zone in either *P* or *S*. In the inversion, we allowed the perturbations to develop zeroth-order discontinuities at depths of 100 and 220 km, as well as at the existing 400-km and 670-km discontinuities.

The crust for the western Pacific starting model was a modified version of PEM-O [*Dziewonski et al.*, 1975] with a water-sediment interface deepened to 5 km. Using forward-modeling experiments as a guide, we set the thickness of the constant-velocity lid at 100 km and the base of the low-velocity zone (LVZ) at 180 km. We initially tried a structure with continuous velocities at the base of the LVZ

but found it necessary to introduce a small discontinuous increase at the latter depth to avoid cycle-skipping nonlinearities associated with mismatching the differential travel times between the first higher mode and the fundamental.

Separate inversions were performed on the two data sets using these elastic starting models and the attenuation structure of *Masters and Gilbert* [1983]. The compressional and shear velocities were allowed to vary in each layer, as were the positions of all layer boundaries. Since the data used in this study are relatively insensitive to density structure and the density variations are expected to be small [*Jordan*, 1979], the density profiles were fixed at PREM values in the mantle and at appropriate regional values in the crust. A synthetic complete to the seventh overtone ($N = 7$) was calculated for each of the 27 seismograms, and the records were normalized to unit integrated power. Branch cross-correlation functions were computed out to the fourth overtone ($M = 4$), yielding a total of 70 BCCFs for the Eurasian paths and the 65 BCCFs for the western Pacific paths. To emphasize the signal near zero lag, the BCCFs were tapered with a 240-s Hanning (cosine-squared) window centered about $\tau = 0$. This weighted version of equation (10) was then inverted by a damped least-squares algorithm. Convergence was rapid for both data sets, requiring at most five iterations of the inner loop (seismogram recalculation using the perturbed dispersion) and only one iteration of the outer loop (complete eigenfunction recalculation using the perturbed structure). The final models are designated EU0 and PA0, respectively, and are plotted in Figure 2. The synthetic BCCFs are compared with the observed BCCFs in Figure 3, and the fit to the complete seismogram set is displayed in Figure 4.

In the initial inversions, all seismograms were weighted equally. The resulting models provided good fits to the observed BCCFs except for the three northern Eurasia paths 1-KEV, 1-KON and 3-COP and the single western Pacific path 5-RAR. As seen in Figure 4, the seismograms for the latter two have low SNRs and show significant distortion of the higher-mode wavegroups by noise. The paths 1-KEV and 1-KON were the northernmost of the Eurasian data set, and their fundamental Rayleigh waves are observed to be delayed significantly relative to the other paths (Figure 3). The anomalous group arrival times of these two Rayleigh waves appear to be indicative of the lower shear velocities associated with the rapid northward thinning of the continental tectosphere along the Eurasian margin, a feature clearly evident in *Sipkin and Jordan's* [1976] ScS_n-ScS_m differential travel times (see their Figure 10) and in our own work on surface-wave dispersion [*Lerner-Lam and Jordan*, 1983b] (see also *Feng and Teng* [1983]). Based on these explanations of the misfits, we downweighted the BCCFs for the four seismograms relative to the other data by a factor of ten and reinverted to get the final models, EU0 and PA0. The reweighting resulted in perturbations which were not substantially different from the originals.

The other BCCFs in the two data sets are well matched by the EU0 and PA0 synthetics in both amplitude and phase, including the higher modes excited by the three deep-focus earthquakes. The adequacy of the fit is reflected in the good agreement between the observed and synthetic seismograms plotted in Figure 4. In particular, the complex wave groups preceding the fundamental-mode Rayleigh waves are dominated by the multiply reflected body phases *SS* and *SSS*, and the models satisfy their average travel times. Our higher-mode, *P-SV* waveform inversions are thus comparable to the modeling of multiply reflected *SH* body-waves by *Grand and Helmberger* [1984a,b], although our passband is centered at lower frequency.

Models EU0 and PA0 retain the simplicity of the starting models while providing a much better fit to the waveform data; both achieved variance reductions on the order of 70%. Our success in fitting the data with simple radial models is consistent with the path-averaging assumptions embodied in the inversion procedure. The perturbations to the shear-velocity profiles in the upper 400 km of the mantle are small; in particular, no LVZ is introduced to the Eurasian structure. However, the perturbations to the compressional velocities below 180 km and to shear velocities in the lower mantle, which we expect to be poorly constrained by our data sets, are relatively large.

Assessing the significance of structural contrasts as a function of depth is usually couched as a problem in resolving-power analysis [*Backus and Gilbert*, 1968]. Because our waveform-fitting procedure is formulated as a linearized inverse problem, the resolving power of particular data sets can be estimated using the formal linear theory [*Backus and Gilbert*, 1970; *Menke*, 1984], a major advantage over trial-and-error methods employed in most body-wave studies. Resolution and covariance operators have been computed for data sets comparable to those used in this study by *Lerner-Lam* [1982] and *Gee et al.* [1985]. At marginal error levels of 1%, typical resolving lengths for shear-velocity perturbations vary from less than 100 km at 100-km depth to on the order of 200 km at 600-km depth. The resolving power falls off rapidly below 700 km, which is close to the maximum turning depth of the fourth overtone. In these inversions for isotropic structure, the resolving power for compressional velocity is poor for all depths below the uppermost mantle.

SQUEEZING EXPERIMENTS

The resolving kernels indicate that, although models EU0 and PA0 are compatible with the waveforms, some of the differences in their velocity profiles are not required by the data. Rather than trying to make more specific inferences from resolving-power calculations, which can be difficult, we proceed by testing hypotheses regarding the structural contrasts using an inversion scheme we have

dubbed "squeezing." We distinguish the maximum depth of the differences between two particular path-averaged models, z^*, from the depth below which the actual path-averaged structures become insignificant, z_{max}. Because the models are not unique, they provide no basis for asserting a particular relationship between z^*, which is known, and z_{max}, which is not. If for some specified z^*, however, no acceptable models can be found with differences confined above this depth, then we are justified in rejecting the null hypothesis $z_{max} \leq z^*$ in favor of the alternative $z_{max} > z^*$.

The key to the implementation of this hypothesis-testing procedure lies in the definition of what constitutes "acceptable" models. In this paper, models with constrained values of z^* are taken to be acceptable if they are parameterized the same as EU0 and PA0 and fit the waveform data nearly as well. To formalize the last criterion, we denote quantities calculated for Eurasian and Pacific paths by the subscripts 1 and 2, respectively, and the radial reference models EU0 and PA0 by $\bar{\mathbf{m}}_1$ and $\bar{\mathbf{m}}_2$. If $\Delta\mathbf{m}_1$ and $\Delta\mathbf{m}_2$ are perturbations to these models, $\Delta\mathbf{S}_1$ and $\Delta\mathbf{S}_2$ are the associated perturbations to the data vectors, and $\mathbf{A}_1$ and $\mathbf{A}_2$ are the associated partial derivative operators, then the first-order systems

$$\mathbf{A}_1 \Delta\mathbf{m}_1 = \Delta\mathbf{S}_1 \tag{12}$$

$$\mathbf{A}_2 \Delta\mathbf{m}_2 = \Delta\mathbf{S}_2 \tag{13}$$

can be concatenated into a single equation of the form (11) by defining

$$\mathbf{A} = \begin{bmatrix} \mathbf{A}_1 & \mathbf{0} \\ \mathbf{0} & \mathbf{A}_2 \end{bmatrix}, \quad \Delta\mathbf{m} = \begin{bmatrix} \Delta\mathbf{m}_1 \\ \Delta\mathbf{m}_2 \end{bmatrix}, \quad \Delta\mathbf{S} = \begin{bmatrix} \Delta\mathbf{S}_1 \\ \Delta\mathbf{S}_2 \end{bmatrix} \tag{14}$$

The algorithm used to obtain models EU0 and PA0 is equivalent to the iterative minimization of the squared misfit of the models to the discretized, weighted data vector,

$$\chi_d^2(\bar{\mathbf{m}}) = |\mathbf{S}^{obs} - \mathbf{S}(\bar{\mathbf{m}})|^2 \tag{15}$$

Because the data for the two paths are assumed to be independent and their errors uncorrelated, and no other constraints couple the models, the minimization of (15) decomposes at each iteration into independent linear systems for the perturbations $\Delta\mathbf{m}_1$ and $\Delta\mathbf{m}_2$.

In general, we reject an arbitrary combined-path model $\mathbf{m} = [\mathbf{m}_1\ \mathbf{m}_2]^T$ as an acceptable fit to the

data at the 100 (1-α)% confidence level if

$$k^2 = \chi_d^2(\mathbf{m})/\chi_d^2(\bar{\mathbf{m}}) > \kappa_\alpha^2 \tag{16}$$

where κ_α^2 is some critical value. If N is the number of degrees of freedom in the data vector $\mathbf{S}^{obs}$, and M and $\bar{M}$ are the number of independent model parameters in $\mathbf{m}$ and $\bar{\mathbf{m}}$, respectively, the ratio of the two chi-square distributed variables in (16) is F-distributed with $N - M$ and $N - \bar{M}$ degrees of freedom. The appropriate critical value is therefore

$$\kappa_\alpha^2 = (N-M)\,(N-\bar{M})^{-1}\,F_\alpha[N-M, N-\bar{M}] \tag{17}$$

From standard asymptotic expressions for the F distribution [e.g., *Zelen and Severo*, 1965, p.947] we can derive an approximation to (17) valid for $N - \bar{M} >> M - \bar{M} > 1$:

$$\kappa_\alpha^2 \approx 1 + 2x_\alpha\,(N-\bar{M})^{-1/2} + (M-\bar{M}+2x_\alpha^2)/(N-\bar{M}) \tag{18}$$

where x_α is the critical value for the upper Gaussian tail ($x_{.05} = 1.64$) and terms of order $(N - \bar{M})^{-3/2}$ have been ignored.

Equation (18) shows that the critical value κ_α^2 depends only weakly on the number of degrees of freedom, so an exact measure of N is not required. The number of stochastically independent variables describing the data vector is clearly much less than its dimension, owing to the intrinsic smoothness of the surface-wave dispersion relations. For the relatively narrow-band signals employed in this study, the misfit is governed primarily by the phase delay of the theoretical signal relative to the observed at the center frequency of the band, implying approximately one degree of freedom per BCCF. Any variabilty of the theoretical BCCFs not described by an average phase delay (say, due to differential dispersion) will increase this number, whereas covariance among the data (say, due to mode-mode interference) will decrease it. These effects are countervailing, so to compute κ_α^2 we have adopted $N = 135$, the total number of BCCFs for both paths. For unconstrained models with the same parameterization as EU0 and PA0, $M = \bar{M} = 26$ and $\kappa_{.05}^2 = 1.36$: to fit significantly worse at the 95% confidence level, a combined-path model must yield a squared misfit $\chi_d^2(\mathbf{m})$ at least a third again as large as the EU0/PA0 reference model. This level of error is consistent with the authors' eyeball assessment of what constitutes an unacceptable fit to the observed seismograms. Because of the weak dependence of κ_α^2 on the number of degrees of freedom, decreasing the value of N to 100 or increasing it to 200 changes $\kappa_{.05}^2$ by only ±0.09 units, which would not affect the results of the significance tests presented below.

To search for alternative Eurasian and western Pacific models that optimize the fit to the data yet have path differences restricted at depths greater than z^*, we computed the perturbation $\Delta\mathbf{m}$ which minimized the quadratic form:

$$\varepsilon^2 = |\Delta\mathbf{S} - \mathbf{A}\,\Delta\mathbf{m}|^2 + \eta\,|\Delta\mathbf{m}|^2 + \xi\,(\mathbf{m}_1 - \mathbf{m}_2)^T\,\mathbf{W}(z^*)\,(\mathbf{m}_1 - \mathbf{m}_2) \qquad (19)$$

The first term penalizes quadratic misfit, the second regularizes the solution, and the third provides bias against differences between the two path-averaged structures, weighted by the symmetric matrix $\mathbf{W}(z^*)$. The three terms are balanced by the tradeoff parameters η and ξ. Straightforward minimization yields the solution,

$$\begin{bmatrix} \Delta\mathbf{m}_1 \\ \Delta\mathbf{m}_2 \end{bmatrix} = \begin{bmatrix} \mathbf{A}_1^T\,\mathbf{A}_1 + \eta\,\mathbf{I} + \xi\,\mathbf{W} & -\xi\,\mathbf{W} \\ -\xi\,\mathbf{W} & \mathbf{A}_2^T\,\mathbf{A}_2 + \eta\,\mathbf{I} + \xi\,\mathbf{W} \end{bmatrix}^{-1} \begin{bmatrix} \mathbf{A}_1^T\Delta\mathbf{S}_1 - \xi\,\mathbf{W}\,(\bar{\mathbf{m}}_1 - \mathbf{m}_2) \\ \mathbf{A}_2^T\Delta\mathbf{S}_2 + \xi\,\mathbf{W}\,(\mathbf{m}_1 - \mathbf{m}_2) \end{bmatrix} \qquad (20)$$

At each iteration, the starting model $\bar{\mathbf{m}}$ is updated to $\bar{\mathbf{m}} + \Delta\mathbf{m}$ and the right-hand side is recalculated.

For these experiments, we have taken $\mathbf{W}(z^*)$ to be a diagonal matrix with positive weights for parameters describing perturbations deeper than z^* and zero weights for parameters describing perturbations shallower than z^*. In the Bayesian formulation of the estimation problem (discussed, for example, by *Jackson* [1979] and *Tarantola and Valette* [1982]), $(\xi\,\mathbf{W})^{-1}$ plays the role of the covariance matrix specifying a Gaussian prior probability on the model difference $\bar{\mathbf{m}}_1 - \bar{\mathbf{m}}_2$. When $\xi \rightarrow 0$, solution (20) reduces to the usual decoupled, damped least-squares estimates of the model perturbations, and the iteration converges to a local minimum of $\chi_d^2(\mathbf{m})$. Since the starting models EU0 and PA0 achieve a local minimum by construction, the limit $\xi = 0$ yields $\Delta\mathbf{m} = \mathbf{0}$. As $\xi \rightarrow \infty$, the prior covariance imposed on the model differences contained in the range space of $\mathbf{W}$ goes to zero, and the projection of $\Delta\mathbf{m}$ onto this subspace is fixed such that $\Delta m_1(z) - \Delta m_2(z) = \bar{m}_1(z) - \bar{m}_2(z)$ for $z > z^*$. Hence, the solution converges to one where the structure at depths greater than z^* is adjusted to yield the best fit to the data, but subject to the constraint that the difference between the two path-averaged models vanishes. In general, $\xi \in (0,\infty)$ parameterizes a trade-off curve between the two quadratic forms χ_d^2 and $\chi_m^2 = (\mathbf{m}_1 - \mathbf{m}_2)^T\,\mathbf{W}\,(\mathbf{m}_1 - \mathbf{m}_2)$. We chose the value of this scaling parameter such that the differences below z^* were "seismologically small", typically on the order of 0.01 km/s.

We describe here three squeezing experiments based on EU0/PA0 as the reference models. EU0 and PA0 are characterized by substantial differences in the lower mantle and transition zone--up to 0.4 km/s for V_p and 0.1 km/s for V_s--, too deep to be plausibly explained by tectospheric heterogeneity but

certainly possible in a generally heterogeneous earth. In the first squeezing experiment, we set $z^* =$ 400 km to eliminate these deep-seated differences in both compressional and shear velocity. The resulting combined-path model, designated EU1/PA1, is nearly identical to EU0/PA0 above 400 km and close to a simple average of EU0 and PA0 below this depth (Figure 5). The fit to the data is not quite as good, but good enough to qualify as acceptable according to criterion (16), with EU1/PA1 obtaining $k^2 = 1.27$ against a critical value $\kappa_{.05}^2 = 1.44$. The degradation of the fit is subtle enough to all but escape detection in a cursory comparison of the BCCF and seismograms for EU1/PA1 (Figures 6 and 7) with those for EU0/PA0 (Figures 3 and 4). The hypothesis that $z_{max} \leq 400$ km is clearly consistent with the higher-mode surface-wave data.

One major difference between EU1 and PA1 is the increase in compressional-velocity gradient of the former relative to the latter in the "subchannel" or "high-gradient" layer between 220 and 400 km, which results in a V_p difference of ~0.3 km/s just above the 400-km discontinuity. It is evident from the energy partitioning and resolving kernels that the higher Rayleigh modes resolve (isotropic) V_p structure only poorly in this region of the uppermost mantle. We confirmed this fact by reinverting the data set with z^* maintained at 400 km for V_s structure but raised to 220 km for V_p structure. Squeezing out the V_p differences in the 220–400-km depth interval was accomplished with very little perturbation to structure elsewhere and with no further degradation to the fit; the k^2 for the iterated model, EU2/PA2 (Figure 8), is 1.27, well below its critical value of 1.47. The BCCFs and synthetic seismograms are shown in Figures 9 and 10, respectively. Our waveform-correlation data do not require any differences in the compressional velocities of northern Eurasia and the western Pacific below 220 km.

They evidently do require differences in the path-averaged shear velocities, however. Our third experiment squeezed V_s as well as V_p below 220 km, and the fit of the resulting model, EU3/PA3 (Figures 11-13), is formally unacceptable, with $k^2 = 2.94$ exceeding its critical value of $\kappa_{.05}^2 = 1.51$ by a substantial margin. The EU3/PA3 shear velocities between 220 and 400 km are closer to PA0 than to EU0; consequently, the oceanic structure of PA3 above 220 km is not very different from PA0, and its overall match to the fundamental and higher-mode waveform data nearly as good. In the continental structure EU3, the good fit to the higher-mode waveforms is maintained by compensating the decrease of V_s in the high-gradient region with an increase in the overlying layers, forming a modest low-velocity zone below 220 km. The net effect, however, is to make the fundamental mode of EU3 unacceptably fast; the synthetic Rayleigh waves in Figure 13 are systematically advanced relative to the data by about 10 s across the entire receiver array. According to our scheme of inference, our failure to find an acceptable model with $z^* = 220$ km is justification for rejecting the null hypothesis $z_{max} \leq 220$ km in favor of the alternative $z_{max} > 220$ km.

The inferences drawn from the squeezing experiments are twofold: (1) it is possible to confine the path-averaged structural variations between northern Eurasia and the western Pacific to depths less than 400 km, but (2) significant differences between path-averaged shear velocities extend to depths greater than 220 km, with the values for Eurasia generally higher than the Pacific. Statement (1) is unconditional, having been verified by the construction of the successful models satisfying the constraint $z^* = 400$ km. Statement (2), on the other hand, is conditional on the ability of our parameterization to span the manifold of geophysically plausible models, as well as on our success in finding models with constrained values of z^* that best fit the data. Clearly, more complicated models (ones having large-amplitude, high-wavenumber excursions in radial structure, for example) may exist which are consistent with both the waveform data and $z^* = 220$ km. A more complete range of possibilities could be investigated and a more precise lower bound on z_{max} obtained by replacing the discrete-layer, polynomial representation used in this paper with continuous velocity functions sampled at a large number of knots [e.g., *Cara et al.*, 1980; *Lerner-Lam and Jordan*, 1983a]. Unfortunately, any inferences then become dependent on the smoothness conditions employed to regularize the solutions to the rank-deficient linear systems; to allow the rejection of unphysical, highly oscillatory models, one can either resort to truncating small singular values in the construction of the inverse operator or to imposing some sort of prior probability distribution on the model space [*Jordan*, 1972; *Tarantola and Valette*, 1982]. In either case, the restrictions on geophysical plausibility are subjective and invariably involve the *ad hoc* choice of an "effective number of degrees of freedom" (or its Bayesian equivalent) in the model space (see *Nataf et al.* [1986] for an example of this approach). In the present application, we make this choice in terms of simple layer parameters.

The parameterization problem involves not only the radial dependence of the model functions, but also the specification of the functions themselves. More degrees of freedom are available if the path-averaged structures are generalized to allow for polarization and/or azimuthal anisotropy [e.g., *Anderson*, 1961; *Kirkwood and Crampin*, 1981; *Leveque and Cara*, 1983,1985; *Tanimoto and Anderson*, 1985; *Nataf et al.*, 1986], and we admit the possibility that anisotropic structures satisfying both the waveform data and $z^* = 220$ km may exist. The question of the tradeoff between acceptable values of z^* and the magnitude of anisotropy has not yet been fully explored, but efforts are underway to adapt our squeezing procedures to this problem [*Lerner-Lam*, 1985]. We shall discuss the evidence for polarization anisotropy in the next section.

As a final caveat, we emphasize that the validity of the one-dimensional, average-path approximation deserves more scrutiny than it is given in this paper. Situations can be envisaged where the laterally inhomogeneous sampling by the data of strong along-path variations above some

depth z^* maps into apparent differences in path-averaged models below z^*, biasing any lower bound on z_{max}. We have shown that simple path-averaged models satisfy waveform data for both regions studied, but an assessment of the depth localization of the averaging operations that go into constructing such models will require a more complete analysis of wave propagation and structural inverse problems in three dimensions, as well as a more complete description of the along-path heterogeneity across northern Eurasia and the western Pacific. The progress in two-dimensional waveform modeling of the sort recently reported by *Helmberger et al.* [1985] and *Grand and Helmberger* [1985] should lead to a better understanding of these problems.

COMPARISON WITH OTHER STUDIES

Among the models derived in this study, EU2 and PA2 represent our preferred estimates of path-averaged structures for northern Eurasia and the western Pacific (Table 2). We are willing to accept the slightly degraded fit these models show relative to EU0 and PA0 as the tradeoff needed to eliminate the structural contrasts deeper than 400 km. By the same token, we are unwilling to accept the poor fit offered by EU3/PA3, which is our basis for rejecting the hypothesis $z_{max} \leq 220$ km.

Our results are generally consistent with other recent seismological studies of continent-ocean heterogeneity. Most directly comparable are the analyses of fundamental and higher-mode dispersion across northern Eurasia and the eastern Pacific by *Cara et al.* [1980] and *Lerner-Lam and Jordan* [1983a]. Despite the different parameterizations, inversion procedures and data sets, the models derived in these previous studies are similar to (though smoother than) EU2/PA2, having a well developed oceanic LVZ, little or no LVZ beneath Eurasia, and higher continental shear velocities below 220 km.

Inversions of large sets of multiple-orbit surface waves for the lowest wavenumber components of upper-mantle aspherical structure [*Woodhouse and Dziewonski*, 1984; *Nataf et al.*, 1984] allow us to put our regionalized models in a global context. In M84C of *Woodhouse and Dziewonski* [1984], which is constrained by higher modes as well as the fundamental, anomalously high shear velocities characterize most of the stable continental cratons and platforms to depths exceeding 220 km. To obtain a more quantitative comparison, we integrated the shear-wave travel-time perturbations of M84C along vertical ray paths from 40 to 400 km and projected this degree-eight aspherical function onto the global tectonic regionalization GTR1 [*Jordan*, 1981b]. (The six geographical functions of GTR1 were filtered to degree eight prior to projection; details are given in the Appendix) The scalar value for each tectonic region, given in Table 3, is an estimate of *S*-wave slowness anomaly areally averaged over the region and integrated between 40 and 400 km. As seen in Figure 1, the

surface-wave paths crossing northern Eurasia sample primarily Regions S (shields) and P (platforms), whereas the western Pacific paths sample almost exclusively Region C (old ocean). The average *S*-time difference computed according to C−(S + P)/2 from Table 3 is +2.0 s, which coincides with the corresponding PA2–EU2 *S*-time difference of +2.0 s. Therefore, the PA2–EU2 differential is about the same as the M84C global average for old oceans and old continents.

The projection of M84C onto GTR1 can be subtracted from the original aspherical model to obtain a map of the upper-mantle heterogeneities that do not correlate with large-scale surface tectonics and may thus represent sub-tectospheric structure [see *Jordan et al.*, 1986]. Computed in this manner, vertical *S*-time residuals reveal that portions of both northern Eurasia and the western Pacific traversed by our data are fast by 1-2% with respect to the regionalized averages, with high-velocity features centered over Novaya Zemlya and the Shatsky Rise. These features have horizontal dimensions of just a few thousand kilometers and may not be well represented by the truncated degree-eight parameterization of M84C. In any case, M84C indicates that the upper-mantle velocity differences sampled by EU2 and PA2 should not be substantially greater than other old continents and oceans; we infer that the conclusion z_{max} > 220 km derived for these two paths can be extended globally.

The analysis of higher-mode, *PSV* surface waves employed here is very different from the methodologies recently developed for structural studies of multiply reflected, *SH* body waves at higher frequencies. The most direct comparison is with two regionalized upper-mantle models derived by *Grand and Helmberger* [1984a,b], SNA for stable North America and ATL for the western North Atlantic. The regions sampled by SNA and ATL are tectonically analogous to northern Eurasia and the western Pacific, respectively, yet geographically well separated from them. Moreover, both sets of models were derived from matching the waveforms in the interval following *S*, so the data have comparable sensitivity to structure below 220 km. (Grand and Helmberger fit waveforms by trial-and-error forward modeling and have not yet attempted a formal resolving power analysis, but because they use broader-band signals, their data presumably have even better structural resolution than our own.) The shear-velocity profiles of EU2/PA2 and SNA/ATL are plotted together in Figure 14.

These two sets of models show a number of similarities and several important differences. All four profiles are substantially the same below 400 km, and the continent-ocean contrast ATL- SNA has approximately the same magnitude and distribution with depth as PA2-EU2. The total contrast measured by the 40–400-km vertical *S*-time difference is +2.3 s for the former. In particular, SNA has higher shear velocities than ATL below 220 km, which *Grand and Helmberger* [1984a,b] have

argued are needed to match the waveform and travel-time differences of the multiply reflected *SH* phases; SNA/ATL corroborate the conclusion tnat $z_{max} > 220$ km. Both oceanic models have lid thicknesses of about 100 km capping well developed low-velocity zones, consistent with thermal boundary layer models of old ocean basins [e.g., *Parsons and Sclater*, 1977; *Parsons and McKenzie*, 1978], and they have nearly identical shear velocities below 250 km.

Above 250 km, however, the shear velocities of ATL are consistently higher than PA2 by approximately 0.2 km/s. The continental comparison shows even larger and deeper discrepancies, with SNA 0.3 km/s higher than EU2 at the base of the crust and 0.04 km/s higher just above the 400-km discontinuity. In addition, SNA has a small LVZ at about 200 km, whereas EU2 increases monotonically throughout the upper mantle. The differences in LVZ structure could be due to resolving-power differences or genuine variability among the paths, but such explanations are inadequate to account for the offsets in average upper-mantle V_S . *Grand and Helmberger* [1985] have examined the propagation of multiply reflected *S* waves in Eurasia and found that the Russian platform has a structure almost identical to the Canadian shield. A fraction of the surface-wave corridor for EU2 traverses the tectonically active areas of northeastern Asia, where the velocities are undoubtably lower, but this alone cannot account for the discrepancy. *Grand and Helmberger* [1985] have modeled the transition from the active foldbelts of central Asia to the Russian platform using their multiple-*S* techniques, and the lowest vertically averaged velocities they encountered are still higher than EU2. In fact, averaged over the 40–400-km depth interval, EU2 is slower than the oceanic model ATL.

We suspect that the differences between the *SH* and *P-SV* models are, at least in part, a manifestation of upper-mantle polarization anisotropy of the sort described on a global scale by *Dziewonski and Anderson* [1981]. This hypothesis is consistent with the observations and modeling results of *Cara et al.* [1980] and *Leveque and Cara* [1983,1985], who identified substantial differences in *SH* and *SV* velocities from the inversion of higher-mode Rayleigh and Love waves. In a preliminary analysis of three-component, digitally recorded seismograms for paths crossing northern Eurasia, L. Gee [personal communication, 1986] has shown that, although the observed Rayleigh-wave dispersion agrees with EU2, the Love waves in a pass-band centered at about 20 mHz are phase-advanced by as much as 40 s, consistent with the higher average velocities in SNA. However, the arrival times of *SH*-polarized *SS* and *SSS* waves appear to be delayed by several seconds relative to the observed *SV* arrivals. This limits any polarization anisotropy having $V_{SH} > V_{SV}$ to fairly shallow depths. Despite the potential complications associated with laterally variable, anisotropic structures, it seems unlikely that both the *P-SV* and *SH* data can be modeled consistently with $z^* < 220$ km, especially if the polarization anisotropy must also be confined to the upper couple

hundred kilometers of the mantle.

A definitive statement on the vertical extent of anisotropy must await the application of our squeezing techniques to self-consistent *P-SV* and *SH* data sets, but one complication introduced by anisotropy can be addressed here. By ignoring the effects of *PV-PH* splitting on the propagation velocity of fundamental-mode Rayleigh waves [*Anderson and Dziewonski*, 1981], we could be biasing the EU2-PA2 difference in *SV* velocities (and thereby our lower bound on z_{max}) to high values. If this were true, the EU2-PA2 difference in vertical *S* time should be greater than actually measured by vertically propagating shear waves. In fact, *S* and *ScS* observations show this inequality to be reversed. Three sets of ScS_n measurements have been made which are particularly relevant:

(1) *Sipkin and Jordan* [1976] used ScS_2–*ScS* travel times read from analog WWSSN records to map a systematic increase of about 4 s in one-way vertical *S* delay across the transtion from the Anabar shield to the Arctic ocean basin; the shield-to-ocean gradient in northern Eurasia is thus similar to the increase in *S*-wave station anomalies observed going outward from the Canadian shield [*Doyle and Hales*, 1967; *Wickens and Buchbinder*, 1980].

(2) *Jordan* [1981b, Figure 5] plotted *Sipkin and Jordan's* [1976] global set of ScS_2–*ScS* residuals as histograms for the six regions of GTR1, obtaining a one-way time difference of about 3 s between average old ocean (Region C) and average stable continent (Regions S and P), uncorrected for differences in crustal structure.

(3) *Sipkin and Jordan* [1980] measured ScS_n–ScS_m differential travel times from digitally recorded seismograms by waveform cross-correlation and documented a difference of +2.6 ± 0.6 s between the western Pacific and average continent, again uncorrected for crustal structure.

Crustal corrections increase the difference in one-way vertical *S* time by at least a second, so that the three observations listed above are generally consistent with a mantle contrast between old oceans and old continents of about +4 ± 1 s, twice the value computed from PA2-EU2. Anisotropy may play a role in explaining this *ScS* discrepancy, although at least some of it can be accounted for by the sampling of lower-velocity orogenic zones along about 30% of our northern Eurasia paths (Figure 1). In any case, the comparison indicates that our models underestimate, rather than overestimate, the total integrated *SV* velocity contrast between old cratons and old ocean basins, reinforcing the bound z_{max} > 220 km.

DISCUSSION

The lower bound of 220 km on the vertical extent of continent-ocean heterogeneity lies significantly deeper than the classical demarcations of the lithosphere-asthenosphere boundary, measured either in terms of effective elastic-plate thickness or depth to the Gutenberg low-velocity zone. The maximum elastic plate thickness inferred from loading data varies from ~50 km in old ocean basins [*Watts et al.*, 1980; *McNutt and Menard*, 1982] to ~90 km on cratons [*Karner and Watts*, 1983; *Lyon-Caen and Molnar*, 1983]. Surface-wave estimates of lid thickness in old oceans range from 50 km [*Regan and Anderson*, 1984] to 140 km [*Schlue and Knopoff*, 1977], generally consistent with the 100-km depth for the lid-LVZ transition in PA2. The lid thickness of cratons is not as well constrained (in fact, EU2 has no LVZ and thus no lid), but *Grand and Helmberger's* [1984a] model SNA places the velocity decrease at about 150-200 km. Whatever the significance of this velocity decrease, continent-ocean heterogeneity does not appear to be confined to the layers that lie above it.

Moreover, it is evident from a wide variety of seismic observations that the stable cratons have shear velocities high not only with respect to the oceans, but also relative to orogenically active continental regions [*Knopoff*, 1972; *Jordan*, 1975; *Nakanishi and Anderson*, 1983; *Woodhouse and Dziewonski*, 1984]. Phanerozoic orogenic zones and magmatic belts (Region Q of GTR1) comprise over half of the continental area, and they appear to be underlain by mantle that is either oceanic or transitional between ocean and craton [*Sipkin and Jordan*, 1976; *Jordan*, 1981b; *Grand and Helmberger*, 1984a,b, 1985; *Helmberger et al.*, 1985]. The thickness of the tectosphere in these regions appears to be on the order of a hundred kilometers or so, comparable to the values inferred for old ocean basins. In areas of extensional tectonics, such as the Basin and Range Province of western North America, the plate thickness can be as small as in young oceans. For example, *Grand and Helmberger's* [1984a] model for tectonic North America (TNA) has lower shear velocities than ATL above about 200 km, with an upper-mantle structure similar to what they observe for the East Pacific Rise. TNA and ATL have the same structure at depths greater than 200 km, as expected for a convecting mantle where the potential temperatures below thin plates average to similar regional values [*Sclater et al.*, 1981]

The higher shear velocities below 200 km in SNA and EU2 are thus indicative of lower-than-average temperatures beneath the cratons. The question, of course, is whether these deep-seated, high-velocity zones are part of the continental tectosphere or just represent the cold shadows of the continents in a convecting upper mantle. Although the later is made plausible by the sensitivity of shear velocities to temperature in the vicinity of the solidus [*Sclater et al.*, 1981], the

mechanisms for maintaining such features in a dynamically active mantle are far from obvious. Regardless of specific mechanism invoked, the development of low-temperature zones beneath the continents must be governed by the conduction of heat across boundary layers, and the time needed to organize these features is at least as great as the time it takes to translate the cratons over their characteristic horizontal dimension, say 100 My. As emphasized by *Jordan* [1975], the large lateral gradients in upper-mantle velocities mapped by station anomalies and differential travel times correlate to a remarkable degree with surface heat flow and long-standing patterns in orogenic behavior, whereas they correlate very little with plate velocities and the geoid, as might be expected for dynamically maintained features. The correlation of deep structure with surface tectonics requires that the former translate coherently with the latter over time scales much longer than 100 My. Therefore, we favor the hypothesis which locates the high-velocity zones within the tectosphere.

We infer that, on the average, tectospheric thicknesses exceed 220 km beneath stable continents like northern Eurasia. Plate thicknesses of this magnitude are inconsistent with the unified thermal-boundary-layer model of *Sclater et al.* [1980, 1981], which requires thin (~125-km) plates for both old oceans and old continents.

Some of the implications of a thick continental tectosphere have been explored by *Jordan* [1975, 1978, 1981a]. He has argued that the continental thermal boundary layer cannot grow to such an extreme depth by the usual mechanism of conductive heat loss at the surface, but instead requires the construction of a thick chemical boundary layer to stabilize it against convective disruption. In his model, a layer depleted in major-element basaltic constituents (Fe, Al and Ca relative to Mg) is advectively thickened beneath the continents by large-scale orogenic compression prior to stabilization of a cratonic crust. Dynamical processes are assumed to adjust the deep structure of the continental tectosphere such that the density increase associated with lower temperatures is approximately cancelled by the density decrease due to basalt depletion.

Recent studies of peridotitic inclusions in diamonds indicate that a cold, thick, basalt-depleted root zone has been a feature of the Kaapvaal craton for the last 3000 My [*Kramers*, 1979; *Richardson et al.*, 1984; *Boyd et al.*, 1985], lending addition support to the chemical-boundary-layer hypothesis [*Richter*, 1985]. There remains a discrepancy between the petrological estimates of plate thickness and those derived from seismology, however. From a synthesis of thermobarometric data on kimberlite xenoliths, *Boyd and Gurney* [1986] argue that systematic, nearly discontinuous changes in vertical temperature gradient, mineral texture, and average composition occur at a depth on the order of 200 km beneath the Kaapvaal craton. They are able to follow these changes to shallower depths going outward across the craton's peripheral mobile belts and speculate that this boundary represents

the base of the continental plate in southern Africa. Although adequate seismic data do not specifically exist for southern Africa, a variety of seismological studies, including the one presented here, do not appear to be consistent with a tectosphere thickness ≤ 200 km beneath most cratons.

Elucidating the structure and behavior of the subcontinental mantle has been a seminal problem in geodynamics since the pioneering work of *Brune and Dorman* [1963], *MacDonald* [1963], *Toksöz and Anderson* [1963], and others. Its importance and the attention it has received over the last several decades have been matched by its difficulty. Our own investigations make it clear to us that the questions surrounding the deep structure of the continents will continue to challenge earth scientists for some time to come.

Acknowlegdments. We thank L. Gee for assistance, and L. Gee, P.G. Richards, D.W. Simpson, and C. Scholz for comments on the manuscript. This work was sponsored by the Defense Advanced Research Projects Agency and the Air Force Geophysical Laboratory under contract F19628-85-K-0024. It was completed while ALL was an LDGO Postdoctoral Fellow partially supported under NSF grant EAR85-08988.

APPENDIX

Let $\Delta s(z,\theta,\phi)$ be an aspherical perturbation to the slowness. The corresponding perturbation to the one-way vertical travel-time, calculated between reference depths z_1 and z_2 is

$$\Delta t(\theta,\phi) = \int_{z_1}^{z_2} \Delta s(z,\theta,\phi)\, dz \tag{A1}$$

When the geographical variation of Δs is represented as a spherical harmonic expansion truncated at some wavenumber L, Δt will have the truncated spherical harmonic expansion

$$\hat{\Delta t}(\theta,\phi) = \sum_{l=0}^{L} \sum_{m=-l}^{l} t_{lm}\, Y_{lm}(\theta,\phi) \tag{A2}$$

We are interested in the component of Δt, say Δt_r that correlates with a tectonic regionalization. Δt_r has an expansion in terms of the regional shape functions $r_i(\theta,\phi)$, $i = 1,...,N$ [e.g., *Jordan*, 1981b]

$$\Delta t_r(\theta,\phi) = \sum_{i=1}^{N} \tau_i\, r_i(\theta,\phi) \tag{A3}$$

We first low-pass (A3) by expanding the $r_i(\theta,\phi)$ in spherical harmonics up to angular order L:

$$\hat{\Delta t}_r(\theta,\phi) = \sum_{i=1}^{N} \tau_i \sum_{l=0}^{L} \sum_{m=-l}^{l} \rho_{lm}^{(i)}\, Y_{lm}(\theta,\phi) \tag{A4}$$

The constants τ_i are found by minimizing the quadratic form

$$| \hat{\Delta t} - \hat{\Delta t}_r |^2 \tag{A5}$$

Constants for model M84C [*Woodhouse and Dziewonski*, 1984] projected on GTR1 [*Jordan*, 1981b] are given in Table 3 ($L = 8$, $N = 6$).

REFERENCES

Anderson, D.L., Elastic wave propagation in layered anisotropic media, *J. Geophys. Res.*, **66**, 2953-2563, 1961.

Anderson, D.L., The deep structure of continents, *J. Geophys. Res.*, **84**, 7555-7560, 1979.

Anderson, D.L., and A.M. Dziewonski, Upper mantle anisotropy: evidence from free oscillations, *Geophys. J. Roy. Astr. Soc.*, **69**, 383-404, 1982.

Belyaevsky, N.A, A.A. Borisov, V.V. Fedynsky, E.E. Fotiadi, S.I. Subbotin, and I.S. Volvovsky, Structure of the earth's crust on the territory of the U.S.S.R., *Tectonophysics*, **20**, 35-45, 1973.

Backus, G., and F. Gilbert, Numerical application of a formalism for geophysical inverse problems, *Geophys. J. Roy. Astr. Soc.*, **13**, 247-276, 1967.

Backus, G., and F. Gilbert, The resolving power of gross earth data, *Geophys. J. Roy. Astr. Soc.*, **16**, 169-205, 1968.

Backus, G., and F. Gilbert, Uniqueness in the inversion of inaccurate gross earth data, *Phil. Trans. Roy. Soc. London*, **A266**, 123-192, 1970.

Boyd, F.R., and J.J. Gurney, Diamonds and the African lithosphere, *Science*, **232**, 472-477, 1986.

Boyd, F.R., J.J. Gurney, and S.H. Richardson, Evidence for a 150–200-km thick Archaean lithosphere from diamond inclusion thermobarometry, *Nature*, **315**, 387-389, 1985.

Brune, J.N., and J. Dorman, Seismic waves and earth structure in the Canadian Shield, *Bull. Seismol. Soc. Am.*, **53**, 167-210, 1963.

Bungum, H., S.E. Pirhonen, and E.S. Husebye, Crustal thicknesses in Fennoscandia, *Geophys. J. Roy. Astr. Soc.*, **63**, 759-774, 1980.

Burdick, L.J. and D.V. Helmberger, The upper mantle *P* velocity structure of the western United States, *J. Geophys. Res.*, **83**, 1699-1712, 1978.

Cara, M., Regional variations of higher Rayleigh-mode phase velocities: a spatial filtering method, *Geophys. J. Roy. Astr. Soc.*, **54**, 439-460, 1978.

Cara, M., Lateral variations of *S* velocity in the upper mantle from higher Rayleigh modes, *Geophys. J. Roy. Astr. Soc.*, **57**, 649-670, 1979.

Cara, M., A. Nercessian, and Nolet, G., New inferences from higher mode data in western Europe and northern Eurasia, *Geophys. J. Roy. Astr. Soc.*, **61**, 459-478, 1980.

Crough, S.T., and G.A. Thompson, Numerical and approximate solutions for lithospheric thickening and thinning, *Earth Planet. Sci. Lett.*, **31**, 397-402, 1976.

Doyle, H.A., and A.L. Hales, An analysis of the travel times of *S* waves in the distance range 28°

to 82°, *Bull. Seismol. Soc.*, **57**, 761-771, 1967.

Dziewonski, A.M., Upper mantle models from 'pure-path' dispersion data, *J. Geophys. Res.*, **76**, 2587-2601, 1971.

Dziewonski, A.M., and D.L. Anderson, 1981. Preliminary reference earth model, *Phys. Earth Planet. Int.*, **25**, 297-356.

Dziewonski, A.M., A.L. Hales, and E. R. Lapwood, Parametrically simple earth models consistent with geophysical data, *Phys. Earth Planet. Int.*, **10**, 12-48, 1975.

Dziewonski, A.M., and J.M. Steim, 1982. Dispersion and attenuation of mantle waves through waveform inversion, *Geophys. J. R. astr. Soc.*, **70**, 503-527.

Feng, C.-C., and T.-L. Teng, Three-dimensional crust and upper mantle structure of the Eurasian continent, *J. Geophys. Res.*, **88**, 2261-2272, 1983.

Gee, L.S., A.L. Lerner-Lam, and T.H. Jordan, Resolving power of higher-mode waveform inversion for Eurasian upper-mantle structure, Semiannual report, Defense Advanced Research Projects Agency, 1985.

Grand, S.P., and D.V. Helmberger, Upper mantle shear structure of North America, *Geophys. J. Roy. Astr. Soc.*, **76**, 399-438, 1984a.

Grand, S.P., and D.V. Helmberger, Upper mantle shear structure beneath the northwest Atlantic Ocean, *J. Geophys. Res.*, **89**, 11465-11475, 1984b.

Grand, S.P., and D.V. Helmberger, Uppermantle shear structure beneath Asia from multi-bounce S waves, *Phys. Earth Planet. Int.*, **41**, 154-169, 1985.

Hagiwara, T., A note on the theory of the electromagnetic seismograph, *Bull. Earthquake Res. Inst. Tokyo Univ.*, **36**, 139-164, 1958.

Helmberger, D.V., G. Engen, and S.P. Grand, Long period wave propagation in laterally varying structures, in preparation, 1985.

Jackson, D.D., The use of *a priori* data to resolve non-uniqueness in linear inversion, *Geophys. J. Roy. Astr. Soc.*, **57**, 137-157, 1979.

Jordan, T.H., Estimation of the radial variation of seismic velocities and density in the earth, *Ph.D. thesis*, Calif. Inst. Tech., Pasadena, 199 pp., 1972.

Jordan, T.H., The continental tectosphere, *Rev. Geophys. Space Phys.*, **13**(3), 1-12, 1975.

Jordan, T.H., Composition and development of the continental tectosphere, *Nature*, **274**, 544-548, 1978.

Jordan, T.H., Mineralogies, densities and seismic velocities of garnet lherzolites and their geophysical implications, in *The Mantle Sample: Inclusions in Kimberlites and Other Volcanics*, edited by F.R. Boyd and H.O.A. Meyer, Amer. Geophys. Union, Washington, D.C., 1-14, 1979.

Jordan, T.H., Continents as a chemical boundary layer, *Phil. Trans. Roy. Soc. Lond.*, **A301**, 359-373, 1981a.

Jordan, T.H., Global tectonic regionalization for seismological data analysis, *Bull. Seismol. Soc. Am.*, **71**, 1131-1141, 1981b.

Jordan, T.H., A.L. Lerner-Lam, and K.C. Creager, Seismic imaging of mantle convection: the evidence for deep circulation, in *Mantle Convection*, W.R. Peltier (ed.), in press, 1986.

Kanamori, H., The velocity and Q of mantle waves, *Phys. Earth Planet. Int.*, **2**, 259-275, 1970.

Karner, G.D., and A.B. Watts, Gravity anomalies and flexure of the lithosphere at mountain ranges, *J. Geophys. Res.*, **88**, 10449-10477, 1983.

Kirkwood, S.C., and S. Crampin, Surface-wave propagation in an ocean basin with an anisotropic upper mantle: numerical modelling, *Geophys. J. R. Astr. Soc.*, **64**, 463-485, 1981.

Knopoff, L., Observation and inversion of surface wave dispersion, *Tectonophysics*, **13**, 497-519, 1972.

Kramers, J.D., Lead, uranium, strontium, potassium, and rubidium in inclusion-bearing diamonds and mantle-derived xenoliths from southern Africa, *Earth Planet. Sci. Lett.*, **42**, 58-70, 1979.

Kono, Y., and M. Amano, Thickening model of the continental lithosphere; *Geophys. J. Roy. Astr. Soc.*, **54**, 405-416, 1978.

Leeds, A.R., Lithospheric thickness in the western Pacific, *Phys. Earth Planet. Int.*, **11**, 61-64, 1975.

Lerner-Lam, A.L., Linearized estimation of higher-mode surface wave dispersion, *Ph.D. thesis*, University of California, San Diego, 1982.

Lerner-Lam, A.L., and T.H. Jordan, Earth structure from fundamental and higher-mode waveform analysis, *Geophys. J. Roy. Astr. Soc.*, **75**, 759-797, 1983a.

Lerner-Lam, A.L., and T.H. Jordan, Regional variations of higher-mode dispersion in Eurasia, *Eos, Trans. Am. Geophys. Union*, **64**, 261 (abstract), 1983b.

Lerner-Lam, A.L., Tradeoff between lid thickness and anisotropy using linearized waveform inversion, *Eos, Trans. Am. Geophys. Union*, **66**, 966-967 (abstract), 1985.

Leveque, J.J., and M. Cara, Long-period Love wave overtone data in North America and the Pacific Ocean: new evidence for upper mantle anisotropy, *Phys. Earth Planet. Int.*, **33**, 164-179, 1983.

Leveque, J.J., and M. Cara, Inversion of multimode surface wave data: evidence for sub-lithospheric anisotropy, *Geophys. J. R. Astr. Soc.*, **83**, 753-773, 1985.

Lyon-Caen, H., and P. Molnar, Constraints on the structure of the Himalaya from an analysis of gravity anomalies and a flexural model of the lithosphere, *J. Geophys. Res.*, **88**, 8171-8191, 1983.

MacDonald, G.J.F., The deep structure of continents, *Rev. Geophys.*, **1**, 587-665, 1963.

Masters, G., and F. Gilbert, Attenuation in the earth at low frequencies, *Phil. Trans. Roy. Soc. London*, **A308**, 479-522, 1983.

Masters, G., T.H. Jordan, P.G. Silver, and F. Gilbert, Aspherical earth structure from fundamental spheroidal-mode data, *Nature*, **298**, 609-613, 1982.

McNutt, M.K. and H.W. Menard, Constraints on yield strength in the oceanic lithosphere derived from observations of flexure, *Geophys. J. R. Astr. Soc.*, **71**, 363-394, 1983.

Menke, W.A., *Geophysical Data Analysis: Discrete Inverse Theory*, Academic Press, London, 260 pp, 1984.

Nakanishi, I., and D.L. Anderson, Measurements of mantle wave velocities and inversion for lateral heterogeneity and anisotropy, 1, analysis of great circle phase velocities, *J. Geophys. Res.*, **88**, 10267-10284, 1983.

Nataf, H.-C., I. Nakanishi, and D.L. Anderson, Anisotropy and shear-velocity heterogeneities in the upper mantle, *Geophys. Res. Lett.*, **11**, 109-112, 1984.

Nataf, H.-C., I. Nakanishi, and D.L. Anderson, Measurements of mantle wave velocities and inversion for lateral heterogeneities and anisotropy, 3, inversion, *J. Geophys. Res.*, **91**, 7261-7307, 1986.

Nolet, G., Higher Rayleigh modes in western Europe, *Geophys. Res. Lett.*, **2**, 60-62, 1975.

Nolet, G., The upper mantle under western Europe inferred from the dispersion of Rayleigh modes, *J. Geophys.*, **43**, 265-285, 1977.

Nolet, G., and J. Panza, Array analysis of seismic surface waves: limits and possibilities, *Pageoph.*, **114**, 775-790, 1976.

Nolet, G., J. van Trier, and R. Huisman, A formalism for nonlinear inversion of seismic surface waves, *Geophys. Res. Lett.*, **13**, 26-29, 1986.

Okal, E.A., and D.L. Anderson, A study of lateral inhomogeneities in the upper mantle by multiple *ScS* travel-time residuals, *Geophys. Res. Lett.*, **2**, 313-316, 1975.

Parker, R. L., Inverse theory with grossly inadequate data, *Geophys. J. Roy. Astr. Soc.*, **29**, 123-138, 1972.

Parsons, B., and D.P. McKenzie, Mantle convection and the thermal structure of the plates, *J. Geophys. Res.*, **83**, 4485-4496, 1978.

Parsons, B., and J.G. Sclater, An analysis of the variation of ocean floor bathymetry and heat flow with age, *J. Geophys. Res.*, **82**, 803-827, 1977.

Regan, J., and D.L. Anderson, Anisotropic models of the upper mantle, *Phys. Earth Planet. Int.*, **35**, 227-263, 1984.

Richardson, S.H., J.J. Gurney, A.J. Erlank, and J.W. Harris, Origin of diamonds in old enriched

mantle, *Nature*, **310**, 198-202, 1984.

Richter, F. M., Models for the Archean thermal regime, *Earth Planet. Sci. Lett.*, **73**, 350-360, 1985.

Sclater, J.G., C. Jaupart, and D. Galson, The heat flow through oceanic and continental crust and the heat loss of the earth, *Rev. Geophys. Space Phys.*, **18**, 269-311, 1980.

Sclater, J.G., B. Parsons, and C. Jaupart, Oceans and continents: similarities and differences in the mechanisms of heat loss, *J. Geophys. Res.*, **86**, 11535-11552, 1981.

Schlue, J.W., and L. Knopoff, Inversion of surface-wave phase velocities for anisotropic structure, *Geophys. J. Roy. Astr. Soc.*, **54**, 697-702, 1978.

Sellevoll, M.A., Mohorovi˜ci´c discontinuity beneath Fennoscandia and adjacent parts of the Norwegian Sea and the North Sea, *Tectonophysics*, **20**, 359-366, 1973.

Sipkin, S.A. and T.H. Jordan, Lateral heterogeneity of the upper mantle determined from the travle times of *ScS*, *J. Geophys. Res.*, **80**, 1474-1484, 1975.

Sipkin, S.A. and T.H. Jordan, Lateral heterogeneity of the upper mantle determined from the travel times of multiple *ScS*, *J. Geophys. Res.*, **81**, 6307-6320, 1976.

Sipkin, S.A. and T.H. Jordan, Multiple *ScS* travel times in the western Pacific: implications for mantle heterogeneity, *J. Geophys. Res.*, **85**, 853-861, 1980.

Tanimoto, T., and D.L., Anderson, Lateral heterogeneity and azimuthal anistropy of the upper mantle: Love and Rayleigh waves 100-250 s, *J. Geophys. Res.*, **90**, 1842-1858, 1985.

Tarantola, A., and B. Valette, Generalized nonlinear inverse problems solved using the least squares criterion, *Rev. Geophys. Space Phys.*, **20**, 219-232, 1982.

Toksöz, M.N., and D.L. Anderson, Phase velocities of long period surface waves and structure of the upper mantle, *J. Geophys. Res.*, **71**, 1649-1658, 1966.

Vinnik, L.P., and V.Z. Ryaboy, Deep structure of the east European platform according to seismic data, *Phys. Earth Planet. Int.*, **25**, 27-37, 1981.

Watts, A.B., J.H. Bodine, and M.S. Steckler, Observations of flexure and the state of stress in the oceanic lithosphere, *J. Geophys. Res.*, **85**, 6369-6376, 1980.

Wickens, A.J., and G.G.R. Buchbinder, *S*-wave residuals in Canada, *Bull. Seism. Soc. Am.*, **70**, 809-822, 1980.

Woodhouse, J., and F.A. Dahlen, The effect of a general aspherical perturbation on the free oscillations of the Earth, *Geophys. J. Roy. Astr. Soc.*, **53**, 335-354, 1978.

Woodhouse, J., and A.M. Dziewonski, Mapping the upper mantle: three-dimensional modeling of earth structure by inversion of seismic waveforms, *J. Geophys. Res.*, **89**, 5953-5986, 1984.

Yu, G.K., and B.J. Mitchell, Regionalized shear velocity models of the Pacific upper mantle from observed Love and Rayleigh wave dispersion, *Geophys. J. Roy. Astr. Soc.*, **57**, 311-341, 1979.

Zelen, M., and C. Severo, Probability functions, in *Handbook of Mathematical Functions*, edited by M. Abramowitz and I.A. Stegun, Dover, N.Y., 925-995, 1965.

Table1. Source Parameters and Path Coverage.

Event	Lat.	Long.	Depth (km)	Northern Eurasia						Western Pacific				
				COP	KEV	KON	NUR	STU	UME	AFI	HNR	KIP	RAB	RAR
1	49° 04'N	153° 34'E	134	•	•	•	•	•		•	•	•	•	•
2	44° 12'N	145° 18'E	181	•		•	•		•	•	•	•	•	
3	46° 18'N	142° 30'E	344	•			•		•		•			
4	52° 30'N	153° 36'E	440								•			
5	51° 42'N	150° 54'E	544				•	•				•		•

Table 2. Models EU2 and PA2

Layer	EU2				PA2			
	depth (km)	ρ (Mg/m^3)	V_P (km/s)	V_S (km/s)	depth (km)	ρ (Mg/m^3)	V_P (km/s)	V_S (km/s)
Crust	0 - 3	2.00	2.98	1.42	0 - 5	1.03	1.50	0.00
	3 - 20	2.74	6.08	3.44	5 - 6	1.50	2.01	0.92
	20 -36	3.00	6.78	3.84	6 - 14	2.85	6.41	3.62
Lid	36	3.32	8.19	4.51	14	3.30	8.17	4.54
	100	3.37	8.19	4.51	98	3.36	8.17	4.54
Low-velocity zone	100	3.37	8.19	4.53	98	3.36	8.10	4.24
	220	3.43	8.19	4.53	180	3.41	8.10	4.24
High-gradient zone	220	3.43	8.14	4.53	180	3.41	8.02	4.31
	400	3.54	8.65	4.74	400	3.54	8.63	4.76
Transition zone	400	3.72	9.22	4.97	400	3.72	9.20	4.96
	670	4.06	10.35	5.56	670	4.06	10.34	5.55
Lower mantle	670	4.38	10.80	6.09	670	4.38	10.79	6.08
	721	4.41	10.96	6.24	721	4.41	10.95	6.23
	771	4.44	11.11	6.37	771	4.44	11.11	6.37
	771	4.44	11.11	6.37	771	4.44	11.11	6.37
	1271	4.73	11.93	6.65	1271	4.73	11.93	6.65
	1771	5.00	12.59	6.88	1771	5.00	12.59	6.88
	2271	5.26	13.18	7.09	2271	5.26	13.17	7.08
	2741	5.49	13.73	7.28	2741	5.49	13.72	7.27
	2741	5.49	13.73	7.28	2741	5.49	13.72	7.28
	2871	5.56	13.76	7.28	2871	5.56	13.76	7.28
	2891	5.57	13.77	7.28	2891	5.57	13.76	7.28

Values above 670 km linearly interpolated; values between 670 km and 771 km and between 2741 km and 2891 km quadratically interpolated; values between 771 km and 2741 km quartically interpolated.

Table 3. Average upper-mantle *S*-time anomalies of M84C for six tectonic regions.

Region	Description	Areal fraction	*S* anomaly* (s)
S	Precambrian shields and platforms	.07	−2.7
P	Phanerozoic platforms	.10	−1.3
Q	Phanerozoic orogenic zones	.22	−0.2
C	Old oceans (>100 Ma)	.13	0.0
B	Intermediate-age oceans (25-100 Ma)	.35	0.4
A	Young oceans (< 25 Ma)	.13	1.4

* Shear-wave slowness anomaly of the degree-eight model M84C [*Woodhouse and Dziewonski*, 1984] integrated from 40 to 400 km depth and projected onto the six tectonic regions of GTR1 [*Jordan*, 1981b]. Geographic functions of GTR1 filtered to degree eight prior to projection.

FIGURE CAPTIONS

Fig. 1. Azimuthal equidistant projection showing the distribution of sources (triangles numbered according to Table 1), receivers (solid circles with WWSSN abbreviation) and surface-wave paths (solid lines) used in this study. Cross-hatched area in the western Pacific is oceanic crust with an age greater than 100 Ma (Region C of Jordan [1981b]); dotted areas in Eurasia are Phanerozoic platforms (Region P); and stippled areas are Precambrian shields (Region S). Projection is centered on Event 5.

Fig. 2. Path-averaged models EU0 (solid lines) and PA0 (dotted lines) obtained by the inversion of fundamental and higher-mode waveform data for northern Eurasian and western Pacific, respectively. No constraints were imposed on velocity differences, which persist to the core-mantle boundary. Density structures fixed during inversion.

Fig. 3. Comparison of observed BCCFs (solid lines) with synthetics (dashed lines) for models EU0 (top) and PA0 (bottom), showing entire data set used in the inversions. Each BCCF is the cross-correlation between a complete seismogram, observed or syntheic, and the synthetic for a specific mode branch. Mode-branch numbers label columns; event-station pairs label rows, with event numbers given in Table 1. Asterisks on seismograms 1-KEV, 1-KON, 3-COP and 5-RAR designate seismograms down-weighted in the inversions for reasons described in the text.

Fig. 4. Comparison of observed seismograms (solid lines) with synthetics calculated to the seventh overtone (dashed lines) for models EU0 (left panel) and PA0 (right panel). Seismograms are labelled on the left by event-station pairs, with event numbers given in Table 1, and on the right by epicentral distance; time axes are aligned with respect to a reducing velocity of 3.8 km/s. Asterisks on seismograms 1-KEV, 1-KON, 3-COP and 5-RAR designate seismograms down-weighted in the inversions for reasons described in the text.

Fig. 5. Path-averaged models EU1 (solid lines) and PA1 (dotted lines) obtained by squeezing the differences in compressional and shear velocities above $z^* = 400$ km.

Fig. 6. Comparison of observed BCCFs (solid lines) with synthetics (dashed lines) for models EU1 (top) and PA1 (bottom). Conventions the same as in Figure 3.

Fig. 7. Comparison of observed seismograms (solid lines) with synthetics calculated to the

seventh overtone (dashed lines) for models EU1 (left panel) and PA1 (right panel). Conventions the same as in Figure 4.

Fig. 8. Path-averaged models EU2 (solid lines) and PA2 (dotted lines) obtained by squeezing the differences in shear velocities above $z^* = 400$ km and the differences in compressional velocities above $z^* = 220$ km.

Fig. 9. Comparison of observed BCCFs (solid lines) with synthetics (dashed lines) for models EU2 (top) and PA2 (bottom). Conventions the same as in Figure 3.

Fig. 10. Comparison of observed seismograms (solid lines) with synthetics calculated to the seventh overtone (dashed lines) for models EU2 (left panel) and PA2 (right panel). Conventions the same as in Figure 4.

Fig. 11. Path-averaged models EU3 (solid lines) and PA3 (dotted lines) obtained by squeezing the differences in compressional and shear velocities above $z^* = 220$ km.

Fig. 12. Comparison of observed BCCFs (solid lines) with synthetics (dashed lines) for models EU3 (top) and PA3 (bottom). Conventions the same as in Figure 3.

Fig. 13. Comparison of observed seismograms (solid lines) with synthetics calculated to the seventh overtone (dashed lines) for models EU3 (left panel) and PA3 (right panel). Conventions the same as in Figure 4.

Fig. 14. Comparison of our *P-SV* models EU2 and PA2 (solid lines) with *Grand and Helmberger's* [1984a,b] *SH* models of the upper mantle beneath stable North America (SNA) and the western Atlantic (ATL) (dashed lines).

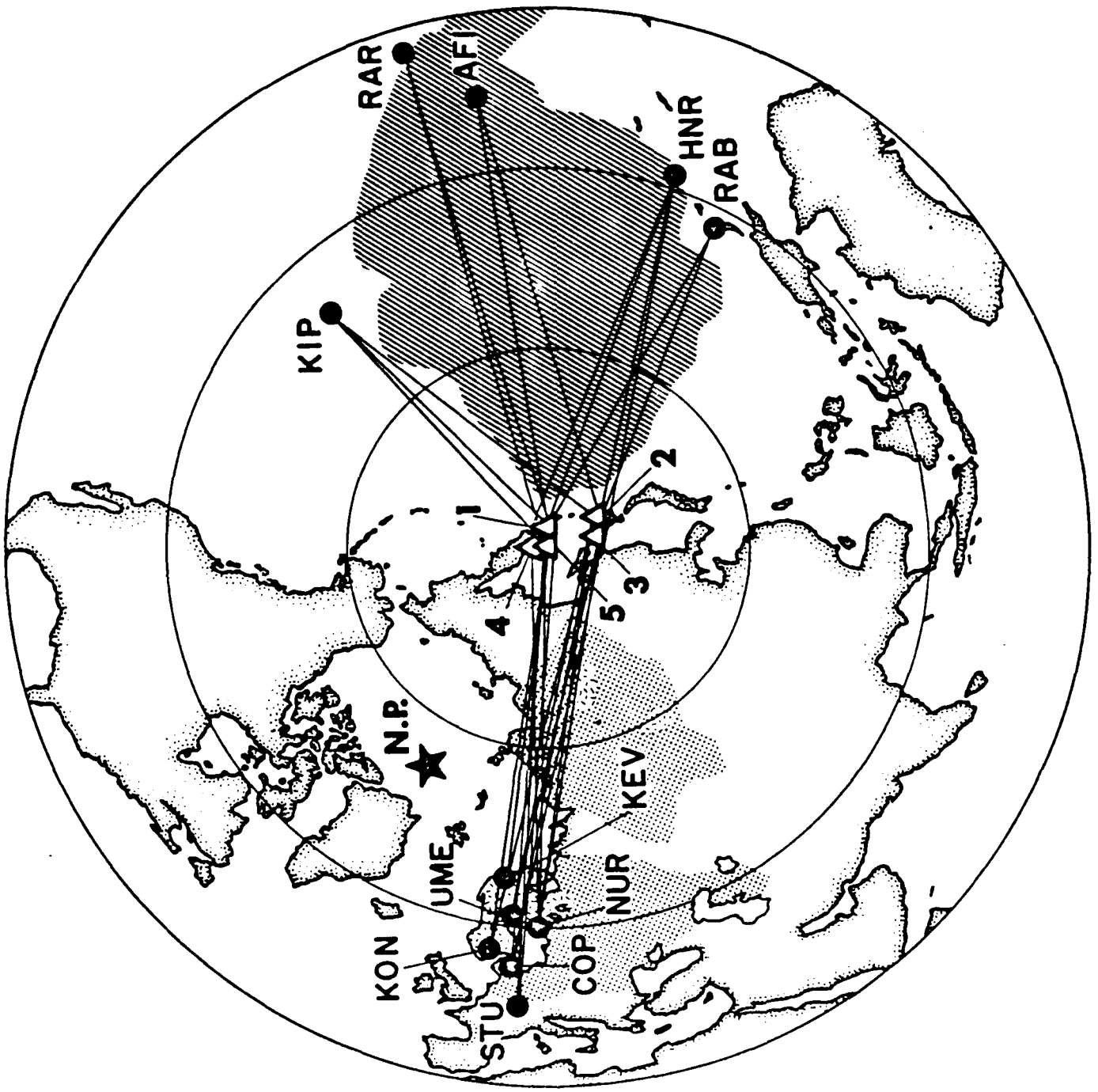

FIG 1

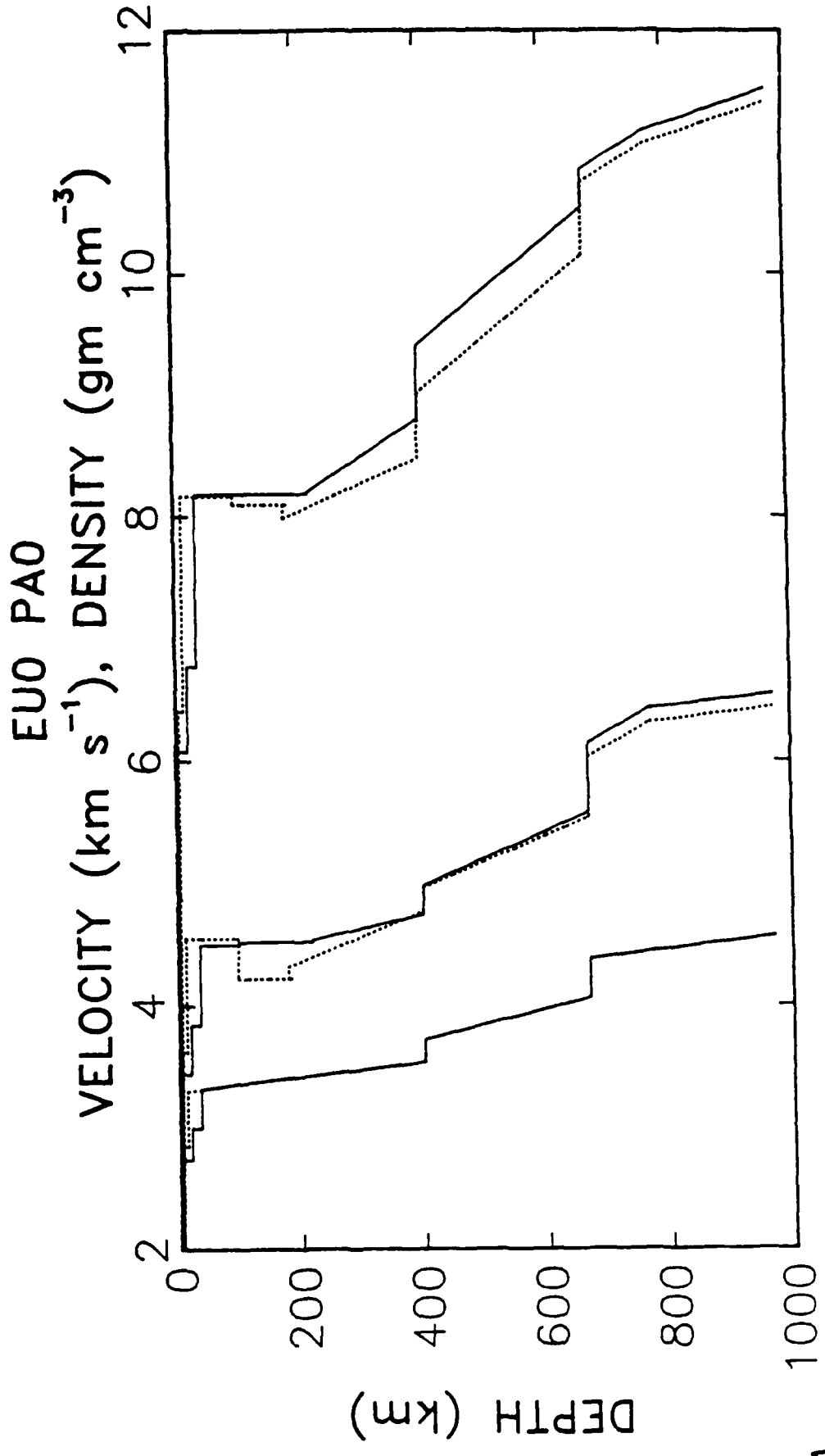
EUO PAO
VELOCITY (km s^{-1}), DENSITY (gm cm^{-3})
2
4
6
8
10
12
0
200
400
600
800
1000
DEPTH (km)

FIG 2

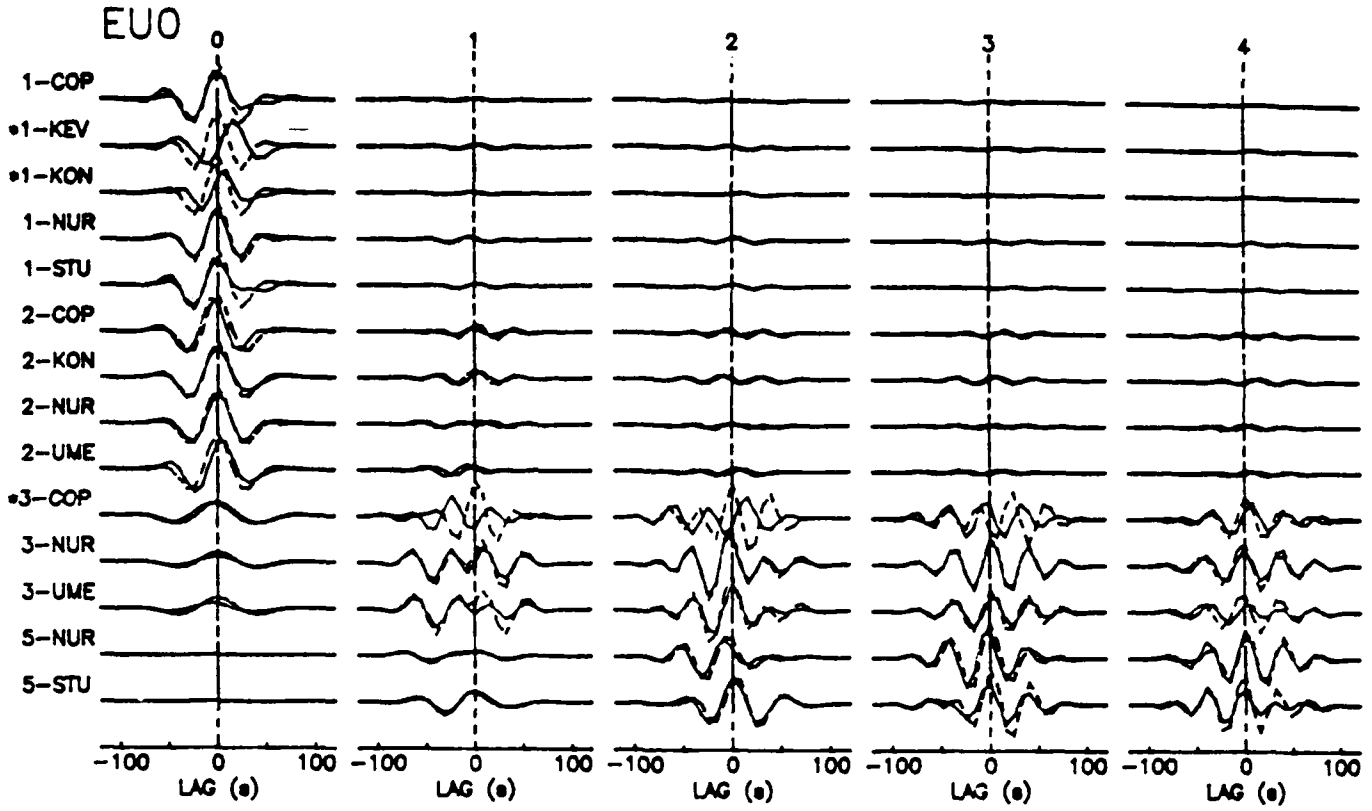
EUO
0
1
2
3
4
1-COP
*1-KEV
*1-KON
1-NUR
1-STU
2-COP
2-KON
2-NUR
2-UME
*3-COP
3-NUR
3-UME
5-NUR
5-STU
-100
0
100
LAG (s)

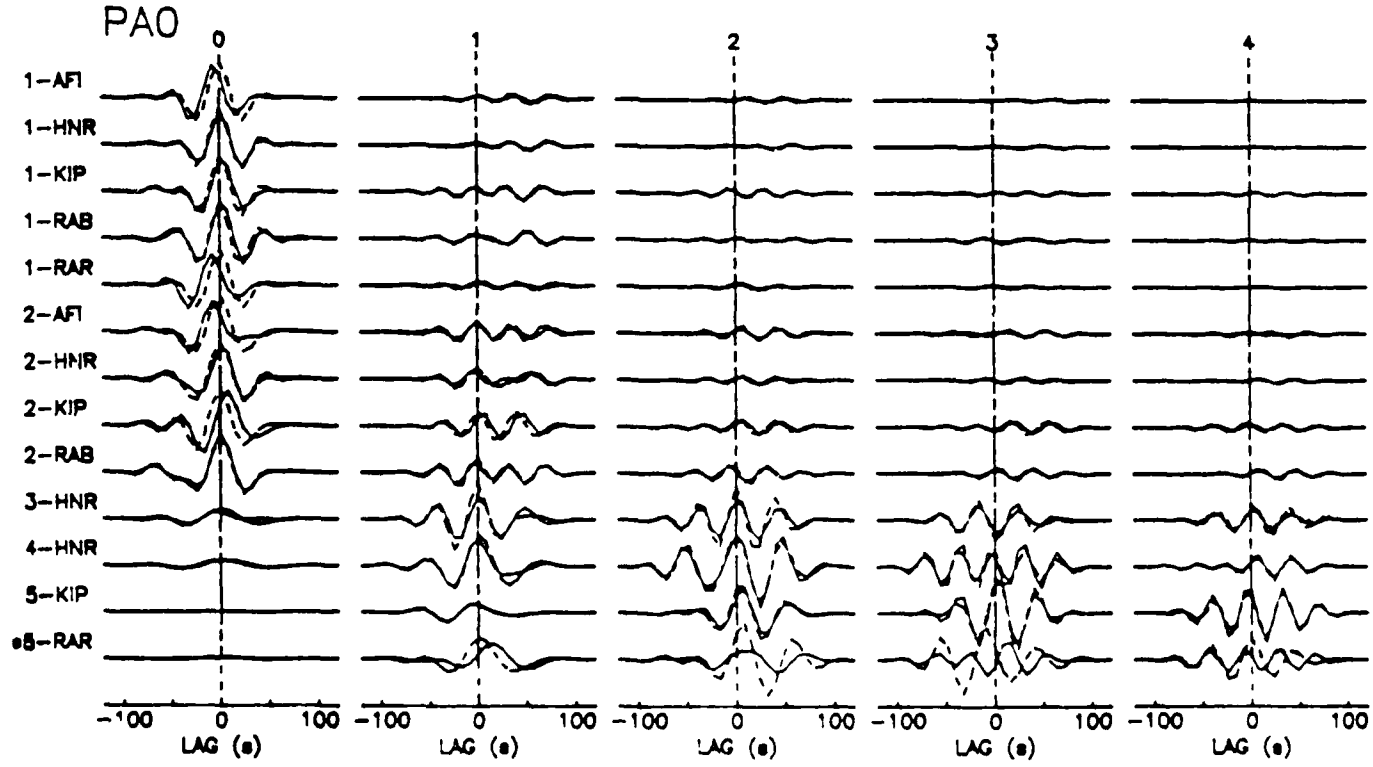
PAO
0
1
2
3
4
1-AFI
1-HNR
1-KIP
1-RAB
1-RAR
2-AFI
2-HNR
2-KIP
2-RAB
3-HNR
4-HNR
5-KIP
*5-RAR
-100
0
100
LAG (s)

FIG 3

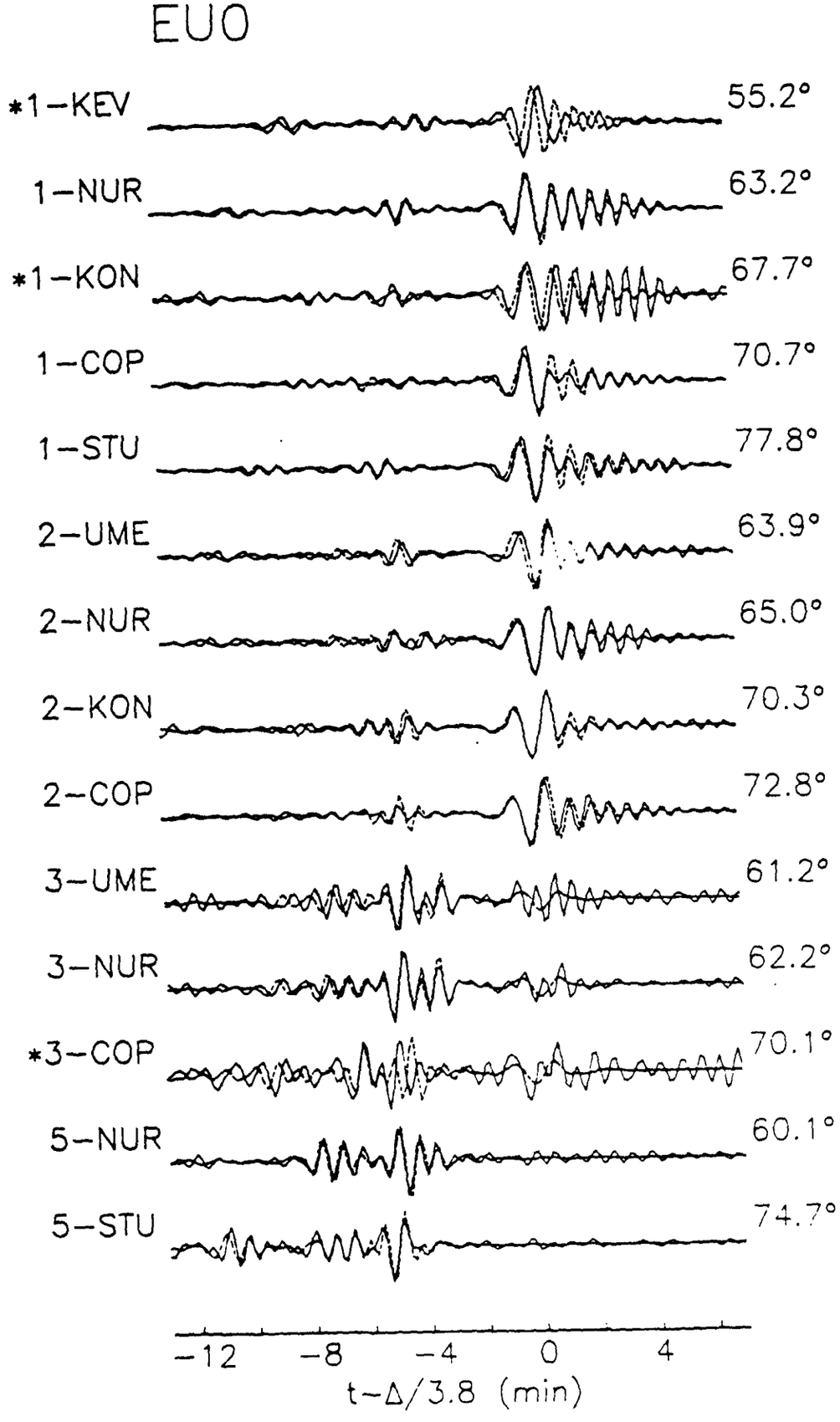
EUO
*1-KEV
55.2°
1-NUR
63.2°
*1-KON
67.7°
1-COP
70.7°
1-STU
77.8°
2-UME
63.9°
2-NUR
65.0°
2-KON
70.3°
2-COP
72.8°
3-UME
61.2°
3-NUR
62.2°
*3-COP
70.1°
5-NUR
60.1°
5-STU
74.7°
−12
−8
−4
0
4
t−Δ/3.8 (min)

FIG 4a

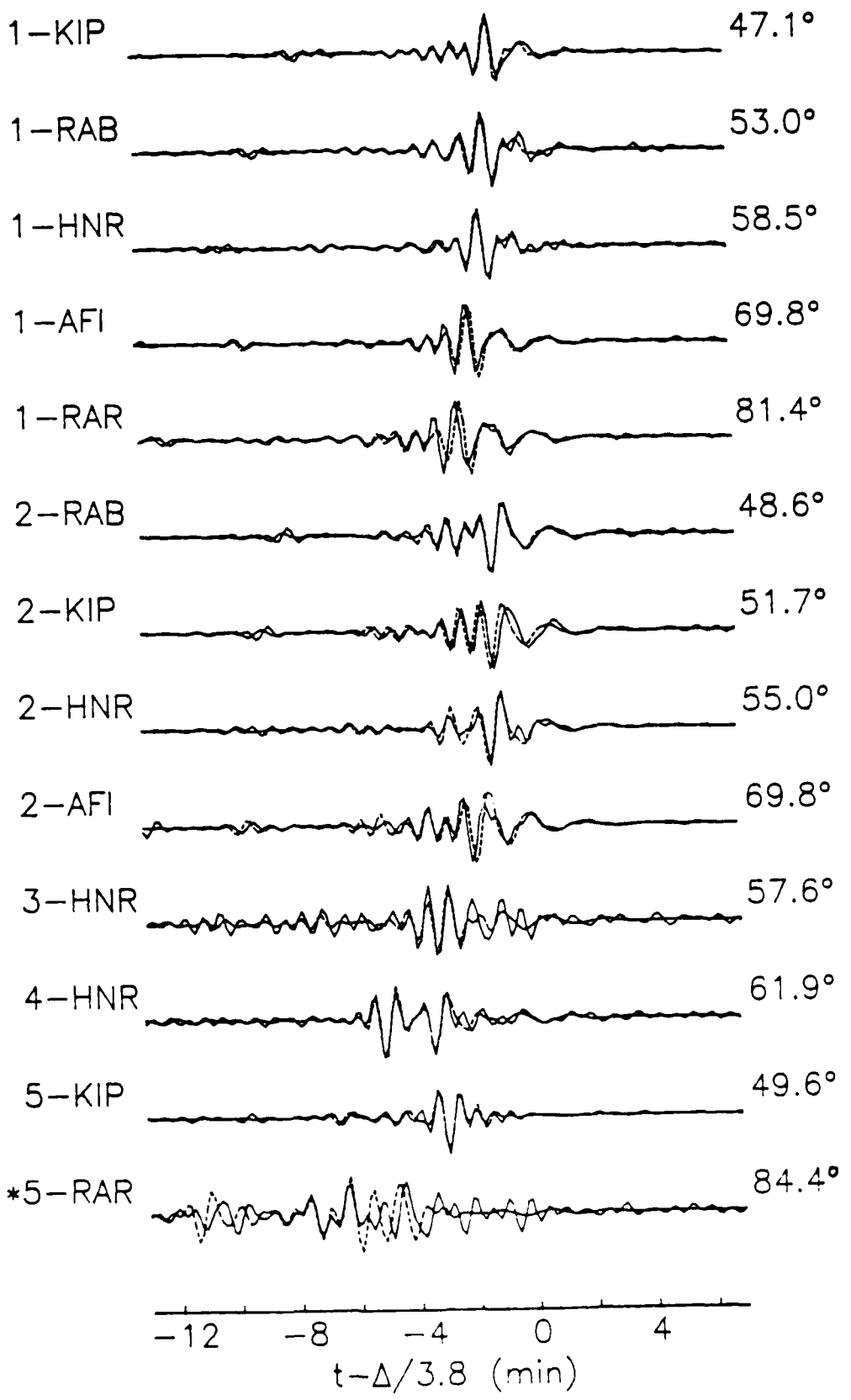
PAO
1–KIP
47.1°
1–RAB
53.0°
1–HNR
58.5°
1–AFI
69.8°
1–RAR
81.4°
2–RAB
48.6°
2–KIP
51.7°
2–HNR
55.0°
2–AFI
69.8°
3–HNR
57.6°
4–HNR
61.9°
5–KIP
49.6°
*5–RAR
84.4°
−12
−8
−4
0
4
t−Δ/3.8 (min)

Fig 4b

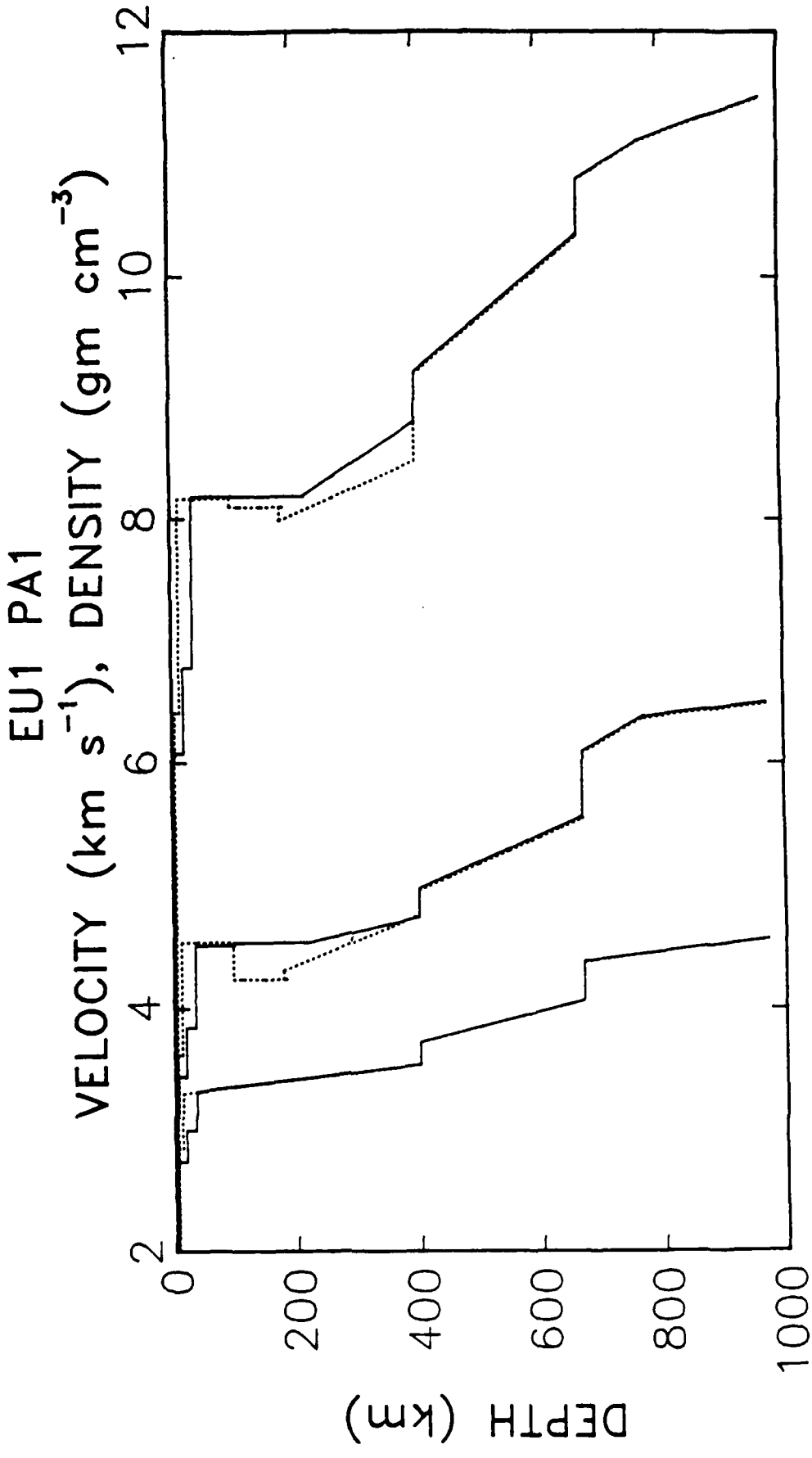
EU1 PA1
VELOCITY (km s^{-1}), DENSITY (gm cm^{-3})
2
4
6
8
10
12
0
200
400
600
800
1000
DEPTH (km)

FIG 5

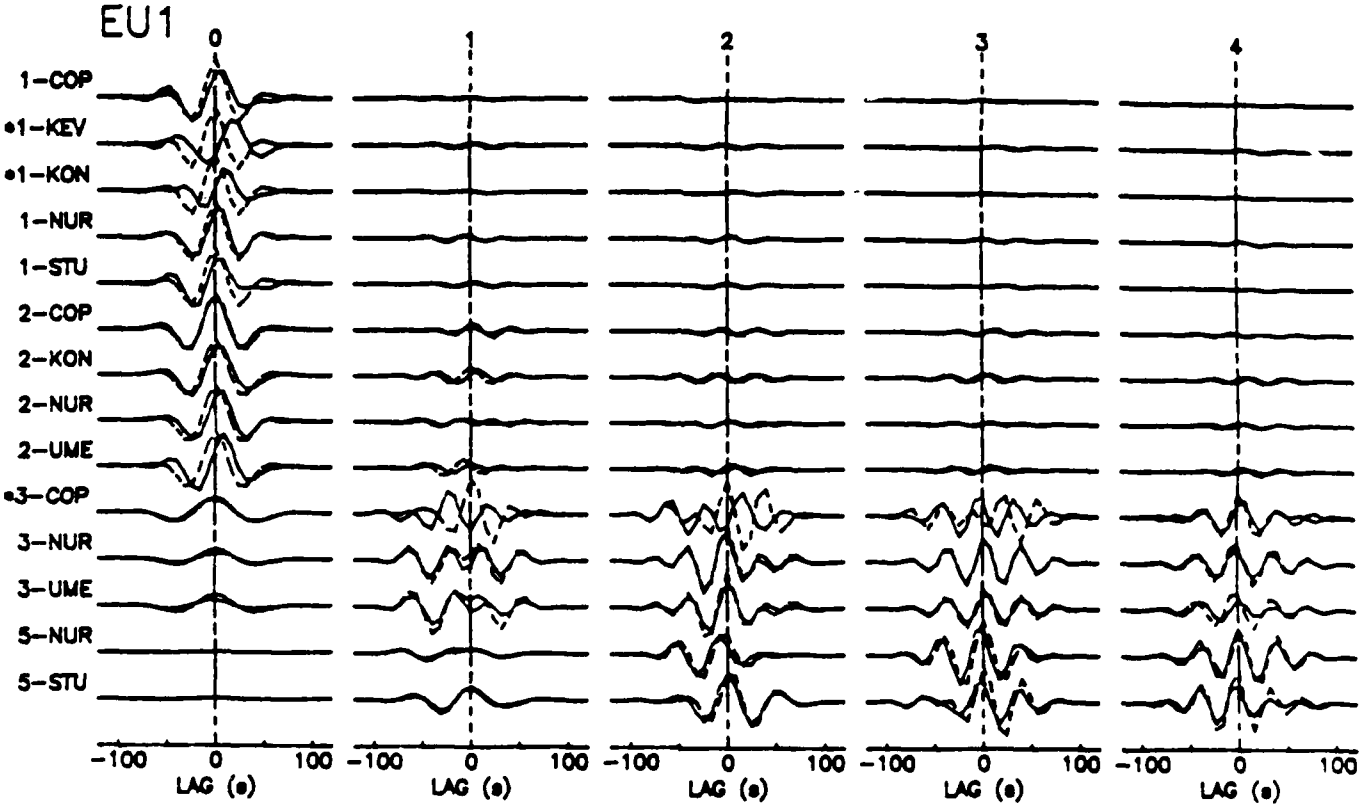
EU1
0
1
2
3
4
1-COP
•1-KEV
•1-KON
1-NUR
1-STU
2-COP
2-KON
2-NUR
2-UME
•3-COP
3-NUR
3-UME
5-NUR
5-STU
-100
0
100
LAG (s)

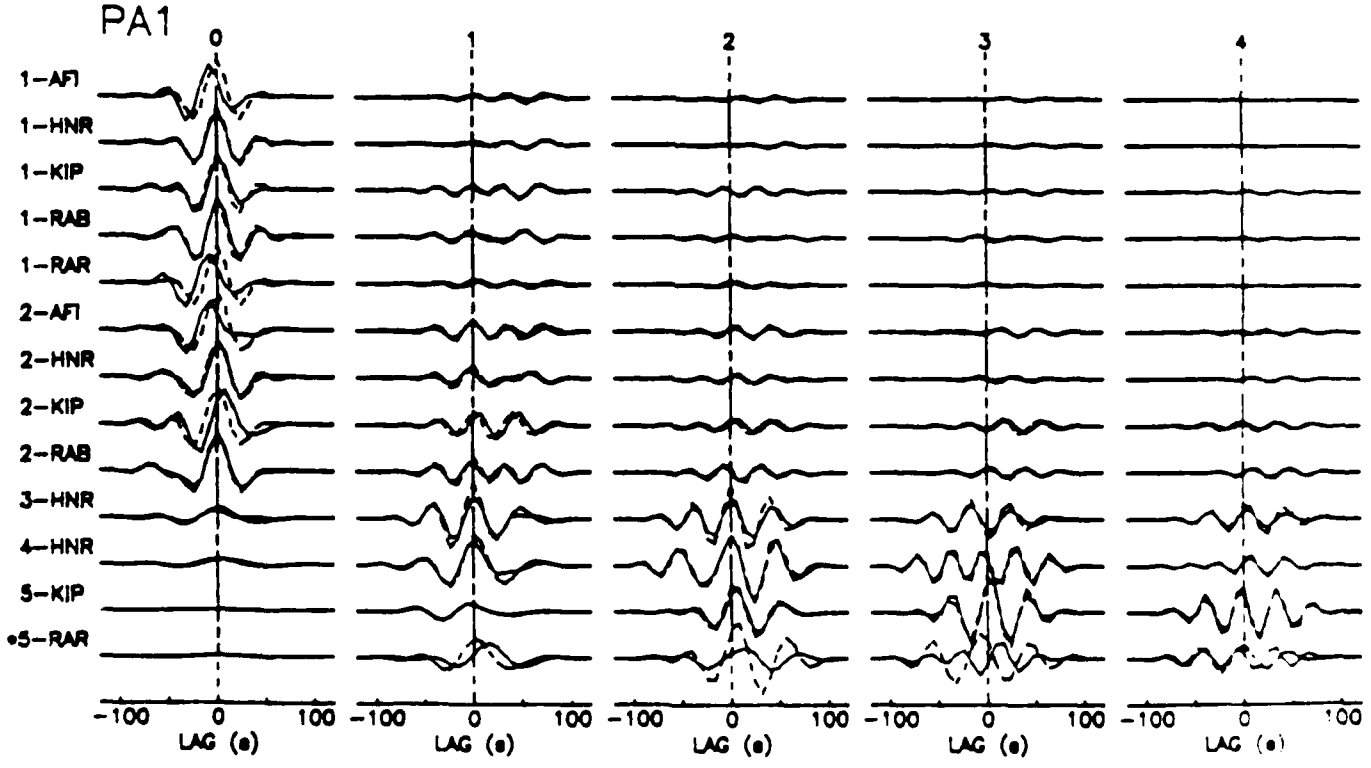
PA1
0
1
2
3
4
1-AFI
1-HNR
1-KIP
1-RAB
1-RAR
2-AFI
2-HNR
2-KIP
2-RAB
3-HNR
4-HNR
5-KIP
•5-RAR
-100
0
100
LAG (s)

FIG 6

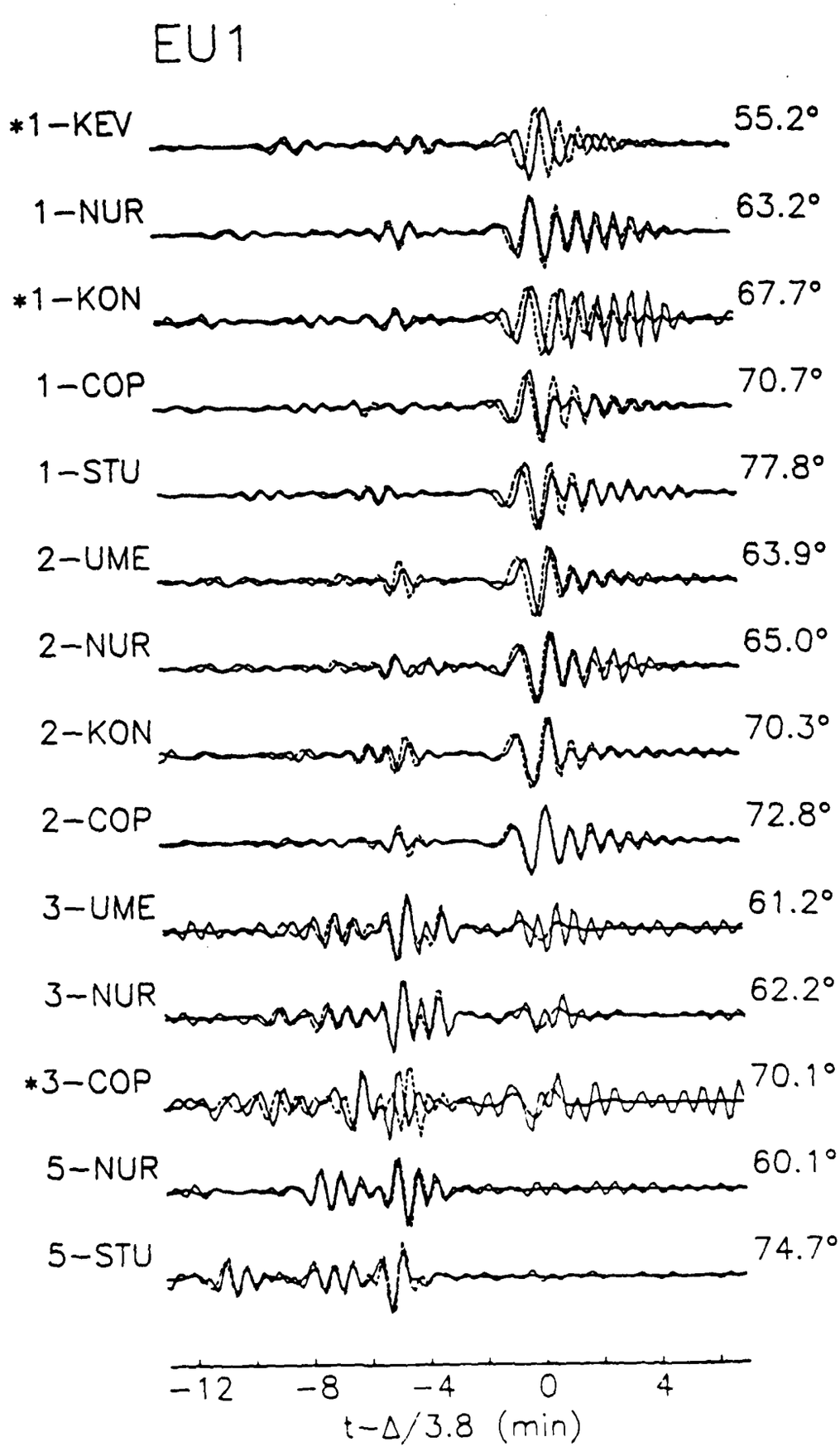
EU1
*1-KEV
55.2°
1-NUR
63.2°
*1-KON
67.7°
1-COP
70.7°
1-STU
77.8°
2-UME
63.9°
2-NUR
65.0°
2-KON
70.3°
2-COP
72.8°
3-UME
61.2°
3-NUR
62.2°
*3-COP
70.1°
5-NUR
60.1°
5-STU
74.7°
-12
-8
-4
0
4
t-Δ/3.8 (min)

FIGURE 7a

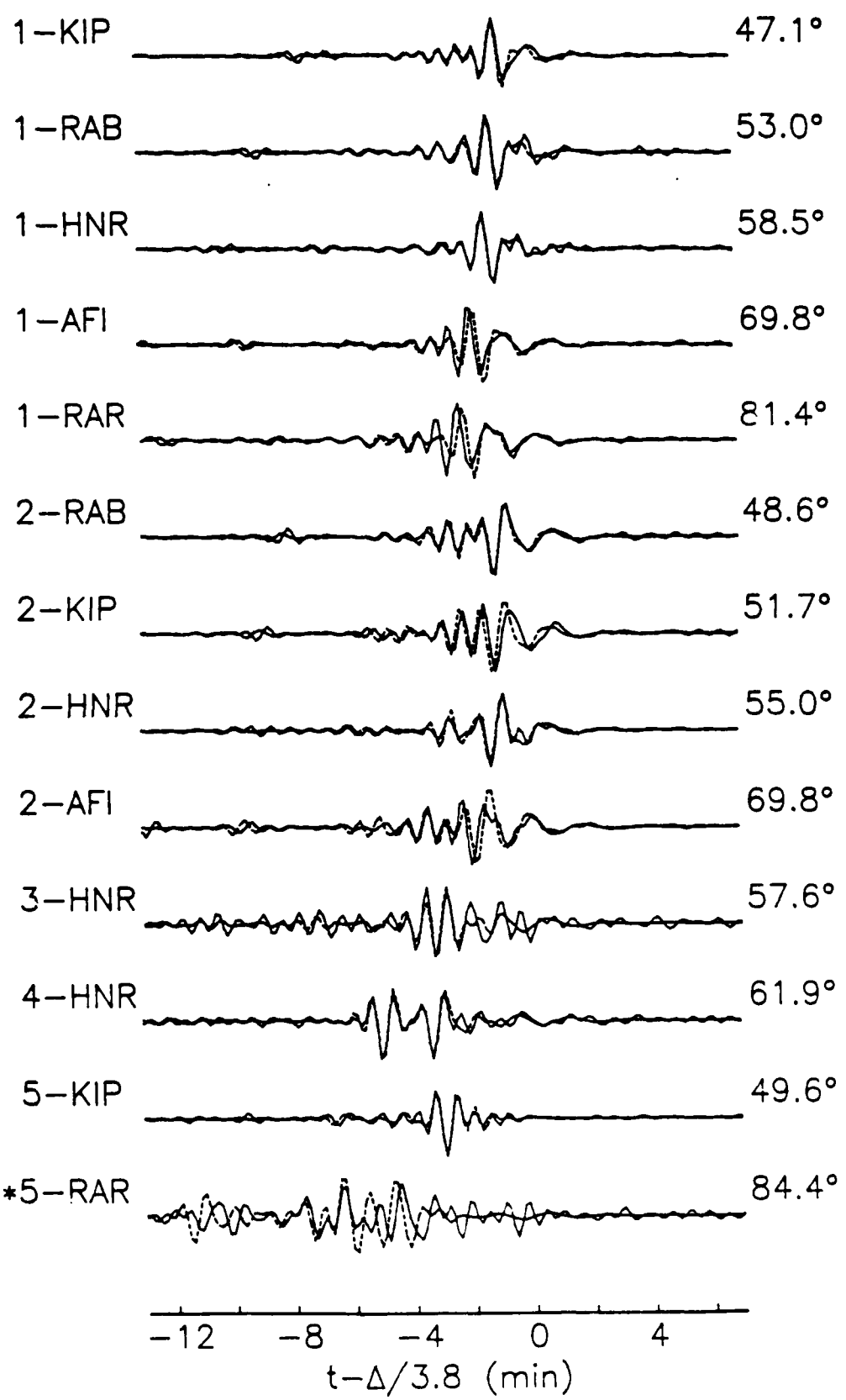
PA1
1–KIP
47.1°
1–RAB
53.0°
1–HNR
58.5°
1–AFI
69.8°
1–RAR
81.4°
2–RAB
48.6°
2–KIP
51.7°
2–HNR
55.0°
2–AFI
69.8°
3–HNR
57.6°
4–HNR
61.9°
5–KIP
49.6°
*5–RAR
84.4°
−12
−8
−4
0
4
t–Δ/3.8 (min)

FIG 7b

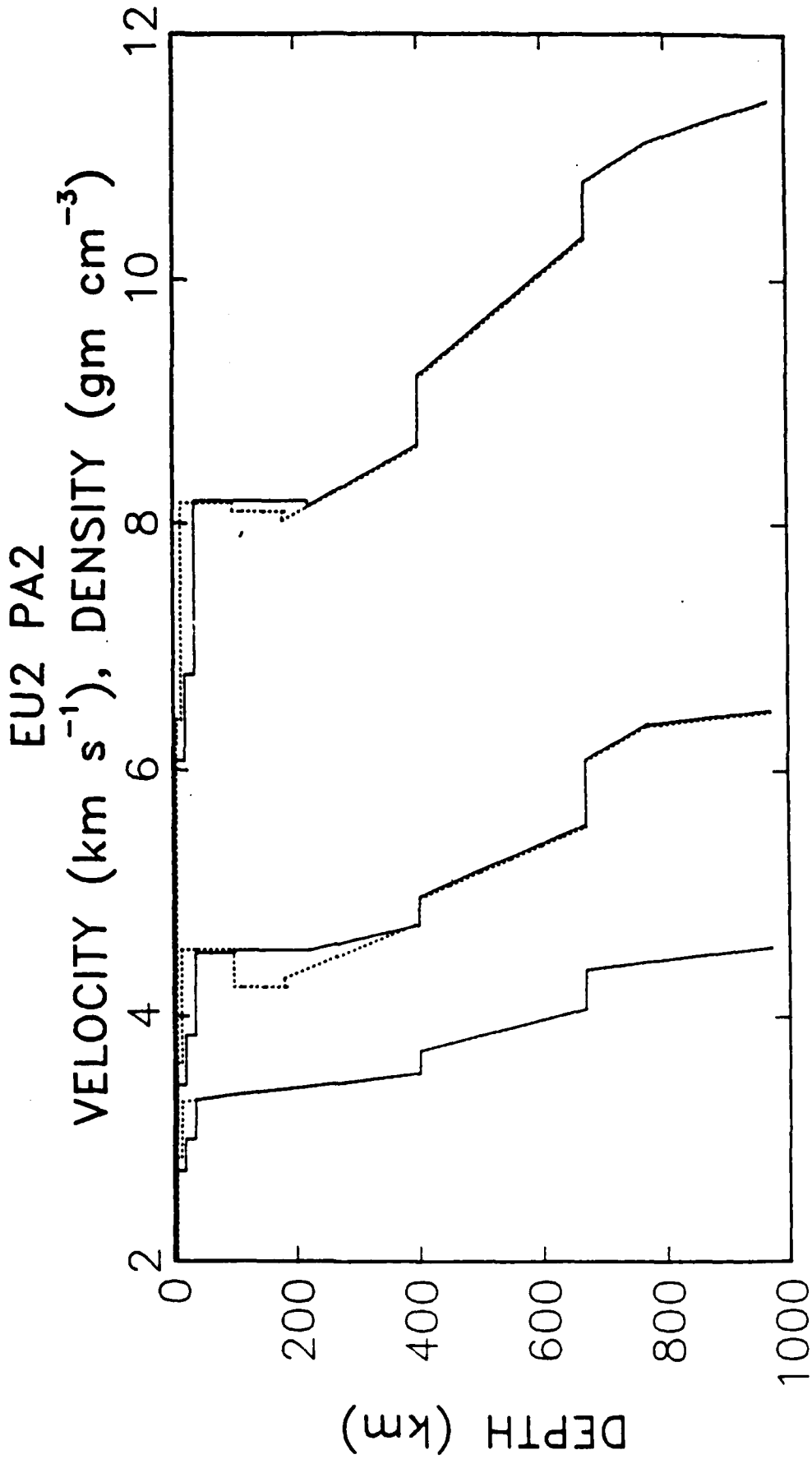
EU2 PA2
VELOCITY (km s^{-1}), DENSITY (gm cm^{-3})
DEPTH (km)
0
200
400
600
800
1000
2
4
6
8
10
12

Fig 8

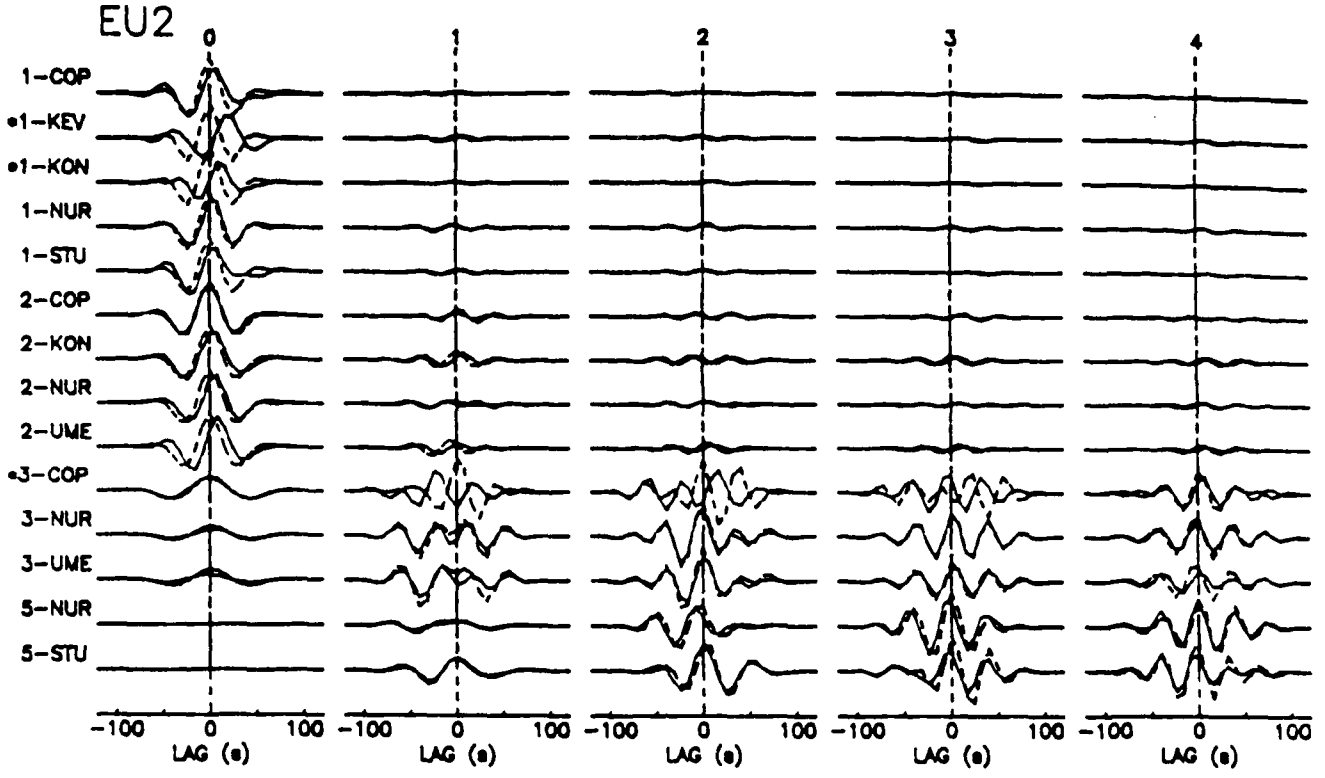
EU2
0
1
2
3
4
1-COP
•1-KEV
•1-KON
1-NUR
1-STU
2-COP
2-KON
2-NUR
2-UME
•3-COP
3-NUR
3-UME
5-NUR
5-STU
-100
0
100
LAG (s)

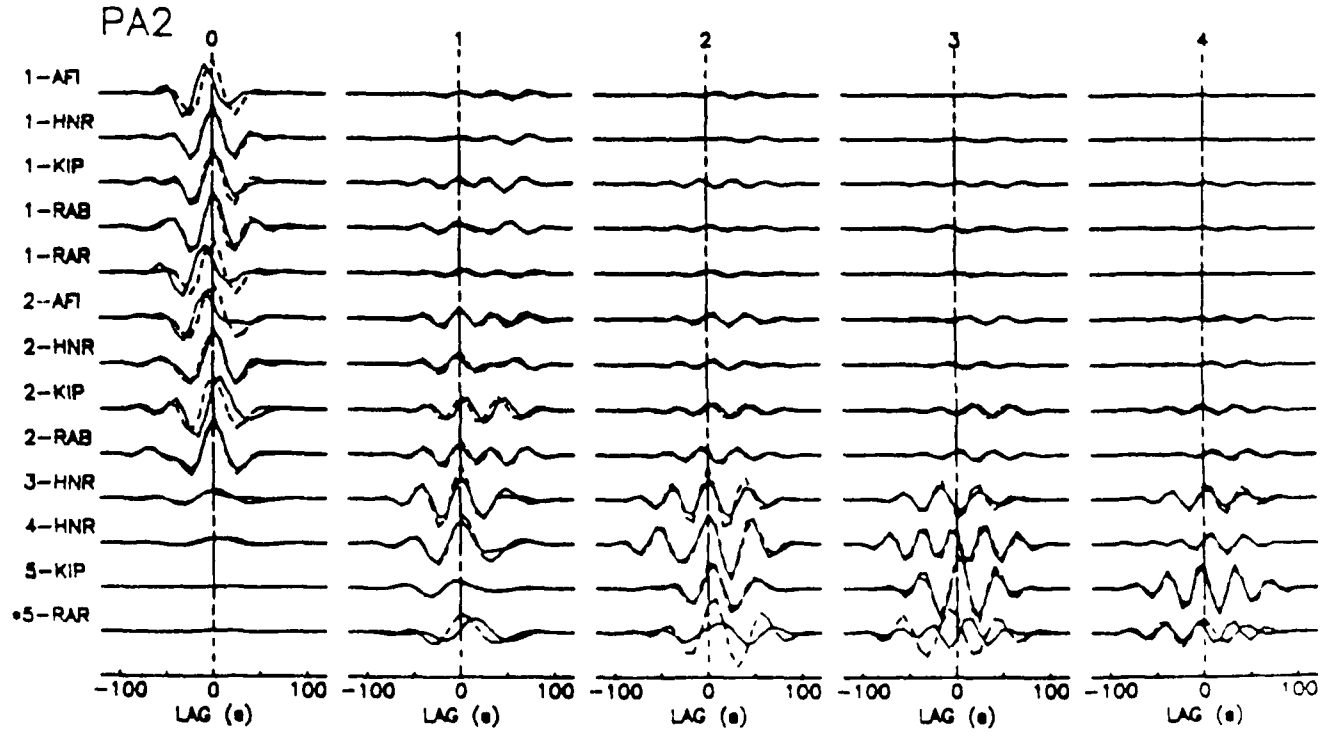
PA2
0
1
2
3
4
1-AFI
1-HNR
1-KIP
1-RAB
1-RAR
2-AFI
2-HNR
2-KIP
2-RAB
3-HNR
4-HNR
5-KIP
•5-RAR
-100
0
100
LAG (s)

FIG 9

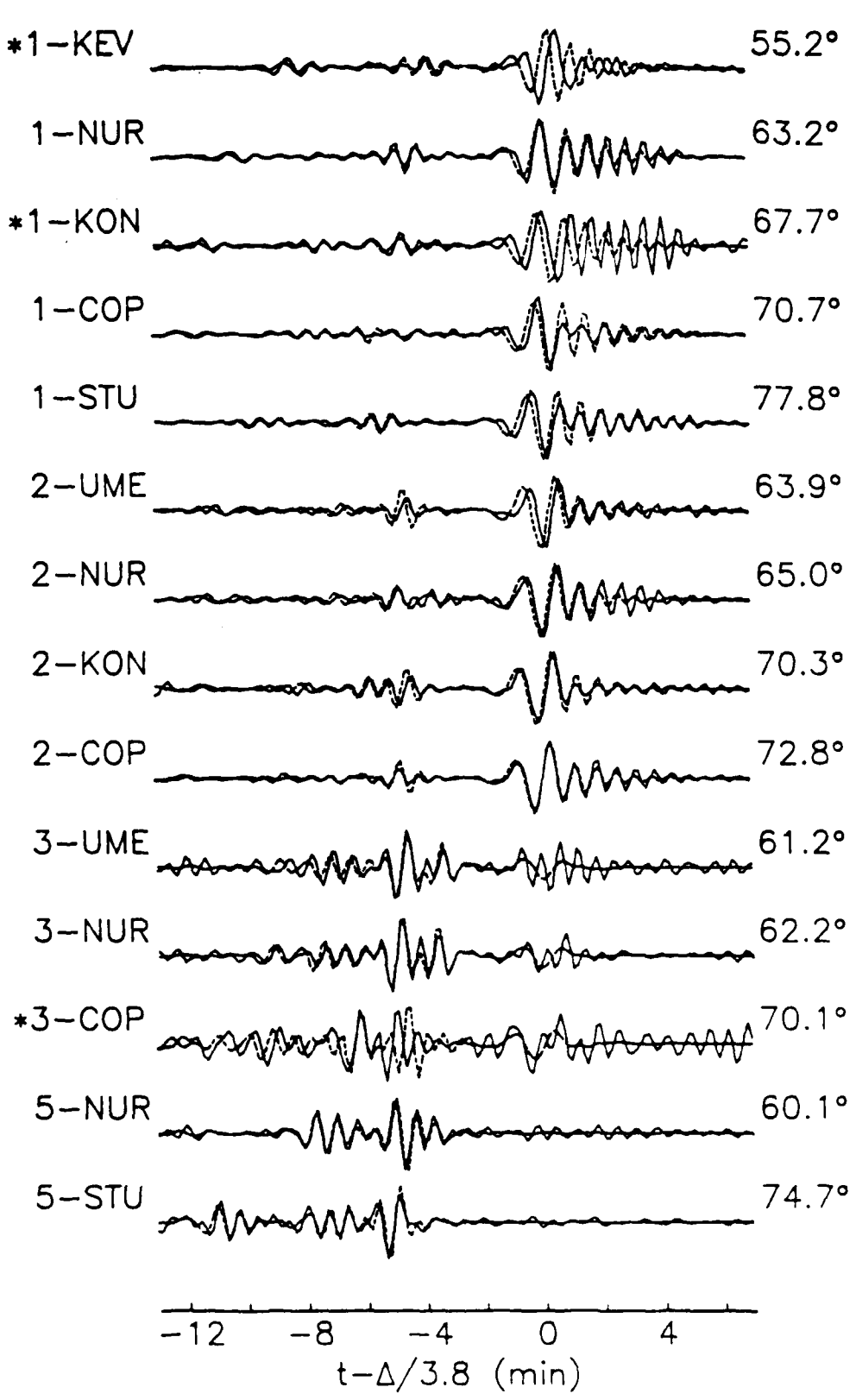
EU2
*1-KEV
55.2°
1-NUR
63.2°
*1-KON
67.7°
1-COP
70.7°
1-STU
77.8°
2-UME
63.9°
2-NUR
65.0°
2-KON
70.3°
2-COP
72.8°
3-UME
61.2°
3-NUR
62.2°
*3-COP
70.1°
5-NUR
60.1°
5-STU
74.7°
−12
−8
−4
0
4
t−Δ/3.8 (min)

FIG 10a

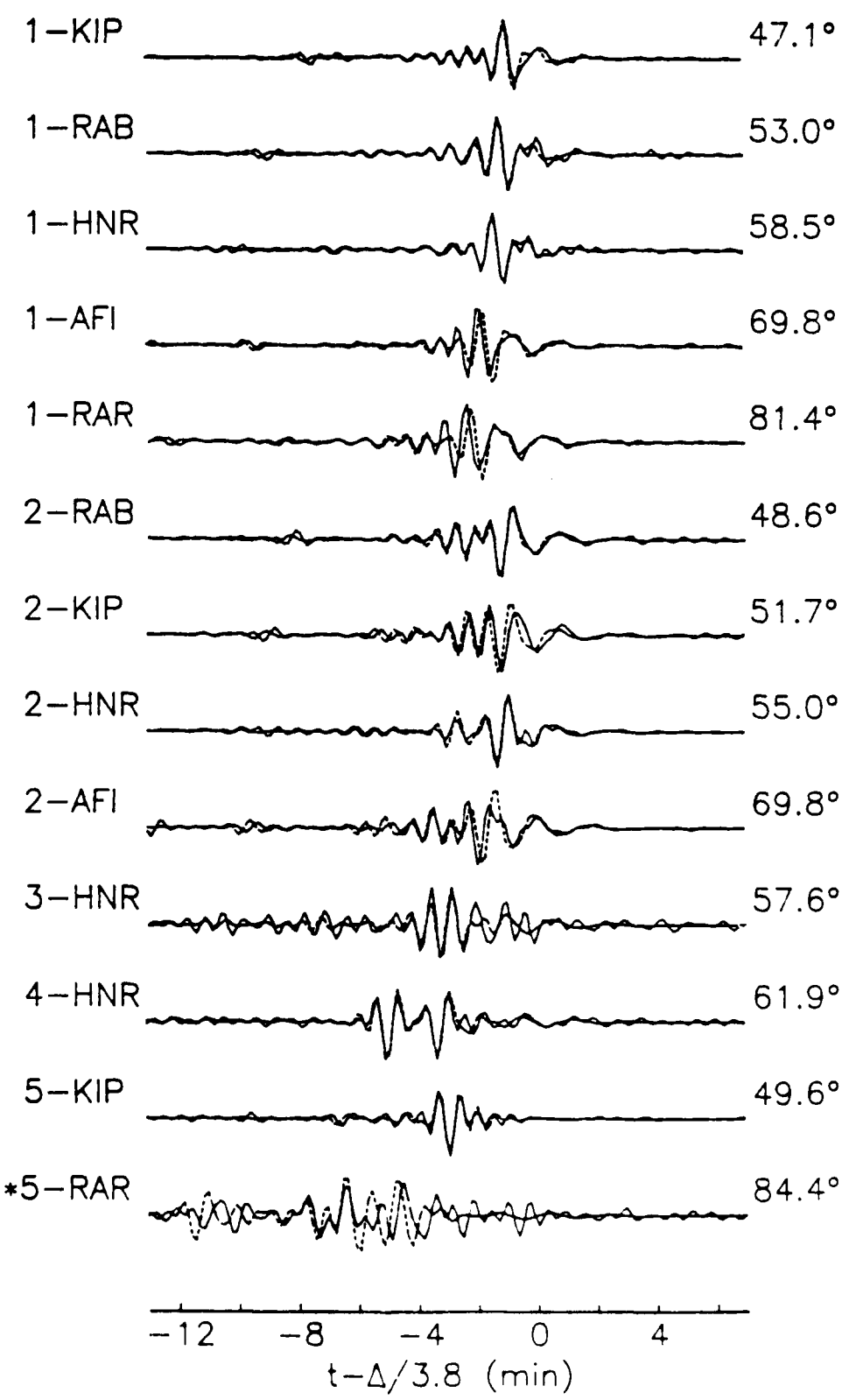
PA2
1–KIP
47.1°
1–RAB
53.0°
1–HNR
58.5°
1–AFI
69.8°
1–RAR
81.4°
2–RAB
48.6°
2–KIP
51.7°
2–HNR
55.0°
2–AFI
69.8°
3–HNR
57.6°
4–HNR
61.9°
5–KIP
49.6°
*5–RAR
84.4°
−12
−8
−4
0
4
t−Δ/3.8 (min)

FIG 10b

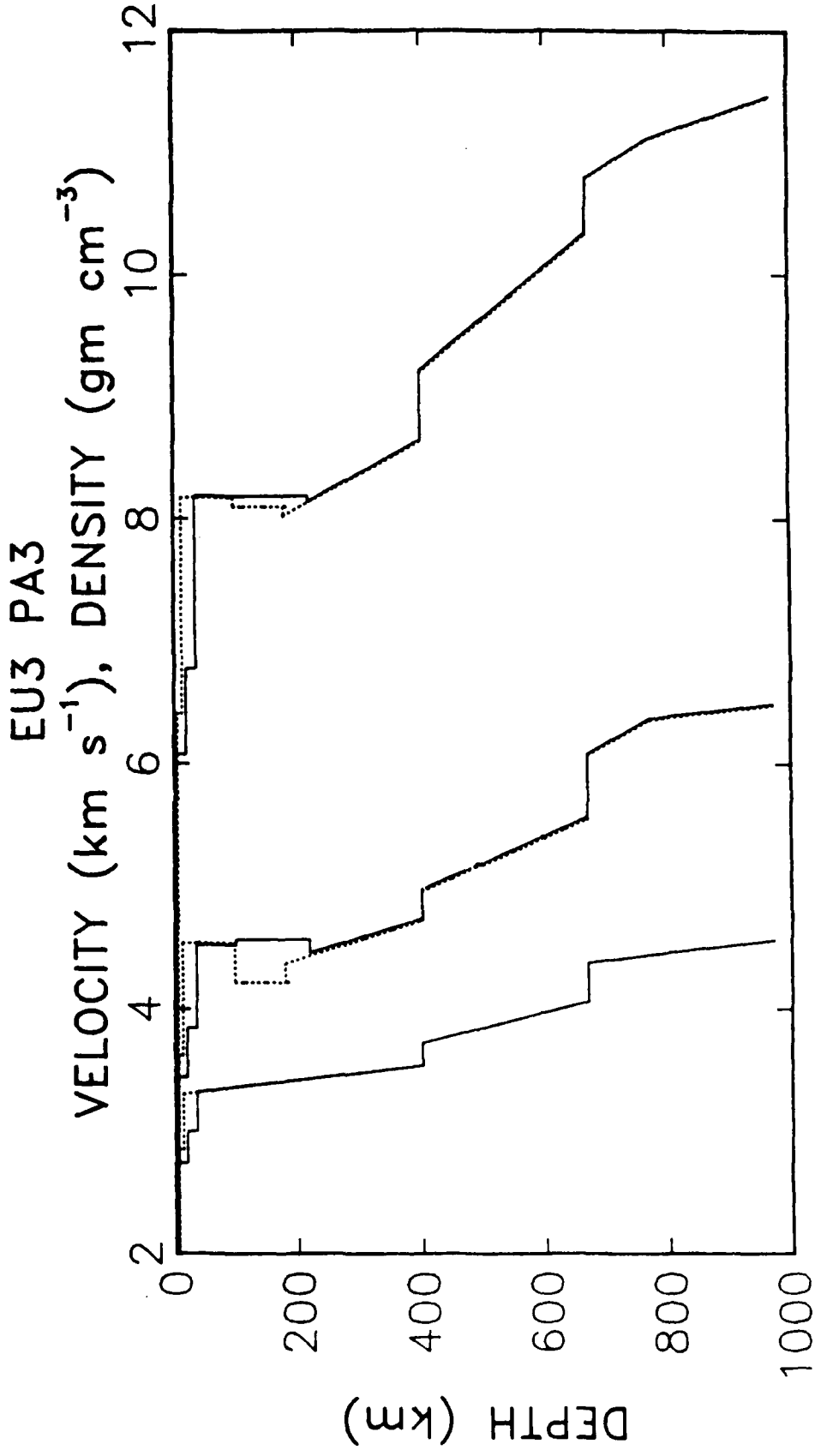
EU3 PA3
VELOCITY (km s^{-1}), DENSITY (gm cm^{-3})
DEPTH (km)
0
200
400
600
800
1000
2
4
6
8
10
12

FIG 11

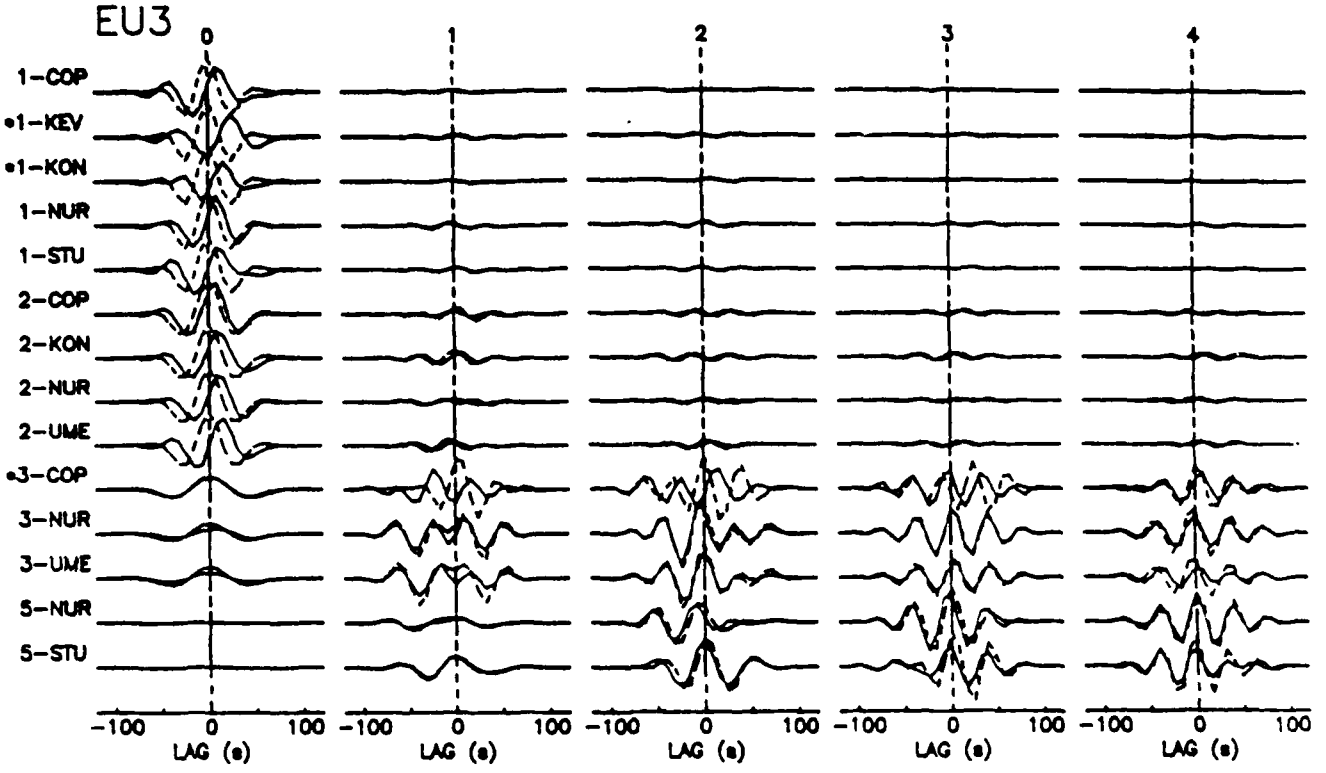
EU3
0
1
2
3
4
1-COP
•1-KEV
•1-KON
1-NUR
1-STU
2-COP
2-KON
2-NUR
2-UME
•3-COP
3-NUR
3-UME
5-NUR
5-STU
-100
0
100
LAG (s)

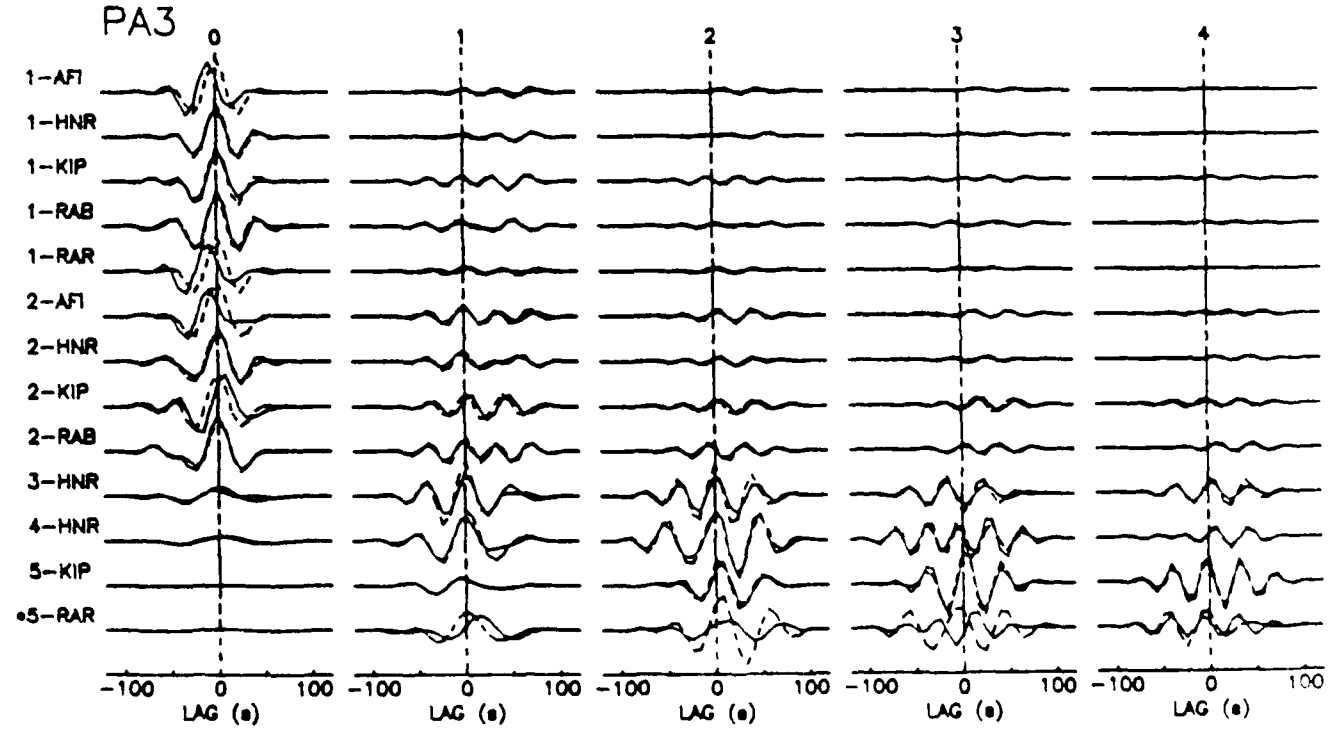
PA3
0
1
2
3
4
1-AFI
1-HNR
1-KIP
1-RAB
1-RAR
2-AFI
2-HNR
2-KIP
2-RAB
3-HNR
4-HNR
5-KIP
•5-RAR
-100
0
100
LAG (s)

FIG 12

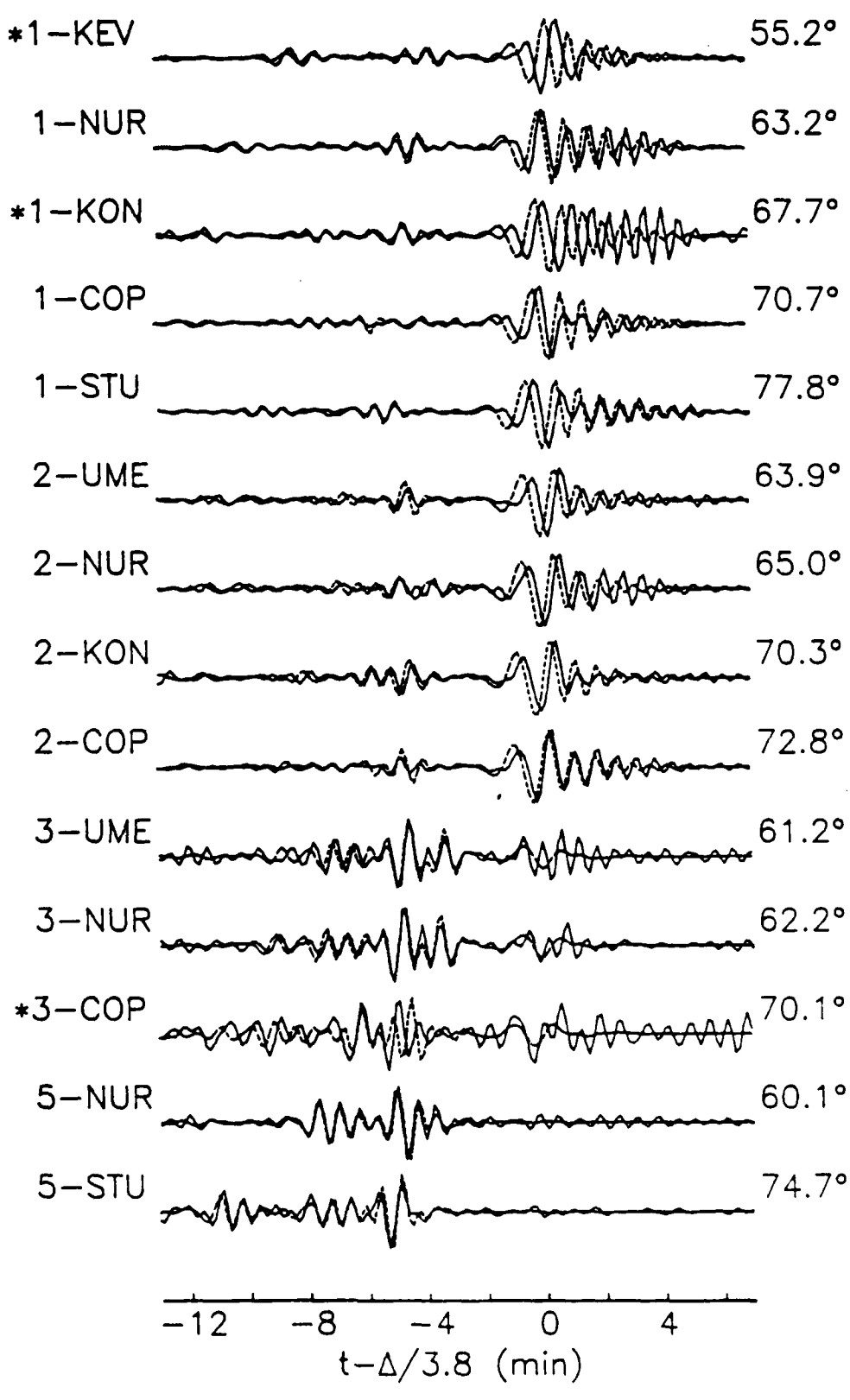
EU3
*1–KEV
55.2°
1–NUR
63.2°
*1–KON
67.7°
1–COP
70.7°
1–STU
77.8°
2–UME
63.9°
2–NUR
65.0°
2–KON
70.3°
2–COP
72.8°
3–UME
61.2°
3–NUR
62.2°
*3–COP
70.1°
5–NUR
60.1°
5–STU
74.7°
−12
−8
−4
0
4
t–Δ/3.8 (min)

FIG 13a

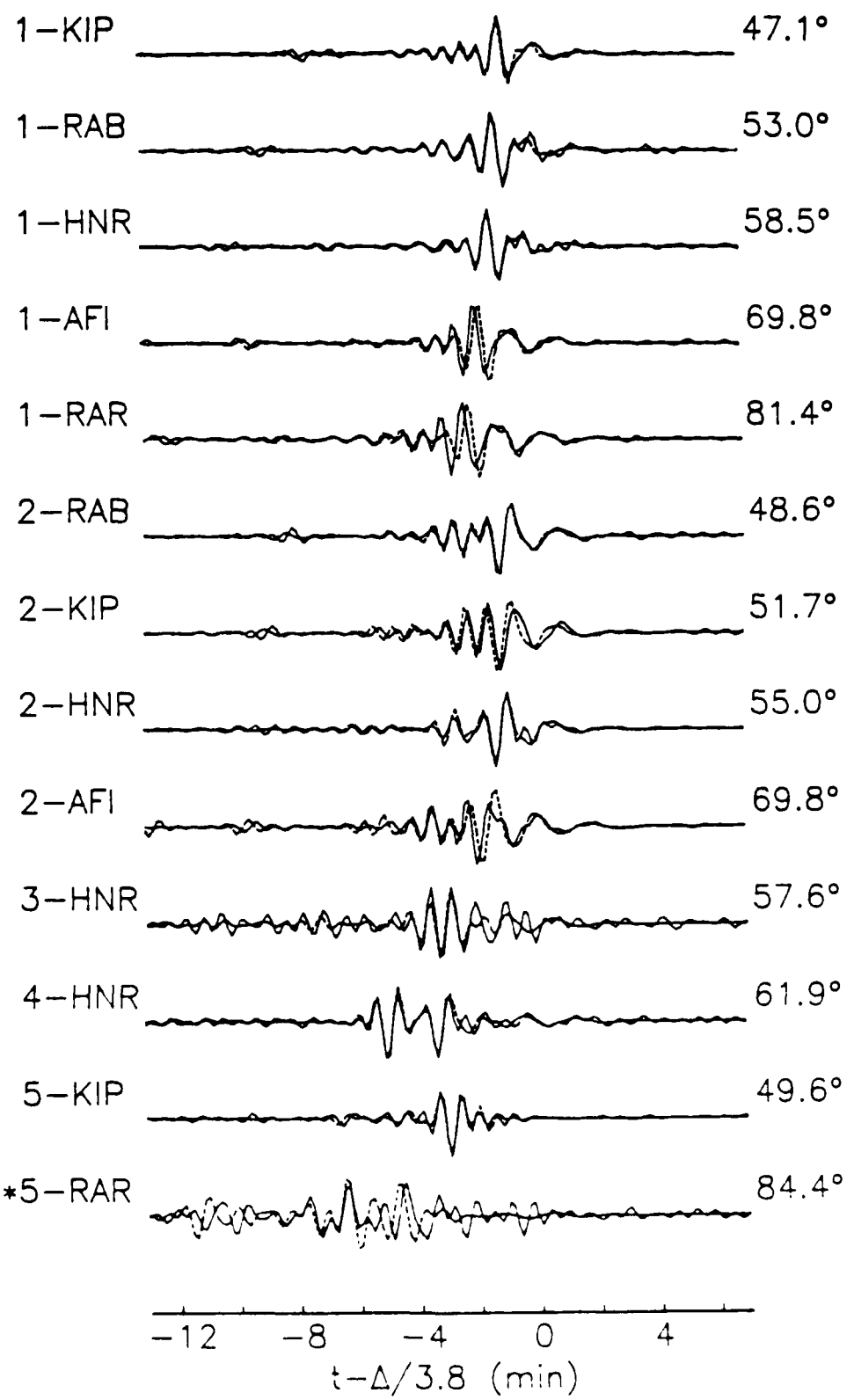
PA3
1–KIP
47.1°
1–RAB
53.0°
1–HNR
58.5°
1–AFI
69.8°
1–RAR
81.4°
2–RAB
48.6°
2–KIP
51.7°
2–HNR
55.0°
2–AFI
69.8°
3–HNR
57.6°
4–HNR
61.9°
5–KIP
49.6°
*5–RAR
84.4°
−12
−8
−4
0
4
t−Δ/3.8 (min)

FIG 13b

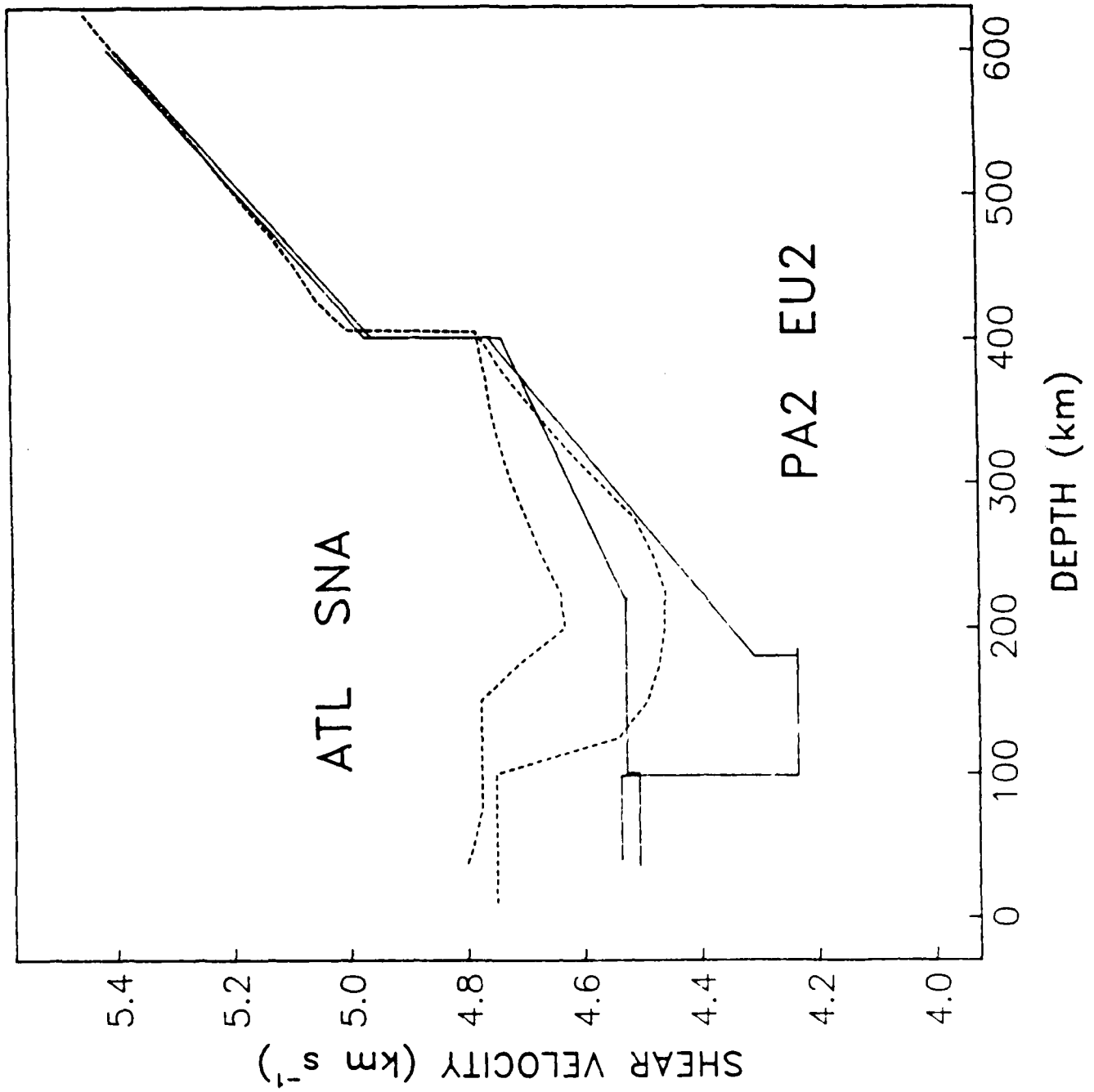
ATL SNA
PA2 EU2
SHEAR VELOCITY (km s^{-1})
DEPTH (km)
5.4
5.2
5.0
4.8
4.6
4.4
4.2
4.0
0
100
200
300
400
500
600

FIG 14

Resolving Power of Higher-Mode Waveform Inversion for Eurasian Upper-Mantle Structure

LIND S. GEE, ARTHUR L. LERNER-LAM*, AND THOMAS H. JORDAN

Department of Earth, Atmospheric and Planetary Sciences
Massachusetts Institute of Technology, Cambridge, MA 02139

In three-dimensional studies of earth structure based on surface-wave tomography, horizontal resolution is limited primarily by the distribution of paths, while vertical resolution is governed by the distribution of mode types. To obtain good vertical resolution below 200-km depth requires the use of higher modes. This paper investigates the vertical resolving power of source and receiver arrays in determining Eurasian crustal and upper-mantle structure using the waveform inversion technique of *Lerner-Lam and Jordan* [1983]. Unlike approaches to higher-mode analysis which rely on stacking to separate modes in the frequency-wavenumber domain, this procedure isolates the modes in the time domain by cross correlating a mode-branch synthetic with the observed and synthetic seismograms. The difference between the observed and synthetic branch cross-correlation functions is approximated as a linear functional of the residual dispersion, which is parameterized in turn by perturbations to earth structure. These differential branch cross-correlation functions are inverted for model perturbations, from which new dispersion curves and synthetic seismograms are computed, and the process is iterated until convergence. This formulation permits evaluation of real and hypothetical data sets by the resolution and covariance analysis of solutions to the linearized inverse problem. The results show that good vertical resolution of upper-mantle structure can be obtained with this method from sparse arrays of sources and/or receivers. Source arrays are particularly effective in enhancing resolution, provided that the source depths are well distributed and the source centroids and moment tensors are well determined. Resolution at depth may be obtained with this technique even with shallow sources, as long as the higher-mode branch cross-correlation functions are weighted appropriately.

INTRODUCTION

Studies of multiply-reflected shear waves, such as ScS_n [*Sipkin and Jordan*, 1976] and *SS* [*Grand et al.*, 1985], as well as studies of Rayleigh-wave dispersion [*Feng and Teng*, 1983], indicate that there are substantial lateral variations in upper-mantle structure underlying the Eurasian continent to depths exceeding 200 km. Recent models of the composition and development of the subcontinental mantle [*Jordan*, 1978, 1981; *Davies*, 1979; *Richter*, 1985] attribute this heterogeneity to compositional and thermal differences associated with the structure of what *Jordan* [1975] has termed the 'continental tectosphere.' These models predict a strong correlation between surface geological features and upper-mantle heterogeneity, a hypothesis which may be tested by detailed seismic imaging of the Eurasian crust and upper mantle.

One approach to such three-dimensional studies in Eurasia employs fundamental-mode Rayleigh waves to constrain lateral variations in structure [*Feng and Teng*, 1983]. While good horizontal resolution is possible with this technique, fundamental-mode dispersion is not sensitive to details in vertical structure at depths greater than 200 km. In principle, the addition of higher-mode data can improve structural resolution, but mode-mode interference complicates the

* Now at Lamont Doherty Geological Observatory, Palisades, NY 10964

measurement of dispersion in both the time and frequency domain [*Cara*, 1978; *Lerner-Lam*, 1982]. One method of analysis of higher-mode information requires sophisticated processing of the data in the frequency-wavenumber domain to separate the modes [*Nolet*, 1975, 1976; *Cara*, 1978, 1979; *Chou and Dziewonski*, 1980]. While this technique has been used successfully in studies of one-dimensional structure in Eurasia [*Nolet*, 1975; *Cara et al.*, 1980; *Chou and Dziewonski*, 1981], the Pacific [*Cara*, 1979], and North America [*Cara*, 1978, 1979], the procedure requires an array of stations distributed over several thousand kilometers and more-or-less aligned along the path from the epicenter. This requirement restricts the number of paths which may be studied with existing seismic networks and therefore limits the applicability of the method to tomographic experiments.

A different approach to higher-mode analysis has been taken by *Lerner-Lam and Jordan* [1983]. They employ waveform inversion to model the difference between an observed and synthetic seismogram as a measure of the departure of an earth model from an average of structure along the path. These differential seismograms are parameterized by perturbations to the fundamental and higher-mode dispersion, which are related to perturbations to the earth model. In traditional waveform inversion methods, the differential seismograms are inverted directly for model perturbations, with some weighting scheme applied on a time point by time point basis. However, *Lerner-Lam and Jordan* [1983] isolate higher-mode information explicitly by cross correlating the differential seismograms with the mode-branch synthetics and windowing the result in the lag-time domain. In addition to enhancing the signal-to-noise ratio for a particular mode and reducing interference from spurious signals and other modes, this approach permits the contribution from each mode to be assessed and weighted individually. The forward problem relating the branch cross-correlation functions to model perturbations is linearized by the application of first-order perturbation theory. Solutions are derived by a generalized least-squares inverse, and the process is iterated to convergence. The information provided by this approach is equivalent to the waveform analysis of multiply-reflected body waves [*Grand and Helmberger*, 1984a,b; *Grand et al.*, 1985], which uses trial-and-error forward modelling techniques. However, the ability of these methods to resolve upper-mantle structure is difficult to assess, whereas the linearized formulation used in this study permits the evaluation of the solutions by the now standard resolving power analysis of linear inverse theory.

In the next few years, millions of dollars will be spent on the deployment of new digital seismic instruments around the world. In particular, the Incorporated Research Institutes for Seismology (IRIS) network and the Portable Array of Seismometers for Studies of the Crust and Lithosphere (PASSCAL) will be coming on-line in the near future. In order to maximize the benefit from this expansion, it is important to understand how various configurations of sources and receivers will affect the resolution of earth structure. For example, an array of seismometers recently has been established in Western Europe. The Network of Autonomously Registering Stations (NARS) array spans 2500 km with 14 receivers [*Nolet, Dost, and Paulssen*, 1984]. One question which needs to be addressed is whether dense, linear arrays such as NARS are essential for detailed studies of upper-mantle structure. While the higher-mode wavenumber-stacking techniques of *Nolet* [1975, 1976] and *Cara* [1978, 1979] require this type of array to obtain the necessary spatial coverage, the waveform inversion technique of *Lerner-Lam and Jordan* [1983], which makes use of *a priori* information about structure along the path, does not. Consequently, a more efficient deployment of such receiver arrays would distribute them over a larger area in order to sample the greatest number of source-receiver paths.

FORMULATION OF THE INVERSE PROBLEM

In the waveform inversion technique of *Lerner-Lam and Jordan* [1983], an observed seismogram is characterized as the sum of the fundamental ($n = 0$) and higher-mode ($n \geq 0$)

surface waves:

$$s(\mathbf{r},t) = \sum_{n=0}^{\infty} u_n(\mathbf{r},t) \qquad (1)$$

where $u_n(\mathbf{r},t)$ is the seismogram for the n^{th} mode branch at a receiver position $\mathbf{r}$ and time t. A synthetic seismogram, $s(\mathbf{r},t)$, is calculated for a particular spherically-symmetric earth model, $m(r)$, complete to radial order N:

$$\bar{s}(\mathbf{r},t) = \sum_{n=0}^{N} \bar{u}_n(\mathbf{r},t) \qquad (2)$$

where $\bar{u}_n(\mathbf{r},t)$ is the synthetic seismogram for the n^{th} mode branch. In our application of this technique, the sum over N is truncated at the seventh higher mode (Figure 1). Although phases of high apparent velocity, such as core reflections, are not well represented as a consequence, these phases are nearly transversely polarized and do not contribute to the vertical-component seismograms used in this study. $u_n(\mathbf{r},t)$ is formulated using an asymptotic approximation to *Gilbert's* [1976] exact travelling-wave representation of the displacement field:

$$\bar{u}_n(\mathbf{r},t) \sim \sum_{s=1}^{S} \int_0^{\infty} \bar{G}_n^s(\lambda,\mathbf{r},t) \cos \bar{\xi}_n^s(\lambda,\mathbf{r},t)\, d\lambda . \qquad (3)$$

In this formulation, λ is the surface spherical wavenumber, and $\bar{G}_n^s(\lambda,\mathbf{r},t)$ and $\bar{\xi}_n^s(\lambda,\mathbf{r},t)$ are the amplitude and phase kernels for the s^{th} orbit of the n^{th} higher mode. Since we are concerned with arrivals corresponding to the first (minor-arc) orbit, we take $s = 1$ and drop the orbital indices.

The difference between an observed and synthetic seismogram, $\Delta s(\mathbf{r},t)$, can be approximated as a radial perturbation, $\Delta m(r)$, to the starting earth model, $m(r)$, where

$$\Delta s(\mathbf{r},t) = s(\mathbf{r},t) - \bar{s}(\mathbf{r},t) = \sum_{n=0}^{N} \Delta u_n(\mathbf{r},t) \qquad (4)$$

and $\Delta u_n(\mathbf{r},t)$ is the differential seismogram for the n^{th} mode branch. In order to estimate $\Delta m(r)$ from $\Delta s(\mathbf{r},t)$, it is necessary to minimize both observational and representational errors. These include random seismic noise and digitizing errors, as well as error processes which scale with signal strength, such as inaccuracies in representing the source, the instrument response, and wave propagation through the earth. One method of enhancing the signal corresponding to a particular mode and reducing the effect of ambient noise and spurious signals is to construct matched filters [*Chou and Dziewonski*, 1980] by cross correlating the differential seismograms with the mode-branch synthetics and windowing the results in the lag-time domain. *Lerner-Lam and Jordan* [1983] define the observed branch cross-correlation function,

$$S_m(\mathbf{r},\tau) = \bar{u}_m(\mathbf{r},t) * s(\mathbf{r},t) \equiv \int_{-\infty}^{\infty} \bar{u}_m(\mathbf{r},t)\, s(\mathbf{r},t+\tau)\, dt \qquad (5)$$

and the synthetic branch cross-correlation function,

$$\bar{S}_m(\mathbf{r},\tau) = \bar{u}_m(\mathbf{r},t) * \bar{s}(\mathbf{r},t) \qquad (6)$$

where τ is the lag time. With this notation, an appropriate functional for the structural inverse problem is the differential branch cross-correlation function:

$$\Delta S_m(\mathbf{r},\tau) = S_m(\mathbf{r},\tau) - \bar{S}_m(\mathbf{r},\tau) \cong \bar{u}_m(\mathbf{r},t) * \sum_{n=0}^{N} \Delta u_n(r,t) \quad . \qquad (7)$$

Using first-order perturbation theory, $\Delta S_m(\mathbf{r},\tau)$ may be related linearly to amplitude and dispersion perturbations through variations to the amplitude and phase kernels of $u_n(\mathbf{r},t)$

$$G_n(\lambda,\mathbf{r},t) = \bar{G}_n(\lambda,\mathbf{r},t)[1 + \gamma_n(\lambda)] \qquad (8a)$$

$$\xi_n(\lambda,\mathbf{r},t) = \bar{\xi}_n(\lambda,\mathbf{r},t) - \Delta\omega_n(\lambda)t \qquad (8b)$$

where $\gamma_n(\lambda)$ is a wavenumber-dependent perturbation to the relative amplitude and $\Delta\omega_n = \omega_n - \omega_n$ is a perturbation to the dispersion of the n^{th} higher mode. In terms of the differential branch cross-correlation function,

$$\Delta S_m(\mathbf{r},\tau) \cong \sum_n \int_0^\infty [C_{mn}(\lambda,\mathbf{r},\tau)\ \gamma_n(\lambda) + B_{mn}(\lambda,\mathbf{r},\tau)\ \Delta\omega_n(\lambda)]\ d\lambda \qquad (9)$$

where $C_{mn}(\lambda,\mathbf{r},\tau)$ and $B_{mn}(\lambda,\mathbf{r},\tau)$ are the cross correlations of the mode-branch synthetics with the Fréchet kernels for the amplitude and dispersion perturbations. This linearization is valid, provided that

$$| \Delta\omega_n t | << 1 \qquad (10a)$$

$$| \gamma_n | << 1 . \qquad (10b)$$

In general, these conditions will not be met, and the inversion must be iterated. Equation (9) can be rewritten in matrix form,

$$\Delta\mathbf{S} = \mathbf{C}\boldsymbol{\gamma} + \mathbf{B}\Delta\boldsymbol{\omega} . \qquad (11)$$

By applying Rayleigh's principle and first-order perturbation theory, the dispersion can be parameterized in terms of perturbations to the reference model [*Woodhouse and Dahlen*, 1978]

$$\Delta\omega = \mathbf{H}\Delta\mathbf{m} \tag{12}$$

where **H** is the Fréchet kernel for the appropriate model parameter. The relationship between the amplitude perturbation and the model perturbation is more complicated, however, and depends on details of the source and path. *Lerner-Lam and Jordan* [1983] apply an orthogonalization procedure to reduce the sensitivity of the branch cross-correlation functions to amplitude differences between the observed and synthetic seismogram. Their approach utilizes a projection operator to annihilate the matrix **C**. In this study, we consider only perturbations to the dispersion and disregard perturbations to the amplitude kernel.

With this formulation, the linearized forward problem between the differential branch cross-correlation function, $\Delta\mathbf{S}$, and perturbations to the reference earth model, $\Delta\mathbf{m}$, reduces to:

$$\mathbf{A}\,\Delta\mathbf{m} = \Delta\mathbf{S} \tag{13}$$

where $\mathbf{A} = \mathbf{BH}$. So far we have not considered the effect of noise or errors in the data functionals. In general, the estimated differential branch cross-correlation function, $\Delta\mathbf{S}_e$, will be the sum of the true branch cross-correlation function, $\Delta\mathbf{S}$, and some error, $\mathbf{n}$, such that:

$$\Delta\mathbf{S}_e = \Delta\mathbf{S} + \mathbf{n} \; . \tag{14}$$

We assume that the expected value of $\mathbf{n}$ is zero,

$$\langle \mathbf{n} \rangle = 0 \tag{15}$$

and therefore its covariance matrix is

$$\mathbf{V}_n = \langle \mathbf{n}\mathbf{n}^T \rangle \; . \tag{16}$$

If the observational errors are uncorrelated, then $\mathbf{V}_n$ will be diagonal. This is almost never the case, but we will follow in the footsteps of many others and assume it to be true. At this point, there is not enough known about the error processes to model them in a more sophisticated way.

Rescaling equation 13 to account for the observational and representational errors:

$$\hat{\mathbf{A}}\Delta\mathbf{m} = \hat{\Delta}\mathbf{S} + \hat{\mathbf{n}} \tag{17}$$

where $\Delta\mathbf{m}$ is now a stochastic process whose mean satisfies equation 13 and

$$\hat{\mathbf{A}} = \mathbf{V}_n^{-1/2}\mathbf{A} \tag{18a}$$

$$\hat{\Delta S} = \mathbf{V}_n^{-1/2} \Delta \mathbf{S} \tag{18b}$$

$$\hat{\mathbf{n}} = \mathbf{V}_n^{-1/2} \mathbf{n} \, . \tag{18c}$$

With this scaling, $\hat{\mathbf{n}}$ is a zero-mean stochastic process whose covariance matrix is equal to the identity operator **I**. In practice, we assume that the diagonal elements of $\mathbf{V}_n^{-1/2}$ corresponding to the j^{th} lag-time point, t_j, of the i^{th} branch cross-correlation function are of the form $\sigma_i^{-1} \mathbf{W}(t_j)$, where $\mathbf{W}(t)$ is a cosine-square taper of width τ. Thus, σ_i is the standard deviation at zero lag.

Lerner-Lam and Jordan [1983] solve the linearized forward problem of equation 17 using generalized least-squares and imposing the conditions of regularization and smoothness:

$$\| \Delta \hat{\mathbf{S}}_e - \hat{\mathbf{A}} \Delta \mathbf{m} \|^2 + \alpha \| \Delta \mathbf{m} \|^2 + \beta \| \mathbf{D}^2 \Delta \mathbf{m} \|^2 = \min \tag{19}$$

where $\| \Delta \hat{\mathbf{S}}_e - \hat{\mathbf{A}} \Delta \mathbf{m} \|^2$ is the least-squares measure of data misfit, $\| \Delta \mathbf{m} \|^2$ is the model perturbation size, $\mathbf{D}^2$ is the second difference operator, $\| \mathbf{D}^2 \Delta \mathbf{m} \|^2$ is the model perturbation smoothness, and α and β are the scalar trade-off parameters which control the weighting of one term relative to another. The regularization has the effect of reducing the contribution of the poorly-determined eigenvalues, while the smoothness constraint controls the oscillations of the solution about the starting model. Together, they stabilize the inversion. The solution to this minimization problem yields an estimate of the model perturbation, $\Delta \mathbf{m}$

$$\Delta \tilde{\mathbf{m}} = \hat{\mathbf{A}}^{\dagger} \Delta \hat{\mathbf{S}}_e \tag{20}$$

where $\hat{\mathbf{A}}^{\dagger}$ is an operator of the form:

$$\hat{\mathbf{A}}^{\dagger} = (\hat{\mathbf{A}}^T \hat{\mathbf{A}} + \alpha \mathbf{I} + \beta \mathbf{D}^{2T} \mathbf{D}^2)^{-1} \hat{\mathbf{A}}^T. \tag{21}$$

Equations 20 and 21 constitute the generalized least-squares solution to the forward problem posed by equation 17. This formulation of the waveform inversion technique is advantageous in that it isolates the modes in the time domain, obviating the need for complicated processing of the data in the frequency-wavenumber domain. In particular, this approach permits the contribution from each mode to be assessed and weighted individually. Extensive tests with synthetic data [*Lerner-Lam*, 1982] show that the linearization of equations 8a and b may break down when the starting model is sufficiently far from the true structure, locking the inversion into a spurious minimum. However, this condition may be identified readily by direct comparison of with the synthetic seismograms with the data and corrected by initializing the inversion with an appropriate perturbation to the starting model.

RESOLVING POWER ANALYSIS

Since the forward problem has been linearized by the application of first-order perturbation theory, its solutions for any particular data set may be evaluated with the full power of linear inverse theory. For example, we can compute the expected value of the estimated model perturbation:

$$\begin{aligned} \langle \Delta\tilde{\mathbf{m}} \rangle &= \langle \hat{\mathbf{A}}^{\dagger}\Delta\hat{\mathbf{S}} + \hat{\mathbf{A}}^{\dagger}\hat{\mathbf{n}} \rangle \\ &= \langle \hat{\mathbf{A}}^{\dagger}\hat{\mathbf{A}}\Delta\mathbf{m} \rangle + \langle \hat{\mathbf{A}}^{\dagger}\hat{\mathbf{n}} \rangle \\ &= \mathbf{R}_m \Delta\mathbf{m} \ . \end{aligned} \tag{22}$$

$\mathbf{R}_m = \hat{\mathbf{A}}^{\dagger}\hat{\mathbf{A}}$ is called the model resolution operator [*Wiggins*, 1972; *Menke*, 1984] and $\Delta\mathbf{m}$ is the exact model perturbation which satisfies equation 13. We can see from this analysis that $\mathbf{R}_m$ acts as a filter on $\Delta\mathbf{m}$. If $\mathbf{R}_m$ is the delta function which satisfies the constraint of unimodularity, then our estimate of the model perturbation will be exact. In general, $\mathbf{R}_m$ is not a delta function and our estimate of $\Delta\mathbf{m}$ is a weighted average of the true model perturbation. A solution is considered to have 'good' resolution if the kernel is narrow and well localized; i.e. if it is peaked and has small sidelobes.

We can also calculate the covariance matrix of the model estimates, $\mathbf{V}_m$:

$$\begin{aligned} \mathbf{V}_m &= \langle (\Delta\tilde{\mathbf{m}} - \langle \Delta\tilde{\mathbf{m}} \rangle)(\Delta\tilde{\mathbf{m}} - \langle \Delta\tilde{\mathbf{m}} \rangle)^{\mathrm{T}} \rangle \\ &= \hat{\mathbf{A}}^{\dagger} \langle \hat{\mathbf{n}}\hat{\mathbf{n}}^{\mathrm{T}} \rangle \hat{\mathbf{A}}^{\dagger\,\mathrm{T}} \\ &= \hat{\mathbf{A}}^{\dagger}\hat{\mathbf{A}}^{\dagger\mathrm{T}} \ . \end{aligned} \tag{23}$$

$\mathbf{V}_m$ characterizes the errors in the model estimates induced by errors in the data. The diagonal elements of the covariance operator represent the marginal variance of the model values, while the off-diagonal elements measure the correlation between the errors at one depth with the errors at other depths.

The properties of $\mathbf{R}_m$ and $\mathbf{V}_m$ depend on the earth model, the source and receiver geometry, and the weighting and windowing operators. There is a well-known trade-off between resolution and covariance [*Backus and Gilbert*, 1970], which is governed by the parameters α and β in this study. Varying α and β in a fixed ratio will translate the solution along a trade-off curve between the ability to resolve detail and the reliability of the estimate.

EXPERIMENTS

Although *Lerner-Lam and Jordan* [1983] recognized that their formulation permitted the

resolving power analysis by standard linear methods, they did not use it to assess their solutions. In this study, we incorporate the resolving power analysis into the waveform inversion technique and use this capability to examine some issues in experimental design. We approach this problem by designing a hypothetical array of five stations, located on the Baltic Shield and distributed over a distance of 1600 km (Table 1). This receiver distribution, which is similar to the configuration used in the study by *Lerner-Lam and Jordan* [1983], is modelled after the NARS array in order to examine the contribution of such dense, linear arrays to studies of upper-mantle structure. A cluster of five earthquakes which occurred in the two-year period 1982-1984 is selected as the source array (Table 2). Located south of Japan, these events range in depth from 119 to 552 km and have well-determined centroids and moment tensors from the Harvard solutions [*Dziewonski et al.*, 1981, 1983, 1984]. Vertical-component synthetic seismograms were calculated in the frequency band from 5 to 35 mHz using Lerner-Lam's asymptotic travelling-wave programs with *Cara et al.'s* [1980] model of Eurasian structure and the attenuation model of *Masters and Gilbert* [1983]. Figure 2 is a map of the source and receiver distribution considered in this study and Figure 3 is an example of the synthetic seismograms generated for this array for a shallow and deep event. The base station of this array, KONO01, coincides with the Global Digital Seismic Network station KONO. Only the fundamental and the first four higher-mode branch cross-correlation functions were included in the resolving power calculations.

With this configuration of sources and receivers, we explore the shear-wave velocity resolving power of the higher-mode waveform inversion technique. In particular, we consider four end-member cases: a single source recorded at one and five receivers and five sources recorded at one and five receivers. We also examine the influence of errors in the data by experimenting with the relative weighting of the branch cross-correlation functions. In the first six experiments, we model the errors as stochastic processes by weighting the branch cross-correlation functions equally. This 'natural' weighting allows the mode branch with the highest amplitude (and consequently the highest signal-to-noise ratio) to control the inversion. In the last two experiments, we model the errors as processes which scale with signal strength by weighting the branch cross-correlation functions accordingly. All the figures discussed below are plotted at a constant scale to facilitate direct comparison of the results.

RESULTS

In our first two experiments, we examine the resolving power of a single source recorded at a single receiver as a function of source depth. Figure 4 presents the resolution and covariance operators for the source at 119 km depth. These operators are plotted as a function of two depth variables, with the vertical axis identified as target depth. Each row of $\mathbf{R}_m$ may be characterized as the resolving kernel for a specific target depth. For example, the kernel at 150 km depth ideally should be a delta function centered at 150 km. Although it is peaked, this particular kernel has a width of approximately 200 km, which indicates that the model perturbation estimate at 150 depth is a weighted average of the true model perturbation from about 50 to 250 km. The absence of sidelobes signifies that the averaging is localized. The amplitude of the resolving kernels in this experiment falls off rapidly with depth and is essentially flat by 300 km, restricting resolution to the top of the upper mantle. The covariance operator describes how errors in the data map into errors in the model perturbation estimate. The diagonal elements of $\mathbf{V}_m$ represent the marginal variances of the model values, while the off diagonal terms measure the correlation between errors at one depth with errors at other depths. In this experiment, the variance is pronounced at shallow depths with high amplitudes in the diagonal and off diagonal elements but decreases with depth. The variance is low where the resolving kernel amplitude is small and higher at shallow depths where the kernel amplitude is large, which is a manifestation of the trade-off between bias and covariance.

Figure 5 depicts the same experiment for a single deep source (h=552 km). In contrast to Figure 4, the resolving kernels are peaked down to target depths as great as 600 km. These kernels

are generally narrower than those for the shallow source, although the width increases with depth. Unlike the kernels in Figure 4, however, these have well-developed sidebands, which indicate that the averaging is not localized. The overall increase in resolution at depth is mirrored by an increase in the variance. The covariance operator for this experiment has high-amplitude diagonal terms and considerable structure in the off-diagonal elements.

Comparison of Figures 4 and 5 illustrates the contribution of higher-mode data to resolution of upper-mantle structure. It is clear from Figure 1 that the seismogram for the shallow source is dominated by the fundamental mode, with very little excitation of the higher modes. With the branch cross-correlation functions all weighted equally, the fundamental mode controls the inversion, restricting resolution to depths shallower than 200 km. On the other hand, the seismogram for the source at 552 km depth contains very little fundamental-mode information; the inversion is controlled primarily by the second, third, and fourth higher modes. Higher-mode dispersion is more sensitive to structures at depth than fundamental-mode dispersion, and this is reflected in the resolution operator of Figure 5.

In the next two experiments, we examine the effect of expanding the number of receivers from one to five. Figure 6 presents the results from the experiment with the deep source recorded at the array of receivers. The resolution operator for this experiment is smoother and the peaks are narrower with higher amplitudes than the kernels in Figure 5. This increase in resolution is not surprising, as the array spans the triplication of *SSS*, a phase which bottoms between 400 and 800 km. Since *SSS* samples the lower part of the upper mantle, the triplication provides valuable information about the stucture at these depths. However, the greatest gain from the expansion of the receiver array is observed in the covariance operator. The array reduces the variance of the solution by nearly a factor of five, since we assumed that the errors in the differential branch cross-correlation functions are uncorrelated. Figure 7 displays the resolution and covariance operators for the experiment with the shallow source and the array of receivers. Comparison of Figures 7 and 4 shows that only a marginal improvement in resolution results in this case, although the amplitude of the covariance operator is decreased by nearly a factor of five.

Although the primary benefit from an array of receivers appears to be the reduction of the covariance operator, we can take advantage of the relationship between resolution and covariance (which is governed by the parameters α and β in equation 19) to exchange some of the decrease in covariance for an increase in resolution. Figure 8 shows the results from increasing α and decreasing β in a fixed ratio for the experiment with the deep source recorded at the array of receivers. Although the resolving kernels are narrower and more peaked for this translation along the trade-off curve, the cost in terms of the reliability of the solution is quite high. The covariance operator for this experiment is not well behaved, with errors at one depth scaling with errors at nearly all depths. Figure 9 presents the results for a translation along the trade-off curve in the other direction. In this case, the resolution operator is highly degraded, while the covariance operator is nearly flat. We can also experiment with the trade-off parameters for the shallow source recorded at the array of receivers, resolution is limited more by the depth of the source (given the 'natural' weighting of the branch cross-correlation functions) than by the number of receivers in this experiment.

Having examined the dependence of the resolution and covariance operators on an array of receivers, we model the effect of an array of sources. Figure 10 shows the results from an experiment with five sources distributed in depth from 119 to 552 km and recorded at a single station. From a comparison of Figures 4 and 5 with Figure 10, it is clear that a distribution of sources can be particularly effective in enhancing resolution. The resolution kernels of Figure 10 have high-amplitude and narrow peaks and show some resolution as deep as 600-700 km depth. The sideband structure is damped, although the averaging is not completely localized. In terms of the covariance operator, an array of sources reduces the variance considerably, but not as effectively as an array of receivers. Figure 11 illustrates the resolution and covariance operators for the optimal experiment of five sources recorded at five receivers. As before, the addition of five

receivers narrows the peaks of the resolution kernels, but the greatest gain is in the reduction of the variance.

In these six experiments, the branch cross-correlation functions are effectively weighted by their relative amplitudes in the inversion, since the error at zero lag, σ_i , is assumed to be independent of the branch number. This 'natural' weighting entails certain implicit assumptions about the error process. If one assumes that errors in the data are introduced strictly by the presence of ambient seismic noise (wind, microseisms, cultural noise, etc.), then this natural weighting by the relative excitation of the modes is most appropriate. In that case, the highest amplitudes carry the greatest weight since they have the best signal-to-noise ratio. However, many errors may be a function of signal strength (such as multipathing, source structure, etc.). If these errors dominate the random processes, then the natural weighting is not appropriate.

We explore the effect of characterizing the error processes by experimenting with the mode branch weights for the shallow source recorded at one and five receivers. By increasing the weight of the higher-mode branches relative to the fundamental, we model the case where the errors scale with signal strength. Figure 12 illustrates the resolution and covariance operators for this experiment. Comparing Figures 4 and 12, it is clear that this weighting of the higher-mode signals has improved the resolution at depth, although these kernels are neither narrow nor localized. The increase in resolution is reflected by an increase in the variance. As before, increasing the number of receivers (Figure 13) marginally improves the resolution, but dramatically decreases the variance of the solution. The results from these two experiments highlight the importance of the assumptions made about the error process. If errors scale with signal strength (which we think is more realistic), then the branch cross-correlation functions need to be weighted accordingly. However, the weighting of the branch cross-correlation functions plays an important role in the resolving power of a particular experiment, as it is possible to obtain some resolution at depth even from a shallow source when the contributions from the higher-mode branches are weighted appropriately.

CONCLUSIONS

In this study, we augment the waveform inversion technique of *Lerner-Lam and Jordan* [1983] with a resolving power analysis and use this capability to examine some issues in experimental design. These experiments have demonstrated several important results. First, fundamental-mode data alone cannot resolve structure at depths greater than 200 km; a fact which has been appreciated by seismologists for many years. Higher-mode information, which samples greater depths, is essential to obtain resolution of the upper mantle. Second, a single station is capable of nearly the same resolving power as a dense array of receivers with this method, since the higher-mode waveform inversion technique does not rely on spatial transforms. The advantage of such an array comes primarily through the reduction of the variance of the solution, although the decrease in covariance may be exchanged for an increase in resolution through the trade-off parameters. Third, source arrays are particularly effective in enhancing resolution at depth, provided that the source depths are well distributed and the source centroids and moment tensors are well determined. Finally, the characterization of the error processes plays an important role in the resolving power analysis of a particular experiment, since the relative weighting of the branch cross-correlation functions will influence the resolution. Since the waveform inversion technique permits the contribution of each branch cross correlation function to be assessed and weighted separately, resolution of structure at depth is possible even with shallow sources.

REFERENCES

Backus, G.E., and J.F. Gilbert, Uniqueness in the inversion of inaccurate gross Earth data, *Phil. Trans. R. Soc. A.*, **266**, 123-192, 1970.

Cara, M., Regional variations of higher Rayleigh-mode velocities: a spatial filtering method, *Geophys. J. R. astr. Soc.*, **54**, 439-460, 1978.

Cara, M., Lateral variations of S velocity in the upper mantle from higher Rayleigh modes, *Geophys. J. R. astr. Soc.*, **57**, 649-670, 1979.

Cara, M., A. Nercessian, and G. Nolet, New inferences from higher mode data in western Europe and northern Eurasia, *Geophys. J. R. astr. Soc.*, **61**, 459-478, 1980.

Chou, T., and A. Dziewonski, Regional variations in the structure of upper mantle from dispersion of overtones of surface waves, unpublished manuscript, 1980.

Davies, G.F., Thickness and thermal history of continental crust and root zones, *Earth Planet. Sci. Lett.*, **44**, 231-238, 1979.

Dost, B., A.V. Wettum, and G. Nolet, The NARS array, *Geol. Mijnbouw*, **63**, 381-386, 1984.

Dziewonski, A.M., T.-A. Chou, and J. Woodhouse, Determination of earthquake source parameters from waveform data for studies of global and regional seismicity, *J. Geophys. Res.*, **86**, 2825-2852, 1981.

Dziewonski, A.M., J.E. Franzen, and J.H. Woodhouse, Centroid-moment tensor solutions for January-March, 1984, *Phys. Earth Planet. Int.*, **34**, 209-209, 1984.

Dziewonski, A.M. A. Friedman, and J.H. Woodhouse, Global seismicity of 1982: centoid-moment tensor solutions for 308 earthquakes, *Phys. Earth Planet. Int.*, **33**, 76-90, 1983.

Feng, C. and Teng T., Three-dimensional crust and upper mantle structure of the Eurasian continent, *J. Geophys. Res.*, **88**, 2261-2272, 1983.

Gilbert, F., The representation of seismic displacements in terms of travelling waves, *Geophys. J. R. astr. Soc.*, **44**, 275-280, 1976.

Grand, S.P. and D.V. Helmberger, Upper mantle shear structure of North America, *Geophys. J. R. astr. Soc.*, **76**, 399-438, 1984a.

Grand, S.P. and D.V. Helmberger, Upper mantle shear structure beneath the northwestern Atlantic Ocean, *J. Geophys. Res.*, **89**, 11465-11475, 1984b.

Grand, S.P., D.V. Helmberger, and L.J. Burdick, Attenuation bias measurements of the Semipalatinsk and North African test sites from multiple S phases, *Report WCCP-R-85-01*, Woodward-Clyde Consultants, Pasadena, 27pp, 1985.

Jordan, T.H., The continental tectosphere, *Rev. Geophys Space Phys.*, **13**, 1-12, 1975.

Jordan, T.H., Composition and development of the continental tectosphere, *Nature*, **274**, 544-548, 1978.

Jordan, T.H., Continents as a chemical boundary layer, *Phil Trans R Soc Lond A*, **301**, 359-373, 1981.

Lerner-Lam, A.L., Linearized estimation of higher-mode surface wave dispersion, *Ph.D thesis*, University of California, San Diego, 1982.

Lerner-Lam, A.L. and T.H. Jordan, Earth structure from fundamental and higher-mode waveform analysis, *Geophys. J. R. astr. Soc.*, **75**, 759-797, 1983

Masters, G. and F. Gilbert, Attenuation in the earth at low frequencies, *Phil. Trans. R. Soc. Lond. A.*, 308, 479-552, 1983.

Menke, W., *Geophysical data analysis: discrete inverse theory*, Academic Press Inc., London, 260 p., 1984.

Nolet, G., Higher Rayleigh modes in western Europe, *Geophys. Res. Lett.*, **2**, 60-62, 1975.

Nolet, G., Higher modes and the determination of upper mantle structure, *Ph.D thesis*, Utrecht, 1976.

Nolet, G., Simultaneous inversion of seismic data, *Geophys. J. R. astr. Soc.*, **55**, 679-691, 1978.

Nolet, G., B. Dost, and H. Paulssen, Intermediate wavelength seismology and the NARS experiment, *Annal. Geophysic.*, (submitted), 1985.

Richter, F., Models for the Archean thermal regime, *Earth Planet. Sci. Lett.*, **73**, 350-360, 1985.

Sipkin, S.A. and T.H. Jordan, Lateral heterogeneity of the upper mantle determined from the travel times of multiple *ScS*, *J. Geophys. Res.*, **81**, 6307-6320, 1976.

Wiggins, R.A., The general linear inverse problem: Implication of surface waves and free oscillations for Earth structure, *Rev. Geophys. Space Phys.*, **10**, 251-285, 1972.

Woodhouse, J. and F. Dahlen, The effect of a general aspherical perturbation on the free oscillations of the Earth. *Geophys. J. R. astr. Soc.*, **53**, 335-354, 1978.

Table 1

The Receiver Array

Station I.D.	Latitude (°)	Longitude (°)
KONO01	59.648	9.597
KONO05	62.318	15.746
KONO09	64.665	23.013
KONO13	66.592	31.520
KONO17	67.989	41.243

Table 2

The Source Array

Date	Latitude(°)	Longitude (°)	Depth (km)	Magnitude
07/04/82	27.92	136.48	551.8	6.3
07/05/82	30.77	130.47	119.0	5.7
09/06/82	29.18	140.65	155.6	6.6
01/01/84	33.38	136.81	383.6	6.5
02/13/84	25.26	122.29	268.2	5.5

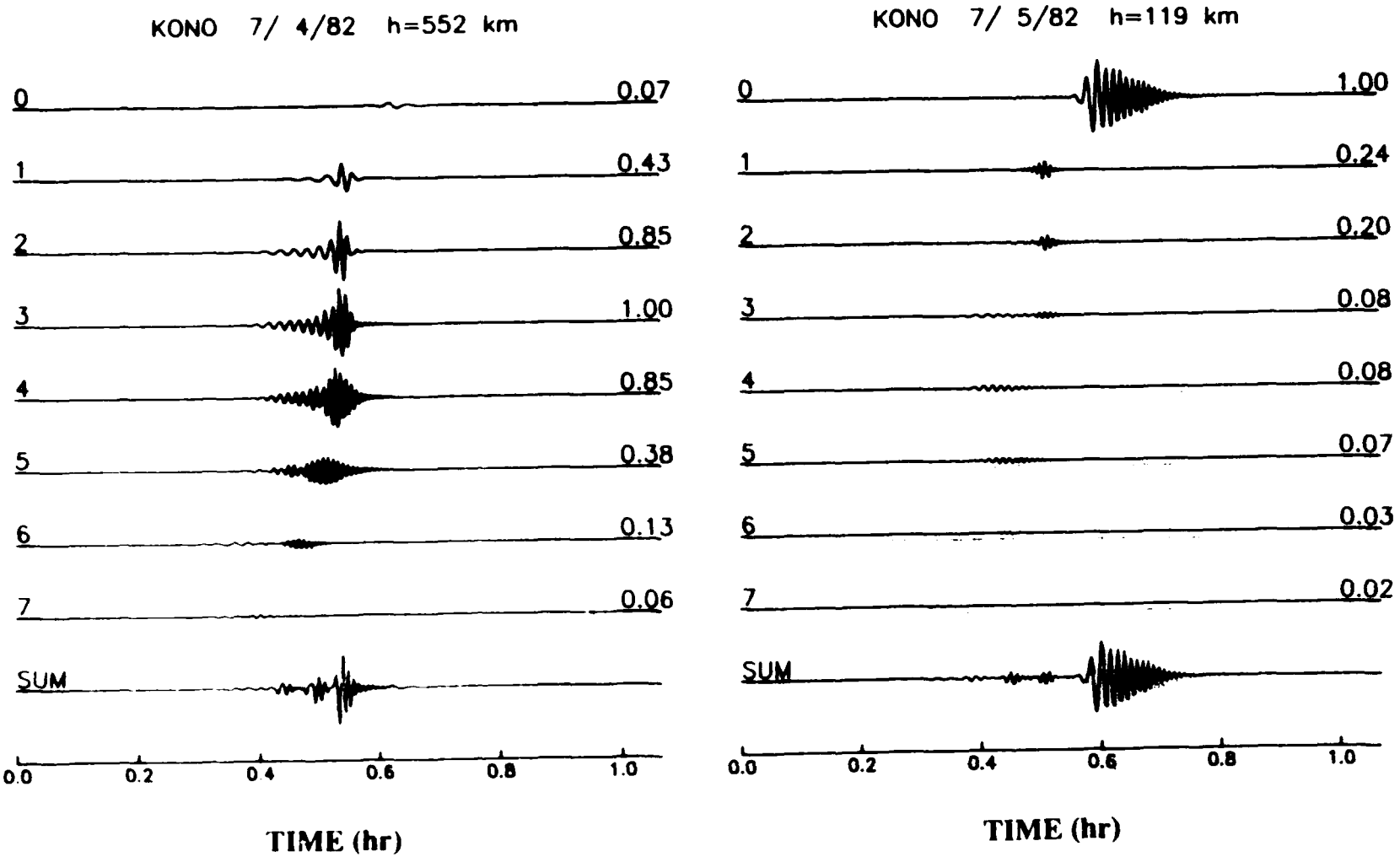

Figure 1: The fundamental and first seven overtone mode-branch synthetics are plotted for events 07/04/82 (h=552 km) and 07/05/82 (h=119 km) at the station KONO01. The numbers on the right of each plot indicate the relative excitation of the various modes, normalized to the highest amplitude. This figure demonstrates the excitation of the modes as a function of depth. The fundamental mode dominates the arrivals in the shallow event, while the higher modes eclipse the fundamental mode in the deeper event.

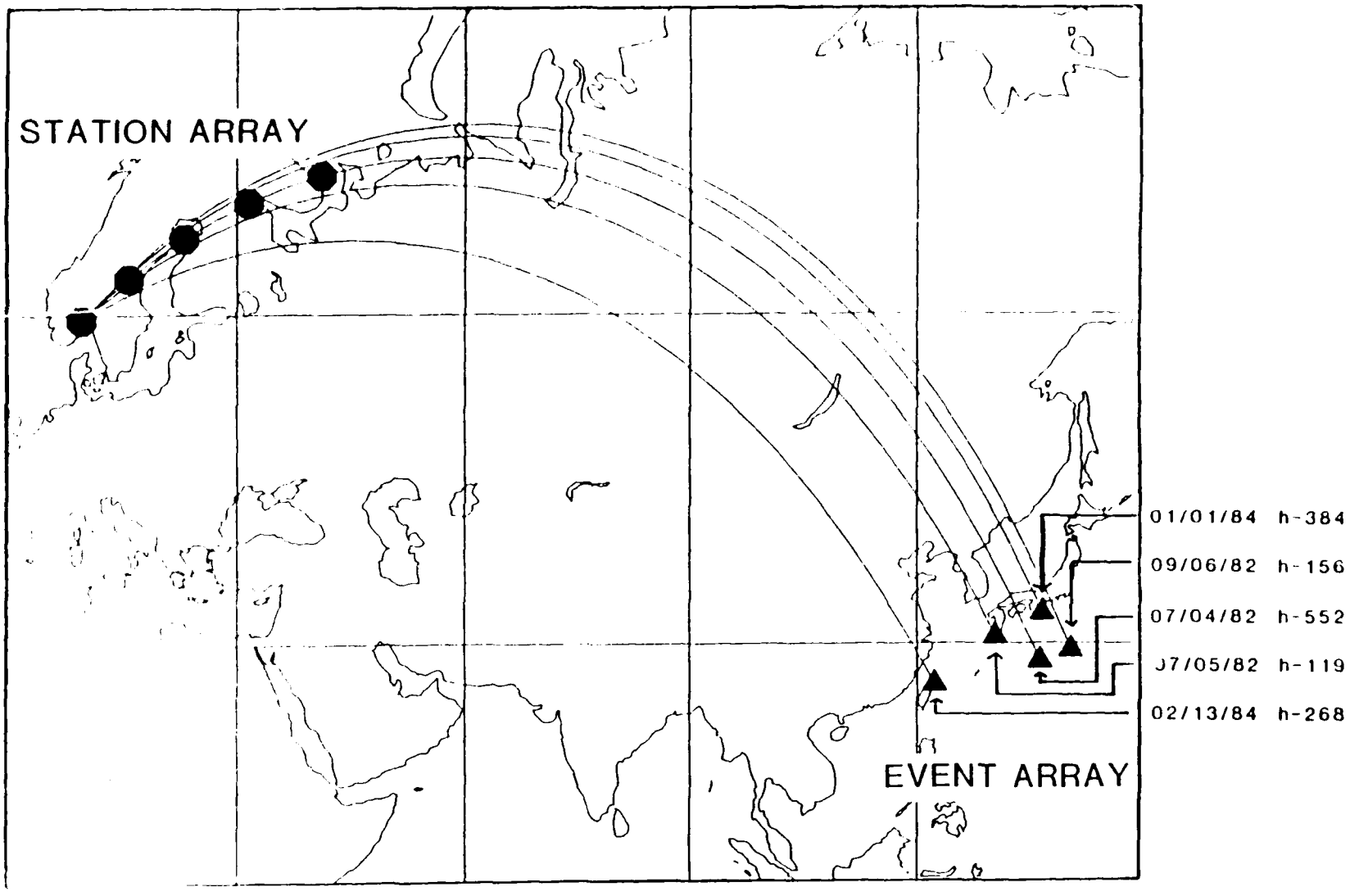

Figure 2. This map shows the configuration of the sources and receivers used in this study. The [illegible] is a cluster of five earthquakes located south of Japan, with source depths ranging [illegible] km. The receiver array is modelled after the NARS array, and spans an aperture [illegible] spacing between stations.

AD-A181 249 INVESTIGATIONS OF EURASIAN SEISMIC SOURCES AND UPPER MANTLE STRUCTURE(U) MASSACHUSETTS INST OF TECH CAMBRIDGE DEPT OF EARTH ATMOSPHERI.. T H JORDAN 2/3

UNCLASSIFIED 06 MAR 87 AFGL-TR-87-0101 F19628-85-K-0024 F/G 8/11 NL

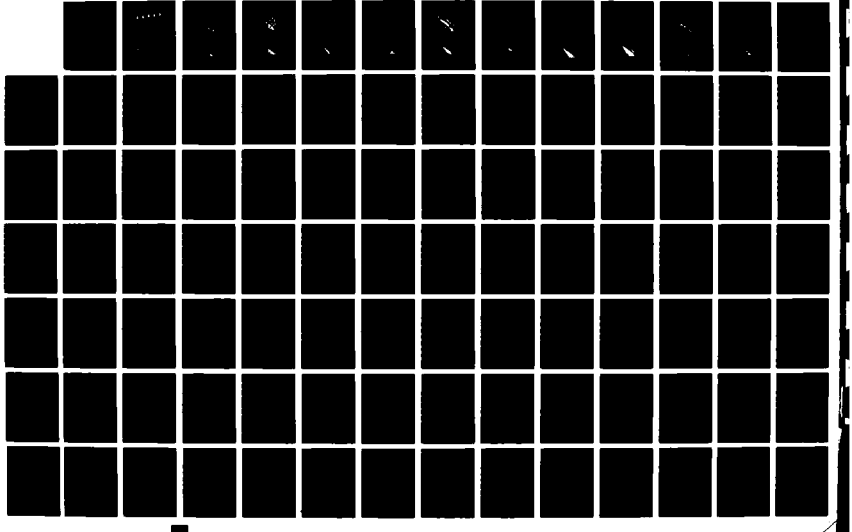

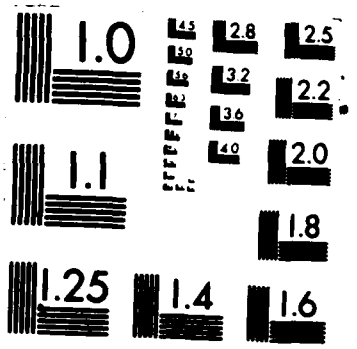
1.0
1.1
1.25
1.4
1.6
1.8
2.0
2.2
2.5
2.8
3.2
3.6
4.0
4.5

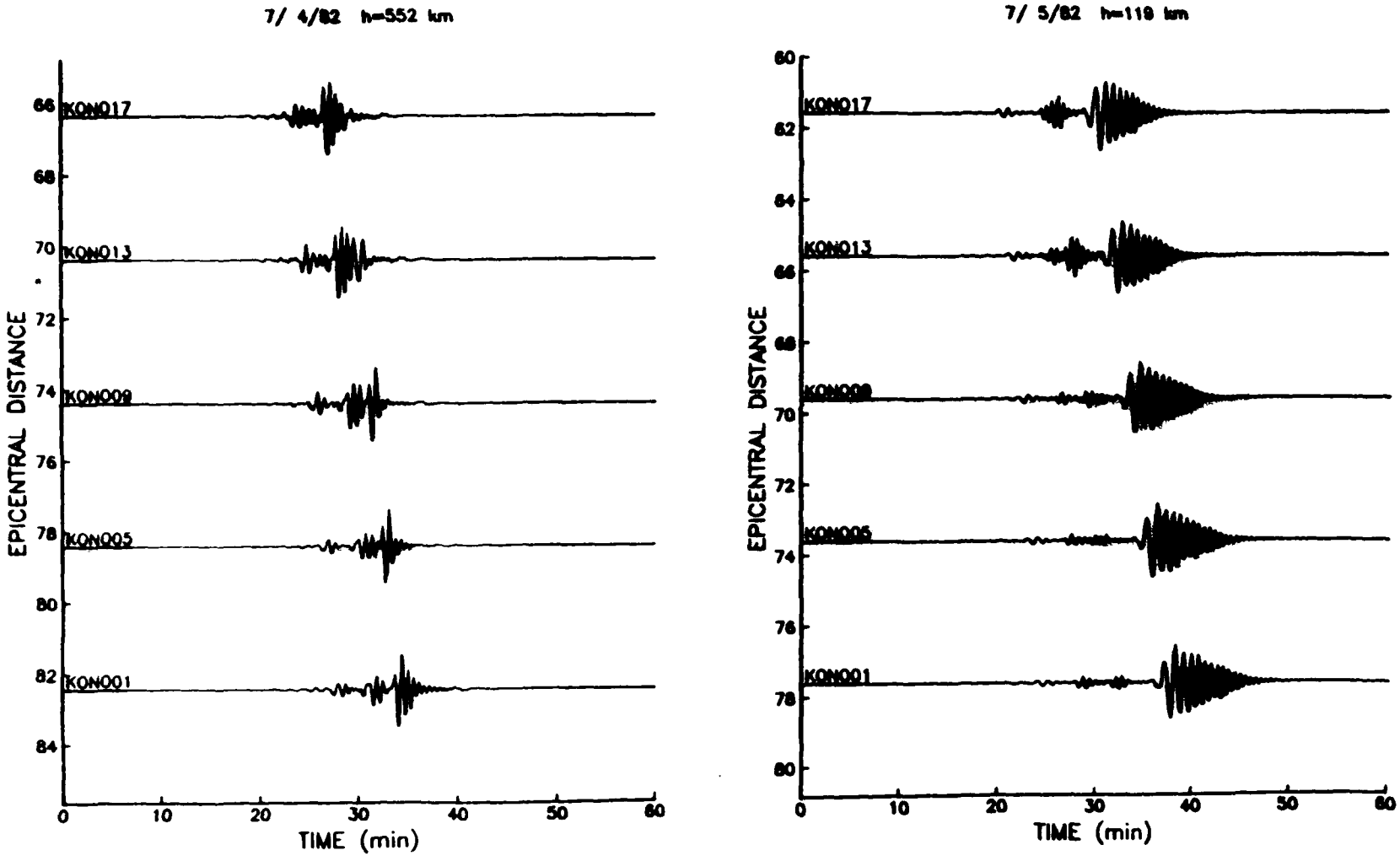

Figure 3: This figure illustrates the synthetic seismograms calculated for the receiver array for the events 07/04/82 and 07/05/82. The stations span the triplication of *SSS*, which provides critical information about the lower part of the upper mantle.

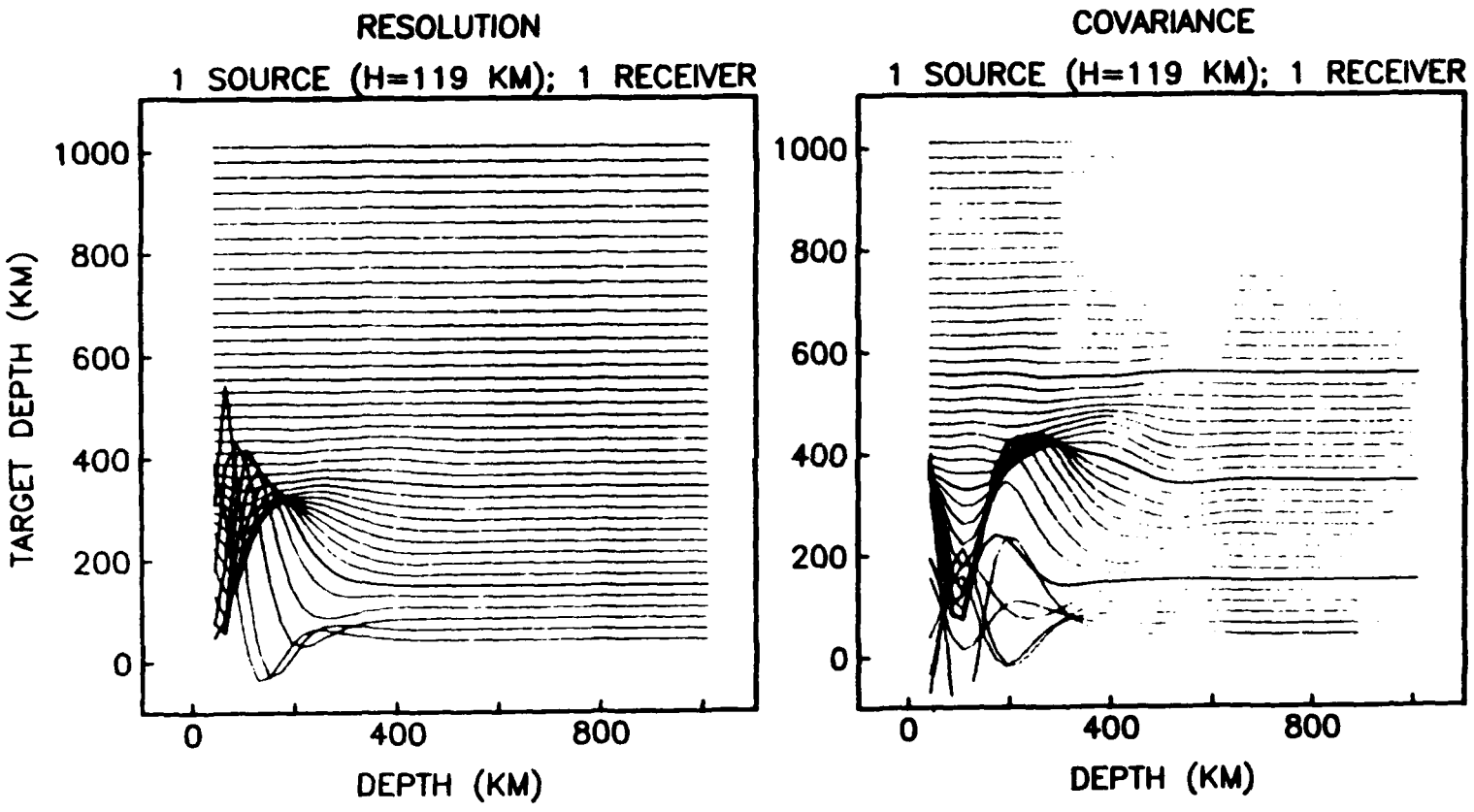

Figure 4: The resolution and covariance operators for the experiment of a shallow source (h=119 km) recorded at a single receiver are presented in this figure, with target depth plotted as a function of depth. The resolving kernels are peaked at shallow depths in this experiment, which reflects the excitation of the fundamental mode. The variance of the solution is high at shallow depths, but deceases rapidly. In the following figures, the resolution and covariance operators have been scaled so that the results of one experiment may be compared with another.

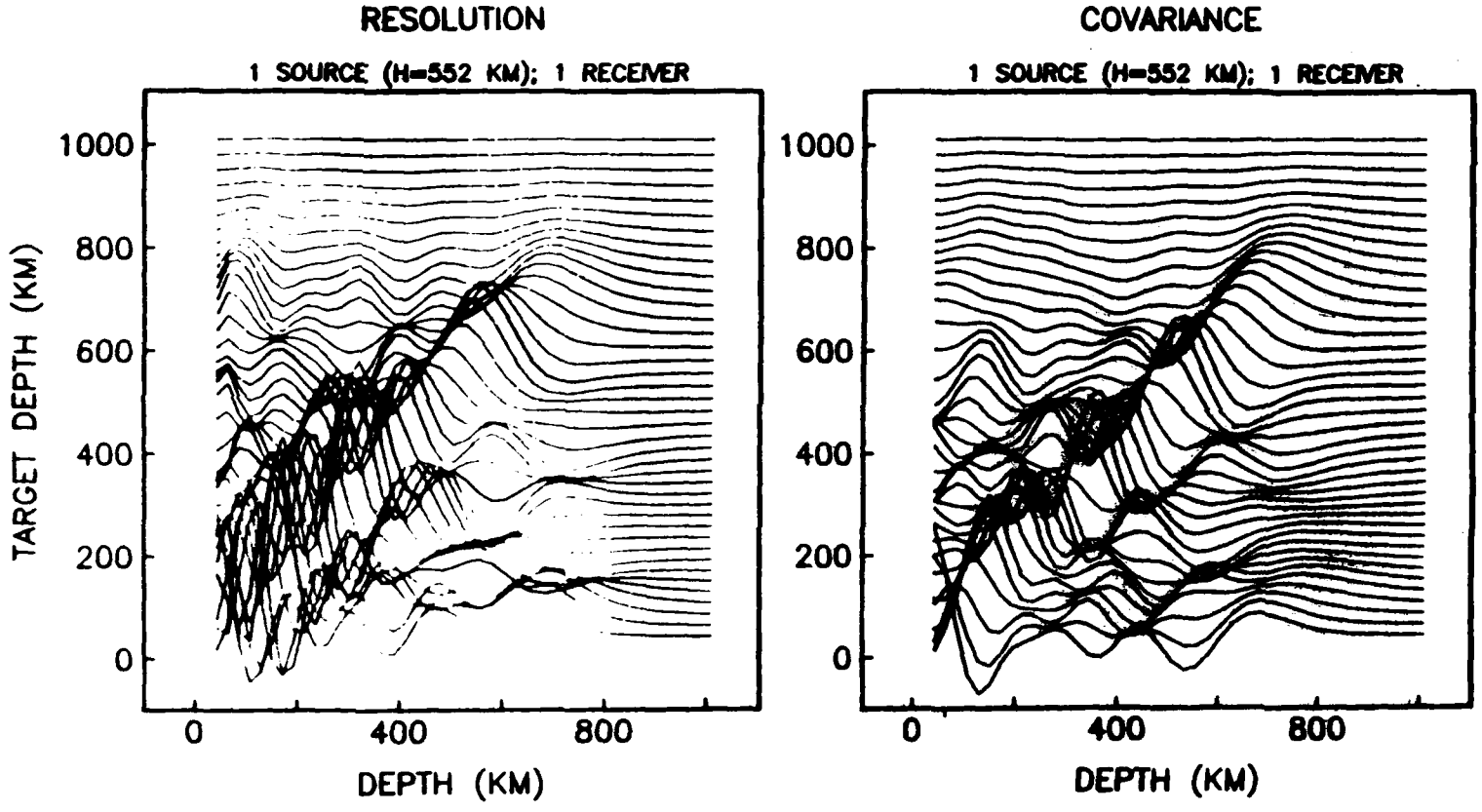

Figure 5: This figure shows the resolution and covariance operators for a deep source (h=552 km) recorded at a single receiver. Comparison with Figure 6 demonstrates how the addition of higher-mode information improves the resolution of upper-mantle structure. In this experiment, the fundamental mode is not excited, and the higher modes dominate the seismogram. Consequently, the resolving kernels are peaked down to 600 km, although the peaks are not well localized.

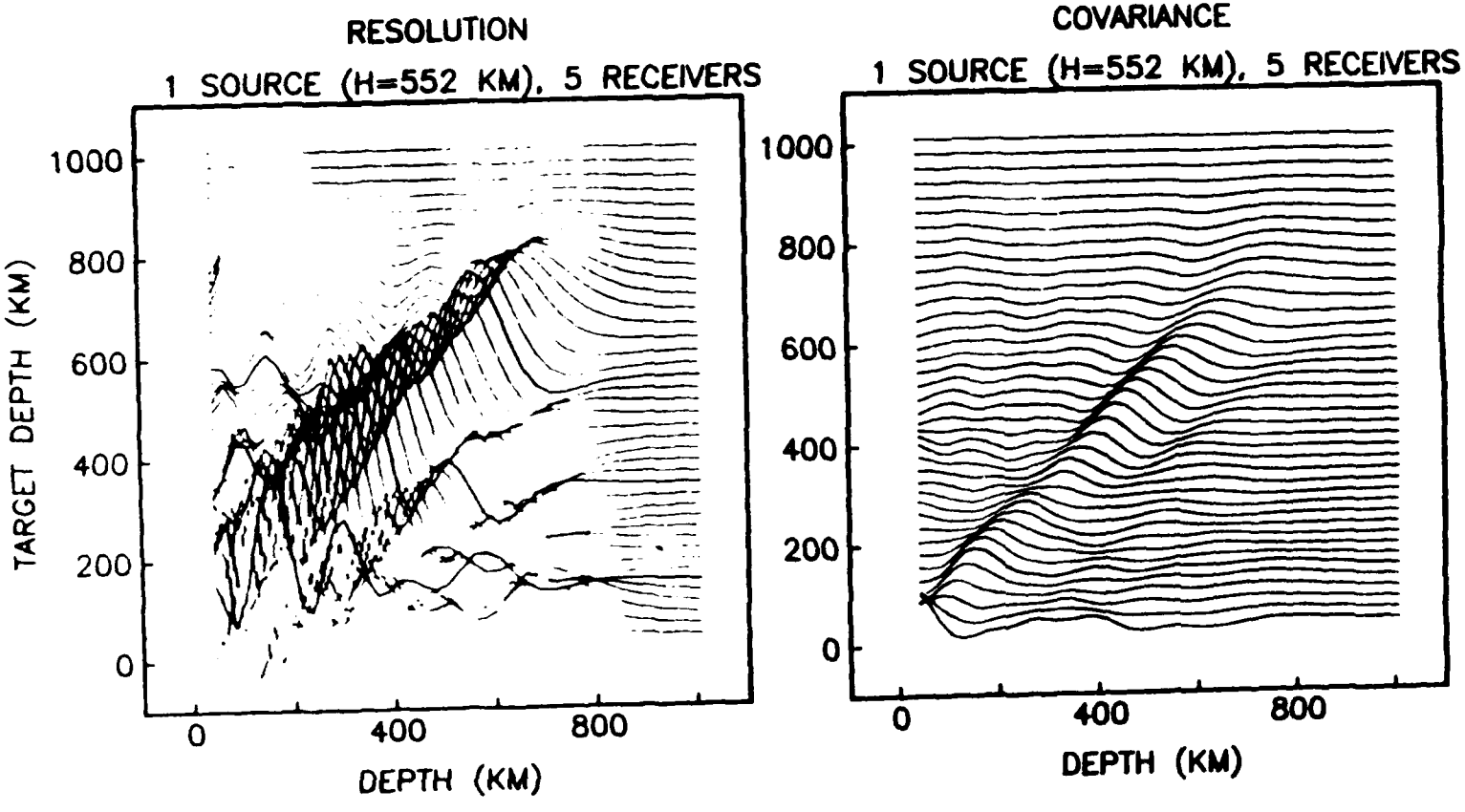

Figure 6: This figure displays the resolution and covariance operators for a deep source recorded at the array of receivers. The resolving kernels have been smoothed and their peaks narrowed in this experiment, while the covariance has come down by a nearly a factor of five.

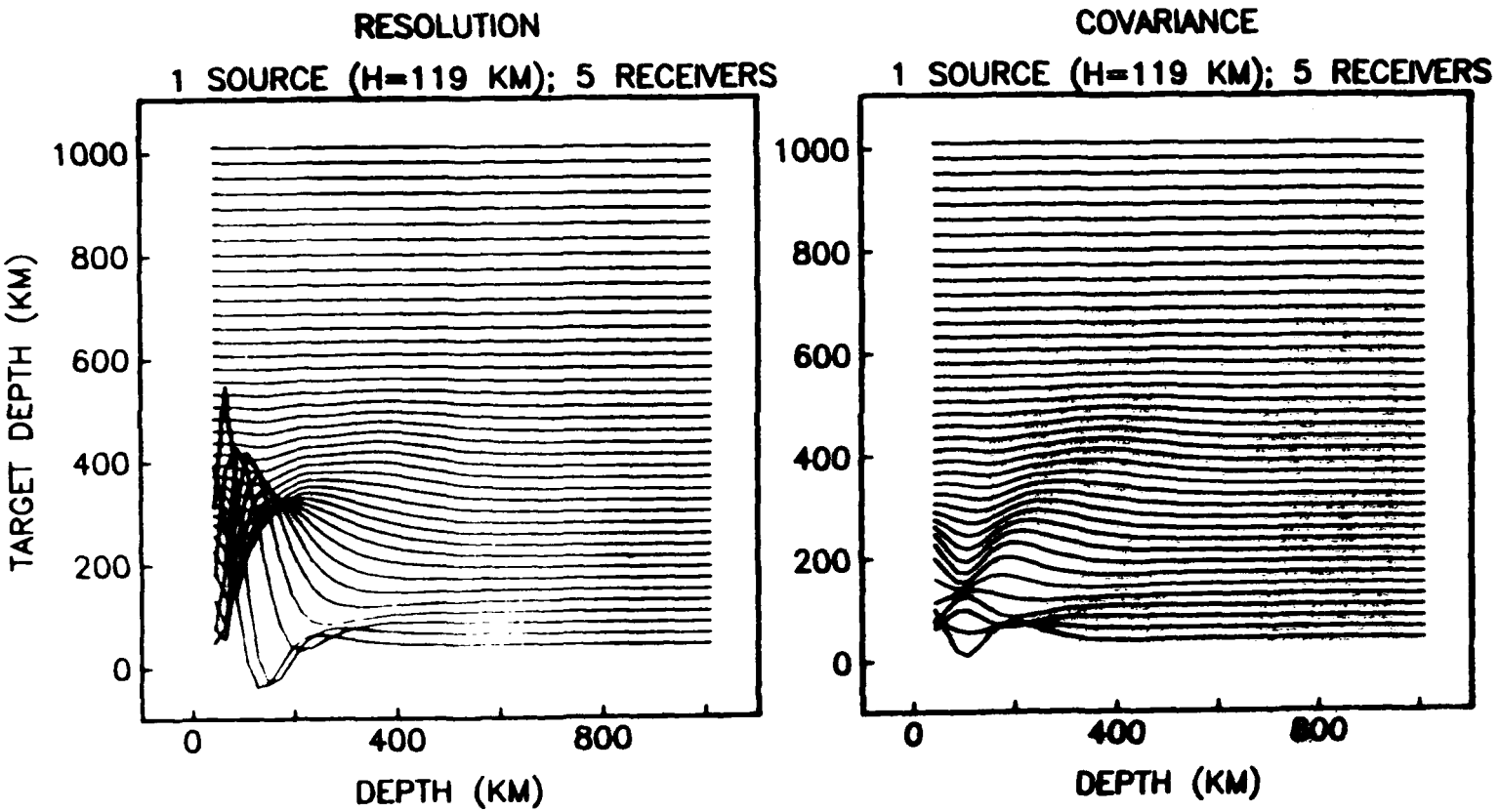

Figure 7: The resolution and covariance operators for the shallow event recorded at five receivers are plotted in this figure. For constant values of α and β, the addition of a receiver array results in marginal improvement in the resolution, although the covariance is cut down by nearly a factor of five. In this experiment, the resolving power is constrained more by the depth of the source than by the number of receivers.

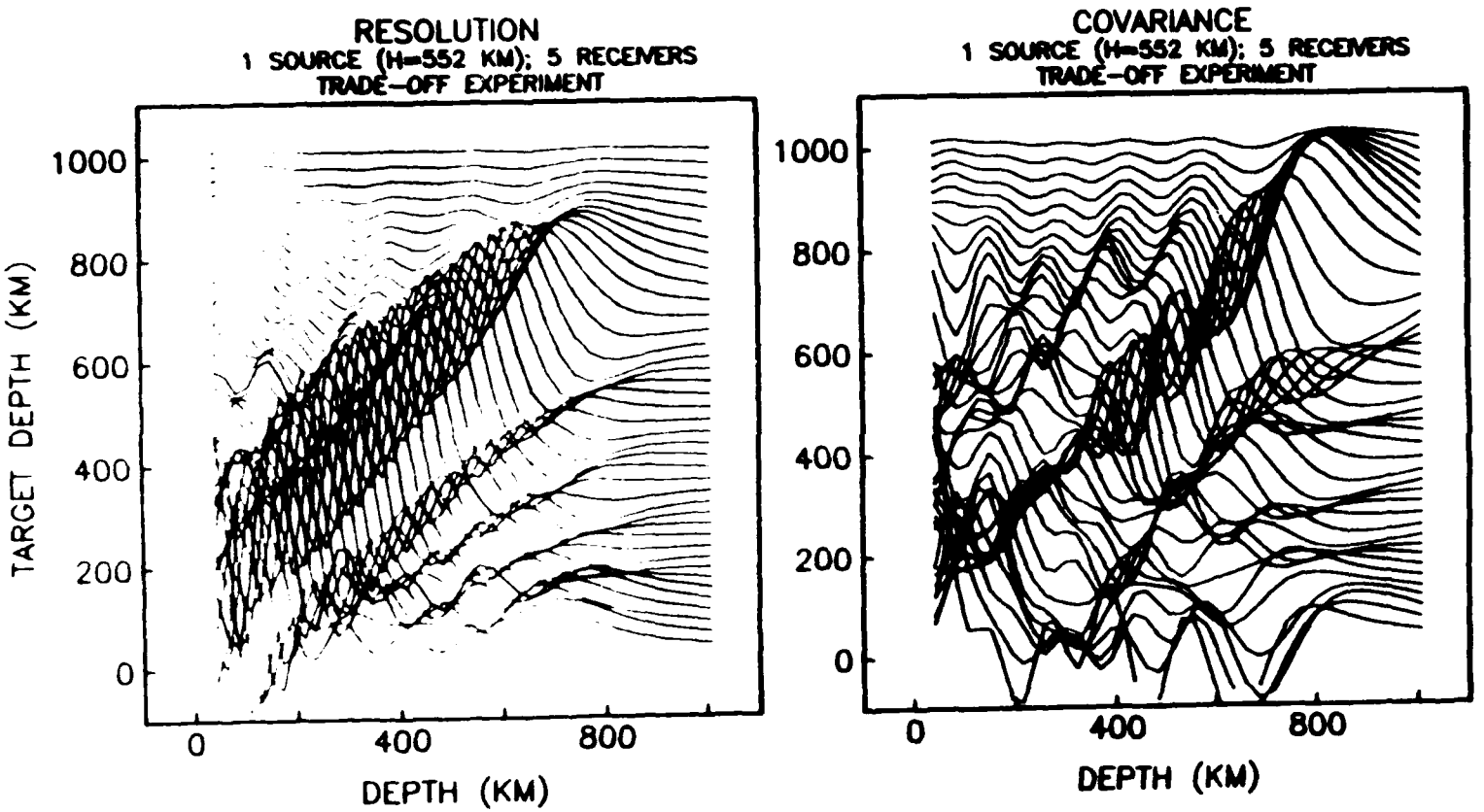

Figure 8: Since the receiver array has reduced the covariance so dramatically, it is possible to experiment with the trade-off curve and exchange the reduction in covariance for an increase in resolution. Figure 8 demonstrates the results from an inversion where α and β were varied in a fixed ratio. Comparing Figures 6 and 8, it is clear that the resolution can be improved, although the cost in terms of the increase in the covariance is quite high.

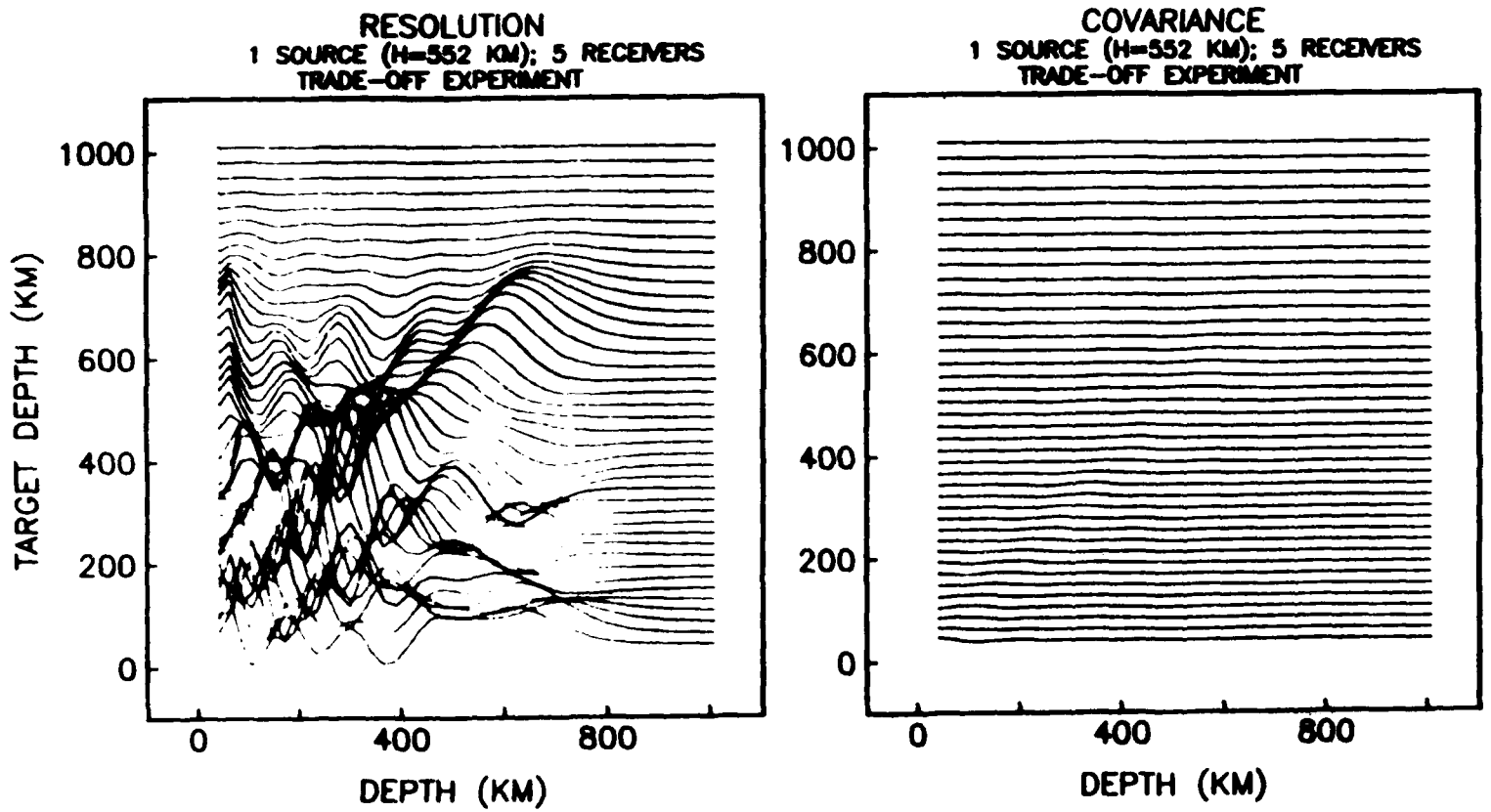

Figure 9: Figure 9 shows the result from moving in the other direction on the trade-off curve. In this case, the covariance is nearly flat, but the resolving kernels have been severely degraded.

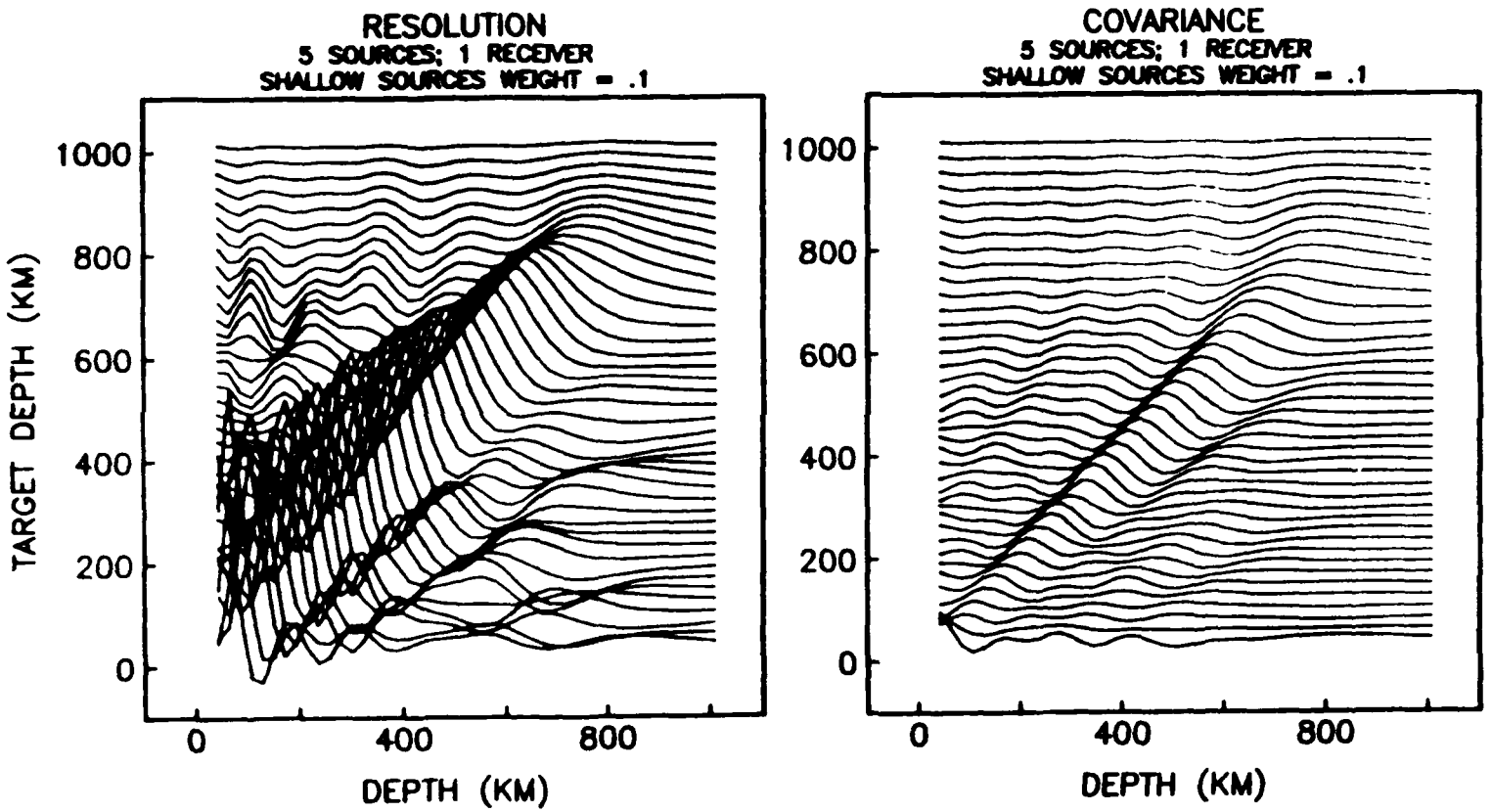

Figure 10: The resolution and covariance operators are displayed for the experiment with five sources recorded at a single receiver. The addition of a source array distributed in depth improves the resolving power considerably. In this experiment, the amplitude of the resolving kernels is peaked and quite narrow, with damped sideband structure, while the covariance is low. The addition of the higher modes, which sample a range of phase velocities, provides critical information for the resolution of upper-mantle structure.

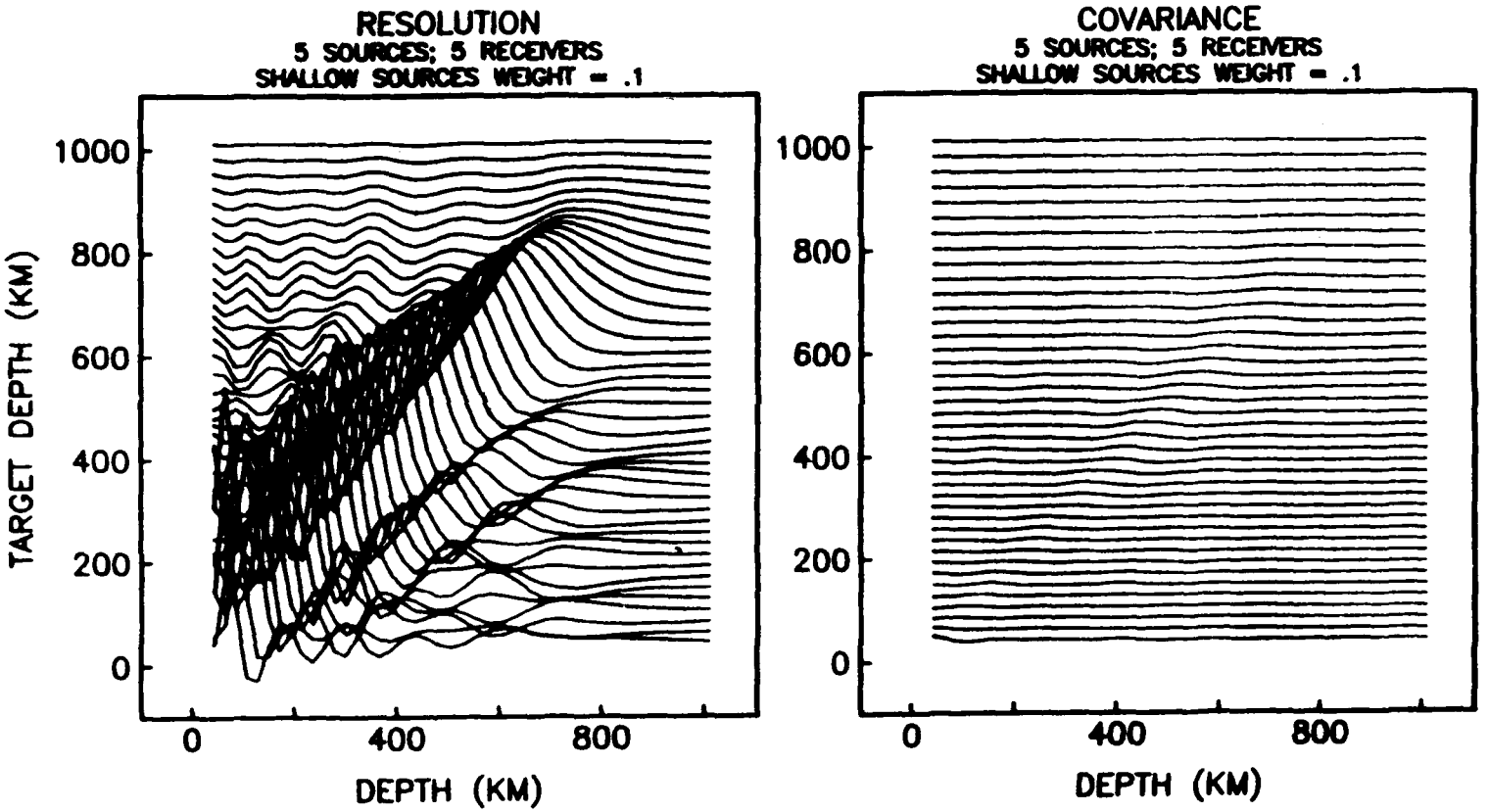

Figure 11: This figure presents the resolution and covariance operators for the optimal experiment of five sources recorded at five receivers. As before, the addition of the receiver array has smoothed the resolving kernels and narrowed the peaks, while damping the covariance. Similar to experiment of Figure 8, this reduction in the covariance may be traded for an increase in resolution.

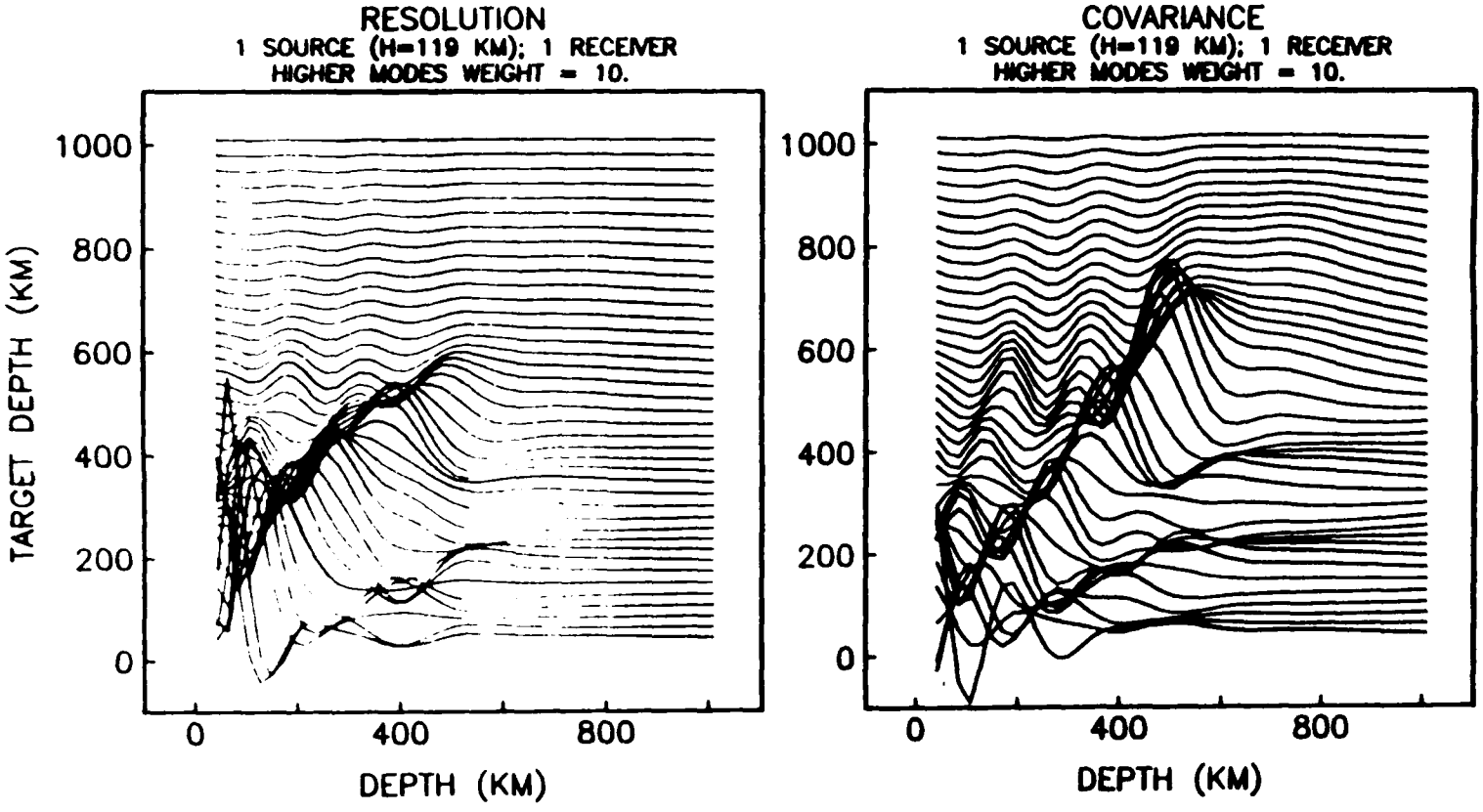

Figure 12: This experiment with the shallow source and a single receiver assumes a noise model where errors scale with signal strength. Consequently, the higher mode branches were given higher weight in the inversion relative to the fundamental mode branch. As a result of the upweighting of the higher modes, the resolution at depth has improved.

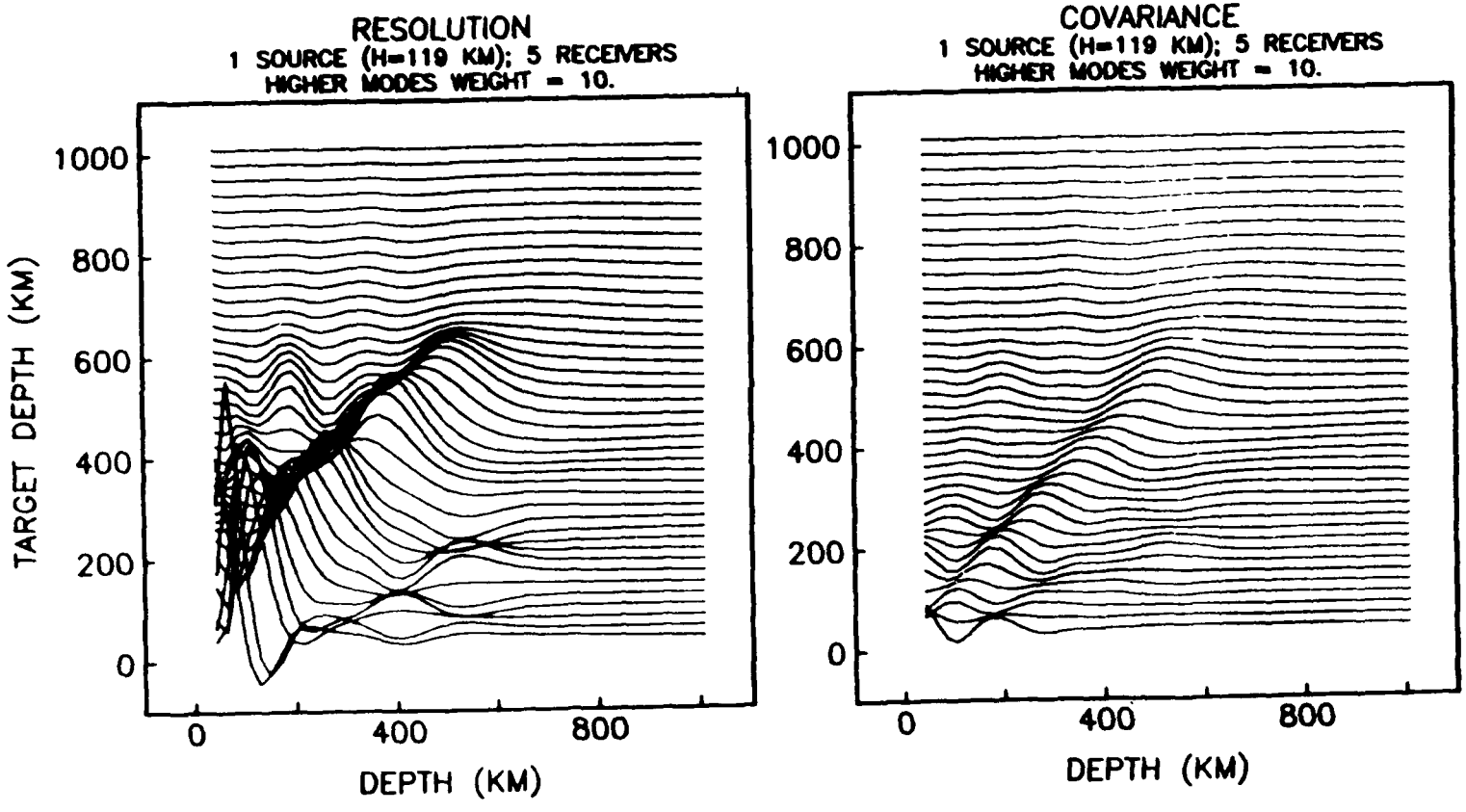

Figure 13: This figure expands the noise model experiment to the shallow source recorded at five receivers. As before, the addition of the receiver array gives a reduction in covariance which may be traded-off for an improvement in resolution.

Seismic Imaging of Boundary Layers and Deep Mantle Convection

Thomas H. Jordan[1]

Arthur L. Lerner-Lam[2]

Kenneth C. Creager[3]

August, 1985
Revised October, 1986

1 Department of Earth, Atmospheric and Planetary Sciences, Massachusetts Institute of Technology, Cambridge, MA 02139

2 Lamont-Doherty Geological Observatory, Palisades, NY 10964

3 Geophysics Program, University of Washington, Seattle, WA 98195

1. Introduction

Although much has been recently learned about the surface manifestations of convection in the earth's mantle, and few geophysicists would dispute its existence, there has not yet developed a consensus on the answers to some of the most fundamental questions regarding the nature of this convection. A vigorous debate is currently focused on the vertical extent of the convecting layer comprising the lithospheric plates. According to one school, this layer is limited from below by a chemical discontinuity at a depth of approximately 700 km; according to another, it extends over most if not the entire depth of the mantle. Geophysical thinking has been divided along these lines for the last ten years, and it is now widely appreciated that further progress on mantle dynamics will be inhibited until one or the other of these models (or both) can be convincingly excluded.

It is perhaps less appreciated that the question of stratified versus whole-mantle convection was raised nearly two decades before the advent of plate tectonics. In September, 1950, a UNESCO-sponsored colloquium was convened in Hershey, Pennsylvania, to consider "Plastic Flow and Deformation Within the Earth" [Gutenberg et al., 1951]. The participants included Vening Meinesz, Griggs and Hess, among others. They were by-and-large faithful to the mobilistic theories which sought to explain surface tectonics in terms of convective processes in the deep interior. Their faith was shaken by Francis Birch, who presented a paper concerning the *inhomogeneity of the mid-mantle transition zone*. He concluded that, "the layer between 200 and 800 km may be interpreted as a region in which the transition to the high-pressure form takes place, probably with a change in chemical composition as well... To assume unimpeded circulation in this region is to ignore its definitely transitional nature." In the vigorous discussion following his report, J.H.F. Umbgrove summarized the quandry very succinctly: "If chemical change is involved, we have to give up the hypothesis of convection currents passing through this zone. If it is only a change of phase, the problem remains whether Birch's results flatly oppose the hypothesis of convection currents over the entire 2900-km sector of the mantle, or whether there is a way out of the apparent difficulty. *A positive answer to this question seems crucial with regard to any further discussion of convection currents*" (emphasis added). It was in this context that the Dutch geophysicist P.P. Bijlaard, then at Cornell, submitted the diagram reproduced in Figure 1.1 and commented, "It might be possible that, as a consequence of differences in temperature, convection currents (I) between depths of 900 and 2900 km would occur, which might induce secondary currents (II) in the higher regions of the mantle." Figure 1.1 juxtaposes Bijlaard's scheme with a similar diagram of stratified, quadrupolar convection extracted from a recent paper by Busse [1983]. The comparison provides one measure of how far our thinking on this subject has evolved

in the ensuing three and a half decades.

Convection currents of the sort illustrated in Figure 1.1 involve lateral temperature contrasts of several hundred degrees over scale lengths of thousands of kilometers, and these contrasts will induce heterogeneity in the speeds of seismic waves. At conditions appropriate to the deep mantle, the logarithmic variation of seismic velocities with temperature ranges from about $-5 \times 10^{-5}\ °C^{-1}$ for compressional waves to $-1 \times 10^{-4}\ °C^{-1}$ for shear waves, so that the magnitude of the velocity heterogeneity will be several percent, regions of higher temperature having lower wave speeds. If the large-scale flow within the mantle were as well organized as hypothesized in Figure 1.1, a strong quadrupolar signature of this convective pattern should be present in the aspherical variations of wave speeds, especially in the transition zone comprising the boundary layers separating the two systems, and a correlative signature should also exist in the quadrupolar components of the geopotential field. In fact, Busse's sketch in Figure 1.1 was motivated by the recent discoveries by Dziewonski et al. [1977] and Masters et al. [1982] of a quadrupolar components of mantle heterogeneity with just these properties.

The results of Dziewonski et al. [1977] and Masters et al. [1982] do not, unfortunately, discriminate satisfactorily between models of shallow and deep circulation, nor do the considerable refinements in the mapping and interpretation of large-scale aspherical structure made in the subsequent studies of Woodhouse and Dziewonski [1984], Nataf et al. [1984, 1986], Dziewonski [1984], and Hager et al. [1985]. A particular problem is a "resolution gap" in the ability of present methods to image the mid-mantle transition zone, which has thus far prevented the detailed global mapping of lateral heterogeneity in this critical region. Nevertheless, these studies mark the coming-of-age of three-dimensional structural seismology, which holds the promise of providing a much refined picture of mantle convection.

This chapter purports to review some of the contributions seismology has made to the long-standing problems of mantle dynamics. The earth is a complex body with elastic and anelastic properties that are anisotropic and heterogeneous on many scales. Extracting useful information about this complexity from inaccurate and often woefully insufficient data sets derived by eyeballing or numerically processing a bunch of wiggly lines is a technically difficult endeavor--some would say an art form--and its practitioners have developed a healthy skepticism regarding any physical interpretations extrapolated from the results. As in any actively moving field, conflicting interpretations by reputable groups of investigators abound, bewildering as much as informing the non-specialists. On the other hand, an historical perspective suggests that, once

the smoke has cleared, many conclusions which now appear controversial will be seen as clearly established or clearly refuted by papers published years ago. Recognition of these facts breeds a certain timidity among reviewers, especially those who wish to affect a disinterested stance. Aware of these difficulties, we have abandon any attempt to write an objective, comprehensive and balanced account of the subject, and have chosen to concentrate on a few topics where our opinions are well informed (or at least well formed) by direct exposure to seismological data.

We begin our review with a discussion of plate structure in Section 2, placing particular emphasis on the boundary layer configurations of the continents. The existence of deep-seated "roots" beneath the continental cratons, only recently a very controversial subject, has now been confirmed by a variety of seismic methods. We infer that the average thickness of the plates in these regions is substantially greater than allowed by the simple thermal boundary models of classical plate tectonics. These cratonic structures appear to be dynamically controlled by a chemical boundary layer in the uppermost mantle with large lateral variations in thickness. Section 3 addresses the fate of subducted oceanic lithosphere, around which many dynamical issues revolve. We summarize the information on deep-focus seismic zones, concentrating on recent high-resolution images of near-source structure obtained by residual-sphere analysis. These images indicate the penetration of descending slabs into the lower mantle beneath a number of western Pacific subduction zones and, therefore, the existence of significant mass flux across the 650-km discontinuity. On the basis of this evidence, we conclude that the hypothesis of rigorous stratification of convection into an upper-mantle system and a lower-mantle system of differing compositions is not consistent with the available seismological data. The data on the large-scale structure of the mantle beneath the plates is reviewed in Section 4. We discuss the global models of aspherical heterogeneity obtained by the techniques of body-wave and surface-wave tomography and some of the questions they pose for dynamical models. In particular, we present the evidence for low-wavenumber, large-amplitude heterogeneity in the vicinity of the core-mantle boundary derived from core-penetrating *PKP* waves and argue that this heterogeneity is most plausibly explained by the existence of chemical, as well as thermal, boundary layers at this interface.

2. Structure of the Tectonic Plates

In the simplest model of plate tectonics, the plates are themselves the upper thermal boundary layer of the mantle convection system [Turcotte and Oxburgh, 1967], deriving their rigidity and ability to transmit deviatoric stress from the cold, strong mechanical boundary layer forming their outer parts [Elsasser, 1969]. The thermal boundary layer theory of plate structure has enjoyed great success in explaining the large-scale physiography and evolution of the major ocean basins, as well as many of their smaller scale features. Attempts have been made to integrate the continents into this thermal boundary layer model, but these have been less successful.

Continents are the most obvious manifestation of lateral heterogeneity in the earth and the most dynamically important component of a surficial chemical boundary layer (Figure 2.1). Whereas the thin basaltic crust of the oceans is continually being recycled into the mantle via the subduction process, the thicker, silica-rich crust of the continents remains buoyantly trapped at the surface. The disposition of continental crust thus exerts considerable control on plate kinematics [Isacks et al., 1968; McKenzie, 1969]. Moreover, crustal thickness is a significant parameter in determining the overall rheology of the lithosphere and consequently the strain field within the plates caused by the forces exerted at plate boundaries [Isacks et al., 1968; McKenzie, 1969; Vink et al., 1984]. It has been conjectured that these recognized crustal properties are sufficient to explain the various peculiarities of continental tectonics visible at present or evident in the geological record, including the diffuse nature of continental seismicity, the complexity of continental plate boundaries and continent-continent interactions, the tendency for continental masses to collect into "supercontinents", the age distribution of continental rocks, and so forth. According to the conventional theory of plate tectonics, the thermal, mechanical and chemical properties of the lithospheric plates below a depth of 100 km or so are largely independent of crustal type and can be couched in a unified model of boundary layer evolution without endowing special properties to the sub-continental mantle or special dynamics to continental drift [Crough and Thompson, 1976; Kono and Amano, 1978; Sclater et al., 1980, 1981]. The conventional model of plate structure is illustrated in Figure 2.2.

It has become clear from seismological studies, however, that the continental cratons are underlain by an extensive layer of anomalous mantle material, geographically variable and up to several hundred kilometers thick which translates with the continents during the course of plate motions. Since it was first proposed ten years ago [Jordan, 1975a], the hypothesis that the plates

in old continental regions are, on average, much thicker than even the oldest oceanic plate has been controversial. In a review of seismological and other evidence, Anderson [1979] dismissed the thick-plate hypothesis, stating, "Continental roots extend no deeper than about 150-200 km... Oceanic and continental geotherms converge above about 200 km and become less steep than the melting gradient at greater depth." Sclater et al. [1980, 1981] presented a comprehensive analysis of plate thermal structure in both continental and oceanic regions, and concluded that "the range in possible geotherms at depths below 100 to 150 km under continents and oceans overlaps and that the thermal structure beneath an old stable continent is indistinguishable from that beneath an old ocean were it at equilibrium. Oceans and continents are part of the same thermal system" [Sclater et al., 1981, p.11535].

These assessments notwithstanding, simple boundary-layer cooling models such as the one illustrated in Figure 2.2 are no longer tenable. In this section we review the evidence for thick continental plates, emphasizing some of the more controversial seismological issues but also summarizing other geophysical, geochemical and geological data on deep continental structure.

2.a. General Considerations

In discussing plate structure, we shall find it convenient to discriminate among the three types of boundary layers:

Thermal boundary layer (TBL). The TBL is defined by the thermal thickness L_T of the plate, equal to the depth where the geotherm reaches, or comes close to reaching, the mantle adiabat. Heat transfer within the TBL is dominated by conduction, and the thermal gradients are super-adiabatic.

Mechanical boundary layer (MBL). The MBL is defined by the effective mechanical thickness L_M of the TBL for long-term loads; that is, the depth to an isotherm T_M such that the deviatoric stresses at a given (small) strain rate are less than some specified (small) value for $T > T_M$ [McNutt, 1984]. The relationship between L_M and L_T has been investigated by numerical calculations employing realistic upper-mantle rheologies [Bodine et al., 1981], and the flexure data from both oceans and continents have been shown to be consistent with $T_M \approx$ 550-600°C [McNutt, 1984; Kusznir and Karner, 1985].

Chemical boundary layer (CBL). In a layered, convecting body with a chemical composition and evolutionary history as complicated as the earth's, it can be expected that the mechanisms of mass

transport will, over time, build up compositionally distinct boundary layers of intermediate density at the major chemical transitions. At the earth's surface, the most obvious manifestation of a CBL is the continental and oceanic crust, but this CBL also involves the uppermost mantle. The primary process for the major-element modification of the upper mantle is the extraction of basaltic melt, and the residuum left behind by this process has a lower density than the parental rock [O'Hara, 1975; Boyd and McCallister, 1976]. Compositional variations in upper-mantle density are most easily characterized in terms of a normative density ρ, defined to be density of a mineral assemblage equilibrated at mantle conditions (e.g., within the garnet stability field) but referenced to standard pressure and temperature [Jordan, 1979a]. The surficial CBL is defined by the thickness L_C of the crust and any subjacent mantle whose normative density has been significantly reduced by the extraction of a basaltic melt.

Because conduction will dominate over advection only when the mass motions are very small, the TBL must remain effectively coherent during plate motions. From a kinematical point of view, the TBL defines the plate, or lithosphere in the conventional terminology of plate tectonics. Traditionally, however, "lithosphere" denotes the strong outer shell of the earth capable of withstanding large deviatoric stresses over geologically long periods of time [Barrell, 1914; Daly, 1940]. To maintain the distinction between these two types of boundary layers--one kinematical, one dynamical--Jordan [1975a] proposed to adapt Elsasser's [1969] term "tectosphere" to designate the TBL, reserving lithosphere for the MBL. This usage will be followed here.

2.b. Oceanic tectosphere as a simple thermal boundary layer

In the oceans, a CBL comprising a basaltic crust and a subjacent, chemically complementary layer of dunitic and harzbugitic residua and cumulates is emplaced at the spreading centers [Ringwood, 1969; Kay et al., 1970]. The crust has an average thickness of about 6-8 km and the residual layer about 25-30 km, implying $L_C \approx 35$ km. This ophiolitic sequence translates away from the ridge crests with little modification, whereas a conductively cooled TBL and an associated MBL thicken with age. At small ages, the temperature profile of an oceanic plate decays according to a cooling half-space model; in particular, the TBL thickness increases as the square-root of age:

$$L_T = a_T t^{1/2} \tag{2.1}$$

If we define L_T as the depth where the temperature comes within, say, 3% of the mantle adiabat [e.g., Parsons and McKenzie, 1978], then $a_T \approx 15$ km $My^{-1/2}$. The TBL thickness at 70 My is

thus about 125 km. The cooling half-space model predicts that the water depth (corrected for variations in crustal loading) should increase as the square-root of time, which it is observed to do in regions of post-Mesozoic age [Davis and Lister, 1974; Trehu, 1975]. At ages greater than 70 My or so, however, the water depth increases less rapidly than predicted, levelling towards an asymptotic value about 3500 m below the rise crests [Sclater et al., 1975; Parsons and Sclater, 1977]. A number of explanations have been put forward to explain this asymptotic behavior, including radioactivity in the upper mantle [Forsyth, 1977], shear-strain heating [Schubert et al., 1976], phase changes [Wood and Yuen, 1984], and advection of heat from depth by large-scale circulation [Jarvis and Peltier, 1980], small-scale instabilities at the base of the plate [Richter and Parsons, 1975; Parsons and McKenzie, 1978] or localized upwellings beneath hotspots [Heestand and Crough, 1981]. With the exception of phase changes, all of these mechanisms involve retarding the rate of TBL growth by upward heat flux, so that L_T attains an asymptotic value of the order of one hundred kilometers. Such an interpretation implies that the thermal evolution of the oceanic tectosphere is better described by a cooling plate model of the sort suggested by Langseth et al. [1966] and developed by McKenzie [1967] and Sclater and Francheteau [1970] than by a cooling half-space model. From the bathymetry data, Parsons and Sclater [1977] estimate the asymptotic thickness of the plate to be 125 ± 10 km.

Geoid anomalies provide an even more sensitive discriminant between the cooling half-space and cooling plate models than does bathymetry. Half-space cooling implies a geoid anomaly that decays linearly with age at a constant rate of –0.15 m/My [Haxby and Turcotte, 1978], whereas the plate model of Parsons and Sclater [1977] predicts an asymptoic flattening of the anomaly beginning at about 40 My [Parsons and Richter, 1980; Sandwell and Schubert, 1980]. Because subtectospheric heterogeneities dominate the geoid at long wavelengths, this flattening is difficult to observe directly [Sandwell and Schubert, 1980], but it does express itself in the variation of short-wavelength anomalies across fracture zones [Detrick, 1981]. The fracture-zone anomalies observed on the GEOS 3 and SEASAT altimeters are consistent with cooling plate models having asymptotic values of L_T ranging from 70-125 km [Detrick, 1981; Sandwell and Schubert, 1982; Cazenave et al., 1983; Cazenave, 1984; Watts et al., 1985]. The Parsons-Sclater value lies at the upper end of this range.

The observations of flexural rigidity provide direct estimates of the effective elastic thickness of the oceanic lithosphere, which in turn can be related to L_M through an assumed rheology [Beaumont, 1979; Bodine et al., 1981; McNutt, 1984]. Bodine et al. [1981] have demonstrated that the relaxation for typical loads is complete within 1-10 My, and L_M thus depends primarily on

L_T at the time of loading. Therefore, at small ages we expect

$$L_M = a_M t^{1/2} \tag{2.2}$$

where a_M is a constant. Plate flexures observed on the outer rise of trenches and those measured from young volcanic loads show a systematic increase in the effective elastic thickness with the square-root of age, although there is much scatter [Watts et al., 1980; McNutt and Menard, 1982]. The outer-rise data are more suitable for estimating the constant in equation 2.2, because the loading data from mid-plate volcanoes appear to be perturbed by the vulcanism [McNutt, 1984]. Correcting for plate-curvature effects, McNutt [1984] obtains a_M = 3.8-4.2 km $My^{-1/2}$, corresponding to the 550-600°C isotherms of the cooling half-space model. The flexture data in the older oceanic regions are consistent with the cooling plate model having an asymptotic value of L_M equal to approximately 40 km [McNutt, 1984]. Hence, the thickness of the MBL in the ocean basins is only about one-third the TBL thickness.

The plate structure of a thermally mature ocean basin is schematically represented in Figure 2.3. The parameters of the oceanic adiabat are T_0 = 1300°C and $(\partial T/\partial P)_S$ = 0.5°C/km. The value of the average potential (zero-pressure) temperature T_0 is particularly important, since it sets the temperature scale for convection in the upper mantle. Early estimates of T_0 varied widely, ranging from a low of 550°C [McKenzie, 1967] to nearly 1500°C [Sclater and Francheteau, 1970]. Jordan [1975a] considered various types of evidence, including empirical geothermometry on mantle minerals and models of basaltic differentiation, to arrive at the estimate used here. Solomon [1976] criticized this choice, but it has been supported by subsequent studies [Forsyth, 1977; Parsons and Sclater, 1977]. The TBL thickness in Figure 2.3 is 150 km, somewhat larger than Parsons and Sclater's [1977] estimate and the asymptotic values derived from the fracture-zone offsets observed on altimeter records, though not significantly so. An MBL thickness of 60 km is obtained from the depth to the 600°C isotherm. A CBL with L_C = 50 km is defined by the deviation of the normative density profile below a mantle reference assemblage, here taken to be Ringwood's [1966] pyrolite (ρ = 3.40 Mg/m^3). Iron and alumina depletions of the mantle part of the CBL are assumed to reduce the normative density by 0.06 Mg/m^3, equivalent to the removal of about 20 mol % of olivine basalt from pyrolite [Jordan, 1979a].

2.c. Seismological constraints on the structure of the oceanic tectosphere

Seismic refraction experiments utilizing chemical explosions have elucidated the structure of

the crust and uppermost mantle beneath the ocean basins. The models derived from such experiments are generally consistent with ophiolite model of the oceanic CBL [Christensen and Salisbury, 1975; Salisbury and Christensen, 1978; Spudich and Orcutt, 1980]. In particular, the compressional velocities of the uppermost mantle show a strong (~7%) azimuthal variation, the highest velocities being parallel to the spreading direction at the time of crustal formation [Hess, 1964; Raitt et al., 1969; Morris et al., 1969; Keen and Barrett, 1971; Shor et al., 1973; Bibee and Shor, 1976; Shearer and Orcutt, 1985]. This azimuthal anisotropy has been observed in ophiolites and is attributable to the tectonic alignment of olivine and pyroxene crystals during the emplacement of the residual harzburgitic layer at spreading centers [Christensen and Salisbury, 1979; Christensen and Lundquist, 1982; Nicolas and Violette, 1982].

For shallow seismic sources in the oceans, the first-arriving compressional wave out to distances on the order of 2000 km is the P_n phase, a complex, high-frequency wavetrain propagating in the uppermost mantle [Sutton and Walker, 1972; Walker, 1977; Sereno and Orcutt, 1985]. Measurements of P_n apparent velocities in the Pacific Basin east of Japan using ocean-bottom seismometers show significant azimuthal anisotropy out to distances as great as 1000 km [Shimamura and Asada, 1983]. The fast axis of the anisotropy is perpendicular to the local orientation of the magnetic anomalies, not parallel to the present plate motion, indicating that it was frozen in at an earlier stage of plate evolution and is thus tectospheric. Because the velocity gradient is small in the uppermost mantle, the depth sampled at this distance is not well constrained, but the tectospheric anisotropy appears to extend below the CBL, perhaps to depths as great as 70-100 km [Shimamura, 1984].

It is difficult to study the structure of the oceanic upper mantle below the TBL by conventional marine refraction techniques, because the P_n phase obscures the later arrivals from deeper horizons. To obtain constraints on thermal evolution of the oceanic tectosphere, seismologists have resorted to the use of dispersive surface waves, of both the Rayleigh (*P-SV*) and Love (*SH*) type. The former are polarized in the plane of propagation, and the latter normal to it. At a given frequency, the speeds of these waves are observed to increase systematically with the average crustal age along the propagation path, and the variations of this increase with frequency can be used to construct age-dependent models of the oceanic upper mantle. Unfortunately, surface-wave studies are hampered by the limited distribution of seismic sources and receivers in the interiors of the oceanic plates, which restricts the power of the data to resolve lateral variations in structure, and by the limited range of frequencies over which the dispersion can be measured along pure oceanic paths (0.005-0.1 Hz), which restricts the power of the data to resolve radial variations in structure.

Moreover, the whole business is complicated by the existence of upper-mantle anisotropy.

Seismological models of the oceanic upper mantle are usually parameterized by three layers: a high-velocity "lid", a low-velocity "channel", and a "sub-channel" [e.g., Kanamori and Press, 1970; Leeds et al., 1974]. The lid is sometimes referred to as the "seismological lithosphere", although its relationship to either the MBL or the TBL depends on the details of a rheological model [Anderson and Minster, 1980]. In particular, the lid-channel boundary, which appears to be quite sharp, may be controlled by the intersection of the geotherm with the mantle solidus [Anderson and Sammis, 1970; Forsyth, 1977]. We denote the depth to this boundary by L_S.

Nearly all of the detailed studies of the age-dependent properties of the oceanic upper mantle have employed surface-wave paths confined to the Pacific Basin. Leeds et al. [1974] and Le [1975] obtained isotropic models of the Pacific from the age variation of Rayleigh-wave phase velocities; in their models, L_S increased from 12 km at 5 My to 116 km at 150 My. Motivated by the cooling half-space model of the oceanic TBL, Yoshii [1975] adopted the functional form

$$L_S = a_S t^{1/2} \tag{2.3}$$

and showed that Rayleigh-wave group velocities are consistent with $a_S = 7.5$ km My$^{-1/2}$. Forsyth [1975] measured the dispersion of both Love and Rayleigh waves propagating over paths in the eastern Pacific to constrain the anisotropy, as well as the age dependence, of the Pacific and Nazca plates. He found that the azimuthal variation of the surface-wave velocities is small, but that polarization anisotropy (i.e., anisotropy with a vertical axis of symmetry; transverse isotropy) is required to satisfy both data types. In his models, L_S increases rapidly to about 60 km at 10 My and thereafter changes slowly, attaining about 70 km at 50 My. Schlue and Knopoff [1977, 1978] also investigated anisotropy. They were able to satisfy a large set of Love and Rayleigh data with models in which the only anisotropy is a transversely isotropic low-velocity channel and the only lateral variation an increase in L_S with age. Their models approximate equation (2.3) with $a_S = 10$ km My$^{-1/2}$. They identified L_S as the top of a region of partial melting and associated the polarization anisotropy with the distribution of melt in cracks preferentially oriented by a shear-flow gradient in the channel.

Yu and Mitchell [1979] and Mitchell and Yu [1980], on the other hand, concluded that the differences in Love and Rayleigh dispersion are best modelled by an anisotropic lid overlying an isotropic low-velocity channel. They obtained $L_S \approx 110$ km for $t > 100$ My. Their procedures

corrected the surface-wave data for frequency-dependent anelastic dispersion [Liu et al., 1976], which had been ignored in the previous studies.

Isotropic velocity models are specified by two elastic parameters. The analysis of polarization anisotropy employed by Forsyth [1975], Schlue and Knopoff [1977], and Mitchell and Yu [1980] allowed for differences in the propagation speeds of horizontally and vertically polarized shear waves, v_{SH} and v_{SV}, but assumed isotropic compressional velocities, thus approximating a transversely isotropic material with three elastic parameters [Schlue and Knopoff, 1978]. In general, however, a transversely isotropic material has five elastic parameters: the two shear-wave velocities; two compressional-wave velocities, v_{PH} and v_{PV}; and a fifth parameter η, specifying the wave speeds at angles intermediate to the vertical and horizontal [Anderson, 1966]. Anderson and Regan [1983] and Regan and Anderson [1984] have argued that three-parameter models of oceanic anisotropy are inadequate, and they have obtained by trial-and-error structures satisfying the surface-wave data using the full five-parameter formulation. Their models have a high-velocity, nearly isotropic lid that thickens with age and an anisotropic low-velocity channel with age-dependent velocities. In these models, L_S reaches a maximum thickness of only 50 km, about half that obtained in previous work and comparable to L_M values obtained from flexural studies. Anderson and Regan [1983] argue that the thicknesses of both the lid and the MBL may be controlled by effects other than temperature, such as mineralogy, crystal orientation or partial melting.

Figure 2.4.a shows the values of L_S for three surface-wave models--the isotropic structure of Leeds et al. [1974] and Leeds [1975], the pseudo-anisotropic structure of Schlue and Knopoff [1977], and the fully parameterized transversely isotropic structure of Anderson and Regan [1983]--and it compares them with the MBL and TBL thicknesses from the Parsons-Sclater plate model. The seismological estimates vary substantially, but all three fall between L_M and L_T for $t <$ 70 My. The corresponding isotherms calculated from the cooling half-space model range from about 650°C to 1100°C. The higher value is consistent with the proposition that L_S is defined by the intersection of the oceanic geotherm with the mantle solidus [Forsyth, 1977], whereas the lower value is not.

The discrepancies among the velocity structures illustrate the nonuniqueness of seismological models derived from real data sets. Anderson and Regan [1983] argue that their models are superior because they adopt a more general parameterization. It appears, however, that the values of L_S given by the Anderson-Regan model are a factor of two lower primarily because the shear

velocities in their low-velocity channel are as much as 0.3 km/s higher than the other two models. Anderson and Regan [1983] and Regan and Anderson [1984] did not attempt to demonstrate that models with greater values of L_S (and correspondingly lower channel velocities) cannot satisfy the same data sets. Indeed, given the increased flexibility of their five-parameter formulation, the availability of such models is quite plausible. Until the problems of nonuniqueness receive more attention, any conclusions on the physical interpretation of L_S cannot be considered definitive.

Although the ability of the surface-wave data to constrain localized properties such as L_S is limited, they do fix the age dependence of the travel times of shear waves propagating vertically through the upper few hundred kilometers of the oceanic upper mantle. The travel time between depths of z_0 and z_1 is

$$\tau_S(z_0,z_1) = \int_{z_0}^{z_1} v_{SV}^{-1}\, dz \tag{2.4}$$

Figure 2.4.b plots the vertical travel times through the upper 400 km derived from the three surface-wave models of Figure 2.4.a. This functional varies linearly with the square-root of age for all three models over the entire range of the observations (5-150 My). The travel times from the Anderson-Regan structure differ from the other two by a constant offset of about −1.4 s, due primarily to differences in the shear velocities below 220 km, where the fundamental-mode data have poor resolution. However, the changes in travel time with age are nearly identical in all three models, having a slope of 0.27 s $My^{-1/2}$. This slope agrees with direct observations of vertical shear-wave travel times derived from ScS_2-ScS differential travel times [Sipkin and Jordan, 1976] (see Figure 2.5) and S-wave source anomalies [Duschenes and Solomon, 1977].

The fact that the vertical shear-wave travel times continue to decay as the square-root of age beyond 100 My has significant implications for the thermal and convective structure of the oceanic upper mantle. As discussed in the previous section, there is considerable non-seismological evidence that oceanic TBL evolves according to the cooling plate model with $L_T \leq 125$ km in old ocean basins. The values of L_S in Figure 2.4.a conform more with the cooling half-space model, but given their non-uniqueness, it appears that structures consistent with both the surface-wave data and the cooling plate hypothesis are feasible. The vertical travel times in Figure 2.4.b do indicate, however, that the average temperature of the oceanic upper mantle in the upper few hundred kilometers does not become asymptotically constant, but continues to decrease as the square-root of time. That this should be so is suggested by the appreciable flow of heat out of the mantle (~ 50

mW/m^3) in even the oldest ocean basins [Hager and O'Connell, 1981]. If small-scale convection in the upper mantle beneath old ocean basins is the mechanism which regulates the asymptotic value of plate thickness, as hypothesized by Richter and Parsons [1975] and Parsons and McKenzie [1978], then this observation implies that there is a secular cooling of the sub-tectospheric mantle at ages greater than the onset of TBL instability (70 My in the Parsons-McKenzie model). This secular cooling will, in turn, contribute to driving a large-scale flow, which we believe must involve the lower mantle (see Section 3).

2.d. The deep structure of continents

Like the oceans, the continents show a systematic decrease in surface heat flow and elevation and an increase in TBL thickness with age, provided that this age is defined not as the time since the original formation of the crust but as the interval since the last major thermal or orogenic event [Polyak and Smirnov, 1968; Sclater and Francheteau, 1970; Sclater et al., 1981]. The thermal reactivation and subsequent conductive relaxation of a continental TBL have been used to explain a wide variety of epeirogenic phenomena, including continental margin subsidence [Sleep, 1971; Steckler and Watts, 1978], the formation of continental basins [Sleep, 1971; Sleep and Snell, 1976; Haxby et al., 1976; McKenzie, 1978; Sclater and Christie, 1980], and plateau uplift [Crough, 1979]. Within the late Proterozoic and Phanerozoic orogenic belts peripheral to the cratons, where most of the large vertical motions have occurred, the parameters of continental TBL growth are compatible with those observed for the oceans; in particular, the asypmtotic thickness of the epicontinental TBL is similar to the oceanic value [Sleep, 1971; Steckler and Watts, 1978; Sclater and Christie, 1980].

These facts have motivated Sclater et al. [1980, 1981] to extend to the continents the model for TBL evolution advanced by Parsons and McKenzie [1978] for the ocean basins (Figure 2.2). Continents are viewed as superficial crustal edifices that modify the strength of the MBL and, owing to their buoyancy, play an important role in plate tectonics, but they do not correlate with profound differences in tectospheric structure. The TBL configuration of old continents is postulated to be similar to that of old ocean basins: following rejuvenation, both oceanic and continental TBLs grow to an asymptotic thickness of about 125 km, which is regulated in steady-state by small-scale instabilities at the base of the MBL. The ancient cratons are those portions of the continental masses that have escaped any major thermal reactivation and collisional orogenesis since the Precambrian. This model implies that the temperature and composition, and thus the elastic properties, of the TBL underlying old continents should be, on the average, the same as those of an old ocean basin.

Significant local variations may occur due to the thermal fluctuations associated with small-scale convection, but these should not be a strong function of crustal type.

The hypothesis that old continents and old oceans have similar TBL structures can be tested by seismological experiments. Seismologists have known for some time that the average shear velocity in the upper mantle beneath the continental cratons is considerably greater than the averages for oceanic and orogenic provinces [Brune and Dorman, 1963; MacDonald, 1963; Toksöz and Anderson, 1966; Knopoff, 1972], but the depth extent of these variations has been uncertain. Nearly all of the early work on continent-ocean heterogeneity was based on measurments of the phase and group velocities of fundamental-mode surface waves. In the frequency band typically observed over relatively pure oceanic and continental paths (0.005-0.10 Hz), the fundamental-mode data alone have poor resolving power below about 200 km, and they are particularly insensitive to structural variations in the 200-400 km depth range. Dziewonski [1971], for example, was able to satisfy a large, global set of fundamental-mode Rayleigh-wave data with models where the only significant differences between the continental and oceanic structures were confined above 200 km.

Okal [1977] reëxamined the implications of the surface-wave data using an augmented data set and concluded that, "Rayleigh-wave phase velocities for continental areas (both shield and mountainous regions) fall within the range of oceanic models, and the difference between average oceanic and continental velocities is on the same order of magnitude as the variation within the oceanic plates due to age. This is incompatible with Jordan's models of strong, deep lateral heterogeneities between oceans and continents." Okal did not attempt a resolving power analysis; he simply compared his data with the dispersion calculated from published models (in fact, the dispersion curves he attributed to Jordan's [1975b] models are incorrect). A more precise statement is that the fundamental-mode Rayleigh-wave phase velocities *cannot resolve* continent-ocean differences much below about 200 km.

An additional constraint on continent-ocean heterogeneity was introduced by Sipkin and Jordan [1975; 1976], who estimated the lateral variations in the shear velocities integrated over the entire upper mantle from the travel times of ScS_n phases. (ScS_n reflects n times from the core-mantle interface and $n-1$ times from the free surface.) They showed that the differences observed in ScS_n travel times were much larger than predicted by Dziewonski's [1971] regionalized models of continent-ocean heterogeneity. They argued that, since the surface-wave data fix the average velocities in the upper 200 km or so, there must exist substantial lateral

variations below this depth that correlate with crustal type. Jordan [1975a] applied Parker's [1972] quadratic programming technique to obtained a lower bound of 310 km on the depth extent of continent-ocean heterogeneity from two numbers, Sipkin and Jordan's [1975] average *ScS* time difference and Kanamori's [1970] difference in the average phase velocities of 190-s Love waves. Figure 2.5 gives histograms of Sipkin and Jordan's [1976] ScS_2 -*ScS* residuals for each of the six crustal types in the tectonic regionalization of Figure 2.1.

In a parallel study of ScS_2 -*ScS* differential travel times, Okal and Anderson [1975] argued that old continents and old oceans have similar residuals and concluded that the differences between them could be confined above 200 km. The discrepancy between the Sipkin-Jordan and Okal-Anderson results was used by Sclater et al. [1980] to argue against the thick-plate model. However, Sipkin and Jordan [1980] obtained a much larger set of ScS_m -ScS_n differential travel times from the newly installed digital networks. They found a one-way time difference averaging $+2.6 \pm 0.6$ s between western Pacific and continental paths, consistent with the median difference of +3.0 s between old oceans (Region C) and stable continents (Regions S and P) obtained from Figure 2.5.

The strong correlation between average upper-mantle shear velocities and crustal type is critical to the interpretation that most of the lateral variation observed in the ScS_n times is caused by tectospheric, not sub-tectospheric, structure [Jordan, 1975a]. Figure 2.6 illustrates this correlation for ScS_2 -*ScS* differential travel times from paths crossing northern Eurasia and the Arctic Basin. These differential times show a spectacular monotonic variation of more than 8 s in two-way travel time (4 s in one-way time) across the Phanerozoic fold belts and continental margin separating the high-velocity Siberian shield from the low-velocity Arctic Basin. This observation supports hypothesis that the transition from the thick tectosphere of the cratons to the thin tectosphere of the oceans typically occurs in the Phanerozoic mobile belts surrounding the cratons.

Additional evidence for the correlation of vertical travel times with surface geology is provided by *S*-wave station anomalies. Station anomalies are derived by averaging the residuals observed at a particular receiver over many seismic sources to reduce the perturbations from heterogeneities far from the station [Doyle and Hales, 1967]. Wickens and Buchbinder [1980] have complied a set of 42 station anomalies for North America, and their contoured anomaly map is shown in Figure 2.7. The smallest *S*-wave vertrical travel times are found for stations on the Canadian Shield and the largest in the Basin and Range Province of the western United States, the total variation being in excess of 5 s. This observation is an indication that the Basin and Range is

underlain by a high-temperature, oceanic-type mantle structure [Doyle and Hales, 1967; Knopoff, 1972; Grand and Helmberger, 1984a], as required by heat-flow studies [Lachenbruch and Sass, 1980].

The strongest gradients in the *S*-wave station anomalies coincide with the Phanerozoic fold belts that bound the North American craton, consistent with the tectonic realtionships observed in the ScS_2 -ScS differential travel times of Figure 2.5. In general, Precambrian shields and platforms (Region S of Figure 2.1) are faster than the stable continental areas covered by platform sediments during the Phanerozoic (Region P), which in turn are faster than the Phanerozoic magmatic belts and orogenic zones (Region Q). On the average, all continental crustal types are underlain by mantle faster than even the oldest oceanic areas (Region C), although there is considerable overlap between the individual observations for Regions Q and C (Figure 2.5). These travel-time differences cannot be explained by, say, differences in the distribution of upwelling and downwelling convective plumes between continents and oceans; the correlation with long-term (~600 My) tectonic behavior of the crust is just too good, and the correlation with other indicators of the mantle flow regime (e.g., the geoid) is too poor [Jordan, 1975a]. Instead, they require profound variations in tectospheric structure. As repeatedly emphasized by Jordan [1975a, 1978, 1979b, 1981b] and Sipkin and Jordan [1976, 1980], the vertical travel-time data in combination with fundamental-mode surface-wave data are sufficient to reject unified TBL models of the sort proposed by Crough and Thompson [1976], Kono and Amano [1978] and Sclater et al. [1980, 1981].

This inference is fully supported by a series of new high-resolution studies of lateral heterogeneity using higher-mode surface waves and multiply reflected body waves. The dispersion of higher-mode Rayleigh waves is capable of giving good resolution in the 200-400 km depth range, where the fundamental-mode data only poorly constrain the structure, but the measurement of this dispersion is complicated by the interference of the various mode groups. Frequency-wavenumber filtering methods have been developed which can separate successfully the mode branches out to the fourth overtone when applied to seismometer arrays having apertures of 1000 km or so [Nolet, 1975, 1977; Nolet and Panza, 1976; Cara, 1978]. Data has been obtained in the band 0.01-0.05 Hz by these techniques over Eurasian [Nolet, 1975, 1977] and Pacific [Cara, 1979] paths. Inversions show substantially greater (>0.2 km/s) shear velocities beneath Eurasia in the depth range 100-200 km; differences as large as 0.1 km/s persist to depths exceeding 250 km [Cara et al., 1980].

The interval on the seismogram corresponding to the group arrival times of the higher modes lies between the direct *S* phase and the fundamental-mode Rayleigh wave. Advances in numerical techniques now make it possible to obtain relatively complete synthetic seismograms for this interval from spherically symmetric structures. To take advantage of this capability, Lerner-Lam and Jordan [1983] have developed an inversion procedure which derives the path-averaged properties of the crust and upper mantle by fitting the observed time-domain waveforms with synthetic waveforms. Because the complex interference patterns among the higher-mode wave groups are modelled directly without attempting to separate the spectral properties of individual higher modes, the method is less susceptible to bias than mode-separation techniques, and good resolution of path-averaged structures can be obtained to depths of 500 km or so with smaller data sets [Gee et al., 1985]. Lerner-Lam and Jordan [1983] applied their procedure to the study of the Eurasian continent and Pacific Ocean, using source and receiver distributions similar to those employed by Cara [1979] and Cara et al. [1980]. They obtained continental and oceanic models with shear-velocity differences to depths on the order of 400 km, consistent with the previous studies.

The waveform-inversion technique of Lerner-Lam and Jordan [1983] has been recently used to study the structural differences between northern Eurasia and the western Pacific [Lerner-Lam and Jordan, 1986]. Isotropic shear-velocity models for these two regions are compared in Figure 2.8.a. EU2 is a structure derived from Kuril-Japan earthquakes recorded by a vertical-component receiver array in western Europe. Although the paths sample a variety of structures in northern Eurasia, from the tectonically active region east of the Verkhoyansk Suture Zone to the Baltic Shield, the waves propagate mostly over stable continent (Regions S and P of Figure 2.1). PA2 is obtained from Kuril-Japan sources recorded by stations in the southwestern Pacific, with paths almost entirely over oceanic crust having ages greater than 100 My (Region C). PA2 features a 100-km thick lid, a well-developed low-velocity channel, and a relatively steep gradient in the *S* velocities between the channel and a discontinuity at 400 km depth. EU2 has no channel and small gradients down to 400 km. EU2 has higher *S* velocities than PA2 above 370 km. Both provide excellent fits to the fundamental and higher-mode waveforms.

Of course, the existence of models with differences to some maximum depth z^* does not imply that such differences must exist. The models are not unique, and all we can really assert is that extending structural differences down to the level z^* is consistent with the data; that is, we cannot reject the null hypothesis that $z_{max} \leq z^*$, where z_{max} is an upper bound on the actual depth of continent-ocean variations. However, if no models with differences confined shallower than z^* can

be found that fit the data adequately, then we have grounds for rejecting the null hypothesis in favor of the alternative $z_{max} > z^*$. Lerner-Lam and Jordan [1986] have applied an inversion technique they call "squeezing" to demonstrate that the data used to derive EU2 and PA2 are inconsistent with $z_m < 220$ km. The higher-mode data alone require deep structural differences between old continents and old oceans independent of any inferences based on vertical travel times.

The waveforms on the seismogram between the direct *S* phase and the fundamental-mode surface waves can be described in terms of the interference of higher modes or, equivalently, as the superposition of various body waves, of which the multiply reflected *S* waves are the most prominent. The modal decomposition used by Lerner-Lam and Jordan [1983, 1986] is more convenient for the *P-SV* system, whereas the body-wave decomposition is more convenient for *SH*. Grand and Helmberger [1984a,b; 1985] have applied a body-wave analysis to the study of *SH*-polarized *S*, *SS* and *SSS* waves in the distance range 10° to 80° and have obtained models satisfying the travel times and waveforms. Figure 2.8.b compares their *SH*-velocity structures for stable North America (SNA) and the western Atlantic Ocean (ATL). The models are identical below the 400-km discontinuity, but SNA is faster than ATL above this depth. Grand and Helmberger inverted their data by trial-and-error and have not yet attempted any quantitative resolving power analysis, but it is clear that their data have a resolution of structural details below 200 km that is at least comparable, if not superior, to the P-SV data used by Lerner-Lam and Jordan [1983, 1986] and Gee et al. [1985].

Therefore, both the *P-SV* and *SH* waveform-modelling techniques demonstrate that the mantle beneath stable continents has higher shear-wave velocities than beneath the old oceans to at least 200-250 km in depth and perhaps to 400 km, consistent with the inferences from vertical travel-time data of Sipkin and Jordan [1975, 1976, 1980]. We note, however, that significant discrepancies remain among the three data sets. Figure 2.8.c compares SNA with EU2, and Figure 2.8.d compares ATL with PA2. Although all four models are essentially identical below the 400-km discontinuity, the *SH*-polarized data give substantially higher shear velocities in the uppermost mantle. The differences between ATL and PA2 exist primarily in the upper 200 km, but SNA is faster than EU2 all the way to 400 km. The SNA shear velocities decrease with depth between 150 and 200 km, forming a low-velocity channel, whereas EU2 has no such channel. This particular difference may be due to a lack of resolving power in one or both data sets, but the large (0.16 km/s) average velocity difference between SNA and EU2 above 400 km is not.

The differences may reflect true regional variations, at least in part, but we are skeptical that

an explanation based entirely on path differences can account for the discrepancies. Grand and Helmbereger [1985] have modelled the transition from the active foldbelts of central Asia to the Russian Platform using their multiple-*S* technique, and, averaged over the uppermost mantle, the *lowest* velocities they find are still higher than EU2, even though the paths used in deriving EU2 traverse primarily the high-velocity shields and platforms of northern Eurasia. In fact, the vertical *S*-wave travel time through EU2 is actually greater than through ATL, in conflict with the ScS_n and station-anomaly observations. We suspect that the discrepancies evident in Figures 2.8.c and 2.8.d are diagnostic of polarization anisotropy. The sign of the velocity differences is consistent with other observations of polarization anisotropy in the upper mantle [e.g., Dziewonski and Anderson, 1981; Anderson and Regan, 1983], and similar model discrepancies have been noted by Cara et al. [1980] and Leveque and Cara [1983] using the dispersion of fundamental and higher-mode Rayleigh and Love waves measured by spatial filtering. A definitive statement must await the treatment of both *P-SV* and *SH* data sets from common paths by the same inversion technique.

Discrepancies also exist between the vertical *S*-wave travel times calculated from the models and the ScS_n observations. Despite the large continent-ocean differences in both sets of models, the vertical time for PA2 (suitably corrected for water depth) is only 1.5 s greater than EU2, and that for ATL is only 1.8 s greater than SNA. In comparison, the observed ScS_2 -*ScS* difference between old oceans (Region C) and Precambrian shields and platforms (Region S) exceeds +3 s (Figure 2.5). The models in Figure 2.8 are isotropic structures, and their vertical travel times may be biased by the existence of polarization anisotropy. It is unlikely, however, that they overestimate the average structural contrasts between the continental cratons and old ocean basins, or the depth to which these contrasts persist.

2.e. The importance of the continental chemical boundary layer

The seismological data reviewed in Section 2.d imply that the stable parts of the continents are underlain by a TBL whose average thickness exceeds 220 km and most likely reaches 400 km, at least locally beneath the old cratons. These data clearly exclude the thin-TBL model of Figure 2.2. The most straightforward alternative is some variant of the cooling half-space model; that is, a thick TBL is grown by the long-term conductive decay of the continental thermal profile, unlimited by small-scale convective instability below the MBL [Chapman and Pollack, 1977]. A cooling half-space model, like the cooling plate model, ascribes only a superficial character to the CBL (although it can play an important kinematical role). Because the continental CBL is buoyant, the thermal ages of the continents are typically much greater than the oceans, thus accounting for the

correlation between tectospheric thickness and crustal type. The cratons are simply those areas that have been tectonically stabilized by the growth of a very thick TBL and have remained undisrupted by large-scale convective activity and collisional orogenesis.

Indeed, a continued increase in L_T according to equation 2.1 for 700 My is sufficient to grow a TBL about 400 km in thickness, which would satisfy the seismological data. At least three major objections can be raised against the cooling half-space model, however:

(1) The local Rayleigh number of the sub-MBL portion of such a thick TBL is large ($>10^4$), indicating that it would be convectively unstable [Jordan, 1975a; Parsons and McKenzie, 1978].

(2) To maintain isostatic balance, the growth of a thick TBL would require subsidence of the continents, just as it does in the oceans. The cratons should thus be covered with several tens of kilometers of sediments, which is not observed [Jordan, 1978; Oxburgh and Parmentier, 1978; Poupinet and de Voogd, 1981].

(3) The geoid anomalies for thick TBLs with near-surface compensation are substantial [Haxby and Turcotte, 1978; Parsons and Richter, 1980], so that the cratons should be evident in the geoid, which they are not [Jordan, 1975a].

It is clear from seismology that there are substantial lateral variations in the thickness of the continental TBL, but it is equally clear from arguments (1)-(3) that the compensation of these variations does not occur in the crust, as required by simple cooling models.

To circumvent these difficulties, a more complex model of the tectosphere has been developed which assigns a major role to an augmented CBL beneath the continental cratons [Jordan, 1975a, 1978, 1981b]. Its basic premise is that the mass excesses associated with cold, thick, cratonic TBLs are locally compensated by variations in the composition of the upper mantle. That is, below the MBL, the normative density of the continental tectosphere is less than the normative density of the oceanic upper mantle at the same depth. The continental TBL is thus stabilized against convective disruption by a thick CBL. This scenario can be inferred directly from the geophysical observations, independent of any petrological model [Jordan, 1975a].

The existence of a thick CBL beneath the cratons is required by the petrological data as well.

The mechanism for chemical compensation of the continental TBL is basalt depletion. Mantle mineralogy in the depth range 70-400 km approximates that of a garnet lherzolite [Ringwood, 1975, Yoder, 1976], and the subtraction of basalt from a garnet lherzolite leaves a residue less dense than the parental material [O'Hara, 1975; Boyd and McCallister, 1976; Green and Liebermann, 1976]. Peridotite nodules from kimberlite pipes in cratonic areas are observed to have major-element compositions depleted in Al_2O_3, FeO and CaO relative to compositions derived for the oceanic upper mantle [Ringwood, 1966; Nixon et al., 1973]. The normative density differences calculated from these compositions are sufficient to account for the thermal differences inferred by geophysical methods [Jordan, 1978, 1979a]. For example, the average continental garnet lherzolite obtained from kimberlite xenoliths by Jordan [1978] has a normative density 1.3% less than Ringwood's [1966] pyrolite, which is sufficient to offset a continent-ocean temperature difference of several hundred degrees. These xenoliths appear to have equilibrated at depths of 150-200 km and temperatures of 1000-1200°C [Boyd, 1973; Finnerty and Boyd, 1984]. In fact, oceanic temperatures at this depth are inferred to be about 300°C higher (Figure 2.3). Other quantitative tests of the basalt depletion hypothesis have been made by Jordan [1978, 1979a] using the xenolith data.

The temperature and normative density profiles of a hypothetical continental craton are sketched in Figure 2.9 assuming L_T = 225 km, L_C = 200 km and L_M = 90 km. These values are consistent with the major-element data from kimberlite xenoliths [Jordan, 1979a; Boyd et al., 1985], as well as a number of geophysical observations, including heat flow and heat production data [Sclater et al., 1980; Nicolayson et al., 1981] and flexural studies [Kusznir and Karner, 1985].

We note, however, that values of L_T and L_C adopted for this diagram probably underestimate those typical for the old, stable cratons, where the seismological data almost surely require L_T > 300 km. The temperature profile in Figure 2.9 was computed assuming the heat production of the sub-crustal tectosphere is negligible, an assumption often made in heat-flow analyses [e.g., Sclater et al., 1980] but one which is likely to be incorrect. Jordan [1981b] has pointed out that a thicker TBL is required if the heat production of the sub-crustal CBL is relatively high, as indicated by the evidence for metosomatic enrichment of the CBL in large-ion lithophile (LIL) elements (see below). A TBL thicker than 225 km can also be inferred directly by comparing subcontinental temperatures derived by empirical geothermometry on mantle xenoliths with oceanic temperatures extrapolated along the mantle adiabat [Jordan, 1975a, 1978].

A continental tectosphere approaching 400 km in thickness is illustrated in Figure 2.10, which shows the transition from a cratonic to an oceanic upper-mantle structure across a typical quiescent continental margin. In this hypothetical model, the largest gradients in L_T occur beneath the Phanerozoic platforms and fold belts peripheral to the cratons. Transitions of this type are found between the Canadian Shield and the Atlantic Ocean at the latitude of Boston and along the northern margin of Eurasia, as is evident from the vertical travel-time data of Figures 2.6 and 2.7.

2.f. Implications for mantle evolution and dynamics

The hypothesis that the continental cratons are underlain by a thick TBL stabilized by thick, basalt-depleted CBL has a number of far-reaching (and thus testable) implications and ramifications regarding mantle evolution and dynamics. We include here a brief catalog of some of the more obvious consequences of the model, most of which have been discussed previously by Jordan [1978, 1979b, 1981b]:

Advective thickening as a mechanism for tectospheric growth. If the CBL controls the thickness of the continental tectosphere, then the TBL cannot grow by simple conductive cooling. In fact, unless there is a mechanism which either steadily depletes the continental upper mantle in its basaltic constituents or adds depleted material to the base of the tectosphere, the continental tectosphere beneath the stable cratons cannot grow progressively with time at all. Impressive outpourings of continental flood basalts do occasionally occur, but the volume of the mantle depleted by these episodes is actually quite small (on the order of 10^6 km^3 in a major episode such as the Miocene flooding of the Columbia River Basin in the northwestern U.S). In comparison, the volume of depleted mantle beneath Regions S and P of Figure 2.1 is on the order of 10^{10} km^3, assuming an average CBL thickness of 200 km. In round numbers, the amount of basalt missing from the subcontinental upper mantle is about twice the present-day volume of the oceanic crust and a little less than half the total volume of the continental crust, orders of magnitude greater than the integrated volume of basalt erupted in continental regions since their stabilization in late-Archean, early-Proterozoic time.

Oxburgh and Parmentier [1978] have suggested that the CBL beneath the cratons could increase progessively by the addition of depleted mantle rising diapirically from the oceanic CBL. Seismic imaging of descending slabs in the northwestern Pacific by residual-sphere techniques (Section 3.d) shows no evidence of slab disruption by such a mechanism, although it is certainly possible that a significant amount of basalt-depleted material from the oceanic CBL has been

transferred to the continents over the course of geological history. We are skeptical, however, that progressive underplating of the cratons coupled with thermal decay of the TBL is a viable model for tectospheric growth, because it is likely that these processes would operate with significantly different spatial and temporal scales and, hence, the balance between chemistry and temperature would be difficult to maintain.

The mechanism we prefer is advective thickening of the continental tectosphere during major episodes of orogenic compression, such as those which accompany the formation of "supercontinents". The advective-thickening hypothesis is the foundation of the evolutionary model proposed by Jordan [1978, 1981b]. Vulcanism along the active continental margins (and to a much lesser extent in intracontinental rifts) generates buoyant, refractory mantle resistant to convective recycling. Augmenting this material is any depleted peridotite transferred from the oceanic CBL by lateral accretion across subduction zones or by diapirism from descending slabs. Dispersed regions of buoyant mantle and their superjacent (but not necessarily chemically complementary) crustal columns are amalgamated during the course of plate motions and eventually swept up and accreted to the major continental masses. Major compressive events at convergent plate boundaries, particularly the violent episodes of continent-continent collision, further consolidate and thicken both the CBL and the TBL by downward advection (Figure 2.11). Competing against these constructive processes are the destructive, double-diffusive instabilities associated with tectospheric heating. These instabilities can lead to thinning of the CBL by continental extension, occasionally initiating Atlantic-type drift. Ultimately, however, perhaps only after repeated orogenic cycles, a thick, cohesive and relatively stable tectosphere--a continental craton--is formed.

Age of the continental tectosphere. This hypothetical scenario for tectospheric development of the continents conforms to actualistic principles and illustrates that a thickened CBL is a plausible consequence of the Wilson cycle. However, the model requires that the primary episodes of basalt extraction precede cratonization. Hence, the CBL structure of an ancient craton as regards major elements (though not necessarily minor ones) must date from its stabilization. Jordan [1981b] emphasized that this is a major, testable prediction of the tectospheric model. He pointed out that the data from South Africa are consistent with this prediction. In particular, he noted Kramers [1979] work on sulphide inclusions in diamonds, which indicated the inclusions were closed to *Pb* in excess of 2000 My ago.

In a recent, more definitive study of southern African diamond inclusions, Richardson et al.

[1984] have obtained *Sm-Nd* and *Rb-Sr* model ages of 3200-3300 My for sub-calcic garnets encapsulated by diamonds. Peridotitic inclusions in diamonds [Gurney et al., 1979] show residual major-element compositions characteristic of the entire kimberlite nodule suite [Mathais et al., 1970], which provides strong evidence that the CBL extends to depths exceeding 150-200 km beneath the Kaapvaal craton. Although Richardson et al. [1984] do not comment on the tectospheric model, their age data are consistent with diamond formation during an episode of advective thickening of the CBL prior to the stabilization of Kaapvaal craton in the late Archean [Hunter, 1974].

If a thick, basalt-depleted CBL formed at this time, then a thick TBL must have also, since the low-density CBL would not otherwise be stable. This consequence of the tectospheric model has been confirmed by the application of geothermometry to monomineralic silicate inclusions in South African diamonds, which show equilibration temperatures of 900-1200°C [Boyd et al., 1985]. These temperature are similar to the range observed in the granular garnet lherzolite xenoliths, but the former were frozen in at the time of diamond formation (presumably of Archean age), whereas the latter were equilibrated in the Cretaceous. These data are consistent with a variety of other evidence (see Richter [1985] for a summary) that the geotherm beneath the cratons was not much different than it is today. Estimates of subcontinental temperatures in the Archean calculated from convection models invoking simple TBL cooling (oceanic-type tectosphere) invariably give much higher temperatures and imply significant melting, inconsistent with these observations [Davies, 1979; Richter, 1985].

The continental CBL as a geochemical reservoir. The cold, refractory CBL of the continental tectosphere constitutes a particularly stable reservoir for large-ion lithophile (LIL) chemical species. Peridotite nodules from kimberlite pipes with residual major-element compositions have generally had their minor-element compositions significantly altered by subsequent metasomatic events [Harte et al., 1975; Menzies and Rama Murthy, 1980], providing direct evidence that the CBL has been impregnated by volatiles and highly differentiated liquids. The ubiquitous and diachronous emplacement of kimberlites in cratonic regions indicates that some of this flux of LIL-rich material may originate in the deep mantle and progressively modify the CBL after its advective thickening, but the isotopic compositions of diamond inclusions suggests that significant LIL enrichment occurred beneath South Africa in the interval between basalt depletion and diamond crystallization [Richardson et al., 1985]. In the context of the evolutionary model discussed above, the most likely site for the metasomatic alteration is the mantle wedge above the descending slab, the metasomatic agent being the fluids released from the slab itself. This leads to a scenario where

subduction drives the initial differentiation of the CBL as well as its subsequent LIL enrichment prior to advective thickening; continued LIL enrichment may then proceed, but presumably at a much lower rate.

Most gec hemical mass-balance calculations [e.g., Jacobsen and Wasserberg, 1979; ONions et al., 1979] have ignored the sub-crustal CBL of the continents as a geochemical reservoir for LIL constituents. If it is as important as the considerations given here and by Jordan [1978, 1981b] suggest, then any conclusions based on these mass-balance calculations must be viewed with some skepticism, particularly those regarding the volume of the mantle which has been differentiated to produce the continents.

Implications for mantle heat flow. Metasomatism of the CBL introduces heat-producing elements to the continental tectosphere that can contibute significantly to the surface heat flux. Because of the alteration by the host kimberlite, it is difficult to infer precisely the heat production directly from the xenolith data, but Jordan [1981b] estimated that the total contribution of the sub-crustal CBL could be as high as 0.15 mW/m^2, about half of the heat flux at the base of the crust. The inference that the heat production of the CBL is high can be made independently by requiring that the conductive geotherm of the continental TBL satisfy the low (1000-1200°C) temperatures in the 150-200 km depth range obtained by empirical geothermometry [Jordan, 1975a]. This conclusion is inconsistent with the thermal models derived by Sclater et al. [1980, 1981], who assumed that the heat production below the upper crust is negligible. (They were able to obtain overlapping bounds between oceanic and continental geotherms only because they made this assumption; if significant heat production is included below the upper crust, much thicker TBLs are required for old continents [Vitorello and Pollack, 1980].)

If the heat production of the continental CBL is as high as these arguments would suggest, then the heat flux at the base of the TBL beneath cratons is estimated to be on the order of 15 mW/m^3, less than half the oceanic value. The difference in sub-tectospheric continetal and oceanic heat flow must be maintained by a large-scale component of mantle circulation, presumably one involving the participation of the lower mantle.

Tectospheric structure and cratonic stability. It is clear from the seismological data presented in Section 2.d that there are large variations in the thicknesses of the continental TBL. According to the tectospheric model, these should be correlated with variations in CBL thickness. Probably the best single measure of these variations is τ_S, the verical travel time of shear waves through the

upper mantle. The data on τ_S given in Figures 2.5-2.7 clearly indicate that the tectosphere is thickest under those parts of the continents that have remained tectonically stable during the Phanerozoic (Regions S and P of Figure 2.1) and thinnest under the Phanerozoic mobil belts and orogenic zones. This correlation suggests strongly that cratonic stability is regulated by variations in the thickness of the continental tectosphere: repeatly active mobile belts and orogenic zones mark regions where a thick CBL never stabilized, whereas the Archean cratonic nuclei are those areas where a deep CBL was stabilized at an early date. This would explain why the present-day distinction between cratons and mobile belts has, in many cases, persisted since mid-Proterozoic time [Watson, 1976] and why continents tend to break apart where they have broken before. Moreover, it suggests that the fundamental transition from Katarchean (> 3000 My B.P.) permobility to Proterozoic linear (geosynclinal and mobil belt) tectonics [Windley, 1977] marks the time when the area occupied by a stable, advectively thickened CBL became significant.

3. Fate of the Subducted Slab

Aside from the plate motions themselves, the most visible manifestation of convection in the earth's mantle is the subduction of oceanic tectosphere beneath island arcs and active continental margins. Plate tectonics postulates that the surface area of the earth remains constant in time, so that the total area created by sea-floor spreading must equal the area destroyed by subduction. The total areal flux calculated from present-day plate motions amounts to 2.9 km^2/yr [Minster and Jordan, 1980]. Since the typical thickness of a mature plate is on the order of 100 km or so [Parsons and Sclater, 1977], the subduction process involves about 300 cubic kilometers of oceanic lithosphere every year, which is sufficient to cycle the entire mantle through the plate system once every 3000 My. Nearly all of the plate consumption is concentrated along the oceanic trenches ringing the Pacific Basin (Figure 3.1). Not surprisingly, it is the seismological study of these subduction zones which tells us most about the depth extent of plate-tectonic convection.

3.a. Earthquakes in subduction zones

Subduction zones are marked by the depth extent of their seismic activity, which includes most of the world's earthquakes. Seismologists traditionally classify an earthquake's hypocental depth h as shallow-focus ($h \leq 70$ km), intermediate-focus ($70 < h \leq 300$ km), or deep-focus ($h \geq 300$ km) [Gutenberg and Richter, 1954]. Although the historical record for some subduction zones shows only shallow seismicity (e.g., the Cascades and southern Chile), most are characterized by earthquakes with foci considerably deeper than 70 km. The first evidence for seismicity below the lithospheric shell came from observations of anomalously early core-refracted (*PKP*) arrivals at distant seismographic stations [Turner, 1922] and anomalously large differences between the travel times of the direct compressional (*P*) and shear (*S*) phases at nearby stations [Wadati, 1928]. The global distribution of 141 deep earthquakes was mapped by Turner [1930], revealing nearly all of the intermediate-focus and deep-focus seismic zones known today. As travel-time tables were extended to account for focal depth [Wadati and Masuda, 1933], and depth-sensitive phases, such as the near-focus surface reflections *pP* and *sP*, were recognized and incorporated into earthquake-location procedures, hypocenter determinations became sufficiently precise to resolve the seismicity into planar features dipping at steep, but variable, angles to depths as great as 700 km [Wadati, 1935; Gutenberg and Richter, 1938].

There was, of course, much speculation on the physical mechanism responsible for these

deep seismic zones. It was recognized that earthquakes of intermediate and deep focus generally have characteristics similar to shallow-focus earthquakes and could be explained by slip on faults [Leith and Sharpe, 1936], and there was an awareness that the driving forces responsible for this faulting might be those associated with convection currents and continental drift [Wadati, 1935; Leith and Sharpe, 1936; Holmes, 1965; Vening Meinesz, 1954]. Benioff [1949, 1954] and Honda and Masatsuka [1952] concluded that deep seismic zones mark huge fault planes along which oceanic upper mantle is being thrust under the island arcs and continental orogenic zones, but they did not appeal to convection as a mechanism.

It was not until three decades after they were first delineated that the Wadati-Benioff zones were explained as the loci of slabs of oceanic lithosphere subducting into the mantle [Oliver and Isacks, 1967; Isacks et al., 1968]. Most of the seismic energy released in subduction zones is by shallow-focus, reverse-faulting earthquakes on the interface between the converging plates, and the slip vectors of these events are consistent with the relative plate motions [McKenzie and Parker, 1967; Isacks et al., 1968]. However, detailed focal-mechanism studies demonstrated that the seismicity below about 70 km is not caused by slip on an interface between two major blocks, as postulated by Benioff and Honda, but represents fracturing within the cold, brittle core of the descending slab [Isacks et al., 1968; Isacks and Molnar, 1969]. From the point of view of mantle convection, deep seismicity thus marks the locus of the detached thermal boundary layer as it recycles into the mantle [Turcotte and Oxburgh, 1968]. The recognition of this fact was one of the final steps in the formulation of the plate-tectonic theory.

Since the establishment of modern global seismic networks in about 1960, it has been possible to locate routinely earthquakes having magnitudes larger than about five with a precision usually less than 20 km. These networks, in combination with local and regional stations, have been used to delineate the seismicity of descending slabs and to determine the focal mechanisms of many of the larger earthquakes in nearly all of the world's subduction zones. Among the numerous constraints on the subduction process established by these studies, two have tended to dominate discussions regarding the fate of the lithospheric slab: (1) seismicity abruptly terminates at depths of 650-700 km, and (2) deep slabs are deforming in response to compression oriented down the dip of the seismic zone.

World seismicity as a function of depth is plotted in Figure 3.2, taken from a recent compilation by Vassiliou et al. [1984]. The number of earthquakes above a given magnitude level decays exponentially to about 300 km, where there is a seismicity minimum, followed by a

resurgence in activity from 500 to 700 km [Leith and Sharpe, 1936; Sykes, 1966; Isacks et al., 1968]. No earthquake has been reliably located below about 700 km, and the statistical uncertainties of the hypocenters are consistent with a sharp cutoff a few tens of kilometers less than this depth [Stark and Frohlich, 1985].

Deep-focus seismic zones invariably involve old, cold oceanic lithosphere being subducted at relatively fast rates, whereas zones lacking deep-focus earthquakes are characterized by young, relatively hot lithosphere and/or lower rates. This suggests that the maximum depth of earthquakes corresponds to a critical temperature above which slab material is too hot and weak to support the stresses needed for brittle failure [Isacks et al., 1968; McKenzie, 1969; Griggs, 1972]. For a particular seismic zone, this depth then defines an "assimilation time" given by the ratio of the length of the zone to its subduction rate, which should correlate with the plate's "cooling time"; i.e., its crustal age prior to subduction. Such a correlation is in fact observed, the former being about one-tenth the latter [Molnar et al., 1979; Wortel, 1982; Shiono and Sugi, 1985].

The concept of a critical temperature does not provide a satisfactory explanation for the sharpness of the deep seismicity cutoff, however. The Mariana and Japan seismic zones, for example, both have deep-focus events and involve old slabs, but the ratios of their assimilation to cooling times differ by nearly a factor of two. Moreover, it offers no explanation for the seismicity minimum at 300-500 km and the resurgence of earthquake activity at greater depths, which is a feature of individual subduction zones as well as the worldwide average [Leith and Sharpe, 1936; Sykes, 1966; Richter, 1979; Vassiliou et al., 1984].

The global seismicity cutoff nearly coincides with a rapid increase in seismic wave velocities at an average depth of 650-670 km [King and Calcagnile, 1976; Given and Helmberger, 1980; Burdick, 1981; Walck, 1984a,b], and the two are thought to be causally related [e.g., Richter, 1979; Stark and Frohlich, 1985]. This 650-km (or 670-km) discontinuity is the deepest of two such high-gradient features in the mid-mantle transition zone [Niazi and Anderson, 1966; Johnson, 1967], both identified with phase changes in major silicate minerals, of which olivine is thought to be the most abundant [Ringwood, 1975; Weidner, 1985]. At approximately 650 km, olivine is expected to transform from its γ phase to a solid solution of magnesiowüstite and perovskite, involving the displacement of silicon cations from four-fold to six-fold coordination [Liu, 1976b; Bell et al., 1979; Ito and Yamada, 1982; Jeanloz, this volume]. A phase transition in the pyroxene-garnet component of the mantle to a perovskite structure occurs near the same depth and also involves a large (~10%) increase in density [Liu, 1976a; Yagi et al., 1979; Ito and Yamada,

1982].

The 650-km discontinuity has become the conventional demarcation between the upper and lower mantle. The basic question posed by its association with the seismicity cutoff is whether or not it presents a barrier to slab penetration. It could act as a barrier if it were a transition to a compositionally denser lower mantle, rather than (or in addition to) a simple phase change [Richter and Johnson, 1974; Liu, 1979; Jeanloz and Thompson, 1983], or if the phase transition at 650 km had a large, negative Clapyeron slope [Schubert et al., 1975; Christensen and Yuen, 1984] or marked a jump to a higher viscosity [McKenzie and Weiss, 1975]. Such a scenario is consistent with the model of stratified mantle convection preferred by many workers [e.g., McKenzie et al., 1974; DePaolo and Wasserburg, 1976; Jeanloz and Richter, 1979; O'Nions et al., 1979; Jacobsen and Wasserberg, 1979; Richter and McKenzie, 1981; Anderson, 1981; Lees et al., 1983; McKenzie, 1983; Giardini and Woodhouse, 1984].

The hypothesis that deep slabs encounter resistance to penetration below about 650 km is indicated both by the higher levels of energy release at the base of deep seismic zones and by the mechanisms of faulting observed during this energy release. In the far field at low frequencies, source mechanisms of deep earthquakes are characterized by a second-order moment tensor [Gilbert, 1971; Randall, 1971] whose principal axes are thought to be controlled by the deviatoric stress field associated with the rupture [Isacks and Molnar, 1969; Knopoff and Randall, 1970]. Although other mechanisms, including isotropic compression due to phase changes, have been postulated in the source processes of deep-focus events [Benioff, 1963; Knopoff and Randall, 1970; Gilbert and Dziewonski, 1975], most appear to conform to the simplest model of faulting, a dislocation described by a double couple [Honda and Masatsuka, 1952; Honda, 1962], or for some of the larger deep-focus multiple events, a series of such dislocations distributed in space and time [Sasatani, 1980].

In an important pair of papers, Isacks and Molnar [1969, 1971] obtained first-motion, double-couple solutions for a number of intermediate-focus and deep-focus earthquakes in subduction zones and noted several systematic features in the orientations of their principal axes:

(1) For a particular continuous piece of slab, either the compressional axes or tensional axes tend to cluster in the down-dip direction.
(2) Within the intermediate-focus zone, slabs are in a state of
    (a) down-dip tension if there are no deep-focus earthquakes,

(b) down-dip tension if there is an aseismic gap between the intermediate- and deep-focus zones, and

(c) down-dip compression if the seismicity is continuous into the deep-focus zone.

(3) Within the deep-focus zone, descending slabs are in a state of down-dip compression.

Generalization (1) motivates the hypothesis that the earthquakes are located in the cold thermal core of the slab and controlled by the dynamics of its flow into the mantle. Generalization (2a) is consistent with the idea that shallow slabs sink under their own weight into a relatively low-viscosity asthenosphere, whereas (2c) and (3) suggest that slab penetration is resisted by a higher viscosity mesosphere at the base of the seismic zone. (2b) then implies that an aseismic gap is indicative of a gap in the slab itself, or at least in its ability to transmit down-dip deviatoric stress.

Vassiliou [1984] has studied the statistics of a large number of focal mechanisms of intermediate- and deep-focus events and confirms generalizations (1) and (3), but shows that, although most intermediate-focus earthquakes in the highly active Tonga seismic zone are in a state of down-dip compression, intermediate-focus events in all other slabs are more consistent with down-dip extension, regardless of the depth to the seismicity cutoff or the existence of an aseismic gap. Therefore, conclusion (2c) does not generally apply.

Isacks and Molnar's original interpretation in terms of an earth mechanically layered into a lithosphere, asthenosphere and mesosphere [Daly, 1940] is now outmoded, since the arguments for a high-viscosity lower mantle [e.g., McKenzie, 1966] or at least an inpenetrable boundary layer immediately below the 650-km discontinuity [McKenzie and Weiss, 1975] appear to be incorrect [Cathles, 1975; Peltier, 1976, 1980; Sammis et al., 1977]. Nevertheless, their observations continue to have a major impact on the dynamical modeling of slab penetration. In discussing the generalizations given above, for example, McKenzie and Richter [1976, pp.73-74] conclude, "The simplest explanation for this behavior is that the slab meets great resistance to its motion at 600 kilometers and is unable to penetrate below 700 kilometers...the convective circulation of which the plates are a part is confined to a region 700 km deep."

That deep-focus zones are in down-dip compression has been confirmed by many subsequent studies [e.g., Richter, 1979], including recent moment-tensor inversions using extensive digital data bases [Giardini, 1984; Vassiliou, 1984]. The idea that penetration into the

lower mantle is resisted at 650 km has also been corroborated by detailed investigations of the Tonga deep-focus zone, the world's most seismically active. The slab in this region appears to be highly contorted [Sykes, 1966], and it is cut by planes of deformation delineated by the distribution of precisely located hypocenters, as well as the focal mechanisms of specific earthquakes [Billington and Isacks, 1975; Billington, 1980; Giardini and Woodhouse, 1984, 1986]. Hypocenters cluster along one or both of the nodal planes suggesting that, like shallow-focus earthquakes, the intermediate- and deep-focus events represent slip on a plane. Giardini and Woodhouse [1984] conclude that, "Both the moment tensor solutions and the seismicity patterns indicate thickening and bottoming out of the descending material, and suggest that subduction experiences great resistance in penetrating the 670-km discontinuity... We observe horizontal displacements of the seismically active portion of the slab, and infer that material moves laterally rather than vertically at the base of the deep seismic zone. This favours the view that subduction does not continue into the lower mantle, although we clearly cannot infer the fate of subducted material after it ceases to be seismically active."

3.b. Thermal structure of subduction zones

A key piece of evidence for the continuity of the subducted slab was the observation by Oliver and Isacks [1967] that high-frequency compressional and shear waves propagating up the Wadati-Benioff zone in the Tonga-Kermadec island arc do so without much energy loss, whereas those propagating in the mantle wedge above the zone are severely attenuated. This effect can be quantified in terms of the seismic quality factor Q, which is proportional to the ratio of the potential energy stored in a wave cycle to that irreversibly lost by internal friction. They obtained path-averaged Q values for the slab that were several times those for the wedge, a fact explained by the relatively cold temperature of the subducted lithosphere. They also demonstrated that the travel times along ray paths through the seismic zone are significantly less than those through the ambient mantle, again as expected for a cold slab. Similar observations had been published for the Japan seismic zone by Japanese seismologists using their own local networks [see review by Utsu, 1971]. These and many other studies of upward propagating waves [Mitronovas and Isacks, 1971; Suyehiro and Sacks, 1979; Hubert and Frohlich, 1981] and downward propagating waves [Davies and McKenzie, 1969; Jacob, 1972; Sleep, 1973] have established that lithospheric slabs above deep-focus zones have seismic velocities averaging 5-10% higher than the surrounding mantle. This velocity contrast implies a temperature differential on the order of 1000°K.

The temperature structure of the oceanic lithosphere as a function of its age is reasonably well

described by simple thermal-boundary-layer models [Parsons and Sclater, 1977]. Since the age of the plate can be determined directly from its magnetic signature seaward of the trench, the temperatures in the subducting plate are known near the surface. By combining this initial condition with the subduction velocity and the geometry of the seismic zone, one can calculate the thermal history of the descending slab, subject to certain assumptions regarding thermodynamic parameters and heat production of the slab and the kinematics of flow in the vicinity of the slab [Hasebe et al., 1970; Minear and Toksöz, 1970; Andrews and Sleep, 1974]. Simple plate models indicate that large temperature contrasts between the slab and ambient mantle should exist at depths of 700 km [McKenzie, 1969; Griggs, 1972]; lithosphere which has cooled down for 100 My cannot thermally re-equilibrate with the hot mantle in the 10 My or so it takes to reach the base of the seismic zone. This conclusion is unmodified by adding the effects of radioactive heating [Toksöz et al., 1973] and phase changes [Schubert et al., 1975]. The importance of shear-strain heating has been more controversial. By assuming strain heating to be very large, Minear and Toksöz [1970] and Toksöz et al. [1971] were able to construct slab models that thermally equilibrated at depths on the order of 700 km. However, the high levels of strain heating used in their calculations do not appear to be physically reasonable, either on the basis of rheology [Turcotte and Schubert, 1973; Andrews and Sleep, 1974; Bird, 1978] or energy balance [Griggs, 1972; Creager, 1984].

Thermal models of descending slabs have proven to be successful in predicting the variation of seismic wave velocities between the slab interior and the ambient mantle. For this purpose, the relationship between lateral velocity anomaly and lateral temperature anomaly is usually linearized and some value of the effective thermal coefficient of velocity, $\partial v_p/\partial T$, is specified. By calibrating the velocity structure of the slab using travel times from the nuclear explosion LONGSHOT, Sleep [1973] obtained an empirical value for this coefficient of –0.9 m/s/°K. A 1000°K thermal anomaly at a depth of a few hundred kilometers thus yields a velocity contrast of about 10%, which is roughly consistent with the observations. (As discussed below, more recent estimates suggest Sleep's value is about 50% too high.) Three-dimensional wave-speed models constructed in this manner have been used to study the perturbing effect of slab structures on *P*-wave travel times [Toksöz et al., 1971; Sleep, 1973; Creager and Jordan, 1984, 1986a], *P*-wave amplitudes [Sleep, 1973], fault-plane solutions from *P*-wave first motions [Engdahl et al., 1977], and earthquake locations [Engdahl et al., 1977; Fujita et al., 1981]. The velocity gradients in these models are sufficiently high that the ray-bending effects are large [Toksöz et al., 1971] and an accurate computation of travel times requires the use of three-dimensional ray tracing algorithms, such as those discussed by Julian and Gubbins [1977].

3.c. Additional arguments against aseismic extensions of slabs

If the slab penetrates the mantle as a simple detached thermal boundary layer, unimpeded and without disruption, then the thermal-history calculations show that the large thermal contrasts of old lithosphere subducted at typical plate speeds (50-100 km/My) will persist to great depths. These thermal anomalies should be marked by zones of high seismic velocities along aseismic extensions of the slabs below the deepest earthquakes.

To image a velocity anomaly beneath a seismic source requires the use of teleseismic body phases, downward propagating waves which travel to great distances from the epicenter. A basic diagram employed for this purpose is the *residual sphere*, defined by Davies and McKenzie [1969] to be the graph of travel-time residuals on the unit focal sphere: the difference between the observed travel time and the time computed from a standard, spherically symmetric earth model is plotted at the take-off angle and azimuth of the ray path as it leaves the source. These authors made *P*-wave residual-sphere diagrams for shallow-focus events in subduction zones to display the teleseismic signature of high-velocity lithospheric slabs. Mitronovas and Isacks [1971] looked for a systematic variation in teleseismic *P*-wave residuals as a function of azimuth for deep-focus Tonga events; they found no evidence for an aseismic extension of the slab but suggested that the best way to answer this question would be to analyze the residual spheres of deep-focus earthquakes. A number of subsequent searches for evidence of deep penetration using residual-sphere techniques were negative, as indicated by the following quotations:

> "For deep-focus earthquakes, events 8-12 (in Tonga), no clear pattern of travel-time anomalies is evident. The residuals for events 8 and 10 suggest that the seismic zone has a slightly higher velocity than the surrounding mantle, but until more data are available, this conclusion must remain tentative." [Toksöz et al., 1971, p. 1131]

> "We applied the method of Davies and McKenzie [1969] to the Tonga region with a more extensive data set than that used by Toksöz et al. [1971], but, like them, we were unable to find convincing evidence for anomalies associated with the slab below 300 km. The errors in reported travel-time data plus incomplete coverage of the focal sphere combine to make the method of Davies and McKenzie too crude a technique for the definition of slab anomalies as a function of depth in most regions." [Sondergeld et al., 1977, p. 537]

"Plots of travel-time residuals on the focal sphere (of earthquakes in nearly every subduction zone) failed to reveal characteristically large negative residuals which are taken as evidence of source anomalies for shallow earthquakes at island arcs [see, e.g., Toksöz et al., 1971]. Thus, source anomalies, if present at all in deep-focus travel-time data, can safely be ignored." [Sengupta and Julian, 1978 p. 192]

Not only did the application of the Davies-McKenzie technique to large sets of teleseismic *P*-wave travel times by several groups of investigators fail to reveal aseismic extensions of slabs, it did not confirm the large temperature contrasts in deep-focus zones predicted by the thermal history calculations.

These negative results might be explained by either of two effects. First, the thermal equilibration time of the slab, and thus the velocity contrast of deep slab material, could be significantly overestimated by simple subduction models. One mechanism for decreasing the equilibration time is chemically induced instability in the upper mantle (Figure 3.3a). There are significant density variations within the slab associated with the compositional stratification of the oceanic lithosphere: a harzburgitic residuum of basaltic differentiation presumably occupies a layer ~30 km thick subjacent to the oceanic crust, which will have a normative density 1-2% less than undepleted mantle [Green and Liebermann, 1976; Oxburgh and Parmentier, 1977; Jordan, 1979a]. Oxburgh and Parmentier [1977] have discussed the possibility that this low-density layer might detach itself from the slab and rise diapirically through the upper mantle. If so, the cold thermal core of the slab would be advectively disrupted.

A second possibility is that the velocity contrast of deep slab material is as large as the thermal calculations predict, but that the lateral velocity gradients are reduced by the horizontal flow of slab material away from the seismically active regions. One scenario for the fate of the slab consistent with this possibility is Ringwood's [1982] "megalith" hypothesis, illustrated in Figure 3.3b, where the buckling of former oceanic crust and the harzburgite component of the subducted oceanic lithosphere forms a large melange at the 650-km discontinuity. The seismic velocity gradients in the deep-focus zones would also be decreased, of course, if the slab were simply entrained in an upper-mantle convection system bounded by a phase change, a viscosity increase, and/or a compositional discontinuity at 650 km (Figure 3.3c) As discussed previously, this hypothesis is consistent with the deformation of the slab inferred from the focal mechanisms of most deep-focus earthquakes [Isacks and Molnar, 1971] and, in Tonga at least, the distribution of seismicity [Giardini and Woodhouse, 1984].

3.d. Evidence for aseismic extensions

It now appears that near-source anomalies associated with deep slab structure do indeed exist, but the residual-sphere methodology employed in the studies quoted above was inadequate to resolve them. Evidence for deep-seated, high-velocity anomalies in the vicinity of subduction zones began to accumulate about ten years ago. Jordan and Lynn [1974] used the arrival-time differences between core-reflected and direct seismic phases -- *PcP-P* and *ScS-S* differential travel times -- to map a localized, high-velocity anomaly in the lower mantle beneath the Caribbean. They associated this feature with a convective downwelling marked by the Middle America Trench. On the basis of these results, as well as some observations by Weichert [1972] and Engdahl [1975], Jordan [1975b] argued for deep-mantle circulation of subducted material. The existence of the Caribbean anomaly has been corroborated by Lay [1983] and more recently in a tomographic analysis of multiple-*S* times by Grand [1986]. Fitch [1975, 1977] applied a multiple-event technique to the analysis of travel times from earthquakes beneath Peru, Tonga and the New Hebrides, and showed that the *in situ* velocity contrasts at the levels of the deepest events are not much diminished from the 5-10% range inferred for shallower depths, thereby confirming the predictions of the thermal-history calculations. Frohlich and Barazangi [1980] examined the travel times of core-reflected phases from deep-focus Tonga events and concluded they were consistent with high-velocity anomalies beneath the sources.

The first definitive study directly imaging slab penetration into the lower mantle was Jordan's [1977] residual-sphere analysis of the 29 Jan 1971 deep-focus earthquake beneath the Sea of Okhotsk (h = 540 km). The clean waveforms from this event and the good station distribution afforded by its location in the Kuril-Kamchatka seismic zone yielded the spectacular signature of a high-velocity, slab-like feature extending to a depth of about 1000 km with a strike and dip consistent with the geometry of the seismic zone (Figure 3.4, bottom panel). Several aspects of Jordan's analysis differed from previous residual-sphere studies. Rather than using *P*-wave travel times from standard bulletins, he hand-picked the travel times of *S* and *ScS* phases directly from the seismograms. Because these shear waves propagate slower than compressional waves, their travel-time perturbations owing to mantle heterogeneities are a factor of 3-4 larger, and the signal-to-noise ratio (SNR) is correspondingly higher. The amplitude of the slab anomaly shown in the lower diagrams of Figure 3.4 has a peak-to-peak amplitude of about eight seconds, much larger than any timing uncertainties. The global network of seismic stations gave an azimuthal distribution superior to that available for the more active deep-focus zone in Tonga. By

incorporating the travel times of the core-reflected *ScS* phase, he was able to improve the residual-sphere coverage at small take-off-angles, allowing excellent sampling of the quadrapolar anomaly pattern diagnostic of a steeply dipping, aseismic slab. To increase the SNR of this anomaly pattern, he performed two operations on the raw residuals not made in previous residual-sphere studies: the travel times were first corrected for known large-scale heterogeneities, in particular the upper-mantle variations beneath the recording stations described by "station anomalies." (A station anomaly is the mean travel-time residual observed for many events at a given station relative to a network average.) The residuals were then smoothed by a filter specifically formulated to enhance low-wavenumber signals discretely sampled on the unit focal sphere, thereby averaging over random reading errors and higher wavenumber inhomogeneities far from the source region.

For the high-quality *S*-wave data obtained by Jordan [1977], smoothing was hardly necessary, since the slab signature completely dominates the unfiltered residuals (Figure 3.4, bottom left). Unfortunately, reading such travel times from analog seismograms is tedious, and his work was limited to a single event. *P*-wave travel times, on the other hand, are readily available for all teleseismically observed earthquakes, since they are compiled by agencies such as the International Seismological Centre (ISC) to locate hypocenters. Timing and reading errors lower the SNR of these data significantly, and the combination of these errors with the poor coverage obtainable in many subduction zones such as Tonga proved to be a major source of frustration in early attempts to identify deep slabs by residual-sphere methods, as is clear from the comments quoted above.

However, in a follow-up study of the 29 Jan 1971 Okhotsk event and other deep-focus earthquakes in the Kuril-Kamchatka seismic zone, Means and Jordan [1980] were able to derive *P*-wave residual spheres from ISC data which had clear signatures of a deep slab (Figure 3.4, top left). Encouraged by these results, we have developed more sophisticated algorithms for processing ISC *P* times to obtain residual-sphere images of near-source heterogeneity [Creager and Jordan, 1984, 1986a]. The application of these new techniques to deep-focus earthquakes in the Kuril-Kamchatka, Japan, Izu-Bonin and Mariana seismic zones has revealed aseismic extensions of subducted slabs along the entire northwest margin of the Pacific plate.

Travel-time residuals with respect to a spherically symmetric earth model are produced not only by near-source structure, but by heterogeneities integrated along the entire ray path, as well as by random observational errors and mislocation of the hypocenter. We can take advantage of

recent work on aspherical earth structure to correct for the inhomogeneities away from the source that most corrupt the slab's residual-sphere signature. Our procedures adjust the travel times for hydrostatic ellipticity, near-receiver structure as expressed in station anomalies [Dziewonski and Anderson, 1983], and large-scale lower-mantle heterogeneity derived from global inversions of *P* times [Dziewonski, 1984]. Of course, smaller scale heterogeneities not associated with the slab and not predicted by current aspherical earth models do indeed exist, but their spectrum on the residual sphere is shifted to higher wavenumbers relative to near-source heterogeneities of equal spatial scale. To damp out these high-wavenumber components, we follow Jordan's [1977] approach of low-pass filtering the residual sphere. As illustrated in Figure 5 (top), this operation considerably enhances the SNR of near-source structure relative to unmodeled inhomogeneities and random observational errors.

Travel-time residuals are computed with respect to some assumed location of the source, usually one calculated using a radial velocity model and thus biased in some unknown way by the aspherical structure of the earth. Our algorithm adjusts the hypocenter and origin time of each earthquake to fit the corrected residuals in a least-squares sense, which is equivalent to orthogonalizing the residual-sphere anomaly pattern with respect to its degree-zero and degree-one spherical harmonics [Davies and McKenzie, 1969; Creager and Jordan, 1984]. This procedure, like any projection, introduces additional bias but has the advantage that the net mislocation effect can then be precisely specified by a known linear operator.

Because of the mislocation effects, as well as the considerable distortion of the residual sphere by ray-path bending in the vicinity of the focus [Toksöz et al., 1971], the interpretation of the residual-sphere data is greatly facilitated by the comparison of the observed patterns with theoretical graphs generated from three-dimensional models of near-source heterogeneity. We obtain the latter from simple thermal models of the descending slab. Using the techniques developed by Toksöz et al. [1973] and Sleep [1973], the two-dimensional temperature field of the slab is computed assuming an initial, pre-subduction thermal profile and a kinematically prescribed velocity field, which includes entrained mantle flow in the vicinity of the slab and induced corner flow beneath the back-arc basin. A three-dimensional velocity model is constructed by assuming the lateral velocity contrasts are proportional to the thermal contrasts [Sleep, 1973] and rotating the resulting structure about an arc pole [Engdahl et al., 1977]. Theoretical residual spheres are computed by tracing rays through the three-dimensional velocity model for the same station set sampled by the actual data. We can then account for the mislocation bias by projecting the theoretical residual spheres with respect to the location parameters using the identical operator

applied to the data. The bias caused by smoothing the observed residuals is taken into account by applying the same low-pass filter to the theoretical residuals.

Examples of the results obtained by Creager and Jordan [1986a] for a representative set of intermediate-focus and deep-focus events in the Northwest Pacific are presented in Figures 3.5 and 3.6. In every case, the data are well fit by simple models of the descending slab having very few free parameters. The strike, dip and radius of curvature of the slab above the seismicity cutoff are constrained to within 5°-10° by the distribution of well-located hypocenters (some of which are projected onto the model cross-sections in Figure 3.7), and these are consistent with the slab geometry inferred directly from the residual-sphere anomalies of intermediate-focus events.

With the exception of Japan, the strikes and dips of the aseismic extensions obtained from the residual-sphere patterns of deep-focus events are in similar agreement with those extrapolated from the deep-focus seismicity. The simplest geometry is in the Marainas, where the seismically active part of the slab below 200 km and its aseismic extension below 650 km are nearly vertical, yielding very consistent quadrapolar anomaly patterns (Figure 3.5). The amplitude of the residual-sphere anomaly decays by about a factor of two between the shallowest and deepest events shown in Figure 3.5, but this decay is due almost entirely to the increase in ambient seismic velocities through the mantle transition zone, and not to any substantial decay of the velocity contrasts--and thus thermal contrasts--within the slab [Creager and Jordan, 1986a]. (From 200 to 700 km, the compressional-velocity contrast between the cold thermal core of the slab and the ambient mantle is reduced in the model from 0.49 km/s to 0.43 km/s, only 15%. By Fermat's Principle, the travel-time perturbations are approximately proportional to this contrast divided by the squared inverse of the ambient velocity. The latter varies by a factor of two over this depth interval.)

In Kuril-Kamchatka, the geometry is complicated by considerable variations in the dip of the seismic zone, both along strike and with depth. The residual-sphere anomaly patterns from the intermediate-focus earthquakes are very different from the deep-focus ones, implying a slab dip of about 20° less [Jordan, 1977; Creager and Jordan, 1984]. This change of dip or "kink" occurs rather abruptly at about 500 km along the entire length of the slab, and in the northern part of the zone, it is evident in both the seismicity of the region and the orientation of the compressive axes of focal mechanisms [Veith, 1974; Strelitz, 1975; Sasatani, 1976].

The residual-sphere data for Japan require a similar change in dip at about the same depth,

varying from about 30° or less in the seismic zone shallower than 500 km to greater than 50° below the seismicity cutoff near 600 km [Creager and Jordan, 1986a]. Unlike in Kuril-Kamchatka, the cutoff is too shallow to permit adequate resolution by the seismicity alone, and there is no evidence for it at all in the focal mechanisms, which have compressive axes dipping parallel to the shallower seismicity [Yoshii, 1983; Giardini, 1984]. Although the dynamical significance of these kinks is not yet understood, it appears that the flow of material in the Northwest Pacific subduction zones tends to steepen with depth, becoming nearly vertical at the base of the upper mantle.

The velocity anomaly is scaled to the thermal anomaly by an effective thermal coefficient of velocity, $\partial v_p/\partial T$. We have calibrated this parameter using the anomaly amplitudes observed for the intermediate-focus events, which are not sensitive to the slab extent below the seismic zone [Creager and Jordan, 1986a]. The calibration procedure yields $-0.4 \le \partial v_p/\partial T \le -0.6$ m/s/°K for the models shown in Figure 3.7. In these models, the effects of phases changes on the velocity structure of the slab are not included; incorporating them reduces $\partial v_p/\partial T$ by 10-20%, yielding an average value of about –0.4 m/s/°K [Creager and Jordan, 1986a]. Though somewhat lower than the estimate of –0.9 m/s/°K obtained by Sleep [1973] for the Aleutian slab (which would be reduced if this slab extends beyond the seismicity cutoff, as indicated by Spencer and Engdahl [1983]), our empirical thermal coefficients are consistent with recent laboratory measurements of $\partial v_p/\partial T$ on mantle minerals at high temperatures [Sumino et al., 1977, 1983; Sumino, 1979; Suzuki et al., 1983], as well as the value inferred from seismic and geoid modeling of large-scale lower-mantle structure [Hager et al., 1985]. This consistency lends credibility to the modeling assumptions. We note that it implies that $\partial v_p/\partial T$ does not vary substantially between the upper and lower mantle.

With the geometry and velocity contrast of the slab specified by the seismicity and by the travel times from intermediate-focus earthquakes, the extent of the slab is constrained by the times from the deepest events. All of the slab structures displayed in Figure 3.7 are characterized by penetration depths of about 1400 km--twice as deep as any earthquake--and from the good fits these models provide to the data in Figures 3.5 and 3.6 (as well as a number of other deep-focus events not shown here), it can be concluded that penetration depths of this order are certainly consistent with the *P*-wave travel times. To explore more rigorously the constraints the data place on the extent of the slab, the dependence of the residuals on slab length must be considered in detail. If the extent below the hypocenter is small, the amplitude of the residual-sphere anomaly is approximately proportional to this length. If it is large, however, the ray paths will turn out of the slab before they reach its terminus, and arbitrarily increasing the length of the slab will not affect

the residual pattern. This phenomenon is referred to as "saturation" of the residual sphere, and the minimum level at which saturation is achieved, as measured by variance reduction, is termed the "saturation depth" [Creager and Jordan, 1986a]. Obviously, the saturation depth is a *lower bound* to the actual penetration depth of the slab.

Every deep-focus earthquake we have examined in our work thus far appears to be saturated with respect to slab length [Creager and Jordan, 1986a]. For the Marianas and Izu-Bonin, the estimate of the saturation depth is about 1000 km. The saturation depth increases to 1200 km or so for Kuril-Kamchatka, where deeper sources are available and the sharp velocity gradients associated with the upper slab interface are better sampled by the global network. Japan yields an intermediate value of about 1100 km. In the context of our modeling assumptions, slab penetration to at least these depths is needed to obtain fits as good as those shown in Figures 3.6 and 3.7; slab penetration to arbitrarily greater depths is consistent with the data, although not required.

The lower bound of 1000-1200 km on the penetration depths of Northwest Pacific slabs inferred from the residual-sphere data appears to be robust with respect to plausible, unmodeled complications in the near-source velocity structure. A number of these, including the effects of anisotropy, phase changes and variations in slab width, have been considered in detail by Creager and Jordan [1986a]. The models shown in Figure 3.7 do not include the localized velocity anomalies associated with the major phase transitions near 400 and 650 km depth, for example, but incorporating them explicitly into the velocity structure only increases the lower bounds on penetration depths. Furthermore, because of ray-bending effects, the anomaly patterns are surprisingly insensitive to slab width, and the residuals for the deep-focus events cannot be explained by shorter but wider slab structures.

3.e. Slab pentration into the lower mantle

The penetration of simple, detached thermal boundary layers to depths greater than 1000 km can explain the near-source travel-time anomalies from deep-focus earthquakes in the Northwest Pacific, but given the substantial implications this hypothesis has for models of mantle convection, it is important to inquire whether alternate interpretations are possible. Specifically, are our results compatible with the stratification of the earth's solid shell into an upper-mantle and a lower-mantle convection system having little or no mass flux across the 650-km discontinuity?

The spatial relationships between upwelling and downwelling plumes in a two-layer

convecting system will involve both the temperature contrasts and stresses across the interface separating the layers, as well as its dynamic topography. In situations where the stress coupling dominates the interaction, downwelling plumes in the upper layer will be associated with divergent flows on both sides of the boundary and, hence, upwelling plumes in the lower [McKenzie and Richter, 1981]. This is the relationship usually envisaged in cartoons of two-layer mantle convection ; e.g., Figure 1.1. To the extent that we can expect upwellings in the lower mantle to have lower than average seismic velocities, the convective patterns implied by this relationship are clearly inconsistent with the residual-sphere data, which show high seismic velocities directly beneath the seismic zones. If, however, the flow in the vicinity of the interface is dominated by the temperature contrasts, say because the two systems are mechanically decoupled by a low-viscosity boundary layer, then regions along the interface cooled by downwelling within the upper layer might be the sites of downwelling in the lower layer as well. Models with these features have been the subject of a recent numerical study by Daly and Parsons [1984], who find that alignment can be accomplished in two dimensions, providing the viscosity across the boundary increases by a factor of 10-1000. Slab-like features beneath the deep-focus zones imaged by our techniques may not be themselves lithosphere penetrating from above, but represent downwellings in a separate, lower-mantle convection system induced by the existence of cold slabs in the upper mantle.

A full test of this alternative will no doubt require three-dimensional calculations of stratified convection in a mantle with a realistic temperature structure and rheology, a formidable task. We can argue, however, that the rigorous constraints placed on such a model by the residual-sphere data tend to decrease its plausibility [Creager and Jordan, 1984, 1986a]:

(1) The P-velocity contrasts observed in the lower-mantle extensions of slabs have the same magnitude as their upper-mantle contrasts, and $\partial v_p / \partial T$ is observed to be a weak function of depth; the temperature contrasts in the lower mantle must therefore be nearly the same as in the upper mantle--i.e, on the order of 900°K. The thermal boundary layer at the top of the lower mantle in a two layer convecting system is expected to have a contrast of only about 300°K [Jeanloz and Richter, 1979], which is insufficient to explain the high-velocity zones beneath the deep-focus earthquakes.

(2) The seismic data establish severe constraints on the geometry of the lower-mantle flow. In particular, the slab-like features below 650 km lie along the direct extrapolations of the upper-mantle slabs, matching both their strike and dip. Across the 650-km boundary, the strikes cannot differ by more than about 10°, and the features cannot be laterally offset normal to their

strike by as much as, say, 100 km without destroying the fits to the residual-sphere data shown in Figures 3.5 and 3.6. Moreover, their along-strike extents appear to be very similar. For example, the residual-sphere patterns for deep events in the northern parts of the Japan and Kuril-Kamchatka seismic zones show asymmetries well modeled by the along-strike terminations predicted by the subduction geometry. Therefore, the lower-mantle flow pattern must match a non-steady upper-mantle flow pattern very precisely in both geographical coordinates over a region with a highly contorted slab geometry (where strikes vary by 70°).

(3) Even supposing that a tightly coupled system with sufficient temperature contrasts could be constructed, the thermal gradients in the vicinity of the 650-km interface would be distorted by the horizontal flow of material both above and below it. A substantial decrease in the horizontal temperature gradient normal to the slab strike might be expected throughout a region whose vertical extent equals the combined thicknesses of the thermal boundary layers; say, 100 km or more. The travel-time data from deep-focus events are very sensitive to the lateral gradients in this depth interval, and they show no evidence of this distortion, nor does the seismicity. Indeed, the upper surface of what appears to be a continuous slab is well defined by the sharp transition from positive to negative residuals observed for many of the deep earthquakes (Figure 3.6).

The other seismological evidence pertaining to the subduction zones of the Northwest Pacific is consistent with deep penetration. As elsewhere, the focal mechanisms of deep-focus earthquakes in this region imply down-dip compression of the slab [Katsumata and Sykes, 1969; Isacks and Molnar, 1971; Stauder and Maulchin, 1976; Yoshii, 1983], indicative of some resistance to penetration. The kinematical implications of this dynamical statement are not straightforward, however. A number of authors have shown that a relatively small increase in the viscosity at 650 km, an order of magnitude or so, is sufficient to engender down-dip compression in the deep-focus zone [O'Connell, 1977; Richter, 1979; Vassiliou et al., 1984]. On the basis of their extensive calculations, Vassiliou et al. [1984] conclude that "whether the 670 km barrier is a chemical discontinuity or a viscosity jump is not resolvable by the seismicity data alone. The stress patterns--both orientation and magnitude--are explainable, to first order, with either a chemical discontinuity or a viscosity contrast."

Down-dip compression of the slab in the 300-700 km depth range may also be caused by the forces associated with the elevation or depression of upper-mantle phase boundaries within the slab. A phase transition with a Clapeyron slope γ will be displaced from its unperturbed radius by a distance $\delta r = \gamma \delta T/(dP/dr)$, where δT is the temperature anomaly of the cold slab and dP/dr is the

ambient pressure gradient; the displacement is positive (up) for an exothermic transition (positive γ), and negative (down) for an endothermic transition (negative γ). The Clapeyron slopes for the transformations associated with the two major seismic discontinuities, determined by laboratory experiments at the appropriate temperatures and pressures, are γ_{400} = 3.5 MPa/°K [Suito, 1977] and γ_{650} = −2 MPa/°K [Ito and Yamada, 1982]. The value of γ_{650} is the more uncertain, but Ito and Yamada's recent experimental work confirms earlier estimates [Ahrens and Syono, 1967; Bassett and Ming, 1972] and theoretical arguments [Navrotsky, 1980] that the transition is endothermic. The corresponding deflections of the phase boundaries are +0.10 km (up) and −0.05 km (down) per degree of thermal anomaly, respectively. From the thermal models of the Northwest Pacific slabs derived to match the residual-sphere data, we infer that the regions of anomalous phase should extend on the order of 100 km above the 400-km discontinuity and 50 km below the 650-km discontinuity, if the transitions occur at their equilibrium positions. These perturbed phase boundaries very nicely bracket the region of anomalously intense deep-focus seismicity observed over the interval 300-700 km (Figure 3.2), and both will act to compress the slab between these depths.

The potential influence of phase transitions on slab stresses in the mid-mantle transition zone was recognized by Isacks and Molnar [1971] in their original discussion of focal-mechanism systematics, and calculations of the forces involved have been made by Turcotte and Schubert [1971] and Schubert et al. [1975]. The large uncertainty in the nature and Clapyeron slope of the 650-km transition [Jackson et al., 1974; Anderson, 1976; Jeanloz and Thompson, 1983] and the possibility that the 400-km transition may be displaced downward from its equilibrium position in the slab by kinetic effects [Sung and Burns, 1976a,b; Sung, 1979; Poirier, 1981] prevent any definitive assessment of this mechanism, but the rather large negative value of γ_{650} implied by Ito and Yamada's [1982] experiments makes more plausible the hypothesis that the forces related to the phase transitions control both the seismicity levels and stress orientations of deep-focus earthquakes, at least in the relatively simple deep seismic zones of the Northwest Pacific.

The fate of the Tonga slab is more controversial. It is the most seismically active slab, accounting for half of the deep-focus earthquakes reported in the ISC catalogue, and is highly contorted relative to the seismic zones of the Northwest Pacific. Giardini and Woodhouse [1984] interpreted the seismicity and focal mechanisms as evidence against penetration. When examined in detail, however, these data imply the existence of shear on nearly horizontal planes, with material deep in the slab moving southward relative to shallower material. As pointed out by Giardini and Woodhouse [1986], Tonga-Kermadec is the only major subduction zone where both the

subducting and overriding plates have a significant (~ 50 km/My) along-strike component of velocity in the hotspot reference frame [Minster and Jordan, 1980, Figure 5]. That is, the slab beneath Tonga is apparently being dragged northward through the mantle, so that its deformation may be controlled, at least in part, by this along-strike motion.

S-wave travel-time observations of Frohlich and Barazangi [1980] and our own analysis of *P*-wave residual spheres [Fischer et al., 1986] are consistent with an aseismic, high-velocity zone beneath the deep-focus Tonga earthquakes. The poor distribution of seismic stations relative to these events limits the resolution of slab geometry, but Fischer et al. [1986] have shown that the observed ISC *P* times are well modeled by thermal slab models consistent with the seismicity. Using the thermal coefficient of velocity obtained for northwest Pacific slabs, they obtain saturation depths on the order of 1000 km, which they interpret as a lower bound on the depth of slab penetration beneath Tonga.

There are other regions where the distribution of seismicity suggests the horizontal motion of slabs near 650 km. The seismic zone has a sigmoidal curvature in the northern part of the Izu-Bonin Arc and beneath the Banda Sea [Isacks and Molnar, 1971; Cardwell and Isacks, 1978]. The most extreme case is the deep-focus zone beneath the Fiji Plateau, which when projected normal to the New Hebrides Arc appears as a long, flat slab resting on the 650-km discontinuity [Isacks and Molnar, 1971; Pascal et al., 1973]. This seismicity appears to comprise two separate episodes of subduction, however, the southernmost events being associated with the current subduction in the New Hebrides Arc and the northern set with the now defunct Vitiaz Trench [Chase, 1971; Pascal et al., 1978]. When the northern set is projected on a plane normal to the Vitiaz Trench, the argument for horizontal motion of the slab at 650 km becomes less clear. In general, regions of upward curvature to the deep seismic zone occur where there are significant along-strike changes in the slab geometry; e.g., in the transition from shallow, westward-directed subduction beneath Japan to steep, southwestward-directed subduction beneath Izu-Bonin, or in the tight curvature of the Banda Sea. Given these complications and the resistance to subduction through 650 km implied by the endothermic nature of the phase transitions at this level, the association of these features with a general inability of slabs to penetrate through 650 km seems tenuous.

Indeed, the overall geometry of subduction obtained from vertical cross-sections through most deep seismic zones would appear to imply that the flow of mantle material is directed downward at 650 km. This impression has been quantified in a kinematical study of large-scale

mantle flow by Hager and O'Connell [1978] and Hager et al. [1983]. They find that the dips of the seismic zones are much better matched by the streamlines associated with models of whole-mantle convection than with models where the circulation is restricted above 650 km. Hager and O'Connell's inferences have been rejected because they incorrectly equate the instantaneous particle trajectories given by streamlines with the instantaneous locus of the slab given by seismicity [Garfunkel et al., 1986], but their qualitative conclusions are in agreement with the seismic evidence.

3.f. Implications for mantle convection and the nature of the 650-km discontinuity.

Lithospheric slab penetration into the lower mantle to depths exceeding 1000 km provides a simple and complete explanation of the near-source travel-time anomalies observed for deep-focus earthquakes in the northwest Pacific and Tonga, and it is consistent with the constraints on the subduction process in most other deep-focus seismic zones. The excellent fits achieved by uncomplicated thermal-boundary layer models to the complicated residual-sphere patterns shown in Figures 3.5 and 3.6 cannot be ignored in discussions of mantle dynamics. In our opinion, the seismological evidence is sufficiently strong that models of mantle convection that do not conform with this behavior should be rejected, or at least severely downweighted in any hierarchy of working hypotheses.

Rigorous stratification of the mantle into a two-layer, convecting system with a boundary at 650 km is one such model. Our results imply the flux of mantle material across this boundary must be large. If we consider only the Pacific subduction zones from the Marianas to Tonga and adopt a nominal plate thickness of 125 km [Parsons and Sclater, 1977], the slab flux alone, exclusive of any entrained flow, amounts to 100 km^3/yr (cf. Figure 3.1). If we extend this calculation to include all oceanic subduction zones and therefore the entire plate flux, we obtain approximately 300 km^3/yr. At this rate, the volume of the upper mantle is thrust into the lower mantle about once every billion years. Entrainment could increase the flux severalfold. Exchange rates of this magnitude cannot be easily reconciled with models which isolate the entire lower mantle as a primitive geochemical reservoir [e.g., O'Nions et al., 1979; Jacobsen and Wasserberg, 1979].

Observations of high-frequency, high-amplitude *P'P'* phases reflected from the bottom side of the 650-km discontinuity have been used as evidence that the velocity jump at this depth is caused by an abrupt change in major-element chemistry, rather than a change of phase [Lees et al., 1983]. As discussed by Creager and Jordan [1984, 1986a], the data on the aseismic extensions of

slabs do not favor this hypothesis. The *P*-velocity increase at 650 km is approximately 4% [Given and Helmberger, 1980; Burdick, 1981; Walck, 1984b], which is about equal to the difference between the average velocity in the interior of the slab and the ambient upper mantle due to the thermal contrasts. If the entire increase at 650 km were caused by a compositional change, then the velocity contrast between the slab interior and the ambient lower mantle would be reduced by 4%, assuming the slab has an upper-mantle composition. On the other hand, the residual-sphere data do not allow the slab velocity contrast in the lower mantle to be significantly less than in the upper mantle, so we would then be forced to require that $\partial v_p / \partial T$ increases by a factor of two across the 650-km transition. As discussed above, both laboratory data [Sumino et al., 1977, 1983; Sumino, 1979; Bonczar and Graham, 1982; Suzuki et al., 1983] and direct comparisons of our results with observations of large-scale lower-mantle heterogeneities [Hager et al., 1985] argue against an increase of this magnitude.

We should emphasize that these arguments restrict only the chemical change manifested by an increase in seismic velocities at 650 km. Compositional changes which, say, increase density but decrease compressional velocity (e.g., an increase in iron content [Bonczar and Graham, 1982]) are not limited by our data, insofar as they are consistent with deep slab penetration. Christensen and Yuen [1984] have investigated a range of time-dependent convection models and conclude that a compositional density jump of a few percent would not impede penetration through the 650-km discontinuity, nor would an endothermic phase change with a Clapyeron slope on the order of that derived by Ito and Yamada [1982] (−2 MPa/°K). These hypothetical properties are not excluded by slab penetration, but they could have significant dynamical effects, especially on convection at higher wavenumbers. One can envisage, for example, a mantle where the anomalous properties of this transition impede the average vertical flux across 650 km relative to other levels, although not the penetration of old lithosphere. Such a system might have a structure very different from simple "whole-mantle" convection.

Our current methods are unable to resolve aseismic extensions of slabs much below about 1000 km, which is only one-third the depth of the mantle. Slab penetration to greater depths is consistent with our data, though speculative, so we cannot exclude the existence of stratified convection with boundary layers at this depth or below. Given the slab geometry shown in Figure 3.5, however, the plausibility of convective stratification in the upper half of the mantle must be questioned. Northwest Pacific slabs all have aseismic extensions whose dip angles are greater than or equal to the dips of the seismic zones, so that their net curvature is concave downward. The change in dip with depth is particularly noteworthy in the cases of Kuril-Kamchatka and Japan,

which are characterized by an abrupt change from shallow to steep dips at about 500 km. The dynamical significance of these transition-zone kinks is not understood, but their kinematical implications are important. Garfunkel [1975] and Garfunkel et al. [1986] have argued that slab migration is generally retrograde (i.e., opposite to the subduction direction) at rates of 10-25 km/Ma and, therefore, that migrating slabs do not separate mantle convection cells, but instead are entrained in the circulations beneath the overriding plates. If true, then the motions of slab particles near the base of the convecting layer should be concave upward. The fact that slabs tend to dip more steeply below the seismic zone suggests that the convecting layer is thicker than 1000 km.

4. Structure Beneath the Plates

A three-dimensional map of seismic wave speeds in the mantle will expose the structure of convection beneath the plates, just as a shadow-graph reveals the structure of convection in a laboratory tank. Unlike the clear view obtained in laboratory situations, however, the seismological pictures of mantle convection are strongly distorted by the heterogeneous structure of the plates themselves, and the resolution is limited by the irregular distributions of sources and receivers. The interpretation is further complicated by the need to separate the effects of the temperature variations from compositional heterogeneity and mineralogical anisotropy. Nevertheless, the seismic imaging of interior structure should be able to map a variety of convective features, including the upwelling plumes needed to balance downward plate flux, small-scale convection in the upper mantle beneath the plates, thermal and chemical boundary layers at the core-mantle interface, topography dynamically imposed on the mantle phase transitions, any internal boundary layers separating chemically stratified regions of the mantle, and, of course, the downwellings driven by descending slabs of oceanic lithosphere.

As reviewed in Section 3, the delineation of features in the last category has relied upon the constraints on slab geometry provided by deep seismicity and the understanding of slab structure derived from thermal-boundary-layer theory. Models of mantle convection are not sufficiently advanced to predict the geographic distribution, depth extent, or even the characteristic horizontal dimensions of the other features, so that seismologists must start from scratch, detecting the structures and resolving them from noise, as well as determining their average properties. Any feasible representation of a structural model must involve a limited number of parameters, and both discrete-block grids and orthogonal-function expansions have been employed. In the latter, a perturbation to some spherically symmetric reference earth model $\mathbf{m}_0(r)$ is represented as a sum over fully normalized surface spherical harmonics:

$$\mathbf{m}(r,\theta,\phi) \;=\; \mathbf{m}_0(r) \;+\; \sum_{s=0}^{\infty} \sum_{t=-s}^{+s} \delta\mathbf{m}_s^t(r)\, Y_s^t(\theta,\phi) \qquad (4.1)$$

As written here in terms of the complex surface harmonics Y_s^t [Edmonds, 1960], the coefficients $\delta\mathbf{m}_s^t$ are complex-valued n-tuples of functions satisfying the symmetry conditions $\delta\mathbf{m}_s^{-t} = (-1)^t \delta\mathbf{m}_s^{t}{}^*$, so that there are $2s+1$ independent, real-valued n-tuples per degree. Horizontal resolution is limited by truncating the expansion at some maximum wavenumber s_{max}. Vertical resolution is limited either by truncating an expansion in vertical wavenumber or discretizing the radial

coordinate.

A more fundamental choice involves which functions to include in $\delta\mathbf{m}$. For an isotropic, elastic perturbation, n equals 3, corresponding to variations in the P velocity, S velocity, and density: $\delta\mathbf{m} = (\delta v_p, \delta v_s, \delta\rho)$. However, velocity anisotropy is potentially important, especially near the surface, and additional functions must be introduced to account for anisotropic heterogeneities [e.g., Crampin et al., 1984; Tanimoto and Anderson, 1985]. In the simple case of hexagonal symmetry, for example, five more functions are needed (three elastic parameters and two orientation parameters). Presently available data sets are inadequate to resolve the details of such complex models, so that most workers take the perturbations to be isotropic, assuming anisotropic effects can be averaged out. If this assumtion is false, the resulting models can be biased.

Ideally, all of the information on the seismogram should be used to construct three-dimensional earth models. Although significant progess has been made on the problem of inverting the entire seismogram for earth structure [Dziewonski and Steim, 1982; Lerner-Lam and Jordan, 1983; Woodhouse and Dziewonski, 1984], this is not possible. Simply put, much of the information on the seismogram--an example would be the amplitudes of high-frequency body waves--is too sensitive to the small-scale details of source and earth structure not included in feasible model parameterizations. For this reason, most studies have relied on the phase information derived from coherent wave groups. The basic data functionals containing this information are the travel times of body waves, the phase velocities of surface waves, and the apparent center frequencies of free-oscillation multiplets. These data functionals satisfy variational principles (those of Fermat and Rayleigh), which allow their dependence on model perturbations to be linearized and, just as important, show how they average higher wavenumber heterogeneity. In this section we will be concerned with the constraints placed by these data on low-wavenumber aspherical variations, and our discussion will be focused on global models, rather than regional studies.

4.a. Upper Mantle

Long-period seismograms from large, shallow-focus earthquakes are dominated by the successive passages of fundamental-mode surface waves propagating along the great circles connecting the sources and receivers. Each group can be identified by its wave type (R for PSV-polarized Rayleigh waves; G for SH-polarized Love waves) and orbit number n. Groups traveling the minor arc between source and receiver are designated by odd orbit numbers (n = 1, 3, 5, ...), whereas those traveling the major arc have even orbit numbers (n = 2, 4, 6, ...). By

observing the phase differences between two groups of the same type and orbital direction on the same seismogram (e.g., R_1 and R_3, or G_2 and G_6), one can obtain great-circle averages of the local phase velocities that are insensitive to the source properties and instrument response [Satô, 1958]. Although they can be very precisely measured down to frequencies of 5 mHz or so, these averages constrain only the coefficients in equation (4.1) with s even, corresponding to an "even-parity" perturbation that is symmetric under reflection through the center of the earth [Backus, 1964]. To first order, the odd-parity heterogeneity (s odd) does not affect the phase difference between successive orbits.

Measurements of great-circle phase velocities were used to construct the first global models of upper-mantle heterogeneity [Toksöz and Anderson, 1966; Kanamori, 1970; Dziewonski, 1971; Okal, 1977]. The earth's surface was divided into a number of tectonic regions within which the structure was presumed to be laterally homogeneous. Dispersion curves for the individual tectonic regions were isolated by a regression of the phase-velocity data against the fraction of the path length traversing each structural type, and these curves were inverted for regional velocity profiles. Toksöz and Anderson's [1966] original study used a tectonic regionalization comprising only three crustal types (stable continents, ocean basins, and orogenic zones), whereas Okal's [1977] analysis incorporated seven (shields, mountain belts, trenches and marginal basins, and four oceanic regions based on crustal age). The six-bin regionalization GTR1 [Jordan, 1981a] is shown in Figure 2.1.

Adopting an *a priori* regionalization eliminates the even-parity ambiguity intrinsic to the great-circle data and reduces the unknowns to a managable number, but it also precludes the detection and analysis of heterogeneity not correlated with surface tectonics. The importance of sub-tectospheric variations on the dispersion of long-period waves was first quantified in a free-oscillation study by Masters et al. [1982]. At very low frequencies (less than, say, 5 mHz), the seismogram is most conveniently represented as a sum over discrete normal modes, which for a spherically symmetric earth are collapsed into degenerate multiplets. The effect of aspherical heterogeneity is to split these multiplets [Woodhouse and Dahlen, 1978]. Because the multiplet spectra are broadened by attenuation, the individual spectral lines are difficult to resolve, and the primary effect of asphericity is to shift the apparent center frequency of a multiplet away from its spherically symmetric value by an amount that is linearly related to the heterogeneity [Jordan, 1978b]. This frequency shift can be accurately measured [Silver and Jordan, 1981] and, at high enough wavenumber, can be expressed as an integral of the local eigenfrequency around the great-circle connecting the source and receiver [Jordan, 1978b]. Hence, the apparent center

frequencies of fundamental-mode standing waves provide the same kind of information as the great-circle dispersion of fundamental-mode traveling waves; in particular, they are sensitive to only even-parity heterogeneity.

Using the newly installed IDA network of digital seismometers, Masters et al. [1982] made center-frequency measurements on nearly 4,000 spheroidal-mode multiplets, sampling 557 paths in the frequency range 1.4-5.2 mHz. Automated processing of digital records permitted a dramatic increase in the quantity and quality of the data (consider that Okal's [1977] study of just a few years earlier was based on only 29 paths). The free-oscillation data compiled by Masters et al. [1982] indicated a strong quadrupolar ($s = 2$) component of mantle heterogeneity. The heterogeneity correlated positively with the geoid but only weakly with Jordan's [1981b] GTR1 regionalization (Figure 2.1); the degree-two model gave a total variance reduction of 61%, compared with only 24% obtained from the regionalization. Based on the scaling of the frequency shifts with wavenumber, Masters et al. [1982] argued that this heterogeneity is predominantly sub-tectospheric, and their preferred model localized it in the mantle transition zone between about 400 and 650 km depth. They speculated that it may be related to a large-scale component of mantle convection.

The large amount of digital seismic data which became available in the first part of the present decade also motivated systematic studies of fundamental-mode dispersion using traveling-wave techniques. Nakanishi and Anderson [1983] obtained great-circle phase velocities in the 3–10-mHz band for 198 Love-wave paths and 253 Rayleigh-wave paths. They confirmed the existence of the $s = 2$ heterogeneity discovered by Masters et al. [1982] but, following Kawakatsu [1983] and Souriau and Souriau [1983], interpreted this feature as the degree-two component of trench-related heterogeneity, possibly concentrated at shallow (< 200 km) depths.

If the location, mechanism and time function of an earthquake are known, phase velocities can be measured over the major and minor arcs connecting the source to the receiver, as well as over full great-circle paths. Nakanishi and Anderson [1984] used this single-station method to recover information on both the even-parity and odd-parity components of upper-mantle structure. They constructed maps of phase-velocity variations for Love and Rayleigh waves out to degree and order six from an analysis of about 200 paths. The Nakanishi-Anderson fundamental-mode data set has been inverted for anisotropic, laterally heterogeneous models of the upper mantle by Nataf et al. [1984, 1986]. Tanimoto and Anderson [1985] analyzed a somewhat larger data set for lateral heterogeneity and azimuthal anisotropy.

The most complete analysis of upper-mantle aspherical structure published thus far is the study by Woodhouse and Dziewonski [1984]. Employing a waveform-inversion technique based on high-frequency asymptotic approximations, they inverted some 2000 seismograms over 870 paths for an isotropic aspherical model of shear-velocity perturbations complete to degree and order eight ($s_{max} = 8$). Radial structure was represented by expanding each harmonic coefficient $\delta m_s^t(r)$ as a cubic polynomial in r, so that their parameterization comprised a total of 243 scalar quantities. They presented two models: M84A, for which the data were uncorrected for lateral variations in crustal structure, and M84C, for which the data were corrected for a two-region (continent-ocean) crust. Although the seismograms used by Woodhouse and Dziewonski [1984] are dominated by the large-amplitude groups of the fundamental Love and Rayleigh waves, their waveform inversion scheme does attempt to fit the body-wave and higher-mode signals to frequencies as high as 22 mHz, and the resolving power of their data should be significantly better than data sets comprising fundamental modes alone.

Figure 4.1 shows the M84C structure averaged over the upper 400 km of the mantle, obtained by integrating the S-wave travel-time perturbations along vertical ray paths from 40 km to 400 km. As noted by Woodhouse and Dziewonski [1984], the structure in this depth interval is dominated by the high velocities associated with continental cratons and the low velocities corresponding to actively spreading mid-ocean ridges; i.e., tectospheric heterogeneity of the sort discussed in Section 2. In an attempt to separate tectospheric from sub-tectospheric heterogeneity, we have projected the perturbation in Figure 4.1 onto the GTR1 regionalization. The six geographical functions of GTR1 were filtered to degree eight prior to performing the projection [Lerner-Lam and Jordan, 1986]. The resulting map (Figure 4.2) shows the part of the M84C travel-time perturbation that is correlated with large-scale surface tectonics and therefore plausibly attributable to tectospheric structure. The average one-way S-time anomalies obtained by this procedure are given for the individual regions in the following table:

Region	Description	Areal fraction	*S* anomaly (s)
A	Young oceans (< 25 My)	.13	1.4
B	Intermediate-age oceans (25-100 My)	.35	0.4
C	Old oceans (> 100 My)	.13	0.0
Q	Phanerozoic orogenic zones	.22	−0.2
P	Phanerozoic platforms	.10	−1.3
S	Precambrian shields and platforms	.07	−2.7

The *S* anomalies in the table are generally consistent with recent studies of regional upper-mantle structure derived by high-resolution waveform modeling. For example, the vertical *S*-time difference in the depth interval 40-400 km calculated from Grand and Helmberger's [1984a,b] models ATL (western Atlantic) and SNA (stable North America) is +2.3 s, which compares with the C−(P+S)/2 difference of +2.0 s computed for M84C. The latter value is essentially identical to the difference obtained from Lerner-Lam and Jordan's [1986] models PA2 (western Pacific) and EU2 (northern Eurasia), discussed in Section 2.d.

Figure 4.3 displays the difference between Figures 4.1 and 4.2. Removing the components of M84C correlated with the GTR1 regionalization reduces the amplitude of the pattern by about a factor of two and shifts it to higher wavenumber. To the extent that Figure 4.2 adequately represents the thermal boundary layer structure of the plates, this subtraction should produce an estimate of sub-tectospheric heterogeneity. However, the ability of the Woodhouse-Dziewonski data set to resolve low-amplitude, short-wavelength features has not been demonstrated. At high wavenumbers, the approximations used in their waveform-inversion procedure are less valid [Jordan, 1978b; Woodhouse and Girnius, 1982]. Moreover, since M84C was parameterized by a spherical harmonic expansion truncated at $s_{max} = 8$ without tapering, some of the energy in the high-wavenumber oscillations may result from sidelobe ringing. Given these caveats and the uncertainties associated with stripping off plate structure, any interpretation of Figure 4.3 in terms of convective processes is risky. For example, a dominant feature on the residual map is the fairly large negative travel-time anomaly centered on the Ural Mountains and Barents Sea. Much of this area is classified in GTR1 as an orogenic zone (Region Q) and therefore is assigned the fairly low

velocity derived by averaging it with other tectonically active areas, whereas it may actually have a plate structure more characteristic of continental shields. Some of the positive features, such as the Red Sea anomaly discussed by Nakanishi and Anderson [1983] and Woodhouse and Dziewonski [1984], may be manifestations of convective upwellings, but these features are rather small, localized anomalies. We conclude that at the present resolution of global seismic studies, lateral heterogeneity in the upper 400 km of the mantle is dominated by tectospheric structure.

4.b. Transition zone

The same is not true for the aspherical heterogeneity of the mid-mantle transition zone. In Figure 4.4 we plot the M84C vertical *S*-time perturbation for the 400–650-km layer. The structure is dominated by two antipodal high-velocity anomalies, one centered in the westernmost Pacific near the equator and one beneath South America. The degree-two component of this structure is compared with the quadrupolar transition-zone model of Masters et al. [1982] in Figure 4.5. The Y_2^0 coefficient is smaller in M84C, but the models are otherwise very similar in both pattern and amplitude. Since the Woodhouse-Dziewonski inversion method provides good constraints on the odd-parity as well as even-parity parts of the aspherical heterogeneity, we conclude that both of the equatorial high-velocity regions are genuine features. In particular, it appears that the South American anomaly can not be explained as simply a "far-side" artifact of shallow trench-related heterogeneity localized in the western Pacific, as advocated by Kawakatsu [1983], Souriau and Souriau [1983] and Nakanishi and Anderson [1983].

The high transition-zone velocities are most likely related to the downward flux of cold material in subduction zones. The western Pacific anomaly shown in Figure 4.5 ecompasses trenches which account for about half of the global plate flux back into the mantle (Figure 3.1), whereas the source of cold material for the South American feature is presumably the slab subducted in the Peru-Chile trench. This hypothesis is supported by the fact that the transition-zone anomalies correlate positively with the degree-two geoid [Masters et al., 1982]. Moreover, Forte and Peltier [1986] have calculated the surface divergence of the tangential velocity field described by Minster and Jordan's [1978] AM1-2 plate-motion model, and they find that the quadrupolar component of this field is very similar to the Masters et al. [1982] anomaly pattern (Figure 4.6). At this wavenumber, the zones of convergence correspond to the high-velocity, high-density regions and the zones of divergence to low-velocity, low-density regions.

The dominance of the second-degree harmonic in the low-wavenumber spectrum of

transition-zone heterogeneity implies some sort of large-scale organization of the flow through this region. Busse's [1983] proposal for opposing quadrupolar convection patterns in a chemically stratified mantle, illustrated in Figure 1.1b, is one possible scheme. The most obvious way to discriminate this kind of model from those involving deeper circulation of upper-mantle material is to examine the relationships among structures on both sides of the 650-km discontinuity. For subduction zones with deep-focus seismicity, this can be done locally using the residual-sphere techniques described in Section 3. The results provide convincing evidence that the old, cold slabs continue across the discontinuity.

The nature of the flow through the transition zone on a larger, more global scale remains unknown, however, and additional information regarding seismic heterogeneity in the vicinity of 650 km is badly needed. Unfortunately, mapping the variations of seismic wave speeds at this depth is difficult. In the frequency range of typical surface-wave experiments (> 5 mHz), the ability of the data to resolve structure below about 400 km is poor. Fundamental-mode free-oscillation data of the sort used by Masters et al. [1982] are affected by inhomogeneities throughout the mantle, but they provide only averages over broad depth ranges. The detailed mapping of the interface between the upper and lower mantle will require extensive sets of body-wave and higher-mode data. Progress in this direction has been recently reported by Grand [1986] and Woodhouse and Dziewonski [1986].

4.c. Lower Mantle

The lower mantle of the earth, Bullen's region D, extends from the seismic discontinuity at a depth of about 650 km to the core-mantle boundary at a depth of 2886 km. There is some evidence for small discontinuities or at least anomalous gradients at several radii within the lower mantle [Johnson, 1969; Chinnery, 1969], especially in its upper 400 km [Muirhead and Hales, 1980] and near its base [Lay and Helmberger, 1983a,b]. But throughout most of the lower mantle, the radial variation of seismic velocities is consistent with the near-adiabatic compression of a homogeneous material [Birch, 1952; Jordan and Anderson, 1974]. It has long been appreciated by seismologists that, at low wavenumbers, the RMS amplitude of lateral heterogeneity in the central part of the lower mantle is much smaller than in the upper mantle. This is not surpising from the point of view of mantle convection. To the extent that the seismological structure is largely determined by thermobaric variations owing to high Rayleigh number convection, the heterogeneity in the mid-mantle is expected to be dominated by downwelling plumes from the transition zone and upwelling plumes from the core-mantle boundary, giving rise to a relatively "white" horizontal

wavenumber spectrum. In contrast, the boundary layers should have "red" spectra, with power concentrated at the low wavenumbers corresponding to the characteristic horizontal scales of the boundary layer flow [Jarvis and Peltier, 1986].

The most obvious manifestations of downwellings are the slab anomalies discussed in Section 3, and there is now good evidence that these account for much of the aspherical structure in the depth range 700-1700 km. The first detailed study of a velocity anomaly in the lower mantle related to convective downwelling was by Jordan and Lynn [1974], who compiled *PcP-P* and *ScS-S* differential travel times at North American stations for two deep-focus earthquakes in South America. By using differential times they were able to reduce the effects of upper-mantle heterogeneity and isolate the signature of a high-velocity region at depths of 800-1400 km beneath the Caribbean, which Jordan and Lynn [1974] and Jordan [1975b] associated with subduction at the Middle America trench. The anomaly has a horizontal (east-west) scale of 500-1000 km and an estimated velocity contrast of 1% or so, implying a temperature contrast on the order of 200°C.

Additional evidence for the Caribbean anomaly and other localized features in the lower mantle was obtained in a more comprehensive travel-time study by Lay [1983]. More recently, Grand [1986] inverted an extensive set of travel times from multiply reflected *S*-waves to image of the mantle beneath North and Central America. In his maps, the Caribbean anomaly extends downward to at least 1700 km and northward beneath the United States, in a position roughly coincident with the locus of subduction during the early opening of the Atlantic. The analysis of regional travel times by Lay [1983] and global inversions of body-wave data by Woodhouse and Dziewonski [1986] indicate that this high-velocity feature continues around the periphery of the Pacific into Eurasia. Although these studies have not yet attained sufficient horizontal resolution to delineate the precise relationship of the high-velocity anomaly to subducted slabs, they do corroborate the evidence for deep slab flux presented in Section 3.

Jordan and Lynn [1974] found that the ratio of *S*-time perturbations to *P*-time perturbations for the Caribbean anomaly is about 3.5:1. The same ratio was obtained for lower-mantle slab anomalies in the northwest Pacific by Creager and Jordan [1984], and a similar value is required to satisfy the *P* and *S* data pertaining to larger scale variations in the lower mantle [Woodhouse and Dziewonski, 1986; Woodhouse, private communication]. This ratio is close to that computed from *S* and *P* station anomalies, which sample upper-mantle inhomogeneities [Doyle and Hales, 1967; Hales and Herrin, 1972], but it is larger than the one derived from laboratory measurements of temperature derivatives. If the lower-mantle velocity perturbations are caused solely by temperature

variations, then the travel-time data imply

$$(\partial \ln v_s / \partial T) / (\partial \ln v_p / \partial T) \approx 2 \qquad (4.2)$$

The ratio calculated for candidate mantle mineralogies from the laboratory data of Anderson et al. [1968] is about 40% less. Hales and Doyle [1967] and Hales and Herrin [1972] suggested that, in the case of the station anomalies, the discrepancy between the seismic and laboratory estimates of $(\partial \ln v_s / \partial \ln v_p)$ could be indicative of partial melting in the upper mantle. Such a mechanism is much less plausible (though not completely excluded) for lower-mantle heterogeneity. A more likely explanation, proposed by Anderson [private communication], is that the ratio in equation 4.2 increases substantially with pressure at low pressures.

Although *S*-waves have been useful in delineating local and regional anomalies beneath subduction zones, most of what is known about the aspherical structure of the lower mantle on a global scale comes from the analysis of *P*-wave travel times. In a pioneering study, Julian and Sengupta [1973] demonstrated that the scatter in *P* times from deep-focus earthquakes increases considerably beyond about 80°, implying that the amplitude of the lateral variations grows as the core-mantle boundary is approached. This hypothesis was confirmed by Sengupta and Toksöz [1976], who inverted 1490 *P* times and 314 *S* times for a lower-mantle model parameterized by velocity perturbations in 1400 blocks (individual block dimensions were 10°×10°×500-km). The sparse distribution of sources and receivers and the relatively small number of times severely limited the resolving power of Sengupta's data set, however.

Dziewonski et al. [1977] improved the sampling of lower-mantle structure considerably by using data from bulletins of the International Seismological Centre (ISC). The ISC compiles *P* times from a global network of several thousand stations for routine hypocenter determination, and over 1000 of these stations have reported enough teleseismic data to allow the estimation of station anomalies [Poupinet, 1979; Dziewonski and Anderson, 1983]. Dziewonski et al. [1977] inverted nearly 700,000 *P* times for a model of the lower mantle comprising 120 blocks, each having approximate dimensions of 36°×60°×750-km. They did not relocate events or correct for station anomalies. The analysis of the ISC data was refined by Dziewonski [1984] using a time-term algorithm that iteratively perturbed lower-mantle structure, event locations, and station anomalies. He represented lower-mantle velocity perturbations to angular degree 6 and radial degree 4 using the same orthogonal-function expansion employed in the upper-mantle study of Woodhouse and Dziewonski [1984].

The compressional-velocity models of Dziewonski et al. [1977] and Dziewonski [1984] show a significant correlation with the geoid at angular degrees 2 an 3. Hager et al. [1985] have investigated this correlation by computing the dynamic response of a viscously stratified mantle [Richards and Hager, 1984]. Their analysis assumes the density perturbations driving the flow are proportional to the seismically observed velocity perturbations, described by the lower-mantle models of Dziewonski [1984] and Clayton and Comer [1983].. (Clayton and Comer's unpublished model is a discrete-block structure derived by a tomographic inversion of ISC *P* times.) Hager et al. [1985] correct the observed geoid for slab-related density anomalies not resolved by the global seismic models [Hager, 1984]. They obtain a good match between the theoretical and observed geoids for mantle models with no chemical stratification, but they infer a viscosity increase by a factor of 10-30 at a depth of about 650 km, consistent with Hager's [1984] conclusion that an increase of 30-100 is needed to match slab-related geoid anomalies. Their calculations account for the dynamically supported topography at the free surface and the core-mantle boundary, with their preferred degree-3 model predicting total topographic amplitudes of about 1.4 km and 3 km, respectively.

The dynamic-response calculations published by Hager et al. [1985] do not account for the effects of upper-mantle and transition-zone structure on the slab-corrected geoid, nor do they allow for lateral variations in viscosity, which may be necessary to establish that average viscosity increases substantially across the mid-mantle transition zone. Hager's hypothesis should be testable by seismic methods, however, since it has considerable implications for the kinematics of mantle flow through this region. For example, the distortion of descending slabs owing to any viscosity increase must be small enough to satisfy the constraints imposed by the residual-sphere data discussed in Section 3. Preliminary calculations by Fischer et al. [1986b] indicate that the compressive thickening of northwest Pacific slabs normal to their strike cannot be much more than a factor of two or three during their transit through the depth interval 500-800 km.

On a more global scale, the resolution gap between the upper-mantle and lower-mantle modeling techniques is again a problem. In Dziewonski's [1984] model L02.56, the power in all harmonics is highest at 650-km discontinuity and decreases rapidly with depth, reaching a minimum near 2000 km before rising towards the core-mantle boundary. The increase at the base of the lower mantle appears to be real, but as Dziewonski [1984] notes, the peak at the top of the lower mantle may be due to the inadequacy of the source and station corrections to account for the structure above 650 km. Problems with these corrections may explain why the seismic models of

Dziewonski [1984] and Clayton and Comer [1983] do not agree very well with each other or correlate well with the geoid above $s = 3$. At higher wavenumbers, the dynamic reponse comparisons will require seismic structures that are continuous through the transition zone. Even at the lowest wavenumbers, such self-consistent structures may be necessary to properly interpret the geoid constraints.

4.d. Core-Mantle Boundary

At the base of the mantle, just above the core-mantle boundary (CMB), lies Bullen's Region D", where the vertical gradients in the seismic velocities are small and the horizontal gradients are large relative to the mid-mantle. Early workers invoked compositional gradients--e.g., an increase in iron content with depth--to account for the anomalous seismic velocity profile in D" [Bullen, 1950], but modern explanations of these gradients have tended to focus on the role of a thermal boundary layer (TBL) at the base of the mantle. A well-developed TBL is expected if there is significant heat flow across the CMB [Jones, 1977; Jeanloz and Richter, 1979; Elsasser et al., 1979; Doornbos, 1983]. Because of the destabilizing effects of a strongly temperature-dependent viscosity, flow at the base of the mantle is expected to be time-dependent, with hot, light material accumulating in pools and venting upward in thermal jets [Yuen and Peltier, 1980; Stacey and Loper, 1983; Loper and Stacey, 1983]. The strong lateral temperature gradients associated with this flow should therefore give rise to seismically detectable aspherical structure.

In this scenario, the magnitude of the seismic heterogeneity in D" is governed by the average temperature drop ΔT_m across a boundary layer whose maximum thickness we take to be h_m. The total variation in vertical P-wave travel time is then

$$|\delta\tau_m| \leq 2 v_p^{-2} (\partial v_p/\partial T)\, h_m \Delta T \tag{4.3}$$

A simple parabolic boundary layer analysis can be used to scale this quantity with the heat flux from the core, F, and material properties in D" [Jeanloz and Richter, 1979]:

$$h_m \Delta T_m \propto (\nu F / g\, \alpha \rho C_p)^{1/2} \tag{4.4}$$

Estimates based on lower-mantle kinematic viscosities of $\nu = 10^{18}$ m^2/s are $h_m \approx 100$ km and $\Delta T_m \approx 500°$ [Jeanloz and Richter, 1979; Elsasser et al., 1979]. Adopting a temperature coefficient of $\partial v_p/\partial T = -0.5$ m/s/°K, inferred for the lower mantle from the slab-related anomalies and geoid-correlated velocity perturbations discussed in Section 3, we obtain $|\delta\tau_m| \leq 0.3$ s.

Aspherical heterogeneity does indeed increase near the base of the mantle [Julian and Sengupta, 1973], and the magnitude of the increase obtained in recent lower-mantle *P*-wave models is commensurate with the predictions of the thermal boundary layer analysis. In the lower 200 km of Dziewonski's [1984] L02.56 structure, for example, the peak-to-peak variation in vertical *P* time is about 0.2 s, an order of magnitude higher than within a comparable layer a thousand kilometers above the CMB. However, evidence is accumulating which indicates that the structure of the CMB may be more complicated than either the *P*-wave or simple TBL models suggest. The amplitude decay of short-period *P*-waves into the core shadow [Ruff and Helmberger, 1982] and the waveforms of *SH* waves at shorter distances [Lay and Helmberger, 1983a,b] imply that the radial velocity gradients within D'' are large and variable, perhaps indicative of compositional layering. Moreover, strong aspherical effects have been observed in many types of seismic waves which interact with the CMB, including P_{diff}, *PnKP*, *SnKS*, *PcP* and *ScS* phases (see reviews by Jordan [1979b], Doornbos [1983], and Lay [1986]), and it is not clear that thermally induced velocity differences are sufficient to explain the large amplitude and broad wavenumber spectrum of the observed variations.

As in the crust and uppermost mantle, the lateral structure at or near the CMB appears to span the spectrum from microscale (< 30 km) to large scale (> 3000 km) heterogeneity [Jordan, 1979b]. Since the density jump across the CMB exceeds that at the free surface (4.4 Mg/m^3 vs. 3.3 Mg/m^3), it is plausible that convection in the mantle and core has deposited chemically differentiated material at the CMB to produce compositionally distinct layers of intermediate density, similar in some respects to the surficial chemical boundary layer (CBL) discussed in Section 2. To explain the seismic data, it has been postulated that interactions with the convective flows above and below the CMB cause variations in the thickness of the CBL, forming continent-like rafts of material with anomalous elastic properties [Jordan, 1979b; Ruff and Anderson, 1980].

This hypothesis has recently received support from a tomographic study of CMB structure using the travel times of core-penetrating *PKP* waves [Creager and Jordan, 1986b]. The existence of large-scale aspherical structure somewhere below the lower mantle is required by the anomalous splitting of the low-degree free oscillations sensitive to core structure [Masters and Gilbert, 1981; Ritzwoller et al., 1986; Giardini et al., 1986] and anomalous travel times of PKP_{DF} [Poupinet et al., 1983; Morelli and Dziewonski, 1986; Morelli et al., 1986; Creager and Jordan, 1986b], but the form and distribution of this structure is as yet uncertain. The models proposed by the various groups have very different distributions of heterogeneity in the inner core, outer core, and lower

mantle. Although aspherical heterogeneity of the outer core can account for core-mode splitting [Ritzwoller et al., 1986], the low viscosity of core fluid makes inhomogeneity of the required magnitude extremely unlikely [Stevenson, 1986]. Based on extensive observational work and modeling studies, seismologists at Harvard University have shown that much of the core-mode splitting and PKP_{DF} travel-time dispersion can be explained by an inner core that is both aspherical and anisotropic [Woodhouse et al., 1986; Morelli et al., 1986]. However, lateral heterogeneity of large amplitude and horizontal scale is also observed in the travel times of PKP_{AB} [Creager and Jordan, 1986b] and PKP_{BC} [Morelli and Dziewonski, 1986], two branches which do not interact with the inner core.

Preliminary maps of CMB structure have been produced by Morelli and Dziewonski [1986] using PKP_{BC} and PcP travel times and by Creager and Jordan [1986b] using PKP_{AB} and PKP_{DF}. The data sets are disjunct, the modeling procedures are very different, and there are discrepancies between the models at even the lowest wavenumbers. For example, in the Morelli-Dziewonski structure, the amplitude of the second-degree zonal harmonic is small, whereas in the Creager-Jordan structure it is large. Nevertheless, the amplitudes of the vertical P-wave travel-time variations through the CMB are about the same; both yield a peak-to-peak value on the order of one second. Creager and Jordan's vertical resolution is very limited, although they argue that their data are not well described by a model with aspherical heterogeneity confined to D", indicating that either CMB topography and/or a core-side boundary layer are involved. On the other hand, because they employ the mantle-side reflection PcP, Morelli and Dziewonski are able to distinguish CMB topography from boundary-layer structure. They find that, when plotted on the CMB, the PcP residuals are anticorrelated with those of PKP_{BC}, which is diagnostic of a structure dominated by the topography. The topography needed to explain the Morelli-Dziewonski data set is on the order of 12 km in total amplitude. If the Creager-Jordan travel-time map is interpreted in terms of CMB topography alone, an amplitude of nearly 16 km is required.

It appears unlikely that topography of this magnitude and scale can be dynamically supported by mantle convection. Hager et al. [1985] have estimated the dynamic topography of the CMB from lower-mantle seismic models and the geoid, and their preferred model, which is characterized by whole-mantle convection with a ten-fold increase in viscosity at the 650-km discontinuity, has a peak-to-peak amplitude of only 3 km, a factor of four or five too small to account for the travel times. Moreover, their predicted topography does not show a very good correlation with either the Morelli-Dziewonski or Creager-Jordan maps. Hence, even if the magnitude of the dynamically supported topography could be increased over Hager et al.'s estimate by increasing the viscosity

gradient in the mantle, satisfying the seismic data would remain difficult.

These considerations motivate the alternate hypothesis that CMB heterogeneity is associated with one or more CBLs trapped by the density contrast at the CMB. The primary advantage of the CBL hypothesis is that it provides a mechanism to induce large velocity variations which are not necessarily correlated positively with density variations. Although Birch's law [Birch, 1961] enforces such a correlation among silicates of roughly equal atomic weight, the admixture of iron, for example, increases density but *decreases* seismic velocities. It is plausible, therefore, to imagine localized areas of the CMB occupied by material of distinct chemistry, temperature and seismic velocities which has very little density contrast with surrounding areas. Such a scenario avoids the need for unrealistic dynamical configurations to support the aspherical heterogeneity.

Given the preliminary nature of the seismic models and the differences in the CMB structures they imply, it is premature to enter into too detailed speculation regarding the properties and behavior of CMB boundary layers. Although the basic argument that the large magnitude and rich spectrum of CMB heterogeneity requires some sort of chemical mechanism appears to be sound, we do not know to what extent the material of anomalous composition is distributed above the CMB or below it. Because of the mantle's high viscosity, Region D" is the preferred site for large-scale chemical inhomogeneity, but the possibility of lateral variations within a thin core-side boundary layer cannot be excluded, especially if the CMB has significant topography. We also have very few constraints on the composition and formation history of the CMB layering. We can envisage at least four mechanisms: (1) the CMB could have inherited a distinct chemistry from the early differentiation of the earth; (2) iron-rich material could be deposited at the base of the mantle by plate-tectonic convection; (3) an alloy-rich slag could accumulate at the top of the core from solidification of the inner core; and, (4) a layer of intermediate density could form by chemical reaction between the mantle and core. Anderson [1975] and Ruff and Anderson [1980] have discussed possibility (1) in terms of a refractory (Ca, Al)-rich assemblage resulting from inhomogeneous accretion of the earth. Knittle and Jeanloz [1986] discuss experimental evidence for possiblilty (4).

5. Conclusions

Boundary layers at the surface and core-mantle interface appear to dominate the large-scale, three-dimensional variation of seismic wave speeds in the earth's interior. In both cases, the seismological data imply a magnitude of heterogeneity difficult to satisfy by simple thermal boundary layer models and appear to require the existence of substantial chemical boundary layers. The mantle part of the surficial CBL resides as thick (> 200 km) accumulations beneath the stable continental shields and platforms. It has been depleted in iron and aluminum relative to magnesium by the extraction of basaltic components, and the low normative density resulting from this depletion locally compensates the low temperatures of the cratonic tectosphere, stabilizing it against convective disruption. The most plausible model for the formation of thick TBLs beneath the cratons is not conductive decay, but advective thickening by continent-continent collision. The low heat flow into the base of the continental tectosphere inferred from thermal modeling and the tendency of continents to be gregarious indicates that the configuration of the continental CBL is intimately coupled to the large-scale convective flow driving plate tectonics and continental drift.

The best seismological constraints on the depth of this convective circulation come from the seismic imaging of subducted slabs by residual-sphere techniques. In all deep-focus zones studied to date, the data favor slab penetration into the lower mantle to depths of at least 1000 km. The slab flux through the 650-km discontinuity is large, probably much greater than 100 km^3/yr. This conclusion appears to be inconsistent with the existence of major chemical discontinuity at 650-km separating an upper-mantle convecting system from a lower-mantle system. At larger horizontal scales, the downwellings associated with subduction zones account for much of the aspherical structure in the depth range 700-1700 km, suggesting that the plate-tectonic circulation extends throughout most of the mantle.

Lateral heterogeneity increases towards the base of the mantle. Recent tomographic mapping indicates that the aspherical structure of the CMB has an amplitude comparable to the earth's outer layers. Although inconsistencies among the various seismological results inhibit detailed inferences, the magnitude and scale of CMB heterogeneity strongly suggests the existence of one or more CBLs whose large-scale accumulations on the surface of the core may in some respects be analogous to the continents.

We therefore envisage an earth comprising four major dynamical parts: the two convecting layers of the mantle and core, and the two CBLs at the outer surface and core-mantle boundary.

Although there has been little quantitative work on the dynamics of such a system, there can be little doubt that its behavior is very different from a planet lacking the CBLs.

6. References

Ahrens, T. J., and Y. Syono, Calculated mineral reactions in the earth's mantle, *J. Geophys. Res.*, *72*, 4181-4188, 1967.

Anderson, D. L., Recent evidence concerning the structure and composition of the Earth's mantle, *Phys. Chem. Earth*, *6*, 1-131, 1966.

Anderson, D. L., Chemical plumes in the mantle, *Geol. Soc. Am. Bull.*, *86*, 1593-1600, 1975.

Anderson, D. L., The 650 km mantle discontinuity, *Geophys. Res. Lett.*, *3*, 347-349, 1976.

Anderson, D. L., The deep structure of continents, *J. Geophys. Res.*, *84*, 7555-7560, 1979.

Anderson, D. L., A global chemical model for the evolution of the mantle, in *Evolution of the earth, Geodynamics Series, Vol. 5*, ed. by R. J. O'Connell, and W. S. Fyfe, pp. 6-18, American Geophysical Union, Washington, D.C., 1981.

Anderson, D. L., and J. B. Minster, Seismic velocity, attenuation and rheology of the upper mantle, in *Mechanismes et Prevision des Seismes, Hommage au Professeur J. Coulomb*, ed. by C. J. Allegre, pp. 109-124, Editions du Centre National de la Recherche Scientifique, Paris, 1980.

Anderson, D. L., and C. Sammis, Partial melting in the upper mantle, *Phys. Earth Planet. Inter.*, *3*, 41-50, 1970.

Anderson, D. L., and J. Regan, Upper mantle anisotropy and the oceanic lithosphere, *Geophys. Res. Lett.*, *10*, 841-844, 1983.

Anderson, O. L., E. Schreiber, R. C. Liebermann, and N. Soga, Some elastic constants on minerals relevant to geophysics, *Rev. Geophys. Space Phys.*, *6*, 491-524, 1968.

Andrews, D. J., and N. H. Sleep, Numerical modelling of tectonic flow behind island arcs, *Geophys. J. R. Astr. Soc.*, *38*, 237-251, 1974.

Backus, G. E., Geographical interpretation of measurements of average phase velocities of surface waves over great circular and great semicircular paths, *Bull. Seismol. Soc. Am.*, *54*, 571-610, 1964.

Barrell, J., The strength of the Earth's crust, *J. Geol.*, *22*, 729-741, 1914.

Bassett, W. A., and L. Ming, Disproportionation of Fe_2SiO_4 to $2FeO+SiO_2$ at pressures up to 250 kbar and temperatures up to 3000 °C, *Phys. Earth Planet. Inter.*, *6*, 154-160, 1972.

Beaumont, C., On rheological zonation of the lithosphere during flexure, *Tectonophysics*, *59*, 347-365,1979.

Bell, P. M., T. Yagi, and H. K. Mao, Iron-magnesium distribution coefficients between spinel $[(Mg,Fe)_2SiO_4]$, magnesiowüstite [(Mg,Fe)O], and perovskite, $[(Mg,Fe)SiO_3]$, *Carnegie Inst. Washington Year Book*, *78*, 618-621, 1979.

Benioff, H., Seismic evidence for the fault origin of oceanic deeps, *Geol. Soc. Am. Buil., 60,* 1837-1856, 1949.

Benioff, H., Orogenesis and deep crustal structure: additional evidence from seismology, *Geol. Soc. Am. Bull., 65,* 385-400, 1954.

Benioff, H., Source wave forms of three earthquakes, *Bull. Seismol. Soc. Am., 53,* 893-903, 1963.

Bibee, L. D., and G. G. Shor, Compressional wave anisotropy in the crust and upper mantle, *Geophys. Res. Lett., 3,* 639-642, 1976.

Billington, S., The morphology and tectonics of the subducted lithosphere in the Tonga-Fiji-Kermadec region from seismicity and focal mechanism solutions, Ph.D. dissertation, Cornell Univ., Ithica, New York, 1980.

Billington, S., and B. L. Isacks, Identification of fault planes associated with deep earthquakes, *Geophys., Res. Lett., 2,* 63-66, 1975.

Birch, F., Elasticity and constitution of the earth's interior, *J. Geophys. Res., 57,* 227-286, 1952.

Birch, F., Composition of the earth's mantle, *J. Geophys. Res., 69,* 4377-4388, 1961.

Bird, P., Stress and temperature in subduction shear zones: Tonga and Mariana, *Geophys. J. R. Astron. Soc., 55,* 411-434, 1978.

Bodine, J. H., M. S. Steckler, and A. B. Watts, Observations of flexure and the rheology of the oceanic lithosphere, *J. Geophys. Res., 86,* 3695-3707, 1981.

Bonczar, L. J., and E. K. Graham, The pressure and temperature dependence of the elastic properties of polycrystal magnesiowüstite, *J. Geophys. Res., 87,* 1061-1078, 1982.

Boyd, F.R., A pyroxene geotherm, *Geochim. Cosmochim. Acta, 37,* 2533-2546, 1973.

Boyd, F.R., J.J. Gurney, and S.H. Richardson, Evidence for a 150-200-km thick Archaean lithosphere from diamond inclusion thermobarometry, *Nature, 315,* 387-389, 1985.

Boyd, F. R., and R. H. McCallister, Densities of fertile and sterile garnet peridotites, *Geophys. Res. Lett., 3,* 509-512, 1976.

Brune, J. N., and J. Dorman, Seismic waves and earth structure in the Canadian shield, *Bull. Seismol. Soc. Am., 53,* 167-210, 1963.

Bullen, K. E., An earth model based on a compressibility-pressure hypothesis, *Mon, Mot. R. Astr. Soc., Geophys. Suppl., 6,* 50-59, 1950.

Burdick, L. J., A comparison of the upper mantle structure beneath North America and Europe, *J. Geophys. Res., 86,* 5926-5936, 1981.

Busse, F. H., Quadrupole convection in the lower mantle?, *Geophys. Res. Lett., 10,* 285-288, 1983.

Cara, M., Regional variations of higher Rayleigh-mode phase velocities: a spatial filtering method,

Geophys. J. R. Astr. Soc., 54, 439-460, 1978.

Cara, M., Lateral variations of *S* velocity in the upper mantle from higher Rayleigh modes, *Geophys. J. R. Astr. Soc., 57,* 649-670, 1979.

Cara, M., A. Nercessian, and G. Nolet, New inferences from higher mode data in western Europe and northern Eurasia, *Geophys. J. R. Astr. Soc., 61,* 459-478, 1980.

Cardwell, R. K., and B. L. Isacks, Geometry of the subducted lithosphere beneath the Banda Sea in eastern Indonesia from seismicity and fault plane solutions, *J. Geophys. Res., 83,* 2825-2838, 1978.

Cathles, L. M., III, *The viscosity of the earth's mantle,* Princeton Univ. Press, Princeton, N. J., 386 pp., 1975.

Cazenave, A., Thermal cooling of the oceanic lithosphere: new constraints from geoid height data, *Earth Planet. Sci. Lett., 70,* 395-406, 1984.

Cazenave, A., B. Lago, and K. Dominh, Thermal parameters of the oceanic lithosphere estimated from geoid height data, *J. Geophys. Res., 88,* 1105-1118, 1983.

Chapman, D.S., and H.N. Pollack, Regional geotherms and lithospheric thickness, *Geology, 5,* 265-268, 1977.

Chase, C., Tectonic history of the Fiji Plateau, *Geol. Soc. Amer. Bull., 82,* 3087-3109, 1971.

Chinnery, M. A., Velocity anomalies in the lower mantle, *Phys. Earth Planet. Int., 2,* 1-10, 1969.

Christensen, N. I., and S. M. Lundquist, Pyroxene orientation within the upper mantle, *Geol. Soc. Am. Bull., 93,* 279-288, 1982.

Christensen N.I., and M.H. Salisbury, Structure and composition of the lower oceanic crust, *Rev. Geophys., 13,* 57-86, 1975.

Christensen, N. I., and M. H. Salisbury, Seismic anisotropy in the oceanic upper mantle: Evidence from the Bay of Islands ophiolite complex, *J. Geophys. Res., 84,* 4601-4610, 1979.

Christensen, U. R., and D. A. Yuen, The interaction of a subducting lithospheric slab with a chemical or phase boundary, *J. Geophys. Res., 89,* 4389-4402, 1984.

Clayton, R. W., and R. P. Comer, A tomographic analysis of mantle heterogeneities from body wave travel times (abstract), *Eos, Trans. AGU, 62,* 776, 1983.

Crampin, S., E. M. Chesnokov, and R. G. Hipkin, Seismic anisotropy--state of the art, II, *Geophys. J. R. Astr. Soc., 16,* 1-16, 1984.

Creager, K. C., Geometry, velocity structure, and penetration depths of descending slabs in the western Pacific, Ph.D. dissertation, University of California, San Diego, 1984.

Creager, K. C., and T. H. Jordan, Slab penetration into the lower mantle, *J. Geophys. Res., 89,* 3031-3049, 1984.

Creager, K. C., and T. H. Jordan, Slab penetration into the lower mantle beneath the Mariana and

other Island Arcs of the Northwest Pacific, *J. Geophys. Res., 91,* 3573-3589, 1986a.

Creager, K.C., and T.H. Jordan, Aspherical structure of the core-mantle boundary from *PKP* travel times, *Geophys. Res. Lett.*, in press, 1986b.

Crough, S.T., Hotspot epeirogeny, *Tectonophysics, 61,* 321-333, 1979.

Crough, S. T, and G. A. Thompson, Numerical and approximate solutions for lithospheric thickening and thinning, *Earth Planet. Sci. Lett., 31,* 397-402, 1976.

Daly, R. A., *Strength and Structure of the Earth,* Prentice-Hall, Englewood Cliffs, 434 pp., 1940.

Daly, S. F., and B. Parsons, Layered convection and its effects on gravity anomalies and surface topography (abstract), *Eos, Trans. AGU, 65,* 1092, 1984.

Davies, G.F., Thickness and thermal history of continental crust and root zones, *Earth Planet. Sci. Lett., 44,* 231-238, 1979.

Davies, D., and D. P. McKenzie, Seismic travel-time residuals and plates, *Geophys. J. R. Astr. Soc., 18,* 51-63, 1969.

Davis, E. E., and C. R. B. Lister, Fundamentals of ridge crest topography, *Earth Planet. Sci. Lett., 21,* 405-413, 1974.

DePaolo, D. J., and G. J. Wasserburg, Inferences about magma sources and mantle structure from variations of $^{143}Nd/^{144}Nd$, *Geophys. Res. Lett., 3,* 743-746, 1976.

Detrick, R. S., An analysis of geoid anomalies across the Mendocino fracture zone: implications for thermal models of the lithosphere, *J. Geophys. Res., 86,* 11751-11762, 1981.

Doornbos, D.J., Present seismic evidence for a boundary layer at the base of the mantle, *J. Geophys. Res., 88,* 3498-3505, 1983.

Doornbos, D.J., S. Spiliopoulos, and F.D. Stacey, Seismological properties of D" and the structure of the thermal boundary layer, *Phys. Earth Planet. Inter., 41,* 225-239, 1986.

Doyle, H. A., and A. L. Hales, An analysis of the travel times of *S* waves to North American stations in the distance range 28° to 82°, *Bull. Seismol. Soc. Am., 57,* 761-771, 1967.

Duschenes, J. D., and S. C. Solomon, Shear wave travel time residuals from oceanic earthquakes and the evolution of oceanic lithosphere, *J. Geophys. Res., 82,* 1985-2000, 1977.

Dziewonski, A. M., Upper mantle models from 'pure-path' dispersion data, *J. Geophys. Res., 76,* 2587-2601, 1971.

Dziewonski, A. M., On regional differences in dispersion of mantle Rayleigh waves, *Geophys. J. R. Astr. Soc., 22,* 289-325, 1971.

Dziewonski, A. M., Mapping the lower mantle: Determination of lateral heterogeneity in *P*-velocity up to degree and order 6, *J. Geophys. Res., 89,* 5929-5952, 1984.

Dziewonski, A. M., and D. L. Anderson, Preliminary reference earth model, *Phys. Earth Planet. Inter., 25,* 297-356, 1981.

Dziewonski, A. M., and D. L. Anderson, Travel times and station corrections for *P*-waves at teleseismic distances, *J. Geophys. Res.*, *88*, 3295-3314, 1983.

Dziewonski, A. M., B. H. Hager, and R. J. O'Connell, Large-scale heterogeneities in the lower mantle, *J. Geophys. Res.*, *82*, 239-255, 1977.

Dziewonski, A. M., and J. M. Steim, Dispersion and attenuation of mantle waves through waveform inversion, *Geophys. J. R. Astr. Soc.*, *70*, 503-527, 1982.

Edmonds, A. R., *Angular Momentum in Quantum Mechanics*, Princeton University Press, 146 pp., 1960.

Elsasser, W. M., Convection and stress propagation in the upper mantle, in *The Application of Modern Physics to the Earth and Planetary Interiors*, edited by W.K. Runcorn, Interscience, New York, 1969.

Elsasser, W. M., P. Olsen, and B. D. Marsh, The depth of mantle convection, *J. Geophys. Res.*, *84*, 147-155, 1979.

Engdahl, E. R., Effects of plate structure and dilatancy on relative teleseismic *P*-wave residuals, *Geophys. Res. Lett.*, *2*, 420-422,1975.

Engdahl, E. R., N. H. Sleep, and M.-T. Lin, Plate effects in north Pacific subduction zones, *Tectonophysics*, *37*, 95-116, 1977.

Finnerty, A. A., and F. R. Boyd, Evaluation of thermobarometers for garnet peridotites, *Geochim. Cosmochim. Acta*, *48*, 15-27, 1984.

Fischer, K., K. C. Creager, and T. H. Jordan, Mapping the Tonga slab, *J. Geophys. Res.*, submitted, 1986a.

Fischer, K., K. C. Creager, and T. H. Jordan, Constaints on the width of deep slabs (abstract), *Eos., Trans. AGU*, *67*, 1114, 1986b.

Fitch, T. J., Compressional velocity in source regions of deep earthquakes: An application of the master earthquake technique, *Earth Planet. Sci. Lett.*, *26*, 156-166, 1975.

Fitch, T. J., In situ *P*-wave velocities in deep earthquake zones of the SW Pacific: evidence for a phase boundary between the upper and lower mantle, in *Island Arcs, Deep Sea Trenches and Back-Arc Basins, Maurice Ewing Ser., Vol. 1*, ed. by M. Talwani and W.C. Pitman, pp. 123-136, American Geophysical Union, Washington, D.C., 1977.

Forsyth, D. W., The early structural evolution and anisotropy of the oceanic upper mantle, *Geophys. J. R. Astr. Soc.*, *43*, 103-162, 1975.

Forsyth, D. W., The evolution of the upper mantle beneath mid-ocean ridges, *Tectonophysics*, *38*, 89-118, 1977.

Forte, A. M., and W. R. Peltier, Plate tectonics and aspherical earth structure: the importance of poloidal-toroidal coupling, *J. Geophys. Res.*, in press, 1986.

Frohlich, C., and M. Barazangi, A regional study of mantle velocity variations beneath eastern Australia and the southwestern Pacific using short-period recordings of *P, S, PcP, ScP* and *ScS* waves produced by Tonga deep earthquakes, *Phys. Earth Planet. Inter., 21,* 1-14, 1980.

Fujita, K., E. R. Engdahl, and N. H. Sleep, Subduction zone calibration and teleseismic relocation of thrust zone events in the central Aleutian Islands, *Bull. Seismol. Soc. Am., 71,* 1805-1828, 1981.

Garfunkel, Z., Growth, shrinking and long-term evolution of plates and their implications for the flow pattern in the mantle, *J. Geophys. Res., 80,* 4425-4432, 1975.

Garfunkel, Z., C. A. Anderson, and G. Schubert, Mantle circulation and the lateral migration of subducted slabs, *J. Geophys. Res., 91,* 7205-7224, 1986.

Gee, L. S., A. L. Lerner-Lam, and T. H. Jordan, Resolving power of higher-mode waveform inversion for Eurasian upper-mantle structure, *AFGL Technical Report 85-0206,* Air Force Geophysical Laboratory, Cambridge, pp. 11-36, 1985. ADA165228.

Giardini, D., Systematic analysis of deep seismicity: 200 centroid-moment tensor solutions for earthquakes between 1977 and 1980, *Geophys. J. R. Astr. Soc.,77,* 883-914, 1984.

Giardini, D., X.-D. Li, and J.H. Woodhouse, Three dimensional structure of the earth from splitting in free oscillation spectra, *Nature,* submitted, 1986.

Giardini, D., and J. H. Woodhouse, Deep seismicity and modes of deformation in Tonga subduction zone, *Nature, 307,* 505-509, 1984.

Giardini, D., and J. H. Woodhouse, Evidence for a horizontal shear flow in the mantle beneath the Tonga Arc, *Nature, 319,* 551-555, 1986.

Gilbert, F., Excitation of normal modes of the Earth by earthquake sources, *Geophys. J. R. Astron. Soc., 22,* 223-226, 1971.

Gilbert, F., and A. M. Dziewonski, An application of normal mode theory to the retrieval of structural parameters and source mechanisms from seismic spectra, *Phil. Trans. R. Soc. Lond., Ser. A, 278,* 187-269, 1975.

Given, J. W., and D. V. Helmberger, Upper mantle structure of northwestern Eurasia, *J. Geophys. Res., 85,* 7183-7194, 1980.

Grand, S. P., A tomographic inversion for shear velocity beneath the North American plate, *Eos, Trans. AGU, 67,* 302 (abstract), 1986.

Grand, S. P., and D. V. Helmberger, Upper mantle shear structure of North America, *Geophys. J. R. Astr. Soc., 76,* 399-438, 1984a.

Grand, S. P., and D. V. Helmberger, Upper mantle shear structure beneath the northwest Atlantic Ocean, *J. Geophys. Res., 89,* 11465-11475, 1984b.

Grand, S. P., and D. V. Helmberger, Uppermantle shear structure beneath Asia from mulit-bounce

S waves, *Phys. Earth Planet. Int., 41*, 154-169, 1985.

Green, D. H., and R. C. Liebermann, Phase equilibria and elastic properties of a pyrolite model for the oceanic upper mantle, *Tectonopyhsics, 32*, 61-92, 1976.

Griggs, D. T., The sinking lithosphere and the focal mechanism of deep earthquakes, in *The Nature of the Solid Earth*, ed. by E. C. Robertson, pp. 361-384, McGraw-Hill, New York, 1972.

Gurney, J.J., J.W. Harris, and R.S. Rickard, Silicate and oxide inclusions in diamonds from the Finsch kimberlite pipe, in *Kimberlites, Diatremes, and Diamonds: Their Geology, Petrology, and Geochemistry*, ed. by F. R. Boyd and H.O.A. Meyer, pp. 1-15, American Geophysical Union, Washington, D.C., 1979.

Gutenberg, B., H. Benioff, J. M. Burgers and D. Griggs, Colloquium on plastic flow and deformation within the earth, *Trans. AGU, 32*, 497-543, 1951.

Gutenberg, B., and C. F. Richter, Depth and geographical distribution of deep-focus earthquakes, *Geol. Soc. Am. Bull., 49*, 249-288, 1938.

Gutenberg, B., and C. F. Richter, *Seismicity of the Earth and Associated Phenomena*, Princeton Univ. Press, Princeton, 310 pp., 1954.

Hager, B. H., Subducted slabs and the geoid: constraints on mantle rheology and flow, *J. Geophys. Res., 86*, 6003-6015, 1984.

Hager, B. H., and R. J. O'Connell, Subduction zone dip angles and flow driven by plate motion, *Tectonophysics, 50*, 111-133, 1978.

Hager, B. H., and R. J. O'Connell, A simple global model of plate dynamics and mantle convection, *J. Geophys. Res., 86*, 4843-4867, 1981.

Hager, B. H., R. J. O'Connell, and A. Raefsky, Subduction, back-arc spreading and global mantle flow, *Tectonophysics, 99*, 165-189, 1983.

Hager, B. H., R. W. Clayton, M. A. Richards, R. P. Comer, and A. M. Dziewonski, Lower mantle heterogeneity, dynamic topography and the geoid, *Nature, 313*, 541-545, 1985.

Hales, A. L., and E. Herrin, Travel times of seismic waves, in *The Nature of the Solid Earth*, ed. by E. C. Robertson, pp. 172-215, McGraw-Hill, New York, 1972.

Harte, B, K.G. Cox, and J.J. Gurney, Petrography and geological history of upper mantle xenoliths from the Matsoku kimberlite pipe, *Phys. Chem. Earth, 9*, 477-506, 1975.

Hasebe, K., N. Fujii, and S. Uyeda, Thermal processes under island arcs, *Tectonophysics, 10*, 335-355, 1970.

Haxby, W. F., and D. L. Turcotte, On isostatic geoid anomalies, *J Geophys. Res., 83*, 5473-5478, 1978.

Haxby, W. F., D. L. Turcotte, and J. M. Bird, Thermal and mechanical evolution of the Michigan

Basin, *Tectonophysics, 36*, 57-75, 1976.

Heestand, R. L., and S. T. Crough, The effect of hot spots on the oceanic age-depth relation, *J. Geophys. Res., 86*, 6107-6114, 1981.

Herrin, E., et al., 1968 seismological tables for *P* phases, *Bull. Seismol. Soc. Am., 58*, 1196-1241, 1968.

Hess, H. H., Seismic anisotropy of the uppermost mantle under oceans, *Nature, 203*, 629-631, 1964.

Holmes, A, *Principles of Physical Geology*, 2nd ed., Ronald, New York, 1288 pp., 1965.

Honda, H., Earthquake mechanism and seismic waves, *J. Phys. Earth, 10*, 1-97, 1962.

Honda, H., and Masatsuka, A., On the mechanism of the earthquakes and the stresses producing them in Japan and its vicinity, *Tohoku Univ., Sci. Rep., Ser. 5, Geophys., 4*, 42-60, 1952.

Hubert, L. N., and C. Frohlich, The *P* velocity within the Tonga Benioff zone determined from traced rays and observations, *J. Geophys. Res., 86*, 3771-3782, 1981.

Hunter, D. R., *Precambr. Res., 1*, 259-326, 1974.

Isacks, B. L., and M. Barazangi, Geometry of Benioff zones: Lateral segmentation and downwards bending of the subducted lithosphere, in *Island Arcs, Deep Sea Trenches, and Back-Arc Basins, Maurice Ewing Ser., Vol. 1*, ed. by M. Talwani and W. C. Pitman III, pp. 99-114, American Geophysical Union, Washington, D. C., 1977.

Isacks, B., and P. Molnar, Mantle earthquake mechanisms and sinking of the lithosphere, *Nature, 223*, 1121-1124, 1969.

Isacks, B., and P. Molnar, Distribution of stress in the descending lithosphere from a global survey of focal-mechanism solutions of mantle earthquakes, *Rev. Geophys. Space Phys., 9*, 103-174, 1971.

Isacks, B., J. Oliver, and L. R. Sykes, Seismology and the new global tectonics, *J. Geophys. Res., 73*, 5855-5899, 1968.

Ito, E., and H. Yamada, Stability relations of silicate spinels, ilmenites, and perovskites, in *High Pressure Research in Geophysics*, edited by S. Akimoto and M. H. Manghnani, pp. 405-419, Center Acad. Pub. Japan, Tokyo, 1982.

Jackson, I. N. S., R. C. Liebermann and A. E. Ringwood, Disproportionation of spinels to mixed oxides: Significance of cation configuration and implications for the mantle. *Earth Planet. Sci. Lett., 24*, 203-208, 1974.

Jacob, K. H., Global tectonic implications of anomalous seismic *P* traveltimes from the nuclear explosion Longshot, *J. Geophys. Res., 77*, 2556-2573, 1972.

Jacobsen, S. B., and G. J. Wasserburg, The mean age of mantle and crustal reservoirs, *J. Geophys. Res., 84*, 7411-7427, 1979.

Jarvis, G. T., and W. R. Peltier, Flattening of ocean bathymetry profiles due to radiogenic heating in a convecting mantle, *Nature, 285*, 649-651, 1980.

Jarvis, G. T., and W. R. Peltier, Lateral heterogeneity in the convecting mantle, *J. Geophys. Res., 91*, 435-451, 1986.

Jeanloz, R., High pressure chemistry of the earth's mantle and core, preprint, 1985.

Jeanloz, R., and F. M. Richter, Convection, composition, and the thermal state of the lower mantle, *J. Geophys. Res., 84*, 5497-5504, 1979.

Jeanloz, R., and A. B. Thompson, Phase transitions and mantle discontinuities, *Rev. Geophys. Space Phys., 21*, 51-74, 1983.

Johnson, L. R., Array measurements of *P* velocities in the upper mantle, *J. Geophys. Res., 72*, 6309-6325, 1967.

Johnson, L. R., Array measurements of *P* velocities in the lower mantle, *Bull. Seismol. Soc. Am., 59*, 973-1008, 1969.

Jones, G. M., Thermal interaction of the core and the mantle and the long term behaviour of the geomagnetic field, *J. Geophys. Res., 82*, 1703-1709, 1977.

Jordan, T. H., The continental tectosphere, *Rev. Geophys. Space Phys., 13*, 1-12, 1975a.

Jordan, T. H., Lateral heterogeneity and mantle dynamics, *Nature, 257*, 745-750, 1975b.

Jordan, T. H., Lithospheric slab penetration into the lower mantle beneath the Sea of Okhotsk, *J. Geophys., 43*, 473-496, 1977.

Jordan, T. H., Composition and development of the continental tectosphere, *Nature, 274*, 544-548, 1978a.

Jordan, T. H., A procedure for estimating lateral variations from low-frequency eigenspectra data, *Geophys. J. R. Astr. Soc., 52*, 441-455, 1978.

Jordan, T. H., Mineralogies, densities, and seismic velocities of garnet lherzolites and their geophysical implications, in *The Mantle Sample: Inclusions in Kimberlites and Other Volcanics*, ed. by F. R. Boyd and H. O. A. Meyer, pp. 1-14, American Geophysical Union, Washington, D. C., 1979a.

Jordan, T. H., Structural geology of the Earth's interior, *Proc. Natl. Acad. Sci. U.S.A., 76*, 4192-4200, 1979b.

Jordan, T.H., The deep structure of the continents, *Sci. Am., 240*, 92-107, 1979c.

Jordan, T. H., Global tectonic regionalization for seismological data analysis, *Bull. Seismol. Soc. Am., 71*, 1131-1141, 1981a.

Jordan, T. H., Continents as a chemical boundary layer, *Phil. Trans. R. Soc. Lond., Ser. A 301*, 359-373, 1981b.

Jordan, T. H., and D. L. Anderson, Earth structure from free oscillations and travel times,

Gephys. J. R. Astr. Soc., 36, 411-459, 1974.

Jordan, T. H., and W. S. Lynn, A velocity anomaly in the lower mantle, *J. Geophys. Res., 79,* 2679-2685, 1974.

Julian, B. R., and D. Gubbins, Three-dimensional seismic ray tracing, *J. Geophys., 43,* 95-113, 1977.

Julian, B. R., and M. K. Sengupta, Seismic travel time evidence for lateral inhomogeneity in the deep mantle, *Nature, 242,* 443-447, 1973.

Kanamori, H., Velocity and Q of mantle waves, *Phys. Earth Planet. Int., 2,* 259-275, 1970.

Kanamori, H., and F. Press, How thick is the lithosphere?, *Nature, 226,* 330-331, 1970.

Katsumata, M., and L. R. Sykes, Seismicity and tectonics of the western Pacific: Izu-Mariana-Caroline and Ryukyu-Taiwan Regions, *J. Geophys. Res., 74,* 5923-5948, 1969.

Kawakatsu, H., Can "pure path" models explain free oscillation data?, *Geophys. Res. Lett., 10,* 186-189, 1983.

Kay, R., N. J. Hubbard, and P. W. Gast, *J. Geophys. Res., 75,* 1585-1613, 1970.

Keen, C. E., and D. L. Barrett, A measurement of seismic anisotropy in the northeast Pacific, *Can. J. Earth Sci., 8,* 1056-1064, 1971.

King, D. W., and G. Calcagnile, P-wave velocities in the upper mantle beneath Fennoscandia and western Russia, *Geophys. J. R. Astr. Soc., 46,* 407-432, 1976.

Knopoff, L., Observation and inversion of surface wave dispersion, *Tectonophysics, 13,* 497-519, 1972.

Knittle, E., and R. Jeanloz, High-pressure metallization of FeO and implications for the earth's core, *Geophys. Res. Lett.,* in press, 1986.

Knopoff, L., and M. J. Randall, The compensated linear-vector dipole: a possible mechanism for deep earthquakes, *J. Geophys. Res., 75,* 4957-4963, 1970.

Kono, Y., and M. Amano, Thickening model of the continental lithosphere, *Geophys. J. Roy. Astr. Soc., 54,* 405-416, 1978.

Kramers, J.D., Lead, uranium, strontium, potassium, and rubidium in inclusion-bearing diamonds and mantle-derived xenoliths from Southern Africa, *Earth Planet. Sci. Lett., 42,* 58-70, 1979.

Kusznir, N., and G. Karner, Dependence of the flexural rigidity of the continental lithosphere on rheology and temperature, *Nature, 316,* 138-142, 1985.

Lachenbruch, A. H., and J. H. Sass, Heat flow and energetics of the San Andreas Fault Zone, *J. Geophys. Res., 85,* 6185-6222, 1980.

Langseth, M. G., X. LePichon, and M. Ewing, Crustal structure of mid-ocean ridges, 5; heat flow through the Atlantic Ocean floor and convection currents, *J. Geophys. Res., 71,* 5321-5355, 1966.

Lay, T., Localized velocity anomalies in the lower mantle, *Geophys. J. R. Astron. Soc., 72,* 483-516, 1983.

Lay, T., Structure of the earth: mantle and core, *Rev. Geophys. Space Phys.*, submitted, 1986.

Lay, T., and D. V. Helmberger, A shear velocity discontinuity in the lower mantle, *Geophys. Res. Lett., 10,* 63-66, 1983a.

Lay, T., and D. V. Helmberger, A lower mantle *S* triplication and the shear velocity structure of D", *Geophys. J. R. Astr. Soc., 75,* 799-837, 1983b.

Leeds, A. R., Lithospheric thickness in the western Pacific, *Phys. Earth Planet. Inter., 11,* 61-64, 1975.

Leeds, A. R., L. Knopoff, and E. G. Kausel, Variations of upper mantle structure under the Pacific Ocean, *Science, 186,* 141-143, 1974.

Lees, A. C., M. S. T. Bukowinski, and R. Jeanloz, Reflection properties of phase transition and compositional change models of the 650-km discontinuity, *J. Geophys. Res., 88,* 8145-8159, 1983.

Leith, A., and J. A. Sharpe, Deep focus earthquakes and their geological significance, *J. Geol., 44,* 877-917, 1936.

Lerner-Lam, A. L., and T. H. Jordan, Earth structure from fundamental and higher-mode waveform analysis, *Geophys. J. R. Astr. Soc., 75,* 759-797, 1983.

Lerner-Lam, A. L., and T. H. Jordan, How thick are the continents?, *J. Geophys. Res.*, submitted, 1986.

Leveque, J. J., and M. Cara, Long-period Love wave overtone data in North America and the Pacific Ocean: new evidence for upper mantle anisotropy, *Phys. Earth Planet. Inter., 33,* 164-179, 1983.

Liu, H.-P., D. L. Anderson, and H. Kanamori, Velocity dispersion due to anelasticity: implications for seismology and mantle composition, *Geophys. J. R. Astr. Soc., 47,* 41-58, 1976.

Liu, L., The high-pressure phases of $MgSiO_3$, *Earth Planet. Sci. Lett., 31,* 200-208, 1976a.

Liu, L., The post-spinel phase of forsterite, *Nature, 262,* 770-772, 1976b.

Liu, L., On the 650-km seismic discontinuity, *Earth Planet. Sci. Lett., 42,* 202-208, 1979.

Loper, D. E., and F. D. Stacey, The dynamical and thermal structure of deep mantle plumes, *Phys. Earth Planet. Int., 33,* 304-317, 1983.

MacDonald, G. J. F., The deep structure of continents, *Rev. Geophys., 1,* 587-665, 1963.

Masters, G., and F. Gilbert, Structure of the inner core inferred from observations of its spheroidal shear modes, *Geophys. Res. Lett., 8,* 569-571, 1981.

Masters, G., T. H. Jordan, P. G. Silver and F. Gilbert, Aspherical earth structure from

fundamental spheroidal-mode data, *Nature, 298,* 609-613, 1982.

Mathais, M, J.C. Siebert, and P.C. Rickwood, Some aspects of the mineralogy and petrology of ultramafic zenoliths in kimberlite, *Contr. Mineral. Petrol., 26,* 75-123, 1970.

McKenzie, D. P., The viscosity of the lower mantle, *J. Geophys. Res., 71,* 3995-4010, 1966.

McKenzie, D. P., Some remarks on heat flow and gravity anomalies, *J. Geophys. Res., 72,* 6261-6273,1967.

McKenzie, D. P., Speculations on the consequences and causes of plate motions, *Geophys. J. R. Astron. Soc., 18,* 1-32, 1969.

McKenzie, D. P., Some remarks on the development of sedimentary basins, *Earth Planet. Sci. Lett., 40,* 25-32, 1978.

McKenzie, D. P., The earth's mantle, *Sci. Am., 249,* 67-78, 1983.

McKenzie, D. P., and R. L. Parker, The North Pacific: an example of tectonics on a sphere, *Nature, 216,* 1276-1280, 1967.

McKenzie, D. P., and F. M. Richter, Convection currents in the earth's mantle, *Sci. Am., 235,* 72-89, 1976.

McKenzie, D.P., and F. M. Richter, Parameterized thermal convection in a layered region and the thermal history of the earth, *J. Geophys. Res., 86,* 11667-11680, 1981.

McKenzie, D. P., J. M. Roberts and N. O. Weiss, Convection in the earth's mantle: towards a numerical simulation, *J. Fluid Mech., 62,* 465-538, 1974.

McKenzie, D.P., and N. Weiss, Speculations on the thermal and tectonic history of the Earth, *Geophys. J. R. Astr. Soc., 4,* 131-174, 1975.

McNutt, M. K., Lithospheric flexure and thermal anomalies, *J. Geophys. Res., 89,* 11180-11194, 1984.

McNutt, M. K., and H. W. Menard, Constraints on yield strength in the oceanic lithosphere derived from observations of flexure, *Geophys. J. R. Astr. Soc., 71,* 363-394, 1982.

Means, J. D., and T. H. Jordan, Slab penetration below 650 km: further evidence, (abstract), *Eos. Trans. AGU, 61,* 1047, 1980.

Menzies, M., and V. Rama Murphy, Enriched mantle: Nd and Sr isotopes in diopsides from kimberlite nodules, *Nature, 283,* 634-636, 1980.

Minear, J. W., and M. N. Toksoz, Thermal regime of a downgoing slab and new global tectonics, *J. Geophys. Res., 75,* 1397-1419, 1970.

Minster, J. B., and T. H. Jordan, Present-day plate motions, *J. Geophys. Res., 83,* 5331-5354, 1978.

Minster, J. B., and T. H. Jordan, Present-day plate motions: A summay, in *Mechanismes et Prevision des Seismes, Hommage au Professeur J. Coulomb,* ed. by C. J. Allegre, pp.

109-124, Editions du Centre National de la Recherche Scientifique, Paris, 1980.

Mitchell, B. J., and G. K. Yu, Surface wave dispersion, regionalized velocity models and anisotropy of the Pacific crust and upper mantle, *Geophys. J. R. Astr. Soc., 63,* 497-514, 1980.

Mitronovas, W., and B. L. Isacks, Seismic velocity anomalies in the upper mantle beneath the Tonga-Kermadec island arc, *J. Geophys. Res., 76,* 7154-7180, 1971.

Molnar, P., D. Freedman, and J. S. F. Shih, Lengths of intermediate and deep seismic zones and temperatures in downgoing slabs of lithosphere, *Geophys. J. R. Astr. Soc., 56,* 41-54, 1979.

Morelli, A., and A.M. Dziewonski, Topography of the core-mantle boundary and lateral homogeneity of the liquid core, *Nature,* in press, 1986.

Morelli, A., A. M. Dziewonski, and J. H. Woodhouse, Anisotropy of the inner core inferred from *PKIKP* travel times, *Geophys. Res. Lett.,* in press, 1986.

Morris, G. B., R. W. Raitt, and G. G. Shor, Velocity anisotropy and delay-time maps of the mantle near Hawaii, *J. Geophys. Res., 74,* 4300-4316, 1969.

Muirhead, K. J., and A. L. Hales, Evidence for *P* wave velocity discontinuities at depths greater than 650 km in the mantle, *Phys. Earth Planet. Int., 23,* 304-313, 1980.

Nakanishi, I., and D.L. Anderson, Measurements of mantle wave velocities and inversion for lateral heterogeneity and anisotropy, 1, analysis of great circle velocities, *J. Geophys. Res., 88,* 10267-10284, 1983.

Nakanishi, I., and D.L. Anderson, Measurements of mantle wave velocities and inversion for lateral heterogeneity and anistrophy, 2, analysis by the single-station method, *Geophys. J. R. Astr. Soc., 78,* 573-618, 1984.

Nataf, H.-C., I. Nakanishi, and D.L. Anderson, Anisotropy and shear-velocity heterogeneities in the upper mantle, *Geophys. Res. Lett., 11,* 109-112, 1984.

Nataf, H.-C., I. Nakanishi, and D.L. Anderson, Measurements of mantle wave velocities and inversion for lateral heterogeneities and anisotropy, 3, inversion, *J. Geophys. Res., 91,* 7261-7307, 1986.

Navrotsky, A., Lower mantle phase transitions may generally have negative pressure-temperature slopes, *Geophys. Res. Lett., 7,* 709-711, 1980.

Niazi, M., and D. L. Anderson, Upper mantle structure of western North America from apparent velocities of *P* waves, *J. Geophys. Res., 70,* 4633-4640, 1965.

Nicolas, A., and J. F. Violette, Mantle flow at oceanic spreading centers: models derived from ophiolites, *Tectonophysics, 81,* 319-339, 1982.

Nicholayson, L.O., and R.J. Hart, The Vredefort radioelement profile extended to supracrustal strata at Carletonville, with implications for continental heat flow, *J. Geophys. Res., 86,*

10653-10661, 1981.

Nixon, P.H., F.R. Boyd, and A.M. Boullier, The evidence of kimberlite and its inclusion on the constitution of the outer part of the earth, in *Lesotho Kimberlites*, ed. by P.H. Nixon, pp. 312-318, Lesotho National Development Corp., Lesotho, 1973.

Nolet, G., Higher Rayleigh modes in western Europe, *Geophys. Res. Lett., 2*, 60-62,1975.

Nolet, G., The upper mantle structure under western Europe inferred from the dispersion of Rayleigh modes, *J. Geophys., 43*, 265-285,1977.

Nolet, G., and J. Panza, Array analysis of seismic surface waves: limits and possibilities, *Pure Appl. Geophys., 114*, 775-790, 1976.

O'Connell, R. J., On the scale of mantle convection, *Tectonophysics, 38*, 119-36, 1977.

O'Hara, M. J., Is there an Icelandic mantle plume? *Nature, 253*, 708-710, 1975.

Okal, E. A., The effect of intrinsic oceanic upper-mantle heterogeneity on regionalization of long-period Rayleigh-wave phase velocities, *Geophys. J. R. Astr. Soc., 49*, 357-370, 1977.

Okal, E. A., and D. L. Anderson, A study of lateral inhomogeneities in the upper mantle by multiple *ScS* travel-time residuals, *Geophys. Res. Lett., 2*, 313-316, 1975.

Oliver, J., and B. Isacks, Deep earthquake zones, anomalous structures in the upper mantle, and the lithosphere, *J. Geophys. Res., 72*, 4259-4275, 1967.

O'Nions, R. K., N. M. Eversen, and P. J. Hamilton, Geochemical modeling of mantle differentiation and crustal growth, *J. Geophys. Res., 84*, 6091-6101, 1979.

Oxburgh, E. R., and E. M. Parmentier, Compositional and density stratification in oceanic lithosphere-causes and consequences, *J. Geol. Soc.,133*, 343-355, 1977.

Oxburgh, E. R., and E. M. Parmentier, Thermal process in the formation of continental lithosphere, *Phil. Trans. R. Soc. Lond., Ser. A, 288*, 415-429, 1978.

Parker, R.L., Inverse theory with grossly inadequate data, *Geophys. J. R. Astr. Soc., 29*, 123-138, 1972.

Parsons, B., and D. P. McKenzie, Mantle convection and the thermal structure of the plates, *J. Geophys. Res., 83*, 4485-4496, 1978.

Parsons, B., and F. M. Richter, A relation between the driving force and geoid anomaly associated with mid-ocean ridges, *Earth Planet. Sci. Lett., 51*, 445-450, 1980.

Parsons, B., and J. G. Sclater, An analysis of the variation of ocean floor bathymetry and heat flow with age, *J. Geophys. Res., 82*, 803-827, 1977.

Pascal, G., J. Dubois, M. Barazangi, B. L. Isacks and J. Oliver, Seismic velocity anomalies beneath the New Hebrides Island Arc: Evidence for a detached slab in the upper mantle, *J. Geophys. Res., 78*, 6998-7004, 1973.

Pascal, G., B. L. Isacks, M. Barazangi and J. Dubois, Precise relocations of earthquakes and

seismotectonics of the New Hebrides Island Arc, *J. Geophys. Res., 83,* 4957-4973, 1978.

Peltier, W. R., Glacial isostatic adjustment - II. The inverse problem, *Geophys. J. R. Astr., Soc., 46,* 669-706, 1976.

Peltier, W. R., Mantle convection and viscosity, in *"Physics of the Earth's Interior", Proceedings of the Enrico Fermi International School of Physics* (Course LXXVIII), ed. by A. Dziewonski and E. Boschi, pp. 362-427, North Holland, New York, 1980.

Poirier, J. P., On the kinetics of olivine-spinel transition, *Phys. Earth Planet. Inter., 26,* 179-187, 1981.

Polyak, B.G., and Y.A. Smirnov, Relationship between terrestrial heat flow and the tectonics of continents, *Geotectonics, 4,* 205-213, 1968.

Poupinet, G., On the relation between *P*-wave travel time residuals and the age of continental plates, *Earth Planet. Sci. Lett., 43,* 149-161, 1979.

Poupinet, G., and B. de Voogd, Some consequences of the differences in seismic properties in old and young continental plates for isostatic compensation, *Earth Planet. Sci. Lett., 56,* 278-286, 1981.

Poupinet, G., R. Pillet, and A. Souriau, Possible heterogeneity of the earth's core deduced from *PKIKP* travel times, *Nature, 305,* 204-206, 1983.

Raitt, R. W., G. G. Shor, T. J. G. Francis, and G. B. Morris, Anisotropy of the Pacific upper mantle, *J. Geophys. Res., 74,* 3095-3109, 1969.

Randall, M. J., Elastic multipole theory and seismic moment, *Bull. Seis. Soc. Am., 61,* 1321-1326, 1971.

Regan, J., and D. L. Anderson, Anisotropic models of the upper mantle, *Phys. Earth Planet. Int., 35,* 227-263, 1984.

Richards, M. A., and B. H. Hager, Geoid anomalies in a dynamic earth, *J. Geophys. Res., 89,* 5987-6002, 1984.

Richardson, S. H., J. J. Gurney, A. J.Erlank, and J. W. Harris, Origins of diamonds in old enriched mantle, *Nature, 310,* 198-202, 1984.

Richter, F. M., Focal mechanisms and seismic energy release of deep and intermediate earthquakes in the Tonga-Kermadec region and their bearing on the depth extent of mantle flow, *J. Geophys. Res., 84,* 6783-6795, 1979.

Richter, F. M., Models for the Archean thermal regime, *Earth Planet. Sci. Lett., 73,* 350-360, 1985.

Richter, F. M., and C. E. Johnson, Stability of a chemically layered mantle, *J. Geophys. Res., 79,* 1635-1639, 1974.

Richter, F. M., and D. P. McKenzie, On some consequences and possible causes of layered mantle

convection, *J. Geophys. Res., 79,* 6133-6142, 1981.

Richter, F. M., and B. Parsons, On the interaction of two scales of convection in the mantle, *J. Geophys. Res., 80,* 2529-2541, 1975.

Ringwood, A.E., The chemical composition and origin of the earth, in *Advances in Earth Composition,* ed. by P. Hurley, M.I.T. Press, Cambridge, Mass, 1966.

Ringwood, A.E., Composition and evolution of the upper mantle, in *The Earth's Crust and Upper Mantle,* ed. by P.J. Hart, *Am. Geophys. Union Monograph, 13,* pp. 1-17, 1969.

Ringwood, A. E., *Composition and Petrology of the Earth's Mantle,* McGraw-Hill, New York, 619 pp., 1975.

Ringwood, A. E., Phase transformations and differentiation in subducted lithosphere: Implications for mantle dynamics, basalt petrogenesis, and crustal evolution, *J. Geol., 90,* 611-643, 1982.

Ritzwoller, M., G. Masters, and F. Gilbert, Observations of anomalous splitting and their interpretation in terms of aspherical structure, *J. Geophys. Res.,* in press, 1986.

Ruff, L., and D.L. Anderson, Core formation, evolution, and convection: a geophysical model, *Phys. Earth Planet. Inter., 21,* 181-201, 1980.

Ruff, L., and D. V. Helmberger, The structure of the lowermost mantle determined by short-period *P*-wave amplitudes, *Geophys. J. R. Astr. Soc., 68,* 95-119, 1982.

Salisbury, M. H., and N. J. Christensen, The seismic velocity structure of a traverse through the Bay of Islands ophiolite complex, Newfoundland, an exposure of oceanic crust and upper mantle, *J. Geophys. Res.,* 805-817, 1978.

Sammis, C. G., J. C. Smith, G. Schubert, and D. A. Yuen, Viscosity-depth profile of the earth's mantle; effects of polymorphic phase transformations, *J. Geophys. Res., 82,* 3741-3761, 1977.

Sandwell, D. T., and G. Schubert, Geoid height versus age for symmetric spreading ridges, *J. Geophys. Res., 85,* 7235-7241, 1980.

Sandwell, D. T., and G. Schubert, Geoid height-age relation from SEASAT altimeter profiles across the Mendocino fracture zone, *J. Geophys. Res., 87,* 3949-3958, 1982.

Sasatani, T., Source process of a large deep-focus earthquake of 1970 in the Sea of Okhotsk, *J Phys. Earth, 24,* 27-42, 1976.

Sasatani, T., Source parameters and rupture mechanism of deep-focus earthquakes, *J. Fac. Sci. Hokkaido Univ., Ser. VII (Geophys.), 6,* 301-384, 1980.

Satô, Y., Attenuation, dispersion, and the wave guide of the *G* wave, *Bull. Seismol. Soc. Am., 48,* 443-459, 1958.

Schlue, J. W., and L. Knopoff, Shear-wave polarization anisotropy in the Pacific Basin, *Geophys J. R. Astron. Soc., 49,* 145-165, 1977.

Schlue, J. W., and L. Knopoff, Inversion of surface-wave phase velocities for an anisotropic structure, *Geophys. J. R. Astr. Soc., 54,* 697-702,1978.

Schubert, G., C. Froidevaux, and D. A. Yuen, Oceanic lithosphere and asthenosphere: thermal and mechanical structure, *J. Geophys. Res., 81,* 3525-3540, 1976.

Schubert, G., D. A. Yuen, and D. L. Turcotte, Role of phase transitions in a dynamic mantle, *Geophys. J. R. Astr. Soc., 42,* 705-735, 1975.

Sclater, J. G., and P. A. F. Christie, Continental stretching: an explanation of the post mid-Cretaceous subsidence of the central graben of the North Sea, *J. Geophys. Res., 85,* 3740-3750, 1980.

Sclater, J. G., and J. Francheteau, The implications of terrestrial heat flow observations on current tectonic and geochemical models of the crust and upper mantle of the earth, *Geophys. J. R. Astr. Soc., 20,* 509-542, 1970.

Sclater, J. G., C. Jaupart, and D. Galson, The heat flow through oceanic and continental crust and the heat loss of the earth, *Rev. Geophys. Space Phys., 18,* 269-311,1980.

Sclater, J. G., L. A. Lawver, and B. Parsons, Comparisons of long wavelength residual elevation and free air gravity anomalies in the North Atlantic and possible implications for the thickness of the lithospheric plate, *J. Geophys. Res., 80,* 1031-1052, 1975.

Sclater, J. G., B. Parsons, and C. Jaupart, Oceans and continents: similarities and differences in the mechanisms of heat loss, *J. Geophys. Res., 86,* 11535-11552, 1981.

Sengupta, M. K., and B. R. Julian, Radial variation of compressional and shear velocities in the Earth's lower mantle, *Geophys. J. R. Astron. Soc., 54,* 185-219, 1978.

Sengupta, M. K., and M. N. Toksöz, Three dimensional model of seismic velocity variation in the earth's mantle, *Geophys. Res. Lett., 3,* 84-86, 1976.

Sereno, T., and J. Orcutt, Synthesis of realistic oceanic P_n wave trains, *J. Geophys. Res., 90,* 12755-12766, 1985.

Shearer, P., and J. Orcutt, Anisotropy in the oceanic lithosphere--theory and observations from the Ngendei seismic refraction experiment in the southwest Pacific, *Geophys. J. R. Astr. Soc, 80,* 493-526, 1985.

Shimamura, H., Anisotropy in the oceanic lithosphere of the northwestern Pacific Basin, *Geophys J. R. Astr. Soc., 76,* 253-260, 1984.

Shimamura, H., and T. Asada, Velocity anisotropy extending over the entire depth of the oceanic lithosphere, in, *Geodynamics of the Western Pacific-Indonesian Region, Geodynamics Series, Vol. 11,* ed. by T. W. C. Hilde and S. Uyeda, pp. 121-125, American Geophysical Union, Washington, D.C., 1983.

Shiono, K., and N. Sugi, Life of an oceanic plate: cooling time and assimilation time,

Tectonophysics, 112, 35-50, 1985.

Shor, G. G., R. W. Raitt, M. Henry, L. R. Bentley, and G. H. Sutton, Anisotropy and crustal structure in the Cocos plate, *Geofis. Int., 13*, 337-362, 1973.

Sipkin, S. A., and T. H. Jordan, Lateral heterogeneity of the upper mantle determined from the travel times of *ScS*, *J. Geophys. Res., 80*, 1474-1484, 1975.

Sipkin, S. A., and T. H. Jordan, Lateral heterogeneity of the upper mantle determined from the travel times of multiple *ScS*, *J. Geophys. Res., 81*, 6307-6320, 1976.

Sipkin, S. A., and T. H. Jordan, Multiple *ScS* travel times in the western Pacific: implications for mantle heterogeneity, *J. Geophys. Res., 85*, 853-861, 1980.

Silver, P. G., and T. H. Jordan, Fundamental spheroidal mode observations of aspherical heterogeneity, *Geophys. J. R. Astr. Soc., 64*, 605-634, 1981.

Sleep, N. H., Thermal effects of the formation of Atlantic continental margins by continental breakup, *Geophys. J. R. Astr. Soc., 24*, 325-350, 1971.

Sleep, N. H., Teleseismic *P*-wave transmission through slabs, *Bull. Seismol. Soc. Am., 63*, 1349-1373, 1973.

Sleep, N.H., and N.S. Snell, Thermal contraction and flexure of mid-continent and Atlantic marginal basins, *Geophys. J. R. Astr. Soc., 45*, 125-154, 1976.

Solomon, S. C., Geophysical constraints on radial and lateral temperature variations in the upper mantle, *Amer. Mineral., 61*, 788-803, 1976.

Sondergeld, C. H., B. L. Isacks, M. Barazangi, and S. Billington, A search for velocity anomalies near the deep portions of the inclined seismic zone of Tonga island arc, *Bull. Seismol. Soc. Am., 67*, 537-541, 1977.

Souriou, A., and M. Souriou, Test of tectonic models by great circle Rayleigh waves, *Geophys. J. R. Astr. Soc., 73*, 533-551,, 1983.

Spencer, C. P., and E. R. Engdahl, A joint hypocentre location and velocity inversion technique applied to the Central Aleutians, *Geophys. J. R. Astr. Soc., 72*, 399-415, 1983.

Spudlich, P., and J. Orcutt, Petrology and porosity of an oceanic crustal site: results from wave form modeling of seismic refraction data, *J. Geophys. Res., 85*, 1409-1433, 1980.

Stacey, F.D., and D.E. Loper, The thermal boundary-layer interpretation of D'' and its role as a plume source, *Phys. Earth Planet. Inter., 33*, 45-55, 1983.

Stark, P.B., and C. Frohlich, The depths of the deepest deep earthquakes, *J. Geophys. Res.*, 1859-1869, 1985.

Stauder, W., and L. Mualchin, Fault motion in the larger earthquakes of the Kuril-Kamchatka Arc and of the Kuril-Hokkaido Corner, *J. Geophys. Res., 81*, 297-308, 1976.

Steckler, M. S., and A. B. Watts, Subsidence of the Atlantic-type margin of New York, *Earth*

Planet. Sci. Lett., 41, 1-13, 1978.

Strelitz, R., The September 5, 1970, Sea of Okhotsk earthquake: a multiple event with evidence of triggering, *Geophys. Res. Lett., 2*, 124-127, 1975.

Stevenson, D., Limits on lateral density and velocity variations in the earth's core, *Geophys. J. R. Astr. Soc.*, in press, 1986.

Suito, K., Phase relations of pure Mg_2SiO_4 up to 200 kilobars, in *High Pressure Research, Applications in Geophysics*, ed. by M. H. Manghnani and S. Akimoto, pp. 255-266, Academic, New York, 1977.

Sumino, Y., The elastic constants of Mn_2SiO_4, Fe_2SiO_4, and Co_2SiO_4, and the elastic properties of olivine group minerals at high temperature, *J. Phys. Earth, 27*, 209-238, 1979.

Sumino, Y., O. L. Anderson, and I. Suzuki, Temperature coefficients of elastic constants of single crystal MgO between 80° and 1300° K, *Phys. Chem. Minerals*, 9, 38-47, 1983.

Sumino, Y., O. Nishizawa, T. Goto, I. Ohno, and M. Ozima, Temperature variation of elastic constants of single-crystal forsterite between −190° and 400°C, *J. Phys. Earth, 25*, 377-392, 1977.

Sung, C.-M., Kinetics of the olivine → spinel transition under high pressure: Experimental results and geophysical implications, in *High-Pressure Science and Technology, Vol. 2*, ed. by K. D Timmerhaus and M. S. Barber, pp. 31-42, Plenum Press, New York, 1979.

Sung, C.-M., and R. G. Burns, Kinetics of the olivine → spinel transition: implications for deep-focus earthquake genesis, *Earth Planet. Sci. Lett., 32*, 165-170, 1976a.

Sung, C.-M., and R. G. Burns, Kinetics of high-pressure phase transformations: implications for the evolution of the olivine → spinel transition in the downgoing lithosphere and consequences of the dynamics of the mantle, *Tectonophysics, 31*, 1-32, 1976b.

Sutton, G. H., and D. A. Walker, Oceanic mantle phases recorded on seismographs in the northwestern Pacific at distances between 7° and 40°, *Bull. Seismol. Soc. Am.*, 1972.

Suyehiro, K., and I. S. Sacks, *P*- and *S*-wave velocity anomalies associated with the lithosphere determined from travel-time residuals in the Japan [illegible], *69*, 97-114, 1979.

Suzuki, I., O. L. Anderson, and Y. Sumino, Elastic properties of Mg_2SiO_4, up to 1200° K, *Phys. Chem. Minerals*, [illegible]

Sykes, L. R., The seismicity and deep structure of island [illegible], 1966.

Tanimoto, T., and D. L. Anderson, Lateral heterogeneity [illegible] mantle: Love and Rayleigh 100-250 s, *J. Geophys. Res.*, [illegible]

AD-A181 249 INVESTIGATIONS OF EURASIAN SEISMIC SOURCES AND UPPER MANTLE STRUCTURE(U) MASSACHUSETTS INST OF TECH CAMBRIDGE DEPT OF EARTH ATMOSPHERI.. T H JORDAN 3/3

UNCLASSIFIED 06 MAR 87 AFGL-TR-87-0101 F19628-85-K-0024 F/G 8/11 NL

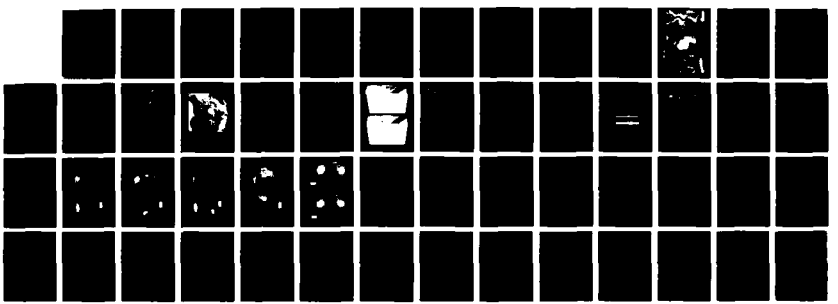

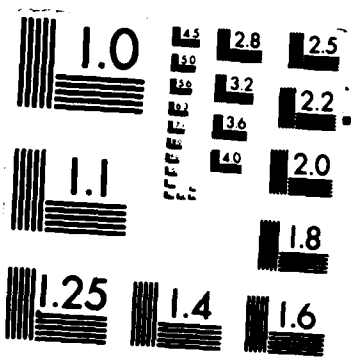
1.0
1.1
1.25
1.4
1.6
1.8
2.0
2.2
2.5
2.8
3.2
3.6
4.0
4.5
5.0
5.6

Toksöz, M. N., and D. L. Anderson, Phase velocities of long period surface waves and structure of the upper mantle, *J. Geophys. Res., 71,* 1649-1658, 1966.

Toksöz, N., J. W. Minear, and B. R. Julian, Temperature field and geophysical effects of a downgoing slab, *J. Geophys. Res., 76,* 1113-1138, 1971.

Toksöz, M. N., N. H. Sleep, and A. T. Smith, Evolution of the downgoing lithosphere and the mechanisms of deep focus earthquakes, *Geophys. J. R. Astr. Soc., 35,* 285-310, 1973.

Trehu, A. M., Depth versus $(age)^{1/2}$: a perspective on mid-ocean rises, *Earth Planet. Sci. Lett., 27,* 287-304, 1975.

Turcotte, D. L., and E. R. Oxburgh, Finite amplitude convective cells and continental drift, *J. Fluid Mech., 28,* 29-42, 1967.

Turcotte, D. L., and E. R. Oxburgh, A fluid theory for the deep structure of dip-slip fault zones, *Phys. Earth Planet. Inter., 1,* 381-386, 1968.

Turcotte, D. L., and G. Schubert, Structure of the olivine-spinel phase boundary in the descending lithosphere, *J. Geophys. Res., 76,* 7980-7987, 1971.

Turcotte, D. L., and G. Schubert, Frictional heating of the descending lithosphere, *J. Geophys. Res., 78,* 5876-5886, 1973.

Turner, H. H., On the arrival of earthquake waves at the antipodes, and on the measurement of the focal depth of an earthquake, *Mon. Not. R. Astr. Soc., Geophys. Suppl., 1,* 1-13, 1922.

Turner, H. H., Deep focus, in *International Seismological Summary for 1927, January, February, March,* pp. 1-108, Oxford, 1930.

Utsu, T., Seismological evidence for anomalous structure of island arcs with special reference to the Japanese region, *Rev. Geophys. Space Phys., 9,* 839-890, 1971.

Vassiliou, M. S., The state of stress in subducting slabs as revealed by earthquakes analysed by moment tensor inversion, *Earth Planet. Sci. Lett., 69,* 195-202, 1984.

Vassiliou, M. S., B. H. Hager, and A. Raefsky, The distribution of earthquakes with depth and stress in subducting slabs, *J. Geodynamics, 1,* 11-28, 1984.

Veith, K. F., The relationship of island arc seismicity to plate tectonics, Ph.D. dissertation, Southern Methodist Univ., Dallas, Tex., 1974.

Vening Meinesz, F. A., Indonesian Archipelago: a geophysical study, *Geol. Soc. Am. Bull., 65,* 143-164, 1954.

Vink, G. E., W. J. Morgan, and W.-L. Zhao, Preferential rifting of continents: A source of displaced terranes, *J. Geophys. Res., 89,* 10072-10076, 1984.

Vitorello, I., and H. N. Pollack, On the variation of continental heat flow with age and the thermal evolution of continents, *J. Geophys. Res., 85,* 983-995, 1980.

Wadati, K., On shallow and deep earthquakes, *Geophys. Mag., 1,* 161-202, 1928.

Wadati, K., On the activity of deep-focus earthquakes in the Japan Islands and neighborhood:, *Geophys. Mag., 8,* 305-325, 1935.

Wadati, K., and K. Masuda, On the travel time of earthquake waves (Part V), *Geophys. Mag., 7,* 269-290, 1933.

Walck, M. C., Teleseismic array analysis of upper mantle compressional velocity structure, Ph.D. Dissertation, Calif. Inst. of Technol., Pasadena, Calif., 1984a.

Walck, M. C., The *P*-wave upper mantle structure beneath an active spreading centre: the Gulf of California, *Geophys. J. R. Astr. Soc., 76,* 697-723, 1984b.

Walker, D., High-frequency P_n and S_n phases recorded in the western Pacific, *J. Geophys. Res., 82,* 3350-3360, 1977.

Watson, J.V., *Phil. Trans. R. Soc. Lond., Ser. A., 280,* 629-640, 1976.

Watts, A. B., J. H. Bodine, and M. S. Steckler, Observations of flexure and the state of stress in the oceanic lithosphere, *J. Geophys. Res., 85,* 6369-6376, 1980.

Watts, A. B., J. R. Cochran, P. Patriat, and M. Doucoure, A bathymetry and altimetry profile across the Southwest Indian Ridge at 31°S latitude, *Earth Planet. Sci. Lett., 73,* 129-139,1985.

Weichert, D. H., *Earth Planet. Sci. Lett., 17,* 181, 1972.

Weidner, D. J., A mineral physics test of a pyrolite mantle, *Geophys. Res. Lett., 12,* 417-420, 1985.

Wickens, A. J., and G. G. R. Buchbinder, S-wave residuals in Canada, *Bull. Seismol. Soc. Am., 70,* 809-822, 1980.

Windley, B. F., *The Evolving Continents,* 385 pp., John Wiley & Sons, Chichester, 1977.

Woodhouse, J. H., and F. A. Dahlen, The effect of a general aspherical perturbation on the free oscillations of the earth, *Geophys. J. R. Astr. Soc., 53,* 335-354, 1978.

Woodhouse, J. H., and A. M. Dziewonski, Mapping the upper mantle: three-dimensional modeling of earth structure by inversion of seismic waveforms, *J. Geophys. Res., 89,* 5953-5986, 1984.

Woodhouse, J. H., and A. M. Dziewonski, Three dimensional mantle models based on mantle wave and long period body wave data (abstract), *Eos, Trans. AGU, 67,* 307, 1986.

Woodhouse, J. H., D. Giardini, and X.-D. Li, Evidence for inner core anisotropy from splitting in free oscillation spectra, *Geophys. Res. Lett.,* in press, 1986.

Woodhouse, J. H., and T. P. Girnius, Surface waves and free oscillations in a regionalized earth model, *Geophys. J. R. Astr. Soc., 68,* 653-673, 1982.

Wortel, R., Seismicity and rheology of subducted slabs, *Nature, 296,* 553-556, 1982.

Yagi, T., P. M. Bell, and H. K. Mao, Phase relations in the system MgO-FeO-SiO_2 between 150 and 700 kbar at 1000°C, *Carnegie Inst. Washington Year Book, 78,* 614-618, 1979.

Yoder, H.S., Jr., *Generation of Basaltic Magma*, 265 pp., National Academy of Sciences, Washington, D.C., 1976.

Yoshii, T., Regionality of group velocities of Rayleigh waves in the Pacific and thickening of the plate, *Earth Planet. Sci. Lett.*, *25*, 305-312, 1975.

Yoshii, T., Cross sections of some geophysical data around the Japanese Islands, in *Geodynamics of the western Pacific-Indonesian Region, Geodynamics Series, Vol. 11*, ed. by T. W. C. Hilde and S. Uyeda, pp. 343-354, American Geophysical Union, Washington, D.C., 1983.

Yu, G. K., and B. J. Mitchell, Regionalized shear velocity models of the Pacific upper mantle from observed Love and Rayleigh wave dispersion, *Geophys. J. R. Astr. Soc.*, *57*, 311-341, 1979.

Yuen, D. A., and W. R. Peltier, Mantle plumes and the thermal stability of the D" layer, *Geophys. Res. Lett.*, *7*, 625-628, 1980.

Figure Captions

Figure 1.1. Two schematic models of stratified mantle convection. Model (a) was proposed by P.P. Bijlaard three and a half decades ago [Gutenberg et al., 1951] and (b) is from a recent paper by Busse [1983].

Figure 2.1. Mercator projection of the globe between 75°N and 70°S showing Jordan's [1981a] tectonic regionalization GTR1. Oceanic crust is partitioned into three age regions: *A*, young ocean (<25 My); *B*, intermediate-age ocean (25-100 My); and *C*, old ocean (>100 My). Subaerial continental crust is divided into three regions based on generalized tectonic behavior during the Phanerozoic: *S*, Precambrian shields and platforms; *P*, Phanerozoic platforms; and *Q*, Phanerozoic orogenic zones and magmatic belts. White areas are regions of submerged continental or transitional crust, including continental margins, island arcs, and oceanic plateaus adjoining continental crust.

Figure 2.2. The unified thermal boundary-layer model of plate structure proposed by Sclater et al. [1981, Figure 13]. In this model, old oceans and old continents have similar sub-crustal thermal structures and a characteristic tectospheric thickness of about 125 km. Heat flow is in units of 1 μcal $cm^{-2}s^{-1}$ (42 mW/m^2).

Figure 2.3. Tectospheric structure of a thermally mature ocean basin, showing the depth extent of its thermal, mechanical and chemical boundary layers.

Figure 2.4. (a). Estimates of seismic lid thickness, L_S, versus the square root of crustal age from three surface-wave models: the isotropic structures of Leeds et al. [1974] and Leeds [1975] (squares), the pseudo-anisotropic structure of Schlue and Knopoff [1977] (triangles), and the fully-parameterized transversely isotropic structure of Anderson and Regan [1983] (circles). MBL and TBL thicknesses are from the Parsons and Sclater [1977] plate model. (b). Vertical one-way *SV* travel times through the upper 400 km of the three surface-wave models, showing square-root-of-age behavior.

Figure 2.5. Histograms of Sipkin and Jordan's [1976] ScS_2–ScS differential travel-time residuals with surface-reflection points classified according to the tectonic regionalization of Figure 2.1. Residuals are relative to Jeffreys-Bullen tables, have been corrected for source

depths, ellipticity, station elevations, and elevations of surface reflection points, and have been normalized to one-way times. Arrows indicate medians for each tectonic region.

Figure 2.6. Transition from the high-velocity Siberian shield to the low-velocity Arctic ocean basin observed in the ScS_2–ScS differential travel times of Sipkin and Jordan [1976]. **Top panel:** Map of northern Eurasia showing the distribution of sources (triangles), receivers (circles), and ScS_2 surface reflection points (squares). Stippling identifies stable continent (regions S and P of Figure 2.1). Projection is azimuth equidistant about a point in the Sea of Okhotsk. **Bottom panel:** ScS_2–ScS residuals plotted against latitude of the surface reflection points. Residuals are two-way times with respect to the Jeffreys-Bullen tables, corrected for elevations of surface-reflection points. The coherent increase of the residuals with latitude is indicative of tectospheric thinning from shield to ocean basin across a quiescent margin of the sort illustrated in Figure 2.10.

Figure 2.7: S-wave station anomalies for North America from Wickens and Buchbinder [1980]. Light contours are spaced at 0.2-s intervals in one-way vertical travel time; heavy contours are at 1-s intervals. Crosses indicate locations of stations used to produce the map. The total variation in station anomaly is in excess of 5 s, and the pattern of variation is very coherent with the tectonic regionalization of Figure 2.1. The coherent increase of the residuals away from the Canadian shield across the quiescent North Atlantic continental margin is indicative of tectospheric thinning of the sort illustrated in Figure 2.10.

Figure 2.8. (a). Isotropic SV-velocity models for northern Eurasian (EU2) and the western Pacific (PA2) from the higher-mode waveform inversions of Lerner-Lam and Jordan [1986]. (b). Isotropic SH-velocity models for the Canadian Shield (SNA) and the western Atlantic (ATL) from the multiple-S body-wave study of Grand and Helmberger [1984a,b]. (c). Comparison of EU2 and SNA. (d). Comparison of PA2 and ATL.

Figure 2.9. Tectospheric structure of an old continental craton. As discussed in the text, the thickness of the TBL is a lower bound to average values inferred for most cratons.

Figure 2.10. Hypothetical model of the transition in upper-mantle structure from a stable continental craton to an old ocean basin across a quiescent margin, from Jordan [1979c]. The top panel shows shear velocities contoured in 0.2-km/s increments. The bottom panel shows temperature contoured in 200°C increments.

Figure 2.11. Schematic illustration of the formation of thick, cool, basalt-depleted continental tectosphere by advective thickening. The thin, inhomogeneous CBL accreted along an active continental margin (**a**) is consolidated and thickened by continent-continent collision (**b**) and subsequent compressive orogenesis (**c**). Dotted pattern is mantle of low normative density depleted in Fe and Al relative to Mg; cross-hatching shows region of melting beneath an active island arc, and arrows indicate relative motions.

Figure 3.1. Global map showing rates of plate creation (positive values) and destruction (negative values) in units of km^2/yr for individual plates and sections of plate boundaries, from Garfunkel et al. [1985, Figure 3].

Figure 3.2. Total number of earthquakes recorded worldwide for the period 1964-80 plotted in 20-km depth intervals, from Vassiliou et al. [1984, Figure 1]. The three curves give cumulative values above the indicated body-wave magnitude.

Figure 3.3. Cartoons depicting three possible fates of the subducted slab. Panel (**a**) shows how the descending slab might be disrupted by convective instability owing to its compositional stratification [from Oxburgh and Parmentier, 1977, Figure 4]. Panel (**b**) depicts Ringwood's [1982, Figure 9] "megalith" model, where the subducted lithosphere buckles to form a melange at the 650 km seismic discontinuity. Panel (**c**) is a schematic illustration of isotherms for subduction flow in a compositionally stratified mantle [from Anderson, 1981]; convection below 650 km is thermally coupled to convection above this discontinuity, so that descending plumes in the lower mantle are aligned beneath descending slabs in the upper mantle.

Figure 3.4. Observed residual spheres for *P*-times (top row), and *S* and *ScS* times (bottom row) of the 29 Jan. 1971 deep-focus earthquake beneath the Sea of Okhotsk. The former were derived from the ISC data base by Creager and Jordan [1984], whereas the latter were hand-picked by Jordan [1977]. Residual spheres are equal-area, lower-hemisphere projections, circumscribed by the locus of rays with take-off angles of 60° from vertical. Circles represent negative residuals, crosses are positive; symbol size is proportional to residual magnitude. Symbol scale shown in box is 1 second for *P* times and 3.5 seconds for *S* times. Lines represent the plane tangent to the slab model shown in Figure 3.7 (cross-section AA'). In the left column, the times have been corrected for ellipticity and station corrections, and *P* residuals have been computed with respect to the relocated hypocenters. In the right

and *P* residuals have been computed with respect to the relocated hypocenters. In the right column, these corrected residuals have been smoothed using the stochastic low-pass filter of Creager and Jordan [1986]. The smoothed resdiual spheres are dominated by negative residuals corresponding to rays propagating in the plane of the slab, indicative of slab penetration into the lower mantle.

Figure 3.5. Observed (left) and theoretical (center) residual spheres for *P* waves of four intermediate- and deep-focus earthquakes in the Mariana slab [from Creager and Jordan, 1986]. Slab Model A, used to compute theoretical diagrams, is shown in cross-section *DD'* (right); no vertical exaggeration. Plotting conventions are identical to Figure 3.4. Lines through NW and SE quadrants represent planes tangent to the slab model, which has a vertical dip below 200 km and a local strike of 147°. *P*-wave velocities on model cross-section are contoured at 0.25 km/s intervals; ambient values are radial model of Herrin et al. [1968]. Velocity perturbations were calculated from a thermal model characterized by slab penetration to 1350 km, assuming $\partial v_p/\partial T = -0.5$ m/s/°K. Circles are projections of well-recorded ISC hypocenters within 150 km of section *DD'* in Figure 3.7 about an arc pole at 20°N, 90°E. Theoretical residual spheres were computed by shooting rays through the 3-D slab structure obtained by rotating the 2-D model about this arc pole. The residual-sphere diagrams for both the data and model have been orthogonalized with respect to location parameters and smoothed according to the procedures described in the text.

Figure 3.6. Observed (left) and theoretical (right) residual spheres for *P* waves of Events 5-8, whose epicenters are shown in Figure 3.7. Plotting conventions are identical to Figure 3.4. Slab models used to compute theoretical times correspond to cross-sections *AA'* (Events 5 and 6), *BB'* (Event 7), and *CC'* (Event 8) of Figure 3.7. Residual-sphere patterns for the deep-focus earthquakes indicate slab penetration to depths exceeding 1000 km in all three regions. They also require an increase in slab dip at about 500 km depth.

Figure 3.7. Mercator projection of the Northwest Pacific showing cross-sections through three-dimensional slab models derived by residual-sphere analysis of several intermediate- and deep-focus earthquakes, including Events 5-8 (solid dots), whose residual spheres are shown in Figure 3.6. In all cases, slabs are assumed to penetrate to 1350 km depth, although penetration depths below 1000-1200 km cannot be resolved by the data. Depths are in km; there is no vertical exaggeration. Contour interval is 0.25 km/s.

Figure 4.1. Degree-eight spherical structure averaged over upper 400 km of the mantle, obtained by integrating the *S*-wave travel-time perturbations from Woodhouse and Dzienwonski's [1984] M84C model along vertical ray paths from 40 km to 400 km. Darker areas are faster regions.

Figure 4.2. Projection of the M84C travel-time anomaly map shown in Figure 4.1 onto the GTR1 tectonic regionalization shown in Figure 2.1. Spherical harmonic expansions of the six geographical functions of GTR1 were truncated at degree eight prior to performing the projection. Darker areas are faster regions.

Figure 4.3. Degree-eight pattern obtained by subtracting Figure 4.2 from Figure 4.1. Darker areas are faster regions.

Figure 4.4. Degree-eight spherical structure averaged over the transition zone, obtained by integrating the *S*-wave travel-time perturbations from Woodhouse and Dzienwonski's [1984] M84C model along vertical ray paths from 400 km to 650 km. Darker areas are faster regions.

Figure 4.5. Comparison of degree-two transition-zone structure derived from Woodhouse and Dziewonski's [1984] M84C model (upper panel) with the transition-zone model of Masters et al. [1982] (lower panel). *S*-wave travel-time perturbations computed by integrating models along vertical ray paths from 400 km to 650 km. Darker areas are faster regions.

Figure 4.6. Degree-two component of surface divergence computed by Forte and Peltier [1986] from Minster and Jordan's [1978] plate-motion model. The close correspondence of convergence (dashed contours) with the high-velocity regions of Figure 4.5 suggests that the transition-zone anomalies seen in the seismic data are dominated by cold downwellings in the large-scale flow.

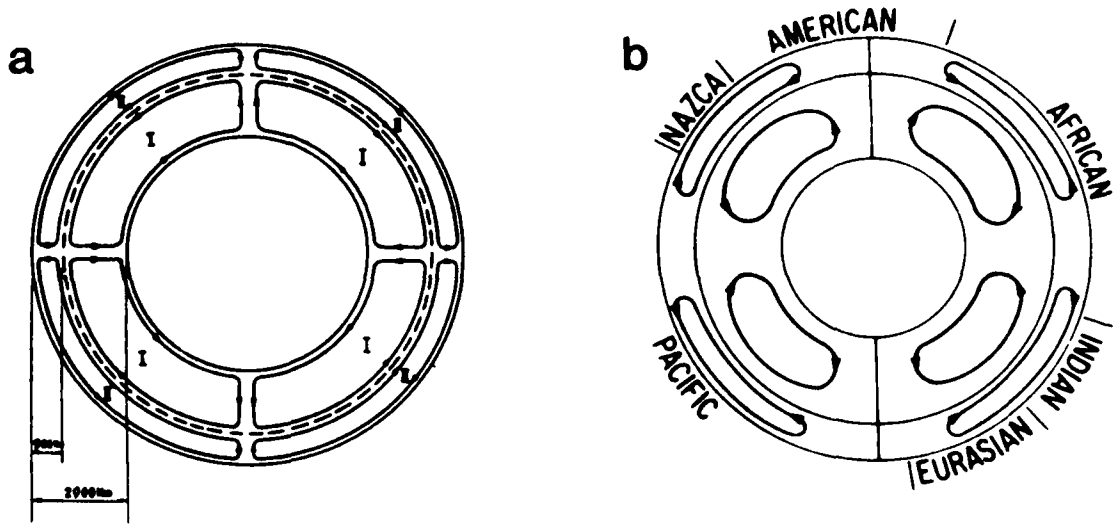

Figure 1.1

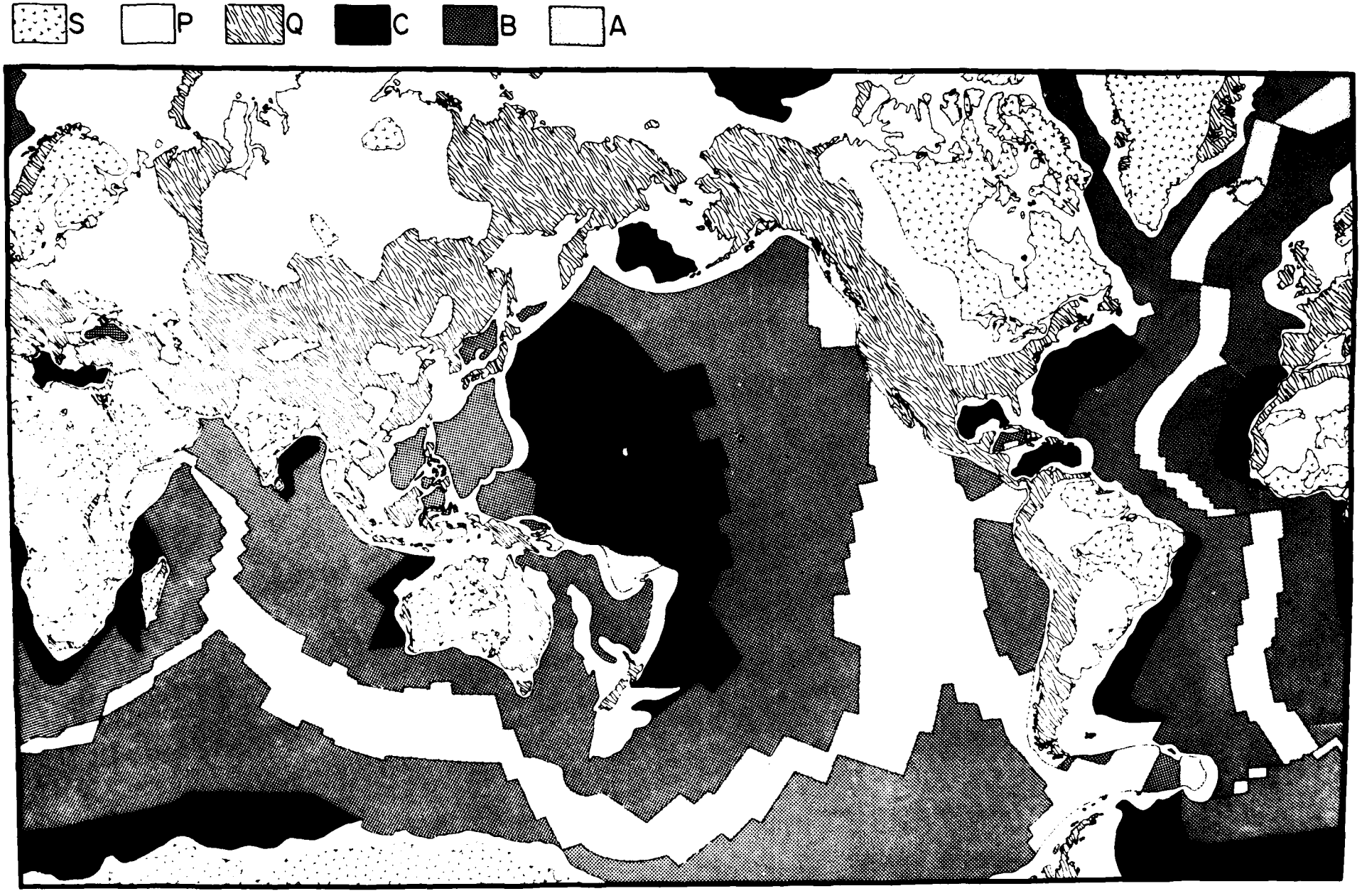

Figure 2.1

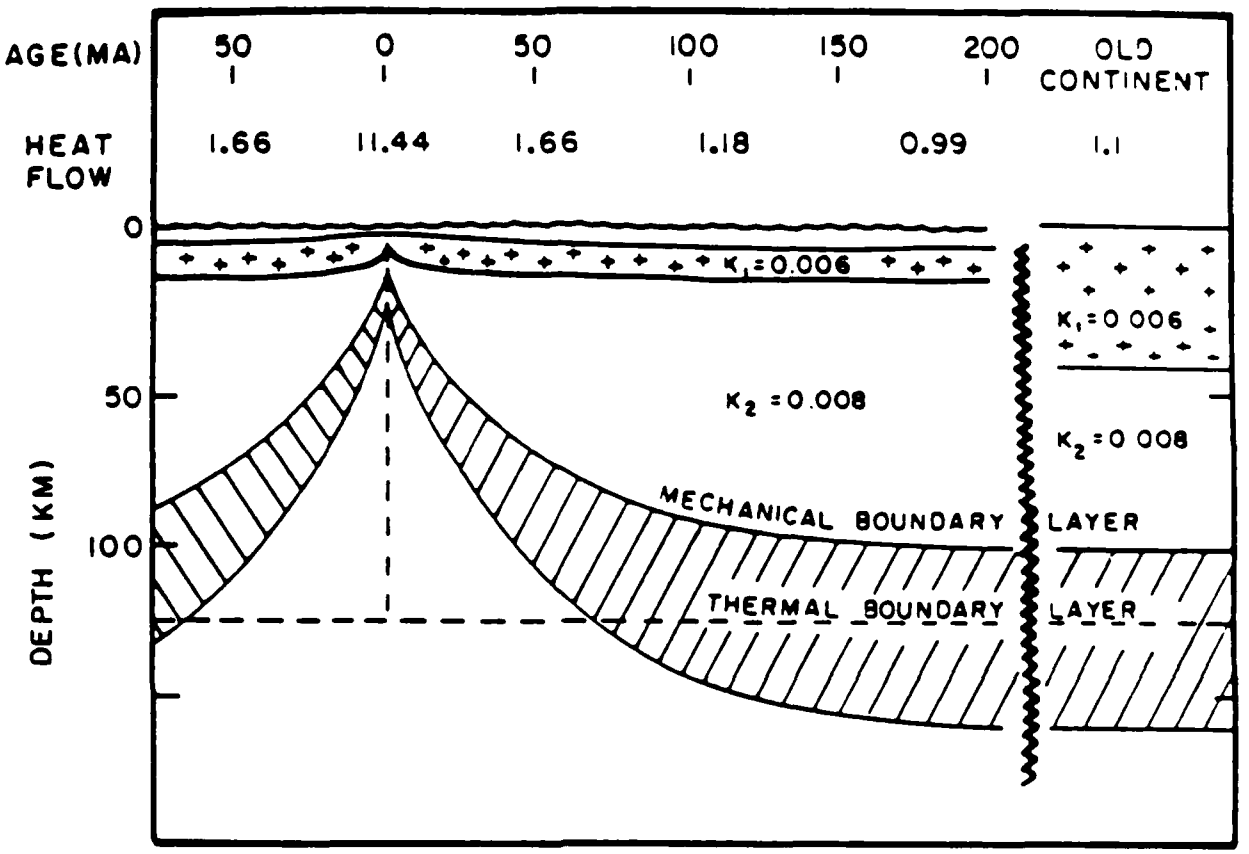
AGE(MA)
50
0
50
100
150
200
OLD CONTINENT
HEAT FLOW
1.66
11.44
1.66
1.18
0.99
1.1
0
50
100
DEPTH (KM)
K1=0.006
K2 =0.008
K1=0.006
K2=0.008
MECHANICAL BOUNDARY LAYER
THERMAL BOUNDARY LAYER

Figure 2.2

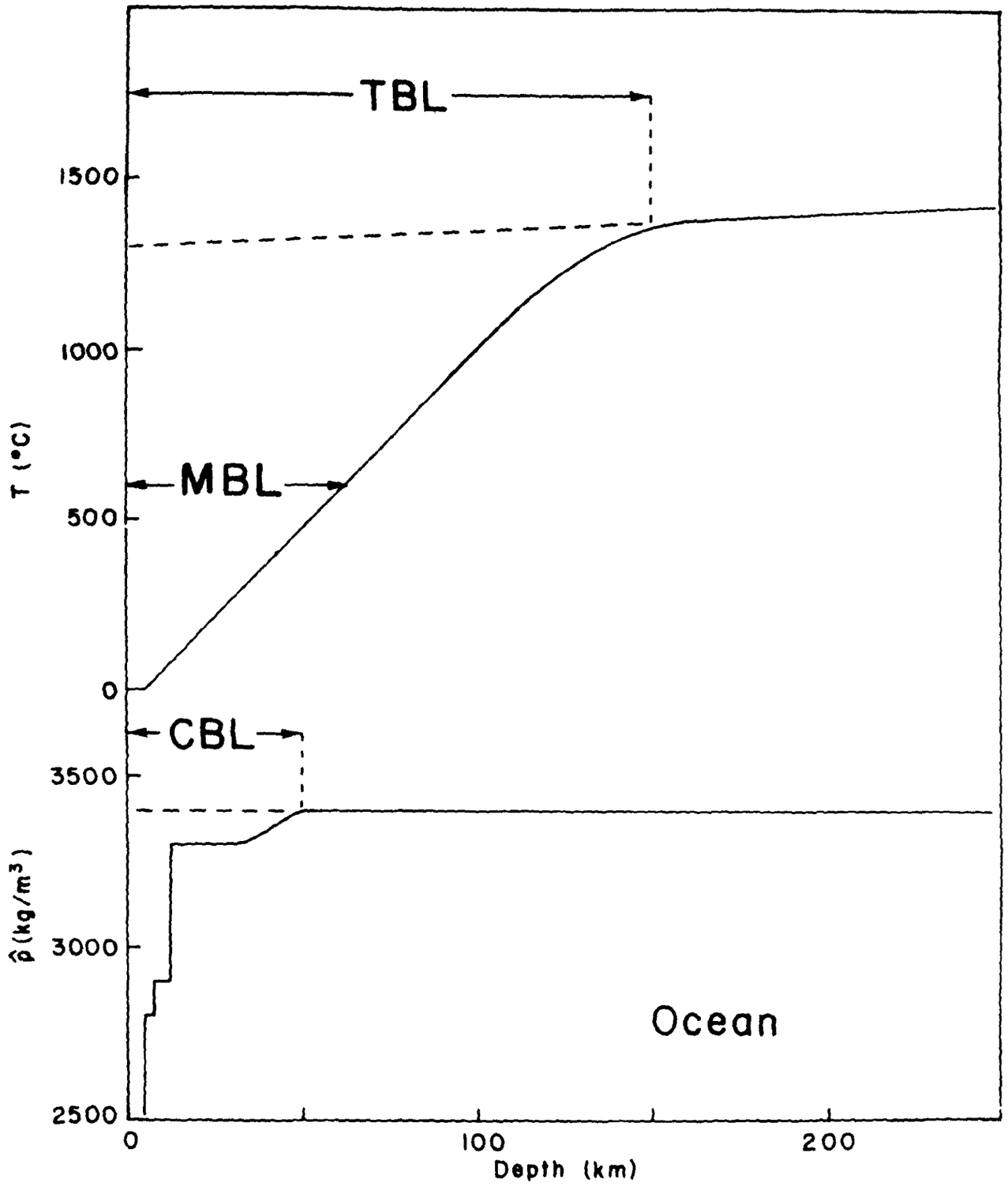
TBL
MBL
CBL
1500
1000
500
0
3500
3000
2500
T (°C)
ρ̂(kg/m³)
Ocean
0
100
200
Depth (km)

Figure 2.3

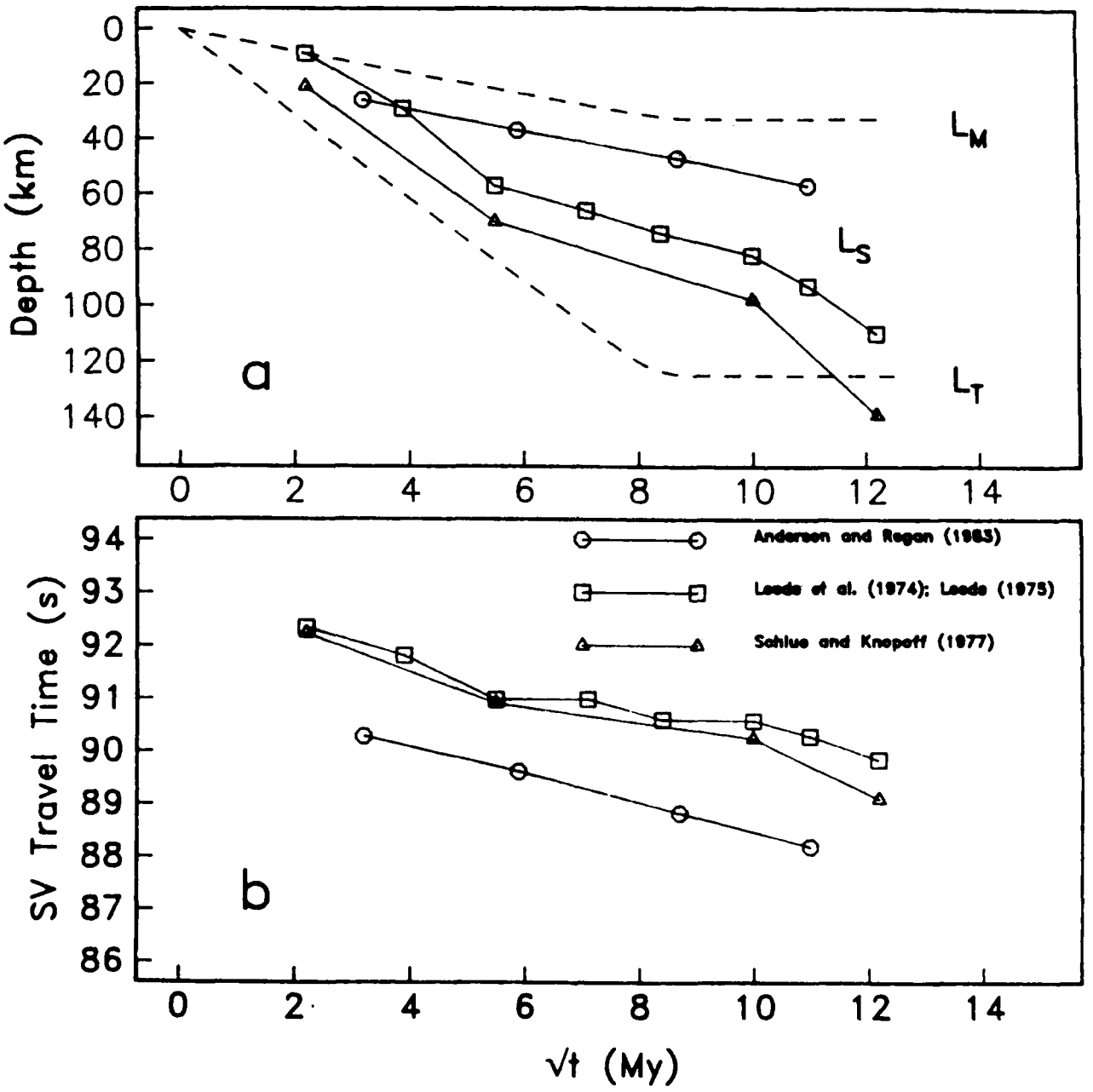
Depth (km)
0
20
40
60
80
100
120
140
a
L_M
L_S
L_T
0
2
4
6
8
10
12
14
SV Travel Time (s)
94
93
92
91
90
89
88
87
86
b
Anderson and Regan (1983)
Leeds et al. (1974); Leeds (1975)
Schlue and Knopoff (1977)
√t (My)

Figure 2.4

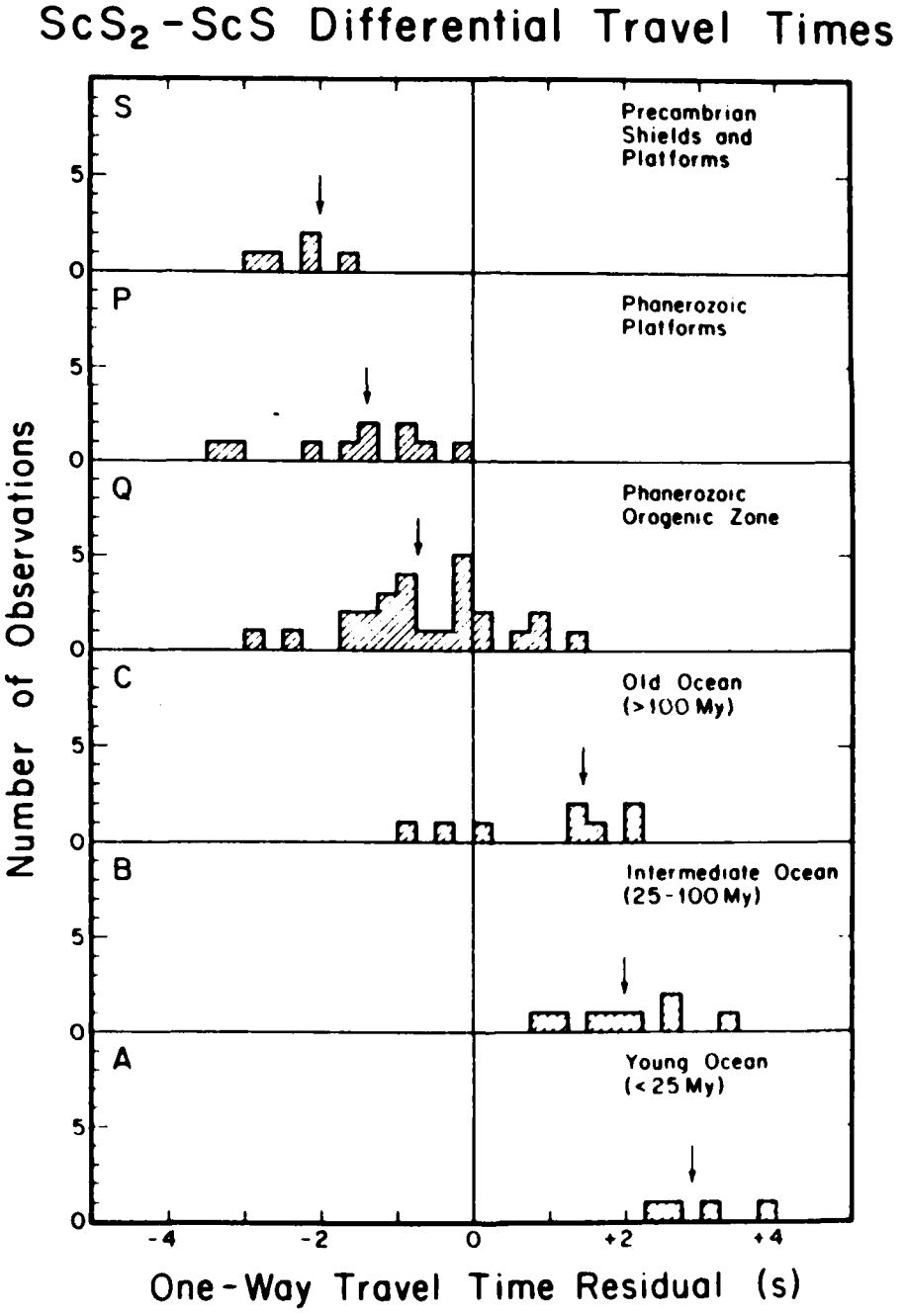
ScS2-ScS Differential Travel Times
S
Precambrian Shields and Platforms
P
Phanerozoic Platforms
Q
Phanerozoic Orogenic Zone
C
Old Ocean (>100 My)
B
Intermediate Ocean (25-100 My)
A
Young Ocean (<25 My)
Number of Observations
0
5
-4
-2
0
+2
+4
One-Way Travel Time Residual (s)

Figure 2.5

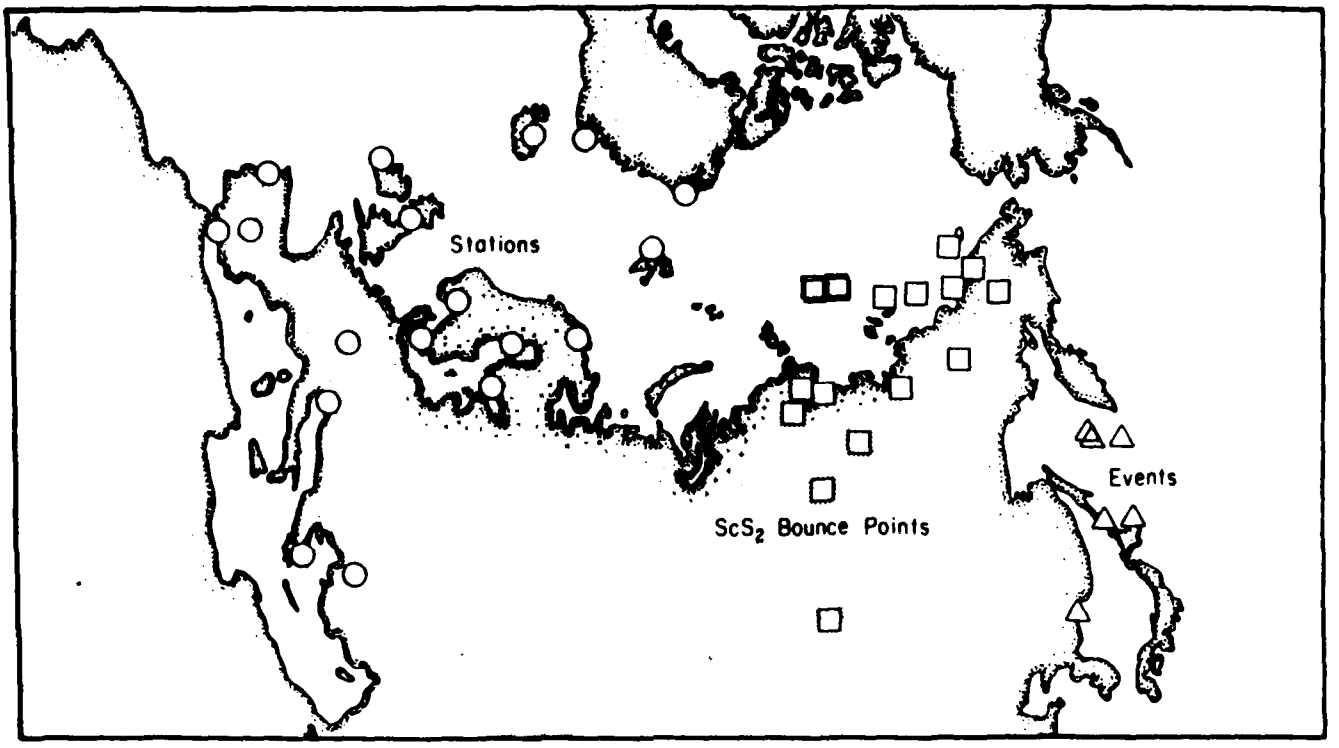
Stations
Events
ScS_2 Bounce Points

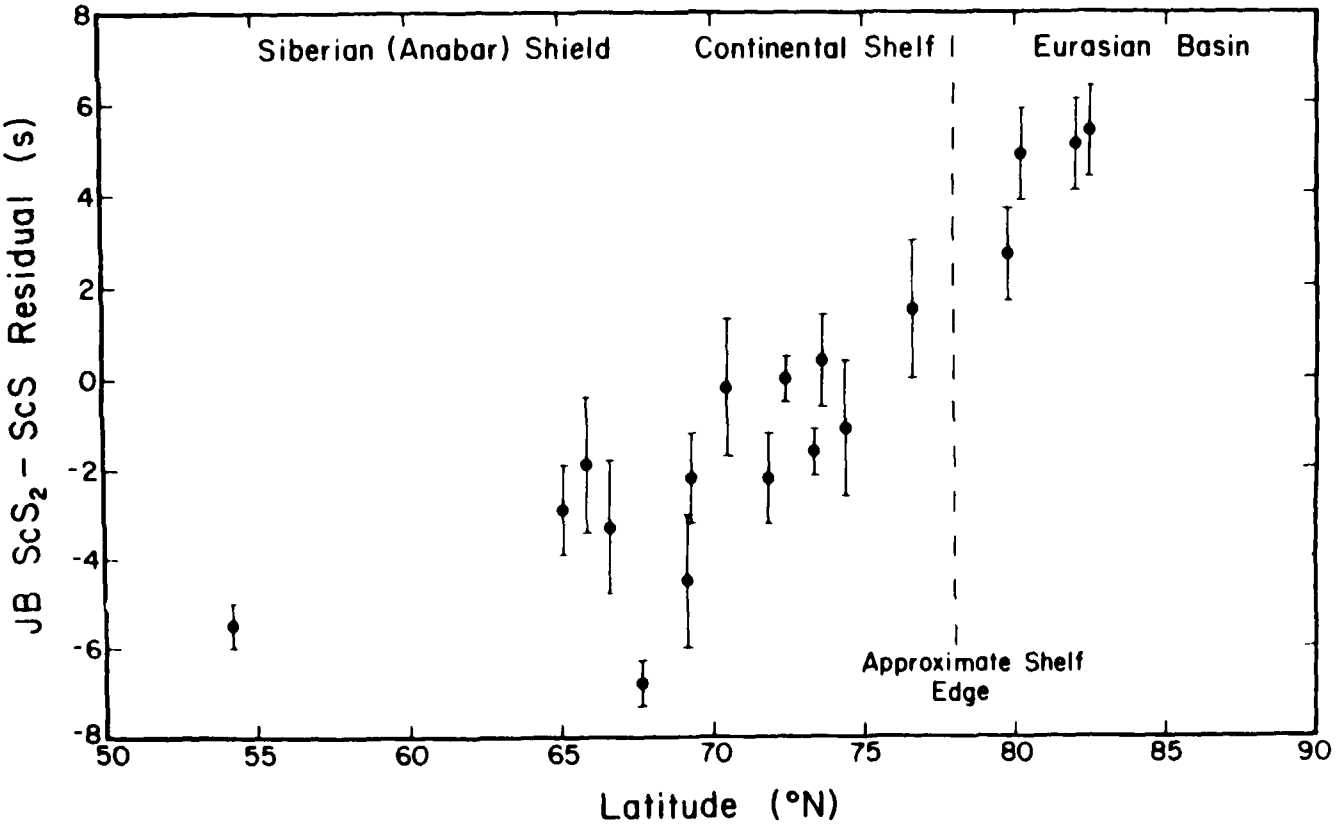
Siberian (Anabar) Shield
Continental Shelf
Eurasian Basin
Approximate Shelf Edge
JB ScS_2 – ScS Residual (s)
Latitude (°N)
8
6
4
2
0
-2
-4
-6
-8
50
55
60
65
70
75
80
85
90

Figure 2.6

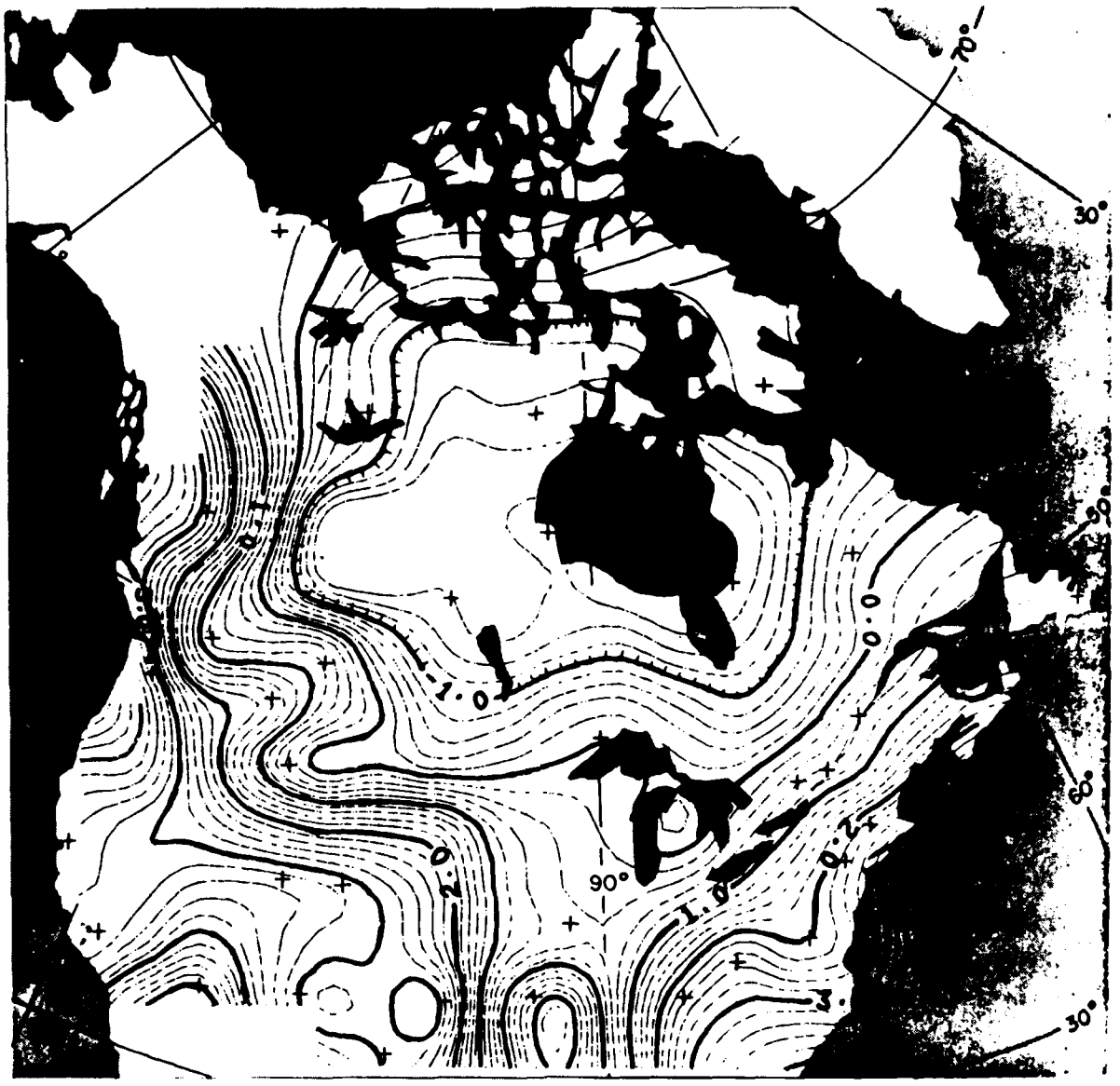

Figure 2.7

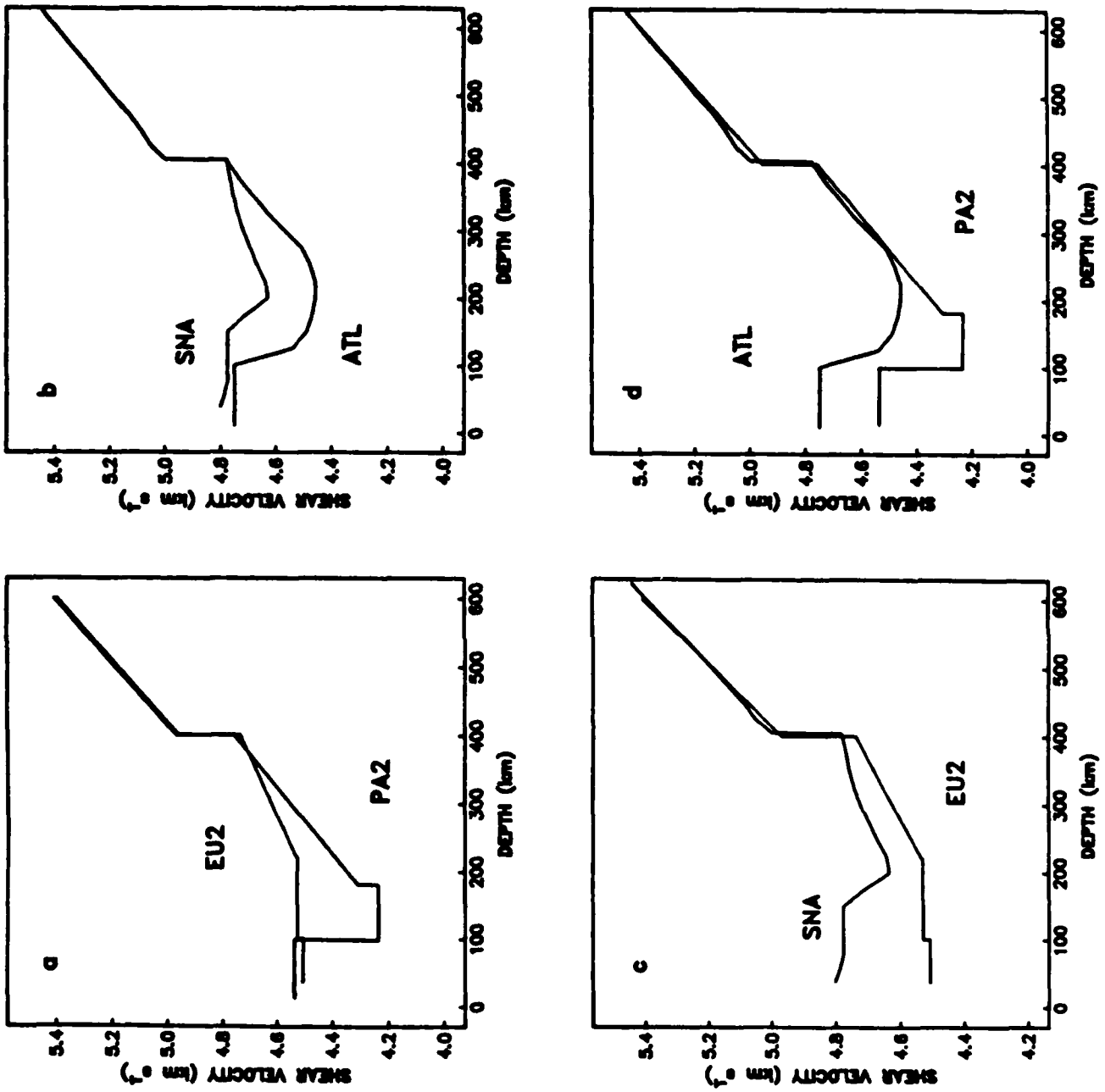
a
EU2
PA2
b
SNA
ATL
c
SNA
EU2
d
ATL
PA2
SHEAR VELOCITY (km s⁻¹)
DEPTH (km)
5.4
5.2
5.0
4.8
4.6
4.4
4.2
4.0
0
100
200
300
400
500
600

Figure 2.8

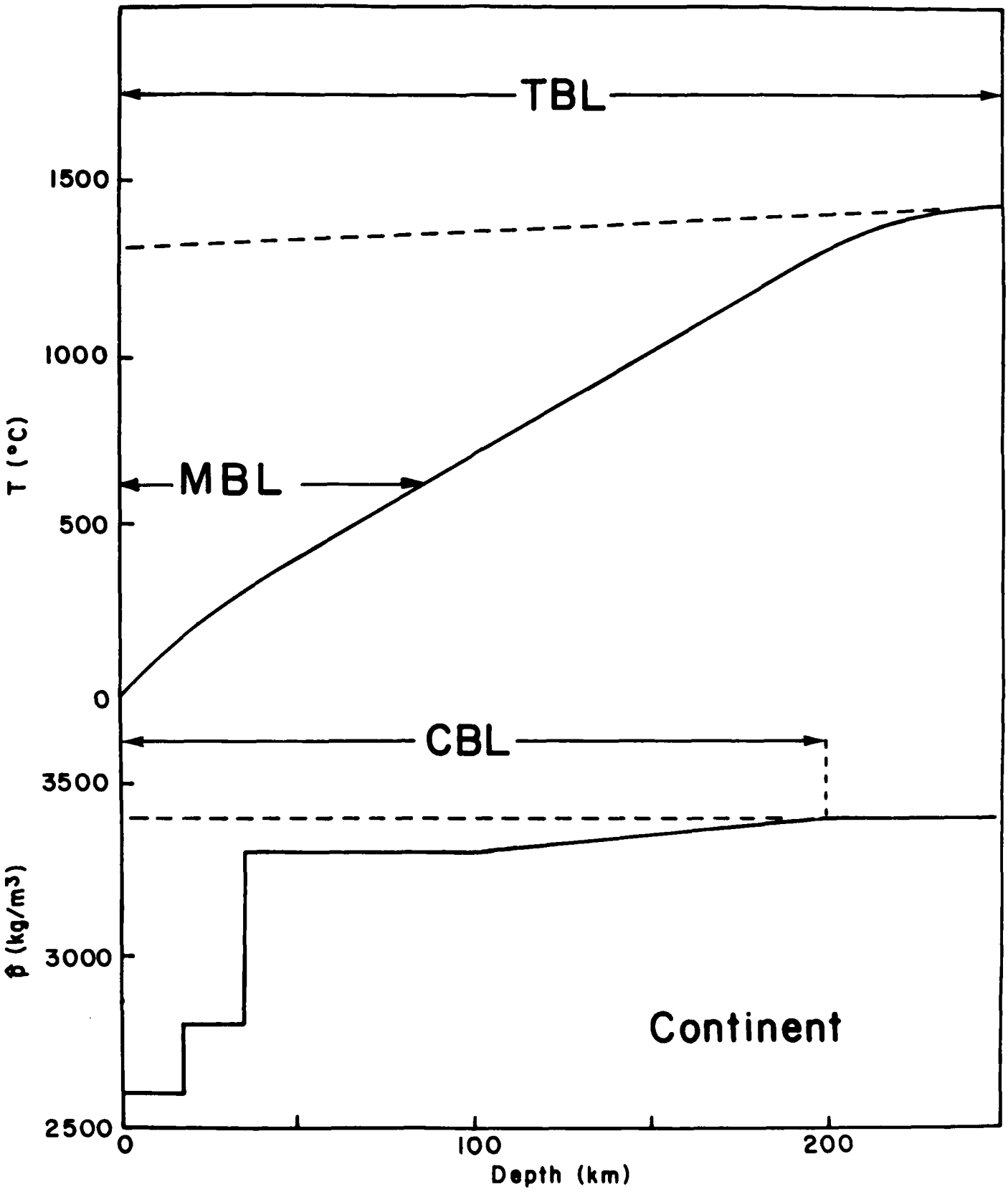
TBL
1500
1000
T (°C)
MBL
500
0
CBL
3500
β (kg/m³)
3000
Continent
2500
0
100
200
Depth (km)

Figure 2.9

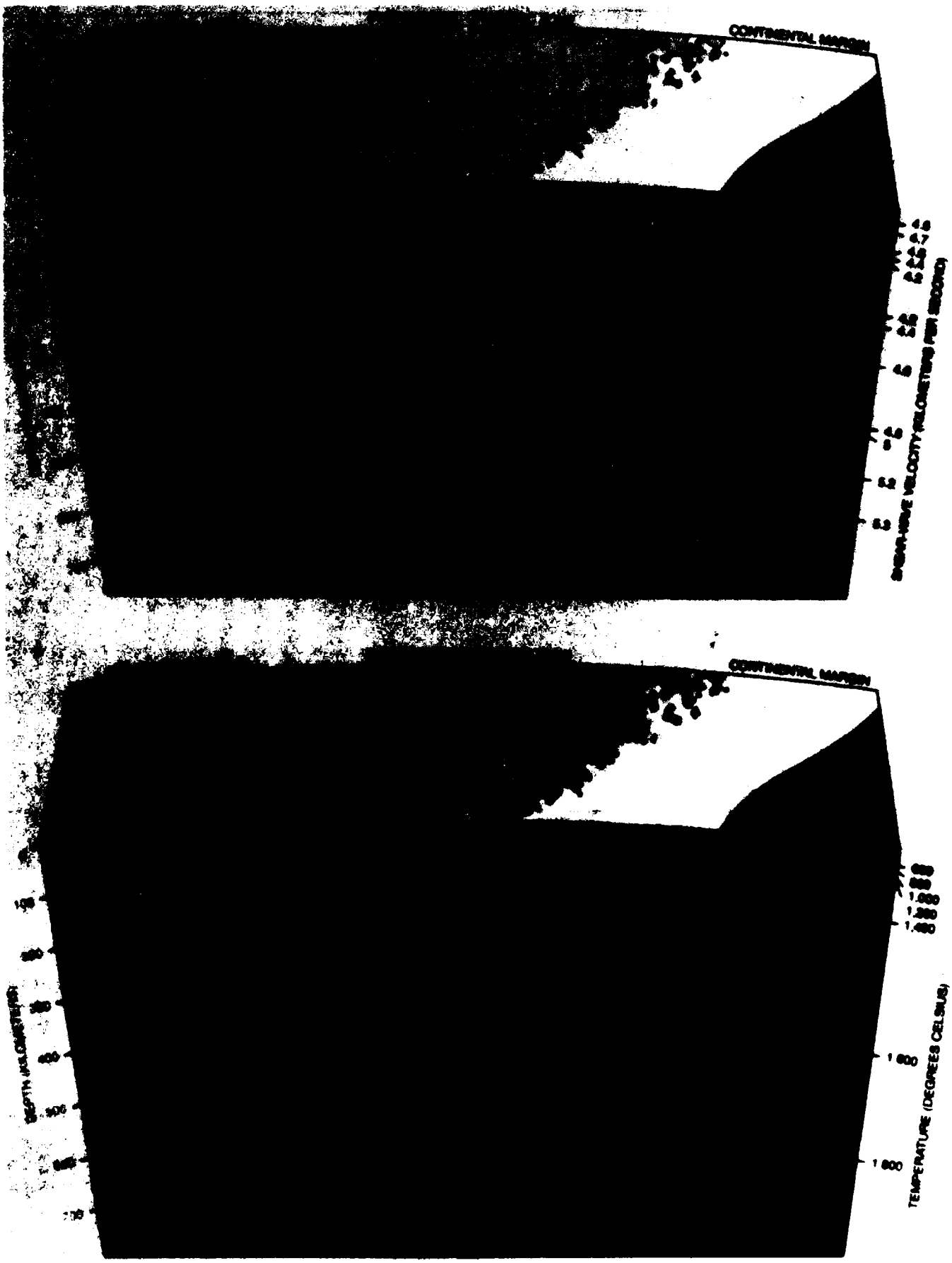
CONTINENTAL MARGIN
CONTINENTAL MARGIN
TEMPERATURE (DEGREES CELSIUS)

Figure 2.10

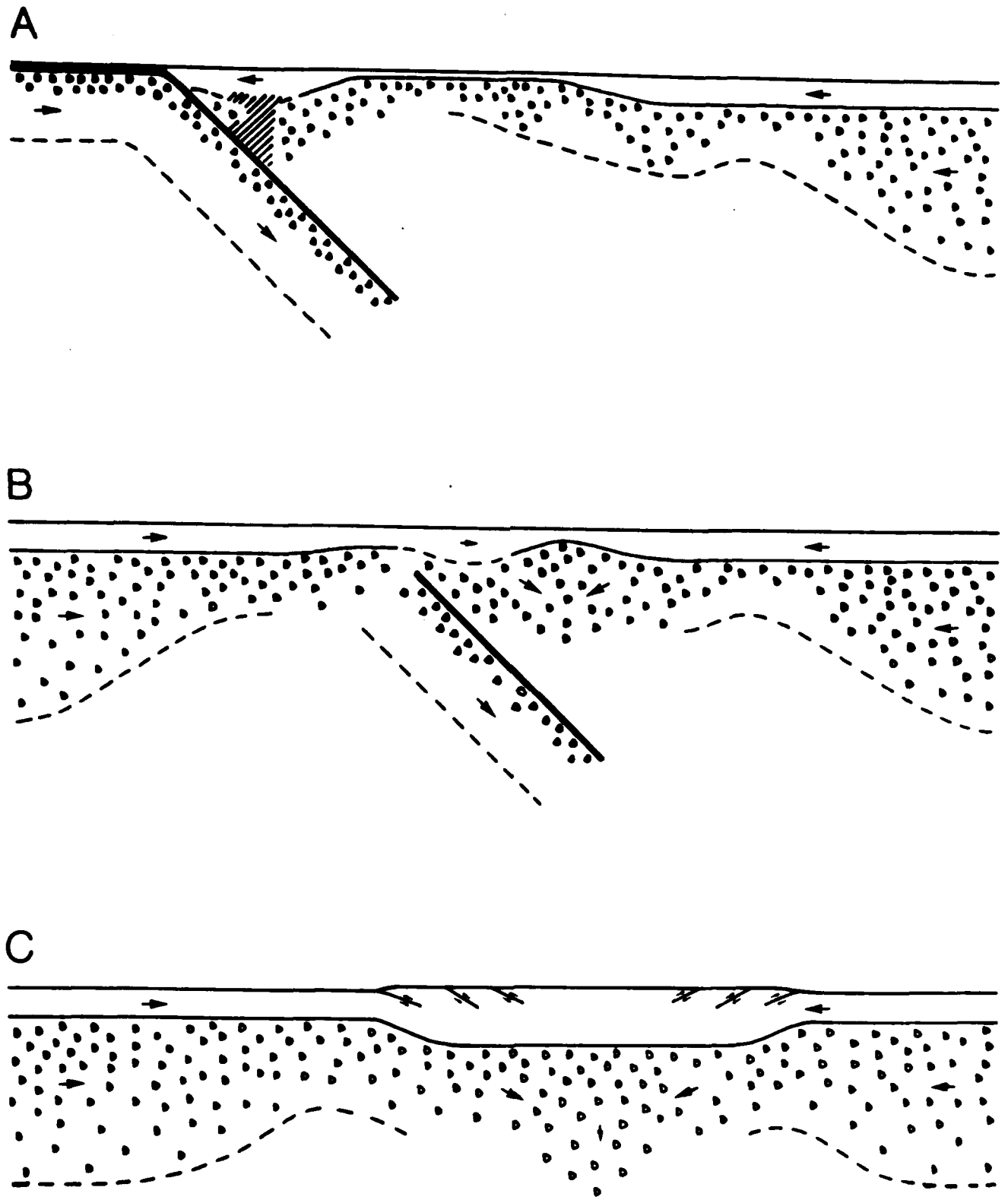

Figure 2.11

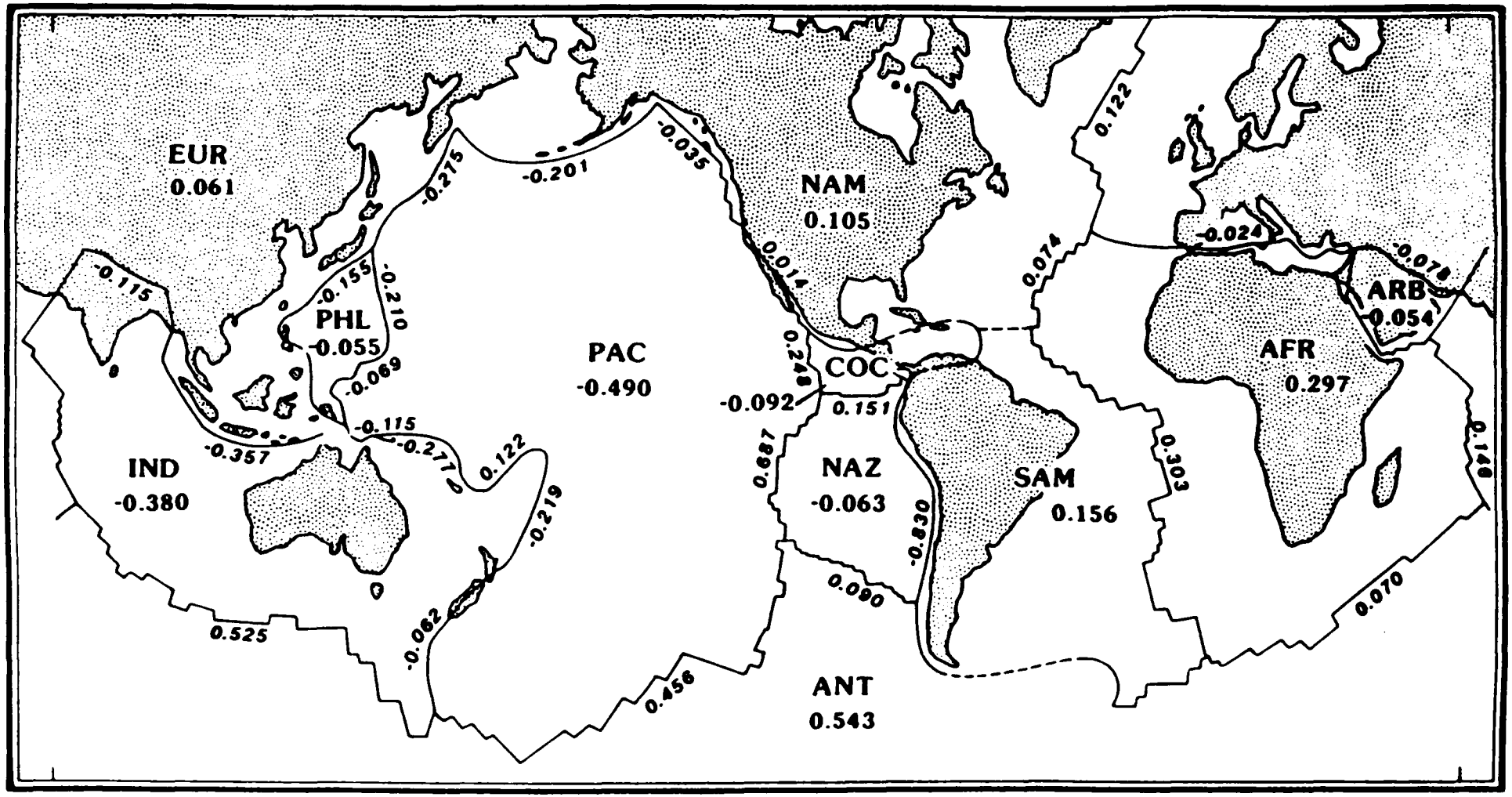
EUR
0.061
PAC
-0.490
NAM
0.105
PHL
-0.055
COC
-0.092
IND
-0.380
NAZ
-0.063
SAM
0.156
AFR
0.297
ARB
-0.054
ANT
0.543
-0.215
-0.201
-0.035
0.122
-0.024
-0.078
0.074
0.014
-0.115
-0.155
-0.210
-0.069
0.248
0.151
-0.115
-0.277
-0.357
0.122
-0.219
0.687
-0.303
-0.830
0.140
0.090
0.070
0.525
-0.062
0.456

Figure 3.1

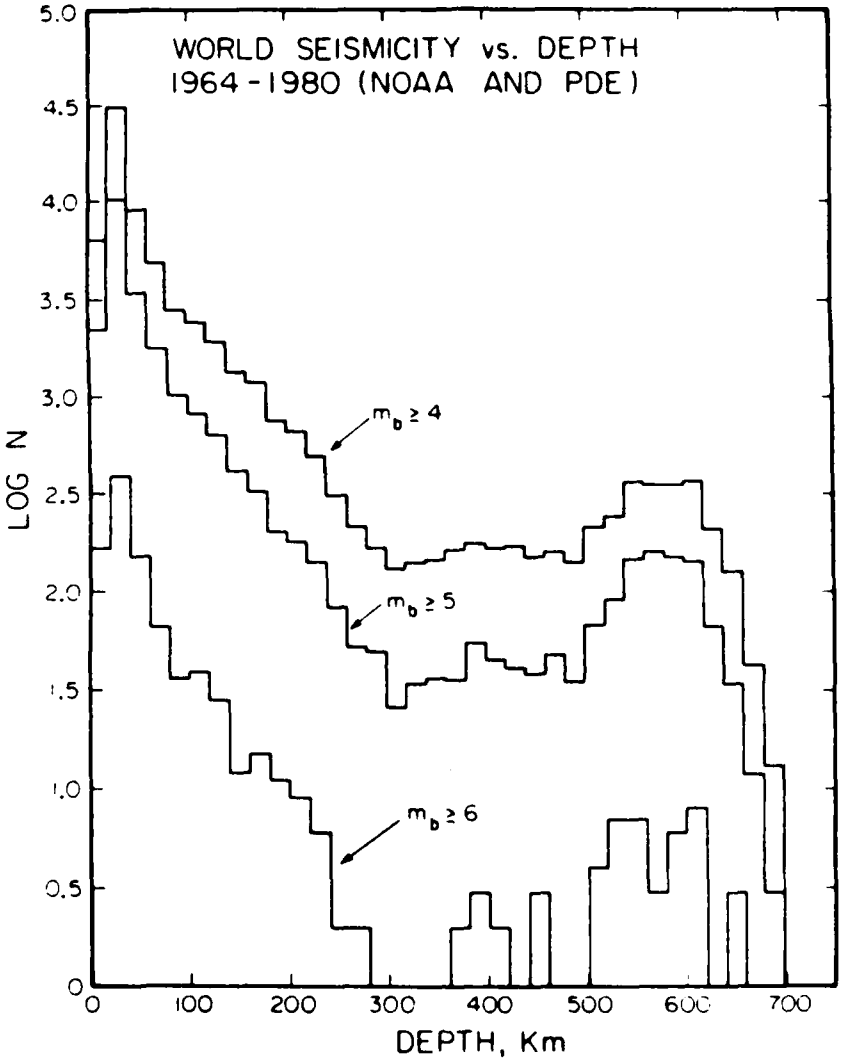
WORLD SEISMICITY vs. DEPTH
1964 - 1980 (NOAA AND PDE)
LOG N
DEPTH, Km
$m_b \geq 4$
$m_b \geq 5$
$m_b \geq 6$
5.0
4.5
4.0
3.5
3.0
2.5
2.0
1.5
1.0
0.5
0
0
100
200
300
400
500
600
700

Figure 3.2

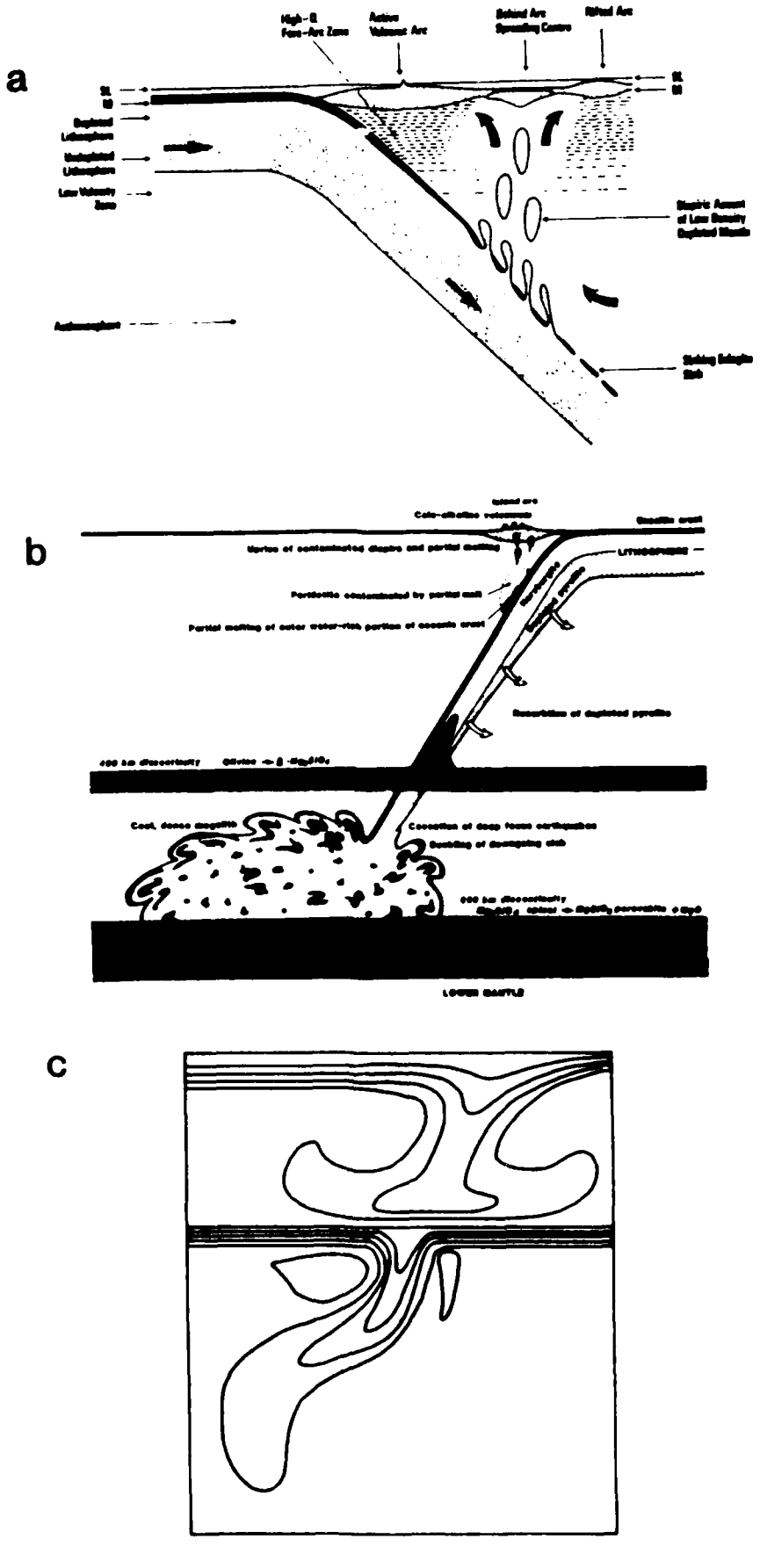

Figure 3.3

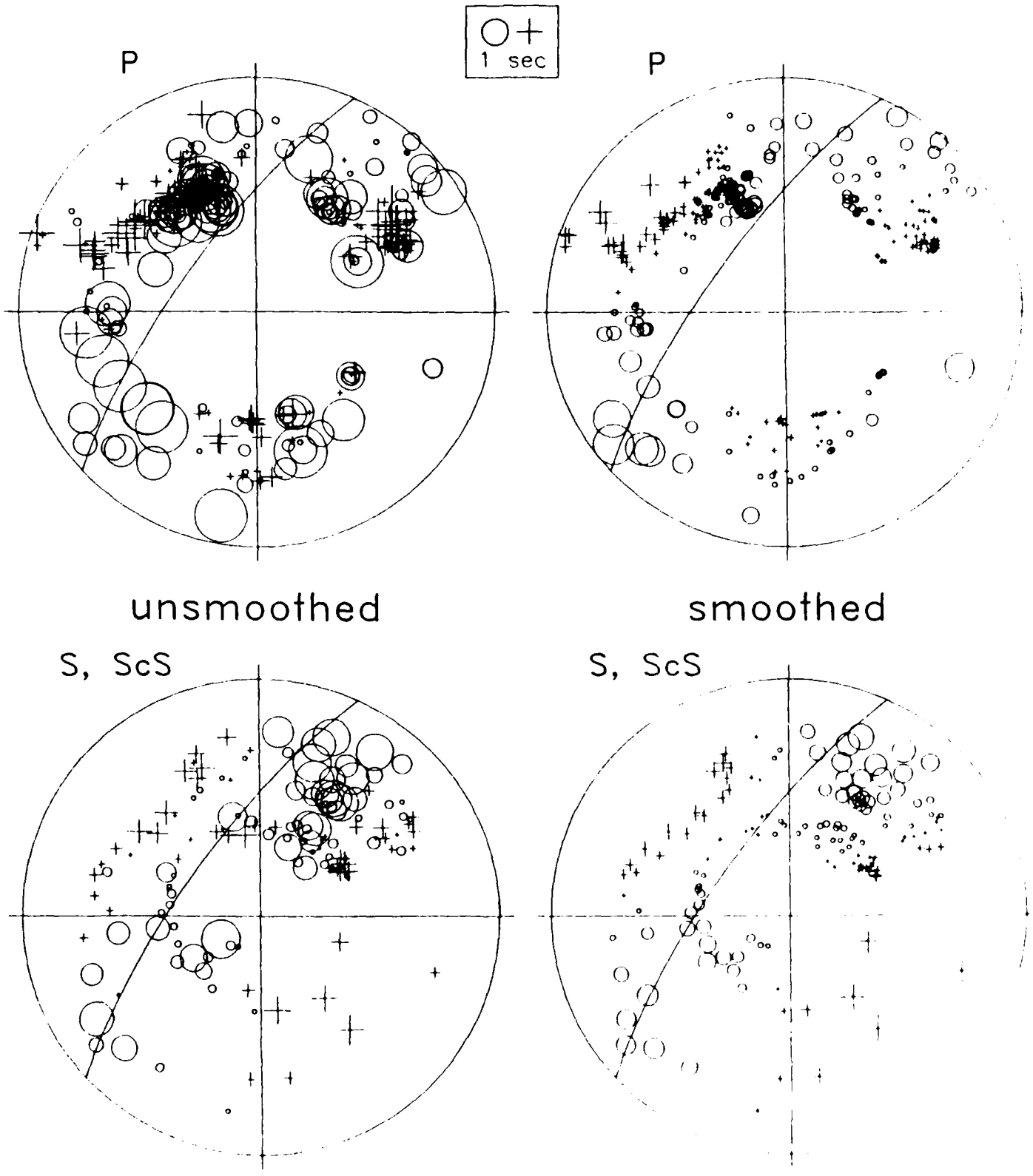

Figure 3.4

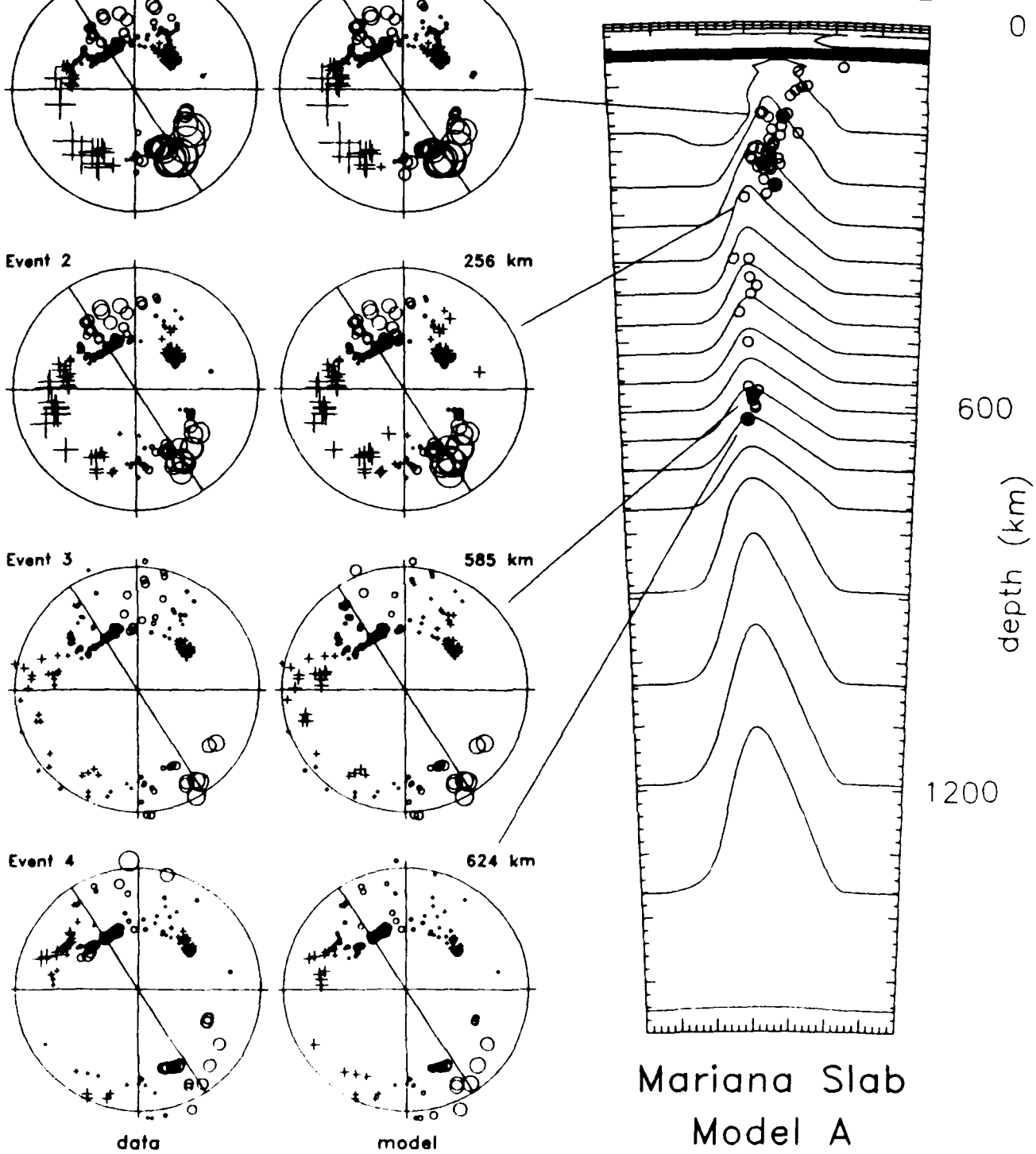
1 sec
Event 1
149 km
Event 2
256 km
Event 3
585 km
Event 4
624 km
data
model
D
D'
0
600
1200
depth (km)
Mariana Slab
Model A

Figure 3.5

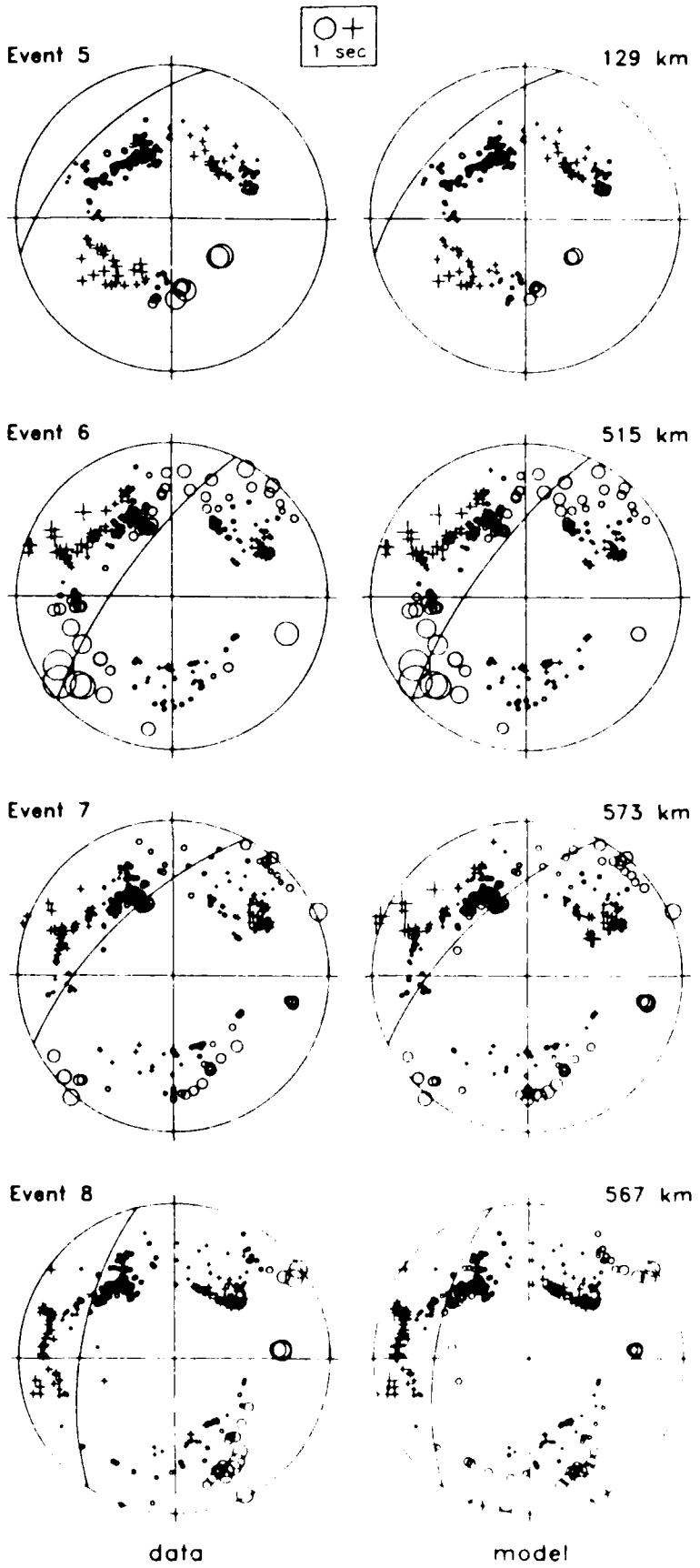
O+
1 sec
Event 5
129 km
Event 6
515 km
Event 7
573 km
Event 8
567 km
data
model

Figure 3.6

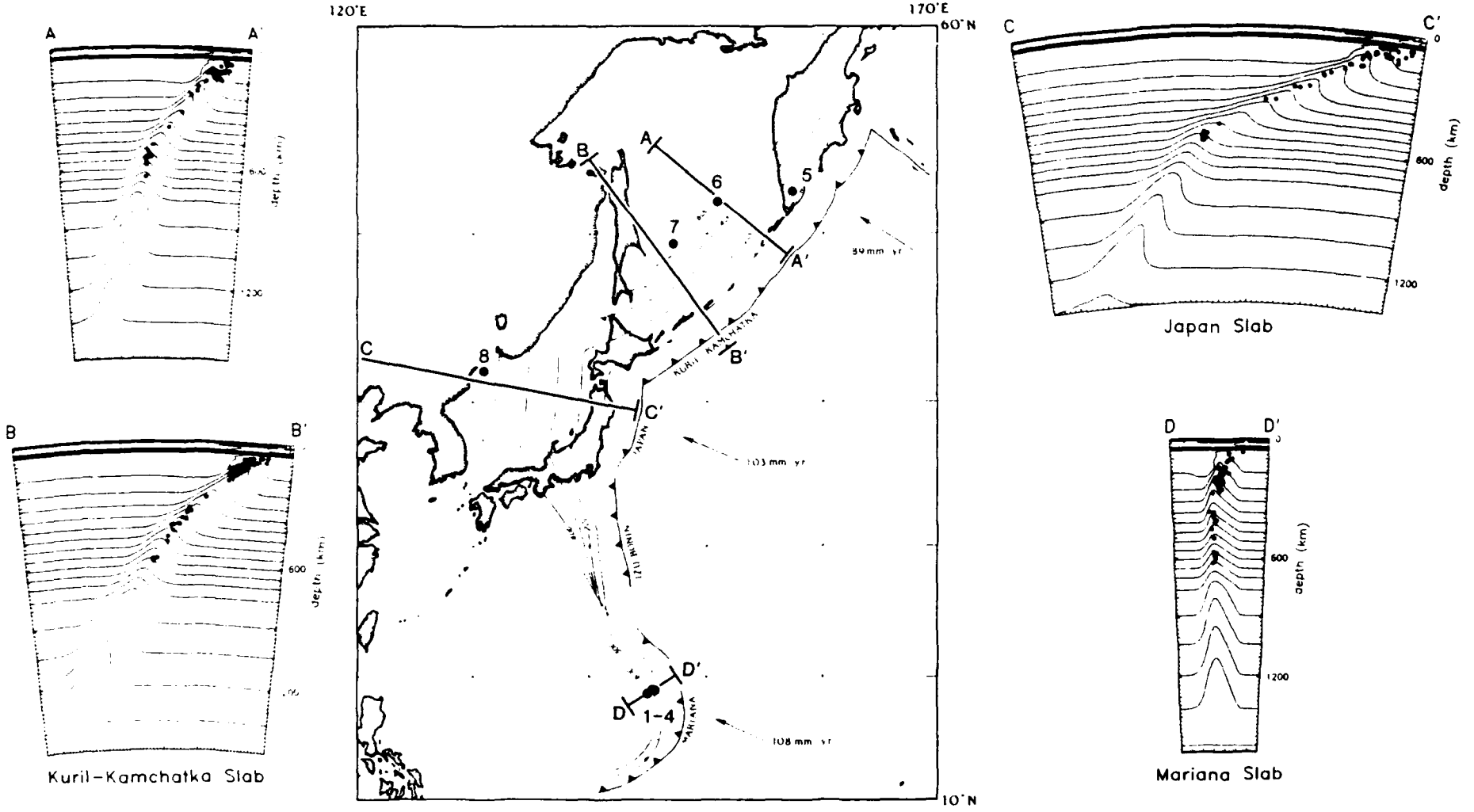
120°E
170°E
60°N
10°N
A
A'
B
B'
C
C'
D
D'
5
6
7
8
1-4
89 mm yr
103 mm yr
108 mm yr
KURIL KAMCHATKA
JAPAN
IZU BONIN
MARIANA
depth (km)
600
1200
Kuril-Kamchatka Slab
Japan Slab
Mariana Slab

Figure 3.7

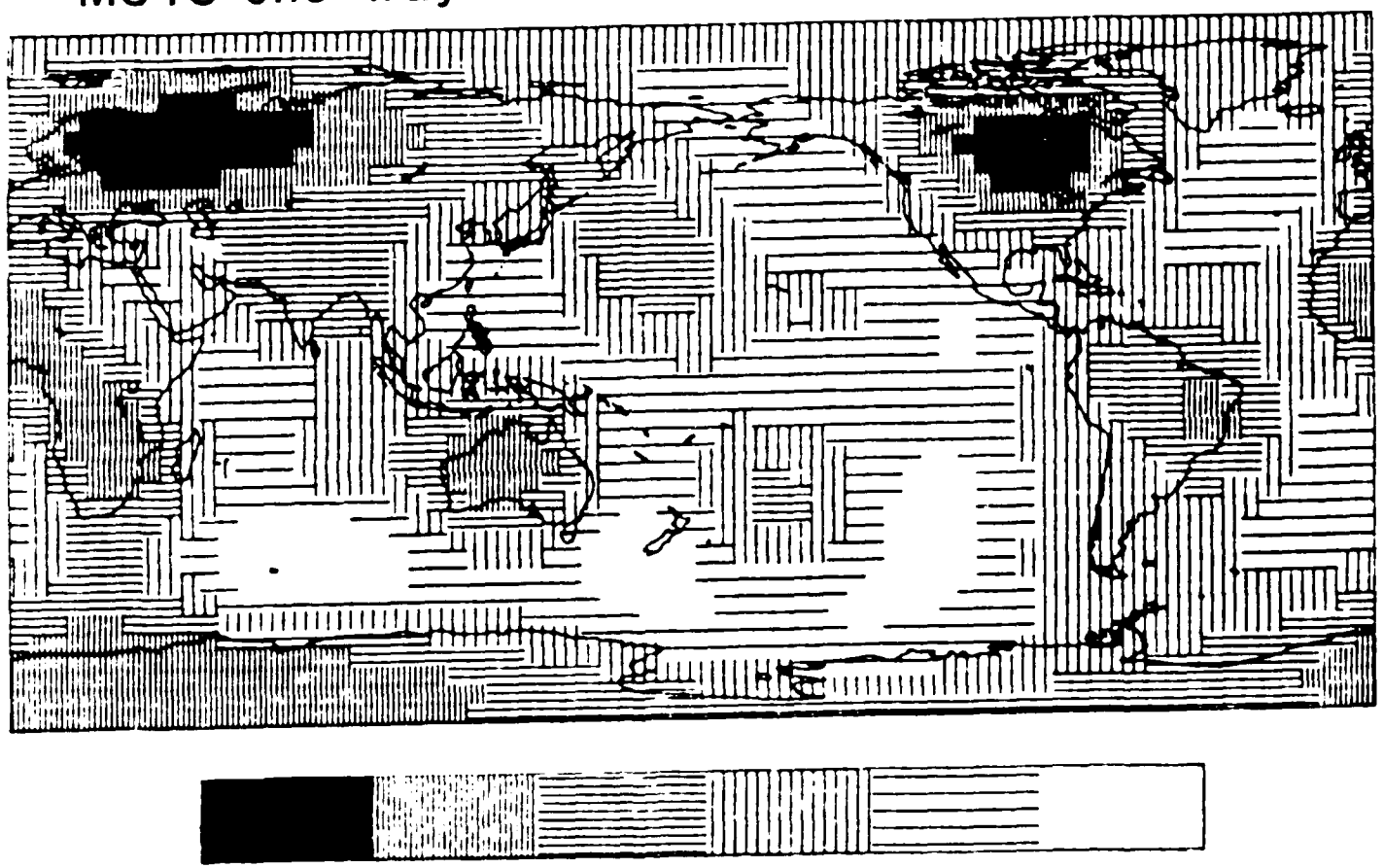
M84C one-way S-time between 400 and 40 km
-4.2%
Vertical S-time Anomaly
+3.1%

Figure
4.1

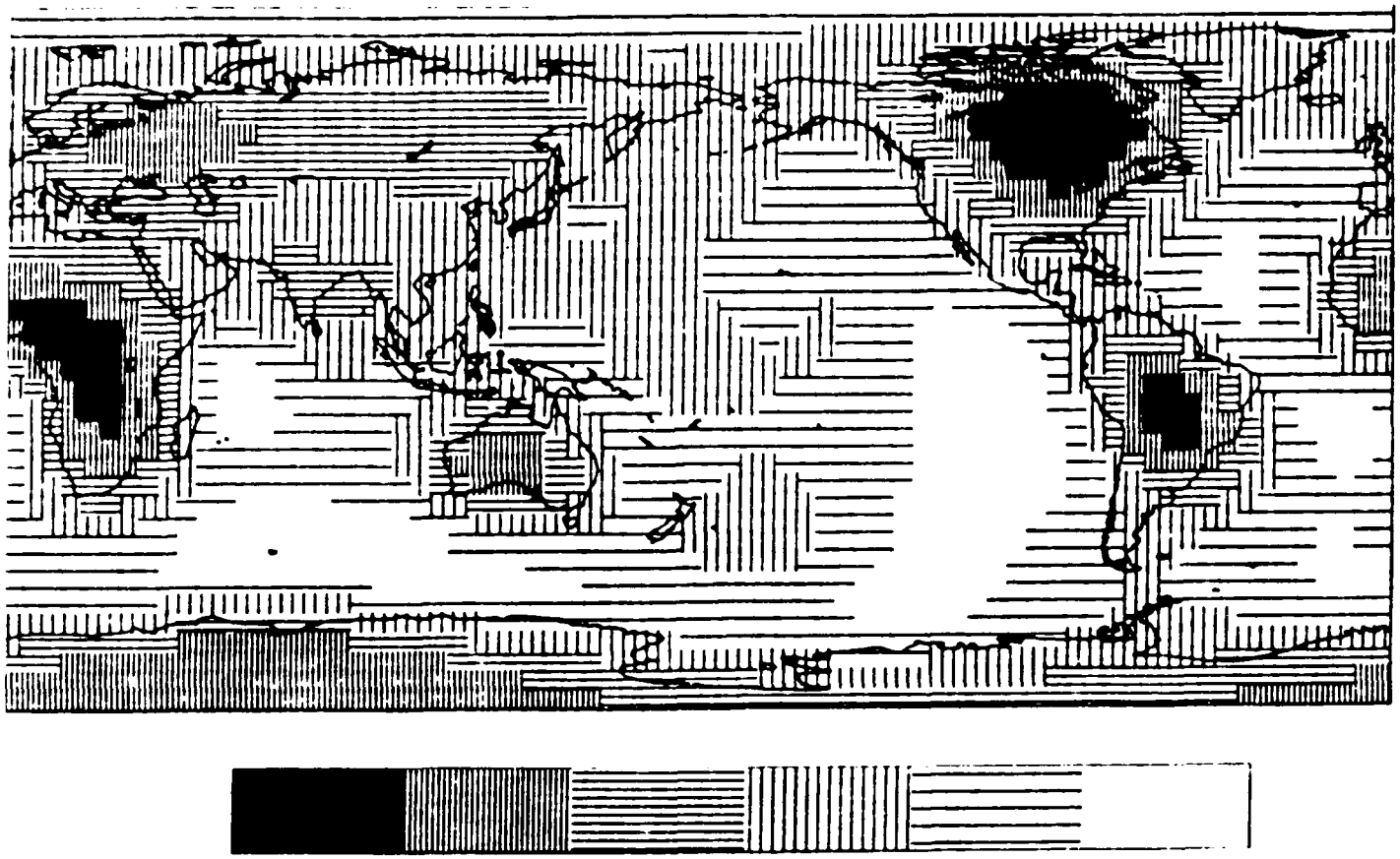

Figure
4.2

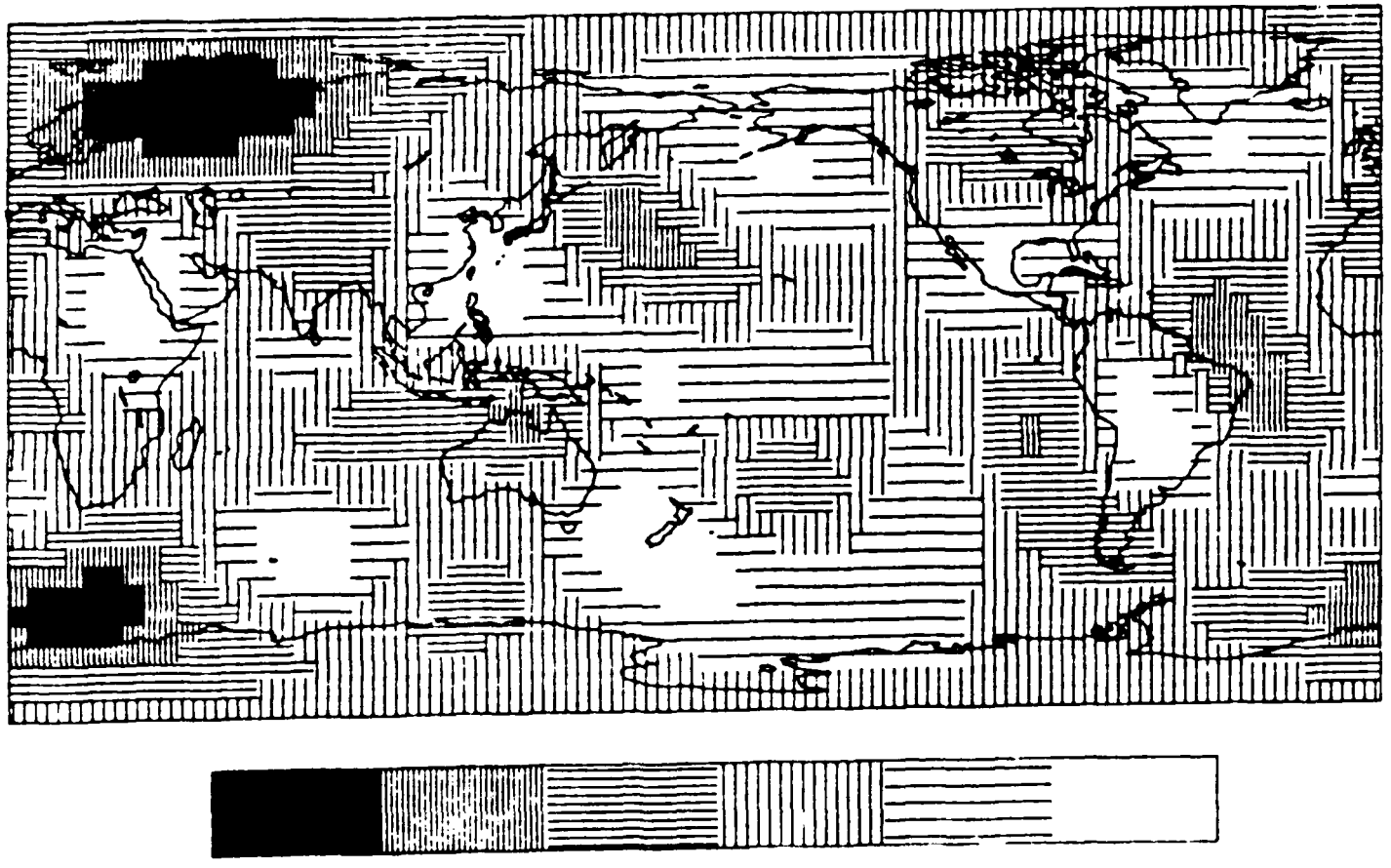
Residual one-way S-time (M84C - projected)
-2.8%
Vertical S-time Anomaly
+1.9%

Figure
4.3

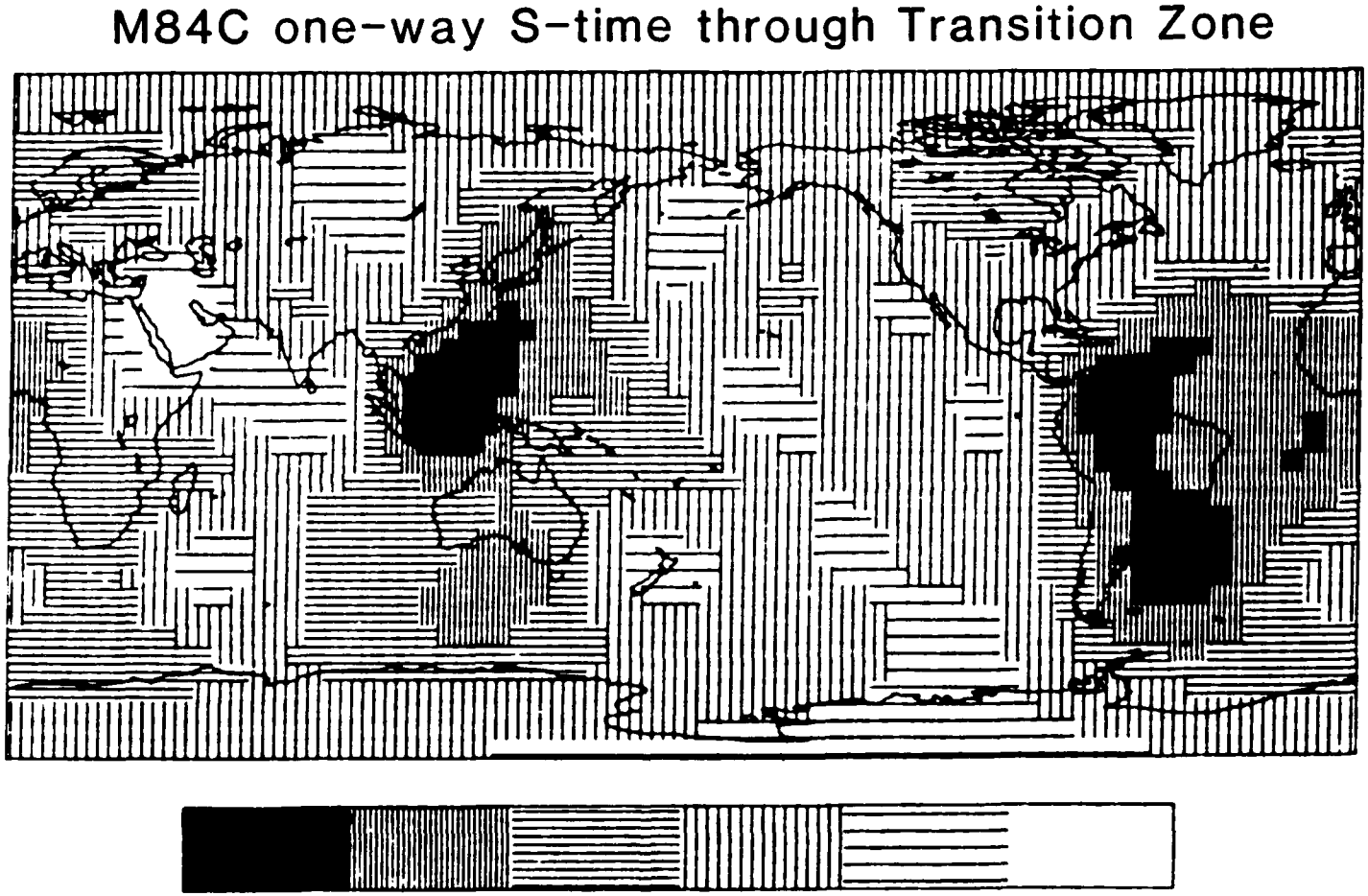
M84C one-way S-time through Transition Zone
-2.0%
Vertical S-time Anomaly
+2.0%

Figure
4.4

M84C

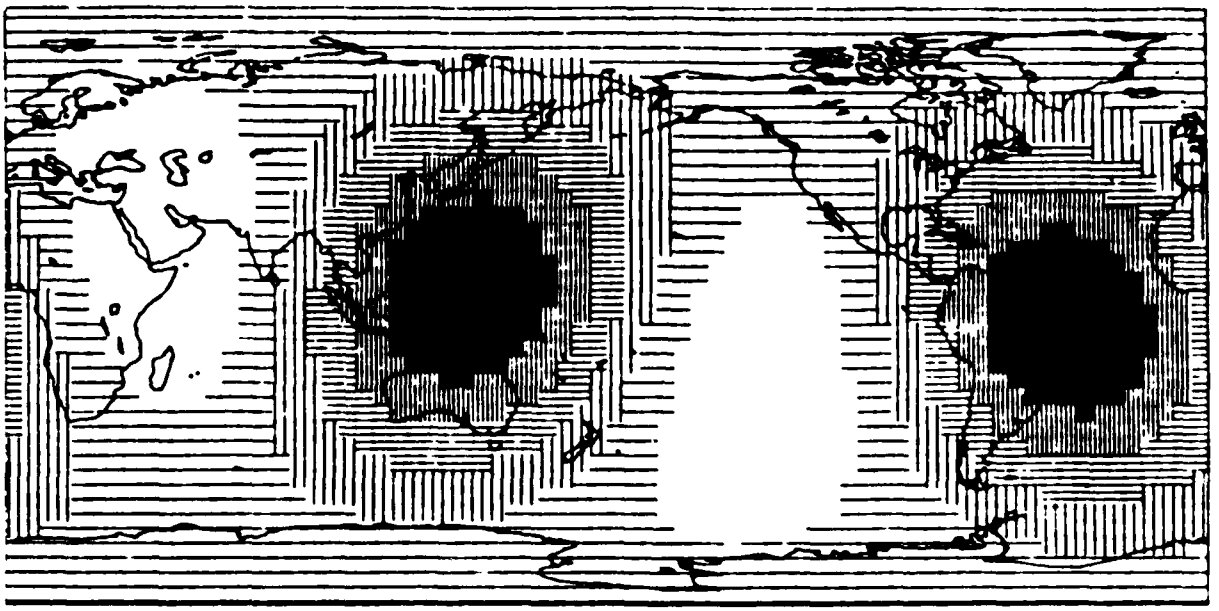

-1.2% Vertical S-time Anomaly +0.8%

Masters et al. (1982)

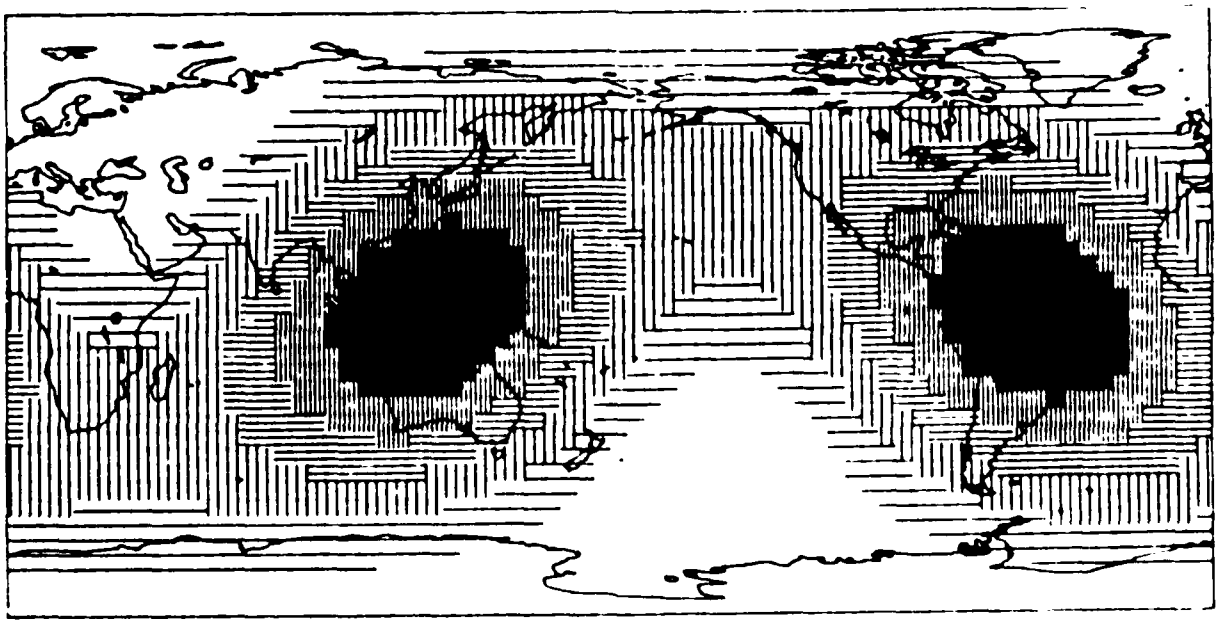

-1.2% Vertical S-time Anomaly +1.0%

Figure
4.5

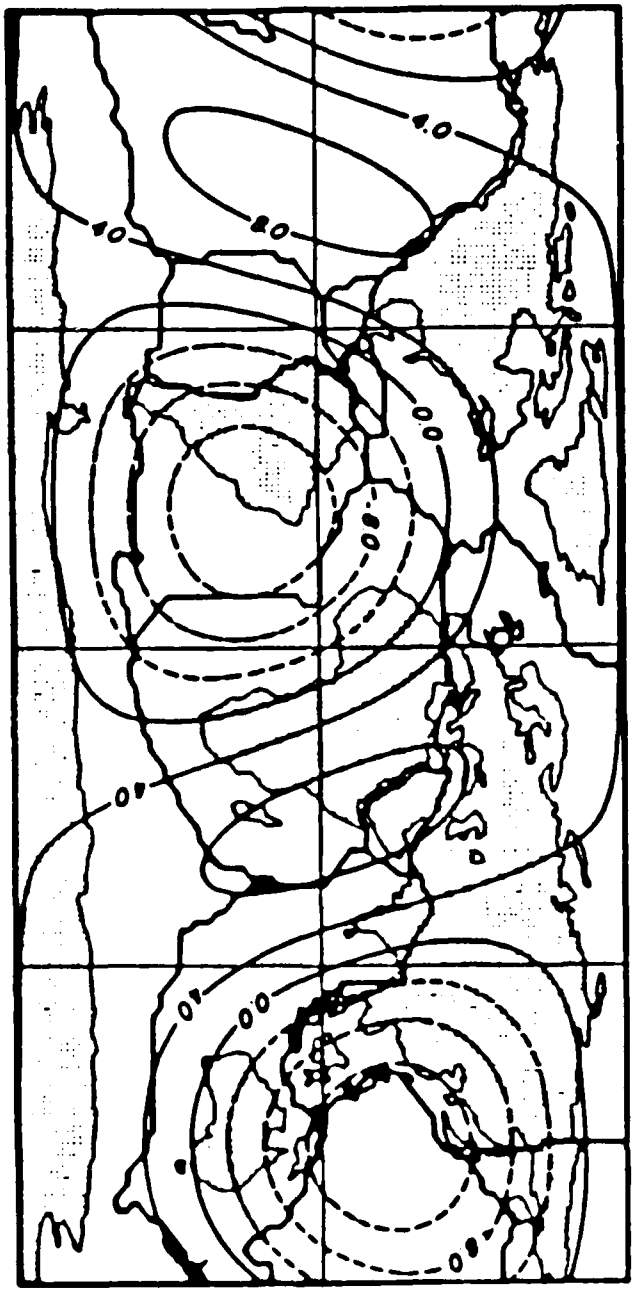

Figure
4.6

Moment-Tensor Spectra of the 19 Sept 85 and 21 Sept 85 Michoacan, Mexico, Earthquakes

MARK A. RIEDESEL

Institute for Geophysics, University of Texas, Austin, TX 78751

THOMAS H. JORDAN AND ANNE F. SHEEHAN

Department of Earth, Atmospheric and Planetary Sciences, MIT, Cambridge, MA 02139

PAUL G. SILVER

Department of Terrestrial Magnetism, Carnegie Institution of Washington, Washington, D.C. 20015

Abstract. IDA records of the 19 Sept 85 Michoacan earthquake and its large aftershock of 21 Sept 85 have been used to estimate their source-mechanism spectra $\hat{\mathbf{M}}(\omega)$ and total-moment spectra $M_T(\omega)$ in 1-mHz bands over the frequency interval 1-11 mHz. Source mechanisms, obtained by the phase-equalization method of Riedesel and Jordan, show no significant frequency dependence and no significant non-double-couple components. The best average double-couple solution has a strike, dip and rake of 289°, 19° and 76° for the main event, and 293°, 24° and 73° for the aftershock. Total-moment spectra, obtained by the power-spectral method of Silver and Jordan, are parametrized by a total integrated moment M_T^0 and a characteristic time τ_c. For the main event, we obtain $M_T^0 = (10.7 \pm 2.0) \times 10^{20}$ N-m and $\tau_c = 49 \pm 7$ s; the corresponding parameters for the aftershock are $M_T^0 = (2.6 \pm 0.6) \times 10^{20}$ N-m and $\tau_c = 30 \pm 11$ s. Both events are relatively slow; in particular, the aftershock has a larger characteristic time than either the fast-rupturing 29 Nov 78 Oaxaca or the 14 Mar 79 Petalan earthquakes, although the static moments are about the same. Our results support the model of the main shock as a multiple-rupture event with moment release occuring as long as 100 s after the initial break.

INTRODUCTION

The Michoacan earthquake of 19 Sept 1985 and its large aftershock of 21 Sept 1985 were well recorded on the International Deployment of Accelerometers (IDA) network of long-period gravimeters. We have employed the data from 13 IDA stations to study the low-frequency source properties of these events. The spectrum of a moment-rate tensor $\mathbf{M}(\omega)$ can be factorized into a total scalar moment $M_T(\omega)$ and a source mechanism $\hat{\mathbf{M}}(\omega)$, a second-rank tensor with unit euclidean norm [*Silver and Jordan*, 1982]:

$$\mathbf{M}(\omega) = \sqrt{2}\, M_T(\omega)\, \hat{\mathbf{M}}(\omega) \tag{1}$$

We have estimated the source-mechanism spectrum $\hat{\mathbf{M}}(\omega)$ by the moment-tensor inversion method of *Riedesel and Jordan* [1986] and the total-moment spectrum $M_T(\omega)$ by the technique of *Silver and Jordan* [1982, 1983].

Twelve stations were employed for each event, with eleven common to both. The data were edited to eliminate nonlinearities in the initial body waves, the R_1 surface-wave packets, and, in some cases, R_2 surface waves. All stations recorded R_3 and later wave groups without any apparent nonlinear distortion. Five hours of record following the first good time point were used in the analysis. Transfer functions relating the moment-rate tensor to acceleration were generated from model 1066A [*Gilbert and Dziewonski*, 1975] assuming the centroid latitudes, longitudes and depths reported by Harvard [D. Giardini, personal communication, 1986]: 17.97°N, 102.07°W, 22km for the main event and 17.61°N, 101.48°W, 22 km for the aftershock.

SOURCE-MECHANISM SPECTRA

The data functionals employed by the moment-tensor inversion method of *Riedesel and Jordan* [1986] are integrals of the complex acceleration spectra over narrow frequency bands (0.1 mHz in this study) centered on the fundamental spheroidal modes. The frequency-domain averaging reduces the sensitivity of the estimates to attenuation and splitting [*Gilbert*, 1973; *Jordan*, 1978]. The algorithm involves a nonlinear phase-equalization procedure to compensate for centroid time shifts, the effects of unmodeled earth structure, and station timing errors. In this study, estimates $\mathbf{M}(\omega_n)$ are obtained over the frequency interval 1-11 mHz by inverting the integrals in discrete 1-mHz bands centered on the frequencies $\omega_n = (n + 1/2)$ mHz; $n = 1, 2, \ldots 10$. This interval contains 101 fundamental modes, about ten per millihertz, so that for the Michoacan earthquakes,

approximately 120 complex numbers are used to derive the moment-rate tensor in each 1-mHz band. *Riedesel and Jordan* [1986] have demonstrated that this procedure yields reliable narrow-band estimates of the source-mechanism spectrum to frequencies as high as 11 mHz and that the errors derived for the estimates adequately model the uncertainties induced by noise in the data, including signal-generated noise.

Good measures of estimation error are essential in testing for the frequency dependence of the source spectrum and the existence of non-double-couple components, but these have generally not been available in the standard procedures for moment-tensor inversion [*Dziewonski et al.*, 1981; *Sipkin*, 1982]. Part of the problem is simply the difficulty in manipulating and displaying the autocovariance of a second-rank tensor. *Riedesel and Jordan* [1982] have devised a graph of the source-mechanism tensor $\hat{\mathbf{M}}$ which facilitates the visualization of its uncertainties and their use in hypothesis testing, and we employ this diagram here. The graph is based on the eigenvector expansion $\hat{\mathbf{M}} = \sum \lambda_i \hat{\mathbf{e}}_i \hat{\mathbf{e}}_i$. Assuming the eigenvectors are ordered such that $\lambda_1 \geq \lambda_2 \geq \lambda_3$, we construct the unit vector $\hat{\boldsymbol{\lambda}} = \sum \lambda_i \hat{\mathbf{e}}_i$. A plot of $\hat{\boldsymbol{\lambda}}$, $\hat{\mathbf{e}}_1$, $\hat{\mathbf{e}}_2$ and $\hat{\mathbf{e}}_3$ on the unit focal sphere is isomorphic to $\hat{\mathbf{M}}$, and thus completely characterizes the source mechanism. On such a plot the three vectors $\hat{\mathbf{d}} = (\hat{\mathbf{e}}_1 - \hat{\mathbf{e}}_3)/\sqrt{2}$, $\hat{\mathbf{l}} = (\hat{\mathbf{e}}_1 - 1/2\ \hat{\mathbf{e}}_2 - 1/2\ \hat{\mathbf{e}}_3)/\sqrt{3/2}$, and $\hat{\mathbf{i}} = (\hat{\mathbf{e}}_1 + \hat{\mathbf{e}}_2 + \hat{\mathbf{e}}_3)/\sqrt{3}$ represent the values of $\hat{\boldsymbol{\lambda}}$ for a pure double-couple, a pure compensated linear vector dipole, and a pure dilatation, respectively. The great circle containing $\hat{\mathbf{d}}$ and $\hat{\mathbf{l}}$ is the locus of all purely deviatoric mechanisms in the eigenvector reference frame. The stationarity of the eigenvalues λ_i with respect to the eigenvectors $\hat{\mathbf{e}}_i$ insures that, to first order, the uncertainties in $\hat{\boldsymbol{\lambda}}$ are uncorrelated with the errors in the eigenvectors and can thus be expressed in the reference frame ($\hat{\mathbf{d}}$, $\hat{\mathbf{l}}$, $\hat{\mathbf{i}}$). These uncertainties are plotted as a 95%-confidence ellipse about $\hat{\boldsymbol{\lambda}}$ on the focal sphere, which allows various hypotheses regarding the source mechanism to be tested by inspection. For example, the hypothesis that $\hat{\mathbf{M}}$ is a double-couple ($\hat{\boldsymbol{\lambda}} = \hat{\mathbf{d}}$) is rejected if $\hat{\mathbf{d}}$ falls outside the $\hat{\boldsymbol{\lambda}}$ confidence ellipse. The marginal uncertainties in the principal axes can be similarly calculated using first-order perturbation theory, and they are also plotted as 95%-confidence ellipses. Therefore, on a single focal sphere we display the source mechanism $\hat{\mathbf{M}}$, including its non-double-couple components, and a complete representation of its uncertainties, except for the covariances between the principal axes.

The source-mechanism spectra for the Michoacan earthquakes are shown in Figure 1. Two sets of mechanisms were calculated for each event. In the first (spectra *A* and *C*), all elements of $\mathbf{M}$ were retained in the solution. The error ellipses for the $\hat{\boldsymbol{\lambda}}$ vector and the principal axes are large at low frequencies, reflecting the poor resolution of the long-period data in determining $M_{r\theta}$ and $M_{r\phi}$

for shallow-focus sources [*Kanamori and Given*, 1981, 1982] and *tr* **M** in general [*Mendiguren and Aki*, 1978]. To examine the constraints on the other components of the source mechanism, we computed a second set of spectra, columns *B* and *D* of Figure 1, where the trace of **M** and its $r\theta$ and $r\phi$ components were treated as "nuisance parameters" and projection operators were applied to annihilate the dependence of the data equations on these components [*Riedesel and Jordan*, 1986]. The error-normalized equations are solved by a generalized inverse, so that the projected components in spectra *B* and *D* are set equal to zero; in particular, the axis corresponding to the maximum eigenvalue is vertical, and the $\hat{\lambda}$ vector is constrained to lie on the deviatoric great circle. It should be emphasized that this solution is not the same as obtained by the standard procedure of fixing *tr* **M**, $M_{r\theta}$ and $M_{r\phi}$ to be zero [e.g., *Kanamori and Given*, 1982], since the estimation errors on the unprojected elements of **M** calculated by the Riedesel-Jordan method are unconditional on the values of the nuisance parameters. In the projected spectra, the estimation errors are generally largest at high frequency and obtain a minimum in the 3–4-mHz band, where the signal-to-noise ratio of the normal-mode data is highest.

None of the spectra in Figure 1 show any significant frequency dependence or any significant non-double-couple behavior. Among the twenty unprojected mechanisms in columns *A* and *C* of Figure 1, for example, the 95% confidence ellipse of $\hat{\lambda}$ contains $\hat{d}$ in all cases but one, as would be expected from random errors. The mechanisms obtained by averaging the variance-weighted, unprojected spectra are listed in Table 1 and displayed in Figure 2. Neither has a significant non-double-couple component. The strike and dip of the best-fitting fault plane are somewhat greater for the aftershock than the main event (Table 1), but given their uncertainties, the two mechanisms are not significantly different at the 95% confidence level (chi-square of 5.9 against a critical value of 11.1). Although there is a trade-off between strike and rake of the best-fitting double couple, both mechanisms show a significant left-lateral strike-slip component, which is consistent with other thrust earthquakes along this section of the Middle America Trench [*Chael and Stewart*, 1982]. The slip-vector azimuth is N33°E for the main event and N40°E for the aftershock, which compares with N37°E predicted by the RM2 plate-motion model [*Minster and Jordan*, 1978].

TOTAL-MOMENT SPECTRA

The size of an earthquake is measured by a total integrated moment $M_T{}^0 \equiv M_T(0)$, and its duration is measured by a characteristic time $\tau_c = 2(\hat{\mu}^{(2)}/\hat{\mu}^{(0)})^{1/2}$, where $\hat{\mu}^{(n)}$ is the n^{th} central moment of the source time function [*Silver and Jordan*, 1983]. Following *Silver and Jordan*

[1983], we derive estimates of τ_c and M_T^0 by fitting total-moment observations with a spectrum of the form

$$M_T(\omega) = M_T^0 (1 + \omega^2 \tau_c^2/8)^{-1} \quad (2)$$

To obtain unbiased estimates of the total-moment spectrum, we have applied the scalar-moment estimation algorithm of *Silver and Jordan* [1982, 1983]. Their algorithm employs frequency-averaged power and cross spectra from a set of seismograms to derive an optimal estimate of M_T conditional on a probability distribution assumed for $\hat{\mathbf{M}}$.

For the Michoacan earthquakes, we constructed a gaussian approximation to the $\hat{\mathbf{M}}$ distribution from the estimates and uncertainties given in Figure 2 according to equation (4.67) of *Silver and Jordan* [1982]. We specialized the total-moment estimation algorithm to power spectra, which were integrated over disjunct 1-mHz bands in the interval 1-11 mHz. The resulting total-moment spectra are plotted in Figure 3, and the parameters derived by fitting equation (2) to these spectra are listed in Table 1.

The static moment of the Michoacan main event is $(10.7 \pm 2.0) \times 10^{20}$ N-m, consistent with the single-station CMT value of 13×10^{20} N-m obtained by *Ekström et al.* [1986]. The large correlated uncertainties in total-moment estimates of Figure 3 reflect their sensitivity to the nodal-plane orientation of the assumed mechanism. A dip of 19° is obtained by averaging $\hat{\mathbf{M}}$ over the entire 1-11 mHz band (Table 1), but this dip could be biased high by our inability to resolve $M_{r\theta}$ and $M_{r\phi}$ at low frequencies. Decreasing the dip to 10° would increase the moment to about 19 $\times 10^{20}$ N-m, in general agreement with the conclusions of *Eissler et al.* [1986]. M_T^0 for the aftershock is about a factor of four less than the main event, which is the average amplitude ratio observed on the IDA seismograms.

The characteristic time τ_c estimated by the Silver-Jordan method is 49 ± 7 s for the main event and 30 ± 11 s for the aftershock. We can compare these times with the difference Δt between the temporal centroid of the earthquake and its origin time measured by high-frequency P waves. Using the temporal centroids from our moment-tensor inversions and origin times from the NEIS, we obtain $\Delta t = 34 \pm 5$ s and 24 ± 5 s for the main shock and aftershock, respectively. Assuming the rate of moment release is constant over the duration of faulting (in which case, $2\Delta t$ is the "source process time" of *Kanamori and Given* [1981]), we can relate the centroid time shift to the characteristic time by the equation $\tau_c = 2\Delta t/\sqrt{3}$; this gives $\tau_c = 39 \pm 6$ s and 28 ± 6 s. Hence, two

independent estimators of characteristic time, one based on spectral roll-off and one based on centroid time shift, yield similar results.

Although not statistically significant at the error levels quoted, the fact that these two estimators of τ_c differ by 10 s for the main event could be an indication that the moment release is not constant during the rupture process, but concentrated towards the origin time. Indeed, the source time functions obtained by *Ekström et al.* [1986] and *Houston and Kanamori* [1986] show that the moment release for the main shock took place in a series of discrete pulses at intervals of about 25 s, with amplitudes diminishing in time. *Houston and Kanamori's* [1986, Figure 5] time function is characterized by moment release up to 100 s after the initial break. The duration parameters calculated from the first three polynomial moments of this time function are Δt = 33 s and τ_c = 46 s, in good agreement with our estimates. Both the main event and the aftershock plot in the slow-earthquake field of *Silver and Jordan* [1983, Figure 20]. In particular, the aftershock apparently has a larger characteristic time than either the fast-rupturing 29 Nov 78 Oaxaca or the 14 Mar 79 Petalan earthquakes studied by *Silver and Jordan* [1983], although its static moment is about the same.

REFERENCES

Chael, E.P., and G.S Stewart, Recent large earthquakes along the Middle American Trench and their implications for the subduction process, *J. Geophys. Res.*, **87**, 329-338, 1982.

Dziewonski, A.M., T.A. Chou, and J.H. Woodhouse, Determination of earthquake source parameters from wave-form data for studies of global and regional seismicity, *J. Geophys. Res.*, **86**, 2825-2852, 1981.

Eissler, H., L. Astiz, and H. Kanamori, Tectonic setting and source parameters of the September 19, 1985 Michoacan, Mexico earthquake, *Geophys. Res. Lett.*, this issue.

Ekström, G., A.M. Dziewonski, and J. Steim, Single station CMT; application to the Michoacan, Mexico, earthquake of September 19, 1985, *Geophys. Res. Lett.*, **13**, 173-176, 1986.

Gilbert, F., Derivation of source parameters from low-frequency spectra, *Phil. Trans. R. Soc. Lond., Ser. A*, **274**, 369-371, 1973.

Gilbert, F., and A.M. Dziewonski, An application of normal mode theory to the retrieval of structural parameters and source mechanisms from seismic spectra. *Phil. Trans. R. Soc. Lond., Ser. A*, **278** 187-269, 1975.

Houston, H., and H. Kanamori, Source characteristics of the 1985 Michoacan, Mexico earthquake at short periods, *Geophys. Res. Lett.*, this issue.

Jordan, T.H., A procedure for estimation lateral variations from low-frequency eigenspectra data, *Geophys. J. R. Astr. Soc.*, **52**, 441-455, 1978.

Kanamori, H., and J.W. Given, Use of long-period surface waves for fast determination of earthquake source parameters, *Phys. Earth Planet. Inter.*, 27, 8-31, 1981.

Kanamori, H., and J.W. Given, Use of long-period surface waves for fast determination of earthquake source parameters 2. Preliminary determination of source mechanisms of large earthquakes ($M_S > 6.5$) in 1980, *Phys. Earth Planet. Inter.*, 30, 260-268, 1982.

Mendiguren, J.A., and K. Aki, Source mechanism of the deep Colombian earthquake of July 31, 1970 from the free oscillation data, *Geophys. J. R. Astr.Soc.*, 55, 539-556, 1978.

Minster, J.B., and T.H. Jordan, Present-day plate motions, *J. Geophys. Res.*, 83, 5331-5354, 1978.

Riedesel, M.A., and T.H. Jordan, Display and assessment of source mechanisms with non-double-couple components, *Eos*, 63, 1027-1028, 1982.

Riedesel, M.A., and T.H. Jordan, Multiple-band estimates of moment tensors at low frequencies and their uncertainties, in preparation, 1986.

Silver, P.G., and T.H. Jordan, Optimal estimation of scalar seismic moment, *Geophs. J. R. astr. Soc.*, 70, 755-787, 1982.

Silver, P.G., and T.H. Jordan, Total-moment spectra of fourteen large earthquakes, *J. Geophys. Res.*, 88, 3273-3293, 1983.

Sipkin, S.A., Estimation of earthquake source parameters by the inversion of waveform data: synthetic waveforms, *Phys. Earth Planet. Inter.*, 30, 242-259, 1982.

TABLE 1. Source parameters for the Michoacan earthquakes.

Source Parameters		19 Sept 85	21 Sept 85
Mechanism:			
$\hat{M}_{rr}$		.495 ± .116	.431 ± .114
$\hat{M}_{\theta\theta}$		−.292 ± .072	−.469 ± .056
$\hat{M}_{\phi\phi}$		−.060 ± .031	−.232 ± .029
$\hat{M}_{r\theta}$		.463 ± .063	.364 ± .052
$\hat{M}_{r\phi}$		−.336 ± .056	−.373 ± .042
$\hat{M}_{\theta\phi}$		.139 ± .036	.252 ± .026
Slip vector azimuth:		33°	40°
Best double couple:			
Strike		289°	293°
Dip		19°	24°
Rake		76°	73°
Total Moment Spectrum:			
M_T^0	(10^{20} N-m)	10.7 ± 2.0	2.6 ± 0.6
τ_c	(s)	49 ± 7	30 ± 11

Source mechanism parameters correspond to the variance-weighted averages of Figure 2. Total scalar moments and characteristic times are obtained from fits of equation (2) to the total-moment spectra of Figure 3.

Figure Captions

Fig. 1. Source-mechanism spectra $\hat{\mathbf{M}}(\omega)$ for the Michoacan earthquake of 19 Sept 85 (columns *A* and *B*) and its large aftershock of 21 Sept 85 (columns *C* and *D*) over the frequency interval 1-11 mHz. Each circle is a focal-sphere plot of the normalized moment tensor $\hat{\mathbf{M}}(\omega)$ in a 1-mHz band derived from 12 IDA records by normal-mode method of *Riedesel and Jordan* [1986]. Columns *A* and *C* are unprojected mechanisms for the main event and aftershock, respectively, whereas columns *B* and *D* are projected mechanisms for which $tr\ \hat{\mathbf{M}}$, $\hat{M}_{r\theta}$, and $\hat{M}_{r\theta}$ have been annihilated by the orthogonalization procedure described in the text. Each $\hat{\mathbf{M}}$ is represented by the source-mechanism diagram introduced by *Riedesel and Jordan* [1982]. The three principal axes $\hat{\mathbf{e}}_1$, $\hat{\mathbf{e}}_2$ and $\hat{\mathbf{e}}_3$, corresponding to eigenvalues $\lambda_1 \geq \lambda_2 \geq \lambda_3$, are plotted as **T**, **N** and **P** on a stereographic projection of the lower focal hemisphere with their marginal 95% confidence ellipses (thin lines). The mechanism is characterized by the unit vector $\hat{\boldsymbol{\lambda}} = \sum \lambda_i \hat{\mathbf{e}}_i$ and its 95% confidence ellipse (thick line), which can be compared with the canonical unit vectors $\hat{\mathbf{d}}$, $\hat{\mathbf{l}}$, and $\hat{\mathbf{i}}$, representing a pure double-couple, a pure compensated linear vector dipole, and a pure dilatation, respectively. The dashed line shows the locus of all deviatoric mechanisms. Vectors are plotted as ∇ if they are on the lower focal hemisphere and as a Δ if they are projected from the upper hemisphere.

Fig. 2. Source mechanisms for the Michoacan earthquake of 19 Sept 85 (left) and its large aftershock of 21 Sept 85 (right) obtained by averaging the spectra *A* and *C* of Figure 1, weighted by their covariance tensors. Plotting conventions are the same as in Figure 1. At the 95% confidence level corresponding to the error ellipses, the mechanism vectors $\hat{\boldsymbol{\lambda}}$ are not significantly different from the double-couple vectors $\hat{\mathbf{d}}$, and the hypothesis that the two events have the same double-couple mechanism cannot be rejected. The source parameters for these average solutions are listed in Table 1.

Fig. 3. Total-moment spectra over the frequency interval 1-11 mHz for the Michoacan earthquake of 19 Sept 85 (squares) and its large aftershock of 21Sept 85 (circles). The spectral estimates and their one-sigma error bars were computed from 1-mHz averages of IDA power spectra using the method of *Silver and Jordan* [1982, 1983]. Estimation errors are correlated from band to band by uncertainties in the source mechanisms of Figure 2. Solid lines are theoretical spectra obtained by fitting equation (2) to the observations; the parameters are $M_T{}^0 = (10.7 \pm 2.0) \times 10^{20}$ N-m and τ_c = 49 ± 6 s for the main event, and $M_T{}^0 = (2.6 \pm 0.5) \times 10^{20}$ N-m and $\tau_c = 30 \pm 10$ s for the aftershock.

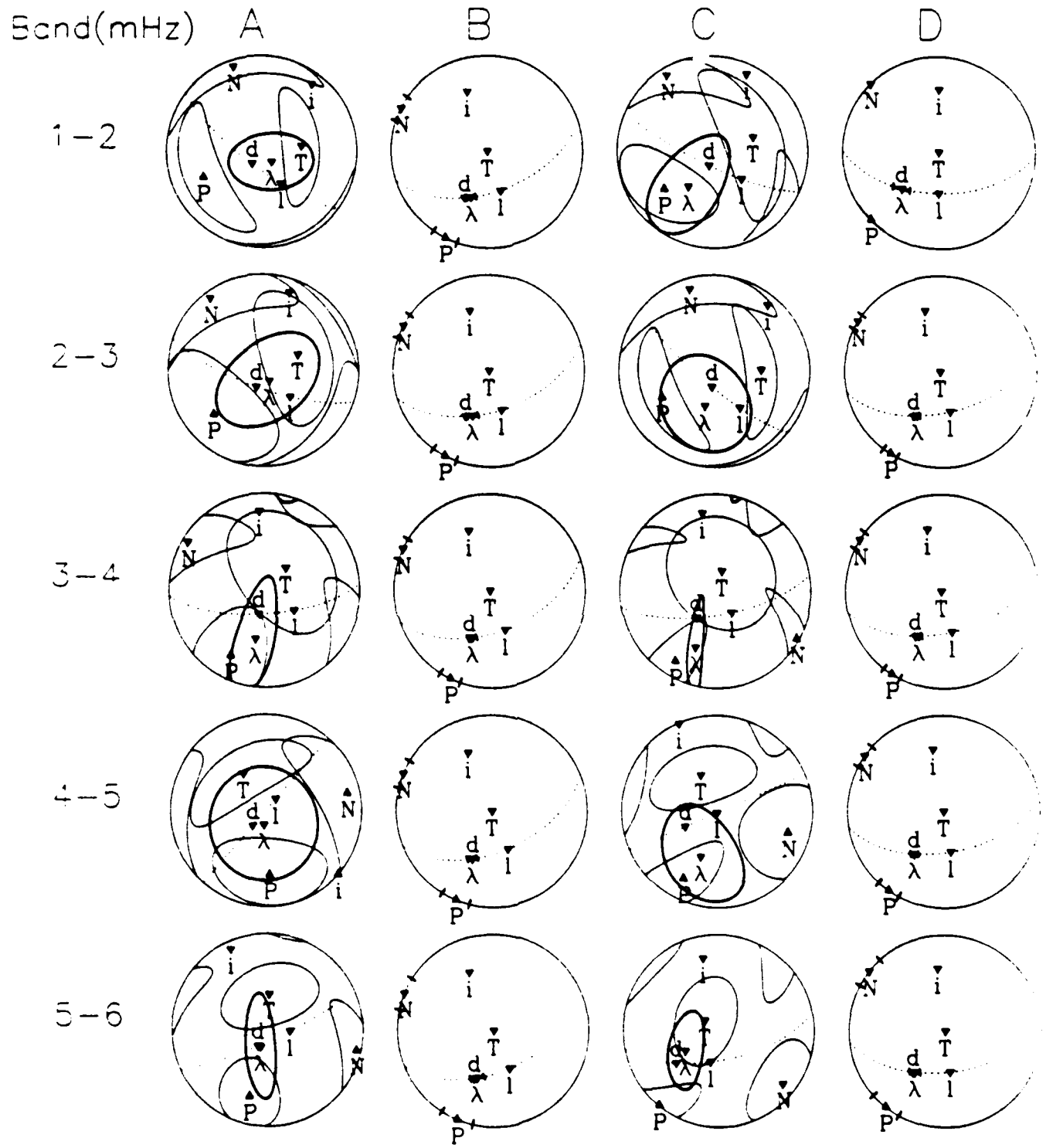

Figure 1

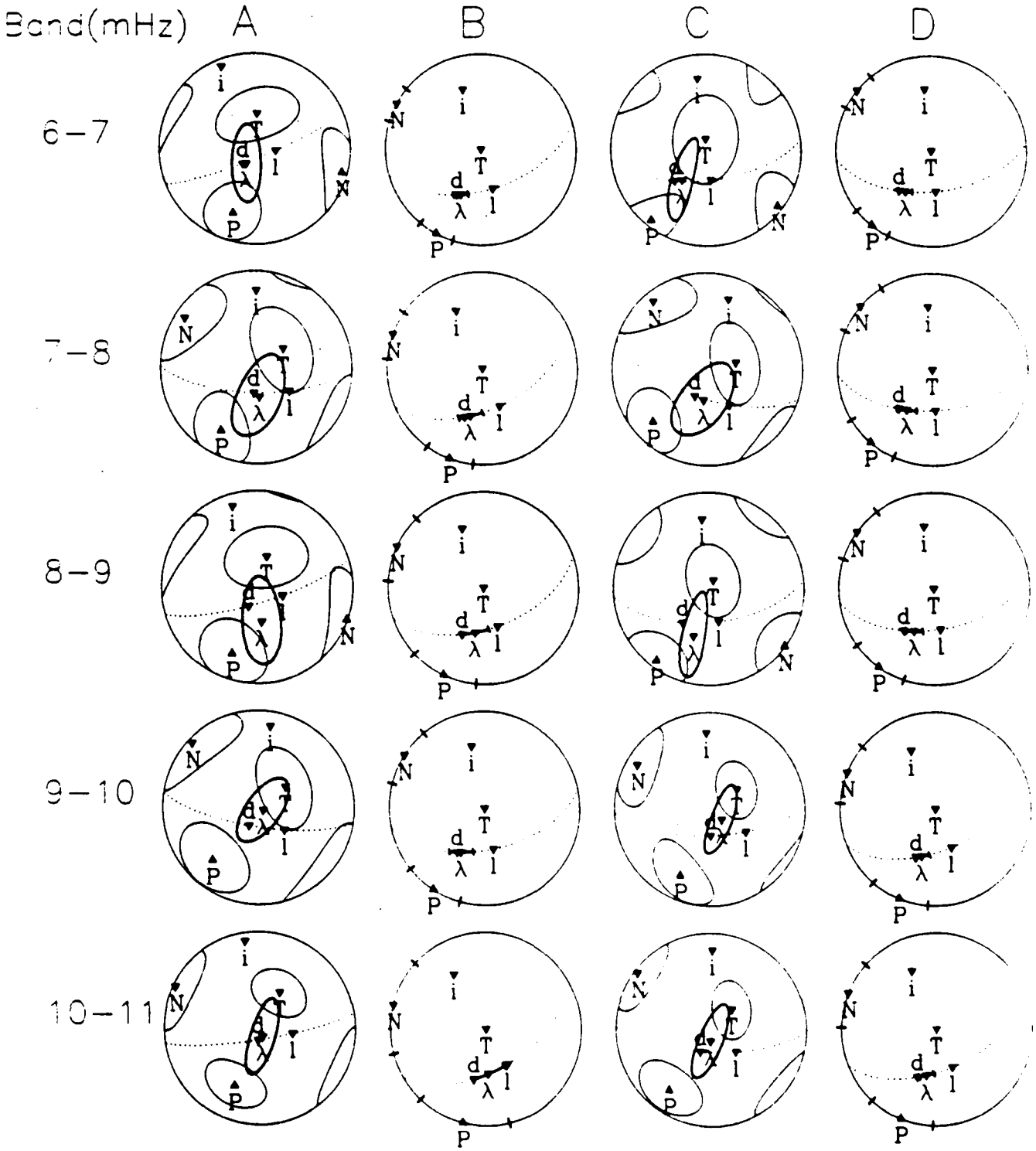

Figure 1 (cont.)

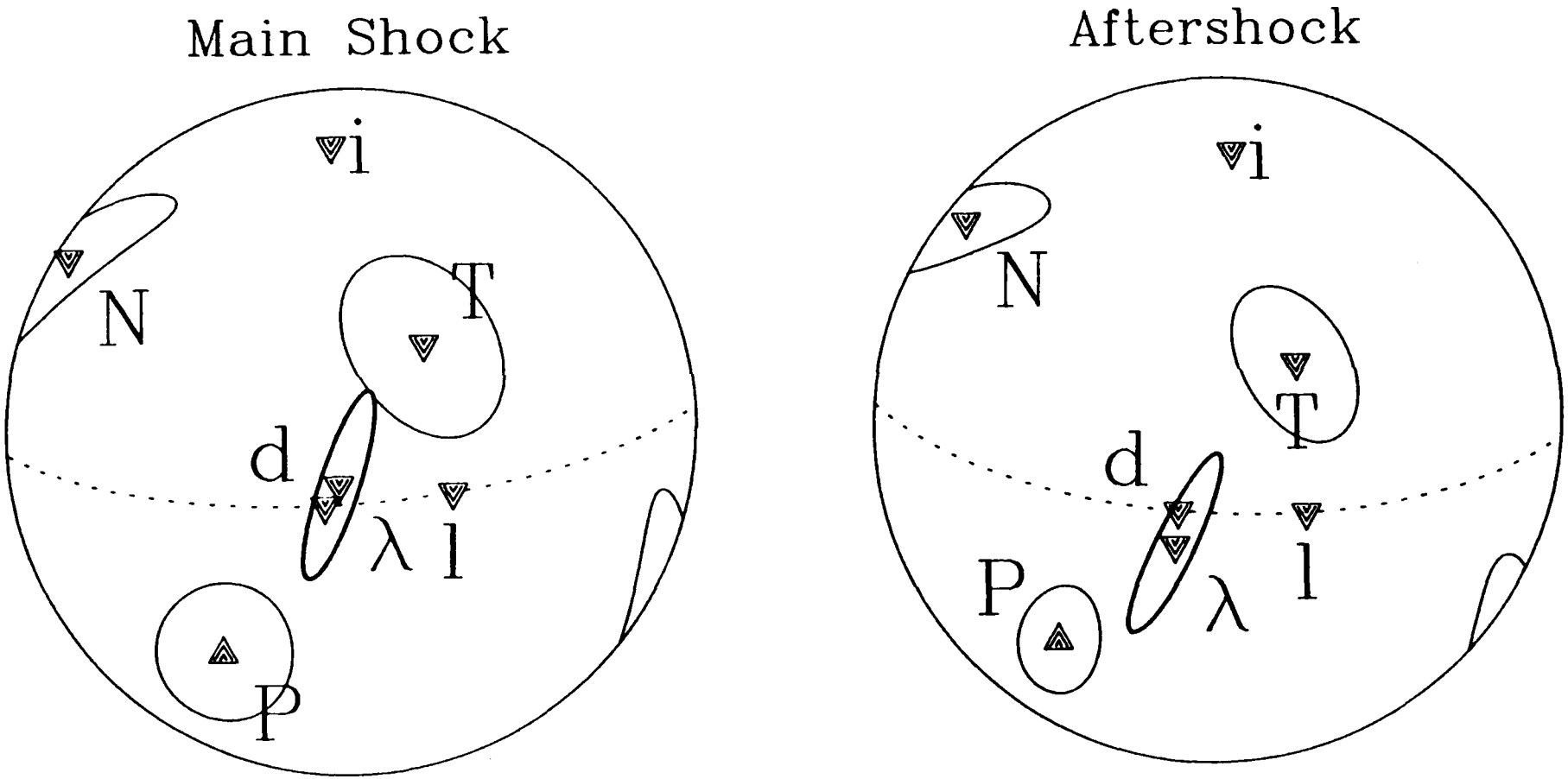

Figure 2

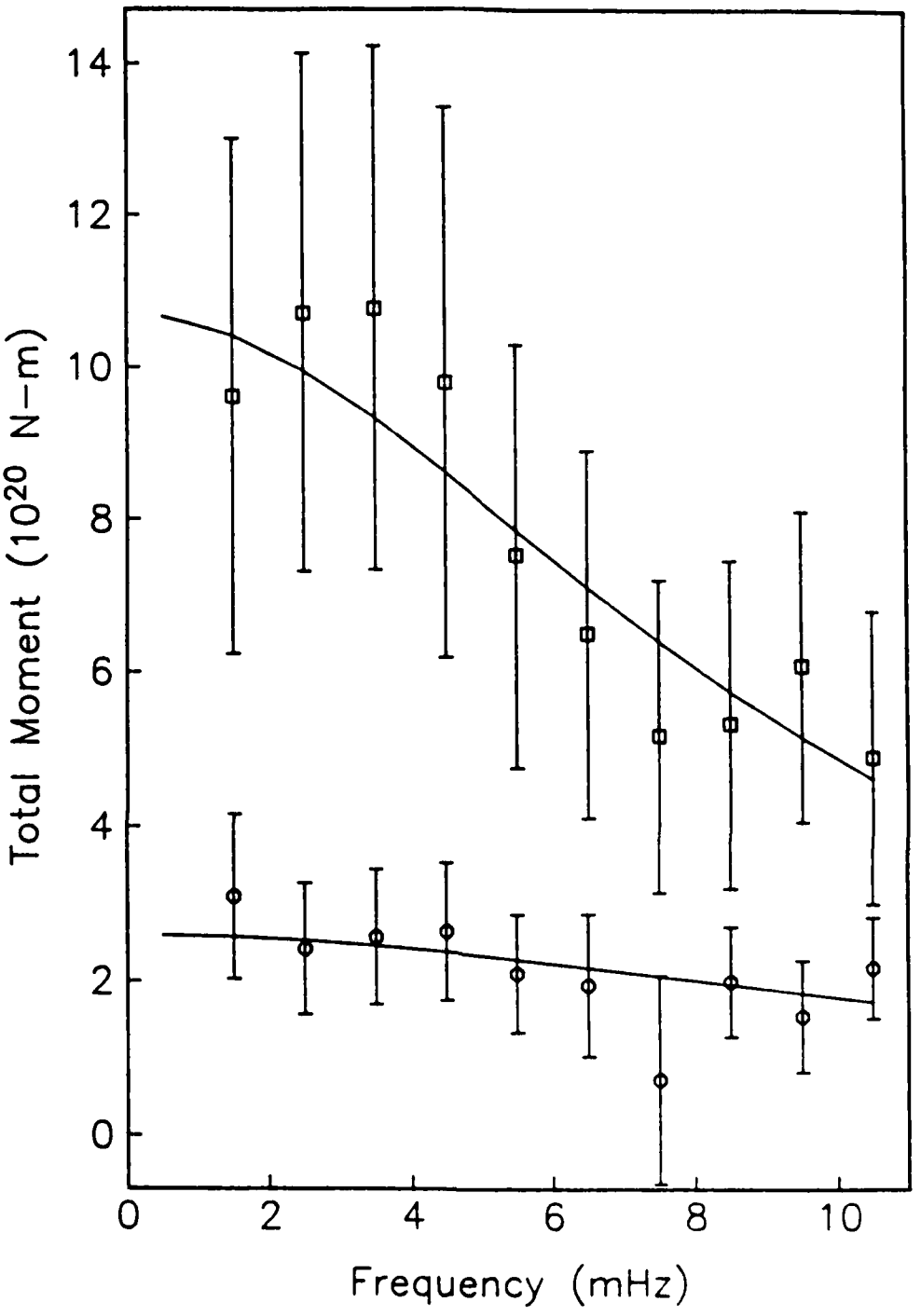

Figure 3

DISTRIBUTION LIST

Dr. Monem Abdel-Gawad
Rockwell International Science Center
1049 Camino Dos Rios
Thousand Oaks, CA 91360

Professor Keiiti Aki
Center for Earth Sciences
University of Southern California
University Park
Los Angeles, CA 90089-0741

Professor Shelton S. Alexander
Geosciences Department
403 Deike Building
The Pennsylvania State University
University Park, PA 16802

Professor Charles B. Archambeau
Cooperative Institute for Research in
Environmental Sciences
University of Colorado
Boulder, CO 80309

Dr. Thomas C. Bache Jr.
Science Applications Int'l Corp.
10210 Campus Point Drive
San Diego, CA 92121

Dr. James Bulau
Rockwell International Science Center
1049 Camino Dos Rios
P.O. Box 1085
Thousand Oaks, CA 91360

Dr. Douglas R. Baumgardt
Signal Analysis and Systems Division
ENSCO, Inc.
5400 Port Royal Road
Springfield, VA 22151-2388

Dr. S. Bratt
Science Applications Int'l Corp.
10210 Campus Point Drive
San Diego, CA 92121

Professor John Ebel
Department of Geology & Geophysics
Boston College
Chestnut Hill, MA 02167

Woodward-Clyde Consultants
Attn: Dr. Lawrence J. Burdick
Dr. Jeff Barker
P.O. Box 93245
Pasadena, CA 91109-3245 (2 copies)

Dr. Roy Burger
1221 Serry Rd.
Schenectady, NY 12309

Professor Robert W. Clayton
Seismological Laboratory
Division of Geological and Planetary
Sciences
California Institute of Technology
Pasadena, CA 91125

Dr. Vernon F. Cormier
Earth Resources Laboratory
Department of Earth, Atmospheric and
Planetary Sciences
Massachusetts Institute of Technology
42 Carleton Street
Cambridge, MA 02142

Professor Anton M. Dainty
Earth Resources Laboratory
Department of Earth, Atmospheric and
Planetary Sciences
Massachusetts Institute of Technology
42 Carleton Street
Cambridge, MA 02142

Dr. Zoltan A. Der
Teledyne Geotech
314 Montgomery Street
Alexandria, VA 22314

Prof. Adam Dziewonski
Hoffman Laboratory
Harvard University
20 Oxford St.
Cambridge, MA 02138

Professor John Ferguson
Center for Lithospheric Studies
The University of Texas at Dallas
P.O. Box 830688
Richardson, TX 75083-0688

Dr. Jeffrey W. Given
Sierra Geophysics
11255 Kirkland Way
Kirkland, WA 98033

Prof. Roy Greenfield
Geosciences Department
403 Deike Building
The Pennsylvania State University
University Park, PA 16802

Professor David G. Harkrider
Seismological Laboratory
Division of Geological and Planetary Sciences
California Institute of Technology
Pasadena, CA 91125

Professor Donald V. Helmberger
Seismological Laboratory
Division of Geological and Planetary Sciences
California Institute of Technology
Pasadena, CA 91125

Professor Eugene Herrin
Institute for the Study of Earth & Man
Geophysical Laboratory
Southern Methodist University
Dallas, TX 75275

Professor Robert B. Herrmann
Department of Earth and Atmospheric Sciences
Saint Louis University
Saint Louis, MO 63156

Professor Lane R. Johnson
Seismographic Station
University of California
Berkeley, CA 94720

Professor Thomas H. Jordan
Department of Earth, Atmospheric and Planetary Sciences
Massachusetts Institute of Technology
Cambridge, MA 02139

Dr. Alan Kafka
Department of Geology & Geophysics
Boston College
Chestnut Hill, MA 02167

Professor Charles A. Langston
Geosciences Department
403 Deike Building
The Pennsylvania State University
University Park, PA 16802

Professor Thorne Lay
Department of Geological Sciences
1006 C.C. Little Building
University of Michigan
Ann Arbor, MI 48109-1063

Dr. George R. Mellman
Sierra Geophysics
11255 Kirkland Way
Kirkland, WA 98033

Professor Brian J. Mitchell
Department of Earth and Atmospheric Sciences
Saint Louis University
Saint Louis, MO 63156

Professor Thomas V. McEvilly
Seismographic Station
University of California
Berkeley, CA 94720

Dr. Keith L. McLaughlin
Teledyne Geotech
314 Montgomery Street
Alexandria, VA 22314

Professor Otto W. Nuttli
Department of Earth and Atmospheric Sciences
Saint Louis University
Saint Louis, MO 63156

Professor Paul G. Richards
Lamont-Doherty Geological Observatory
of Columbia University
Palisades, NY 10964

Dr. Norton Rimer
S-Cubed
A Division of Maxwell Laboratory
P.O. 1620
La Jolla, CA 92038-1620

Professor Larry J. Ruff
Department of Geological Sciences
1006 C.C. Little Building
University of Michigan
Ann Arbor, MI 48109-1063

Professor Charles G. Sammis
Center for Earth Sciences
University of Southern California
University Park
Los Angeles, CA 90089-0741

Dr. David G. Simpson
Lamont-Doherty Geological Observatory
of Columbia University
Palisades, NY 10964

Dr. Jeffrey L. Stevens
S-CUBED,
A Division of Maxwell Laboratory
P.O. Box 1620
La Jolla, CA 92038-1620

Professor Brian Stump
Institute for the Study of Earth
and Man
Geophysical Laboratory
Southern Methodist University
Dallas, TX 75275

Professor Ta-liang Teng
Center for Earth Sciences
University of Southern California
University Park
Los Angeles, CA 90089-0741

Dr. R. B. Tittmann
Rockwell International Science Center
1049 Camino Dos Rios
P.O. Box 1085
Thousand Oaks, CA 91360

Professor M. Nafi Toksoz
Earth Resources Laboratory
Department of Earth, Atmospheric and
Planetary Sciences
Massachusetts Institute of Technology
42 Carleton Street
Cambridge, MA 02142

Professor Terry C. Wallace
Department of Geosciences
Building #11
University of Arizona
Tucson, AZ 85721

Prof. John H. Woodhouse
Hoffman Laboratory
Harvard University
20 Oxford St.
Cambridge, MA 02138

Dr. G. Blake
US Dept of Energy/DP 331
Forrestal Building
1000 Independence Ave.
Washington, D.C. 20585

Dr. Michel Bouchon
Universite Scientifique et
Medicale de Grenoble
Laboratoire de Geophysique
Interne et Tectonophysique
I.R.I.G.M.-B.P. 68
38402 St. Martin D'Heres
Cedex FRANCE

Dr. Hilmar Bungum
NTNF/NORSAR
P.O. Box 51
Norwegian Council of Science,
Industry and Research, NORSAR
N-2007 Kjeller, NORWAY

Dr. Alan Douglas
Ministry of Defense
Blacknest, Brimpton, Reading RG7-4RS
UNITED KINGDOM

Professor Peter Harjes
Institute for Geophysik
Rhur University
Bochum
P.O. Box 102148
4630 Bochum 1
FEDERAL REPUBLIC OF GERMANY

Dr. James Hannon
Lawrence Livermore National Laboratory
P.O. Box 808
Livermore, CA 94550

Dr. E. Husebye
NTNF/NORSAR
P.O. Box 51
N-2007 Kjeller, NORWAY

Dr. Arthur Lerner-Lam
Lamont-Doherty Geological Observatory
of Columbia University
Palisades, NY 10964

Mr. Peter Marshall
Procurement Executive
Ministry of Defense
Blacknest, Brimpton, Reading RG7-4RS
UNITED KINGDOM

Dr. B. Massinon
Societe Radiomana
27, Rue Claude Bernard
75005, Paris, FRANCE

Dr. Pierre Mechler
Societe Radiomana
27, Rue Claude Bernard
75005, Paris, FRANCE

Mr. Jack Murphy
S-CUBED
Reston Geophysics Office
11800 Sunrise Valley Drive
Suite 1212
Reston, VA 22091

Dr. Svein Mykkeltveit
NTNF/NORSAR
P.O. Box 51
N-2007 Kjeller, NORWAY

Dr. Carl Newton
Los Alamos National Laboratory
P.O. Box 1663
Mail Stop C 335, Group ESS3
Los Alamos, NM 87545

Dr. Peter Basham
Earth Physics Branch
Department of Energy and Mines
1 Observatory Crescent
Ottawa, Ontario
CANADA K1A 0Y3

Professor J. A. Orcutt
Geological Sciences Division
Univ. of California at San Diego
La Jolla, CA 92093

Dr. Frank F. Pilotte
Director of Geophysics
Headquarters Air Force Technical
Applications Center
Patrick AFB, Florida 32925-6001

Professor Keith Priestley
University of Nevada
Mackay School of Mines
Reno, Nevada 89557

Mr. Jack Raclin
USGS - Geology, Rm 3C136
Mail Stop 928 National Center
Reston, VA 22092

Dr. Frode Ringdal
NTNF/NORSAR
P.O. Box 51
N-2007 Kjeller, NORWAY

Dr. George H. Rothe
Chief, Research Division
Geophysics Directorate
Headquarters Air Force Technical
Applications Center
Patrick AFB, Florida 32925-6001

Dr. Alan S. Ryall, Jr.
Center for Seismic Studies
1300 North 17th Street
Suite 1450
Arlington, VA 22209-2308

Dr. Jeffrey L. Stevens
S-CUBED,
A Division of Maxwell Laboratory
P.O. Box 1620
La Jolla, CA 92038-1620

Dr. Lawrence Turnbull
OSWR/NED
Central Intelligence Agency
CIA, Room 5G48
Washington, DC 20505

Professor Steven Grand
Department of Geology
245 Natural History Bldg
1301 West Green Street
Urbana, IL 61801

DARPA/PM
1400 Wilson Boulevard
Arlington, VA 22209

Defense Technical Information Center
Cameron Station
Alexandria, VA 22314 (12 copies)

Defense Intelligence Agency
Directorate for Scientific and
Technical Intelligence
Washington, D.C. 20301

Defense Nuclear Agency
Shock Physics Directorate/SS
Washington, D.C. 20305

Defense Nuclear Agency/SPSS
ATTN: Dr. Michael Shore
6801 Telegraph Road
Alexandria, VA 22310

AFOSR/NPG
ATTN: Director
Bldg 410, Room C222
Bolling AFB, Washington, D.C. 20332

AFTAC/CA (STINFO)
Patrick AFB, FL 32925-6001

AFWL/NTESC
Kirtland AFB, NM 87171

U.S. Arms Control & Disarmament Agency
ATTN: Mrs. M. Hoinkes
Div. of Multilateral Affairs, Rm 5499
Washington, D.C. 20451

U.S. Geological Survey
ATTN: Dr. T. Hanks
National Earthquake Research Center
345 Middlefield Road
Menlo Park, CA 94025

SRI International
333 Ravensworth Avenue
Menlo Park, CA 94025

Center for Seismic Studies
ATTN: Dr. C. Romney
1300 North 17th Street
Suite 1450
Arlington, VA 22209 (3 copies)

Dr. Robert Blandford
DARPA/GSD
1400 Wilson Boulevard
Arlington, VA 22209-2308

Ms. Ann Kerr
DARPA/GSD
1400 Wilson Boulevard
Arlington, VA 22209-2308

Dr. Ralph Alewine III
DARPA/GSD
1400 Wilson Boulevard
Arlington, VA 22209-2308

Mr. Edward Giller
Pacific Sierra Research Corp.
1401 Wilson Boulevard
Arlington, VA 22209

Science Horizons, Inc.
Attn: Dr. Bernard Minster
Dr. Theodore Cherry
710 Encinitas Blvd., Suite 101
Encinitas, CA 92024 (2 copies)

Dr. Jack Evernden
USGS - Earthquake Studies
345 Middlefield Road
Menlo Park, CA 94025

Dr. Lawrence Braile
Department of Geosciences
Purdue University
West Lafayette, IN 47907

Dr. G.A. Bollinger
Department of Geological Sciences
Virginia Polytechnical Institute
21044 Derring Hall
Blacksburg, VA 24061

Dr. L. Sykes
Lamont Doherty Geological Observatory
Columbia University
Palisades, NY 10964

Dr. S.W. Smith
Geophysics Program
University of Washington
Seattle, WA 98195

Dr. L. Timothy Long
School of Geophysical Sciences
Georgia Institute of Technology
Atlanta, GA 30332

Dr. N. Biswas
Geophysical Institute
University of Alaska
Fairbanks, AK 99701

Dr. Freeman Gilbert
Institute of Geophysics &
Planetary Physics
Univ. of California at San Diego
P.O. Box 109
La Jolla, CA 92037

Dr. Pradeep Talwani
Department of Geological Sciences
University of South Carolina
Columbia, SC 29208

University of Hawaii
Institute of Geophysics
Attn: Dr. Daniel Walker
Honolulu, HI 96822

Dr. Donald Forsyth
Department of Geological Sciences
Brown University
Providence, RI 02912

Dr. Jack Oliver
Department of Geology
Cornell University
Ithaca, NY 14850

Dr. Muawia Barazangi
Geological Sciences
Cornell University
Ithaca, NY 14853

Rondout Associates
Attn: Dr. George Sutton
Dr. Jerry Carter
Dr. Paul Pomeroy
P.O. Box 224
Stone Ridge, NY 12484 (3 copies)

Dr. M. Sorrells
Geotech/Teledyne
P.O. Box 28277
Dallas, TX 75228

Dr. Bob Smith
Department of Geophysics
University of Utah
1400 East 2nd South
Salt Lake City, UT 84112

Dr. Anthony Gangi
Texas A&M University
Department of Geophysics
College Station, TX 77843

Dr. Gregory B. Young
ENSCO, Inc.
5400 Port Royal Road
Springfield, CA 22151

Dr. Ben Menaheim
Weizman Institute of Science
Rehovot, ISRAEL 951729

Weidlinger Associates
Attn: Dr. Gregory Wojcik
620 Hansen Way, Suite 100
Palo Alto, CA 94304

Dr. Leon Knopoff
University of California
Institute of Geophysics & Planetary
Physics
Los Angeles, CA 90024

Dr. Kenneth H. Olsen
Los Alamos Scientific Laboratory
Post Office Box 1663
Los Alamos, NM 87545

Prof. Jon F. Claerbout
Prof. Amos Nur
Dept. of Geophysics
Stanford University
Stanford, CA 94305 (2 copies)

Dr. Robert Burridge
Schlumberger-Doll Research Ctr.
Old Quarry Road
Ridgefield, CT 06877

Dr. Eduard Berg
Institute of Geophysics
University of Hawaii
Honolulu, HI 96822

Dr. Robert Phinney
Dr. F.A. Dahlen
Dept. of Geological & Geophysical Sci.
Princeton University
Princeton, NJ 08540 (2 copies)

Dr. Kin-Yip Chun
Geophysics Division
Physics Department
University of Toronto
Ontario, CANADA M5S 1A7

New England Research, Inc.
Attn: Dr. Randolph Martin III
P.O. Box 857
Norwich, VT 05055

Sandia National Laboratory
Attn: Dr. H.B. Durham
Albuquerque, NM 87185

Dr. Gary McCartor
Mission Research Corp.
735 State Street
P. O. Drawer 719
Santa Barbara, CA 93102

Dr. W. H. K. Lee
USGS
Office of Earthquakes, Volcanoes,
& Engineering
Branch of Seismology
345 Middlefield Rd
Menlo Park, CA 94025

AFGL/XO
Hanscom AFB, MA 01731-5000

AFGL/LW
Hanscom AFB, MA 01731-5000

AFGL/SULL
Research Library
Hanscom AFB, MA 01731-5000 (2 copies)

Secretary of the Air Force (SAFRD)
Washington, DC 20330

Office of the Secretary Defense
DDR & E
Washington, DC 20330

HQ DNA
Attn: Technical Library
Washington, DC 20305

Director, Technical Information
DARPA
1400 Wilson Blvd.
Arlington, VA 22209

Los Alamos Scientific Laboratory
Attn: Report Library
Post Office Box 1663
Los Alamos, NM 87544

Dr. Thomas Weaver
Los Alamos Scientific Laboratory
Los Alamos, NM 87544

Dr. Al Florence
SRI International
333 Ravenswood Avenue
Menlo Park, CA 94025-3493

END

7-87

DTIC